Sticky Squishy & Stuck

A soft matter approach to membrane failure

Ties van de Laar

Propositions

1. Overestimating the volume fraction makes fragile glasses falsely appear strong. (this thesis)

2. The addition of a dust filter to a membrane microfluidic device is vital to disentangle the effects of sieving and particle-agglomerated clogging. (this thesis)

3. In order to tackle sustainability issues, science-based technical solutions should not be sidetracked by emotional arguments that lack such foundation.

4. Scientific hyping is dangerous, as it will lead to even further erosion of public trust in science.

5. Validation of results through reproducibility studies deserves to get as much attention as novel results.

6. It is a mistake for companies to try and steer the direction of governmental science funding to their short-term goals as it will stop long-term scientific progress on which the success of these very companies is based.

7. Nowadays the endless discussions about food and health have gotten out of hand; eating is a simple thermodynamic balance, what comes in, must go out.

Propositions belonging to the thesis, entitled
'Sticky, Squishy and Stuck; A soft matter approach to membrane failure'

Ties van de Laar
Wageningen, 25 May 2018

Sticky, Squishy & Stuck

a soft matter approach to membrane failure

Ties van de Laar

Thesis committee

Promotor
Prof. Dr C.G.P.H. Schroën
Personal chair at the Laboratory of Food Process Engineering
Wageningen University & Research

Co-promotor
Dr J.H.B. Sprakel
Associate professor, Physical Chemistry and Soft Matter
Wageningen University & Research

Other members
Prof. Dr A.H. Velders, Wageningen University & Research
Prof. Dr I.K. Voets, Eindhoven University of Technology
Prof. Dr M. Wessling, DWI – Leibniz-Institut für Interaktive Materialien e.V., Germany
Prof. Dr S.U. Egelhaaf, Heinrich Heine University Düsseldorf, Germany

This research was conducted under the auspices of
Graduate School VLAG (Advanced studies in Food Technology,
Agrobiotechnology, Nutrition and Health Sciences).

Sticky, Squishy & Stuck

A soft matter approach to membrane failure

Ties van de Laar

Thesis
submitted in fulfilment of the requirements for the degree of doctor
at Wageningen University
by the authority of the Rector Magnificus,
Prof. Dr A.P.J. Mol,
in the presence of the
Thesis Committee appointed by the Academic Board
to be defended in public
on Friday May 25th, 2018
at 11 a.m. in the Aula.

Ties van de Laar
Sticky, Squishy & Stuck— a soft matter approach to membrane failure
262 pages

PhD thesis, Wageningen University, Wageningen, the Netherlands (2018)
With references, with summary in English.

ISBN: 978-94-6343-757-8
DOI: https://doi.org/10.18174/443007

Contents

Chapter 1

Sticky Squishy & Stuck

Introduction

This thesis is the result of research at the interface between two scientific disciplines; membrane technology and soft matter science. The aim of this thesis is to explore common problems encountered in membrane processes by linking them to classical topics of study in soft matter science. In order to do so, we simplify the problems to their basic elements and design model systems to study these challenges in detail and provide new fundamental insights. In the following, we first provide a 'dictionary' linking these two different academic disciplines and provide a brief introduction and context to the three major themes in this thesis.

1.1 A microscopic look at membrane filtration

A membrane is a semi-permeable barrier that blocks the passage of some compounds in a fluid stream, while allowing others to go through, i.e. it acts as a filter. Membranes are widely used in many industrial filtration processes, ranging from desalination[1, 2], waste water treatment[3, 4], separation processes in the food industry such as removal of whey from milk[5, 6, 7], purification of liquids or gasses from fermentations[8, 9], hemodialysis[10, 11], etc. Membrane separation processes can have different purposes; they can be used to concentrate a valuable component in a dilute stream by selectively removing fluid, they can be used for purification, by removing and/or retaining impurities, or to fractionate a mixture of compounds in two (or more) valuable streams. Membranes are available with a wide variety of pore sizes, ranging from several Ås to approximately 10 μm. Filtration devices with pore sizes larger than this are usually classified as sieves, whose pore sizes can range into the millimeter scale. The typical size ranges

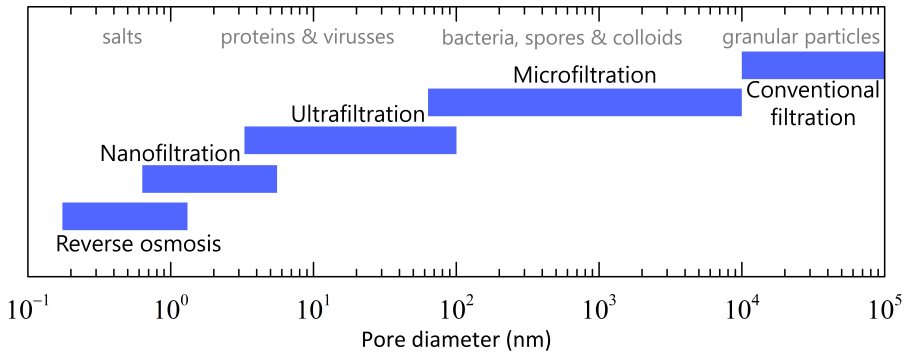

Figure 1.1: Illustration of the size ranges in which various membrane systems can operate, along with some common examples of solutes at that size range, adapted from[12] with permission from John Wiley & Sons, Inc.

and associated classifications and solutes are illustrated in Fig.1.1. Alternatively, membrane processes can be classified based on the driving force to achieve separation: osmotic and hydrostatic pressure, temperature, electrical fields, etc. In this thesis, pressure driven separations are our focus as these are most commonly encountered in industry.

Developments in membrane systems have seen tremendous growth in the past decades[12, 13, 14]. As membrane filtration blocks the passage of solutes in a fluid stream by means of mechanical exclusion, membrane separation uses significantly less energy than other separation techniques that are based on thermal or physical separation[13]. This relative energy efficiency, along with scalability due to the modular design of membranes, have led to a wide-ranging adoption in a large number of industries[12, 13]. Membrane separation processes are also considered very mild, which makes them suitable for the separation or purification of highly valuable compounds that are often heat-liable, for example, pharmaceutical components or delicate biomacromolecules[13].

The engineering approach to describe membrane systems often occurs at a phenomenological level, where fluid dynamics are taken as a natural starting point. E.g. one of the main theoretical frameworks to describe filtration considers the pressure-flux relationship at the *macroscopic* scale, e.g. using Darcy's law[15, 16], which is defined as:

$$J_i = K c_i \frac{\mathrm{d}p}{\mathrm{d}x} \tag{1.1}$$

where J_i is the flux of compound i, K is a coefficient that encodes the membrane properties (permeability, tortuosity and size) and $\mathrm{d}p/\mathrm{d}x$ is the pressure gradient over the membrane of width x. Within this macroscopic approach, all microscopic details of the processes occuring within the membrane are captured in a single phenomenological constant, K, which is often determined empircally, without explicit description of how K depends on geometry or accumulation of components that are retained, which mostly results in membranes beginning to clog and foul.

Membrane fouling is one of the major challenges in the design and application of efficient membrane separations. Fouling, and the associated clogging of membrane pores, is the gradual accumulation of solid or semisolid matter in and on the membrane during its operational lifetime. As a membrane starts to foul, membrane pores become clogged, leading to large reductions in flux, and thus productivity. Additionally, the selectivity of separation is also negatively influenced by the reduced pore size. Mitigating the adverse effects of fouling can be achieved in industrial settings in a variety of ways, such as flushing the membrane, reversal of flow to remove built-up particulates, extensive cleaning in-place or ultimately replacement of the membrane all together[13]. Delaying, or preventing fouling would increase the lifetime of membranes, and thus lead to more efficient and sustainable processes.

Solving this complex challenge by adopting a macroscopic fluid dynamics approach has proven impossible. The origins of fouling and clogging are so complex that to design effective strategies for delaying or preventing them requires fundamental insight into what occurs within a membrane at the microscale. Interestingly, many of the phenomena we find at this scale can be mapped onto classical topics in colloid and soft matter science (see Fig.1.2). The filter cake that results as fouling occurs can be treated as a densely packed suspension of particles, or in soft matter terms, a colloidal glass. Similarly, clogging of membrane pores can be considered as a flow-induced aggregation problem. Finally, the complex flows that occurs near the membrane surface where the concentration of solutes can become high due to concentration polarisation are known in

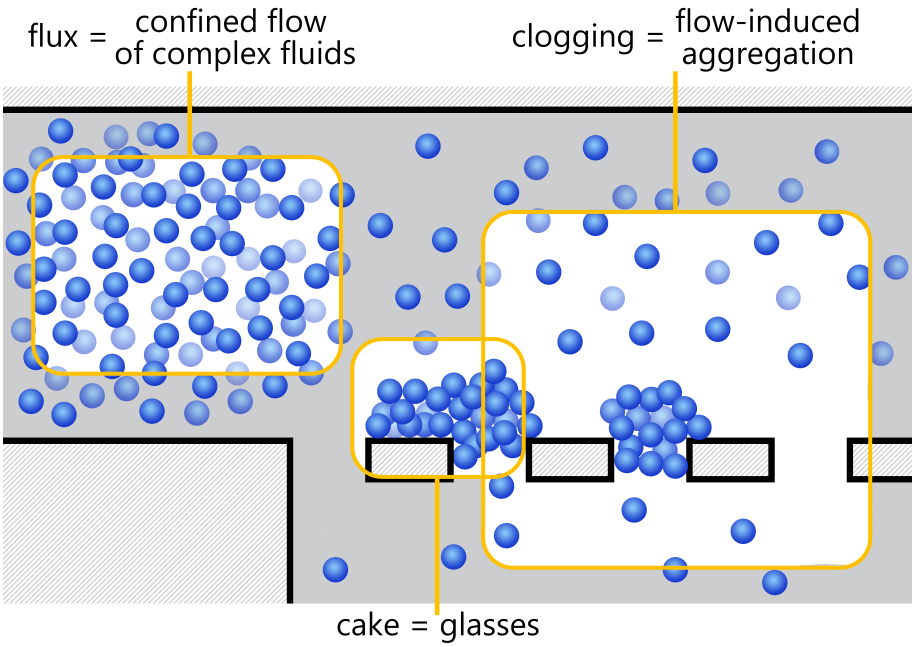

Figure 1.2: Schematic representation of a membrane system where a particle suspension flows through, showing the three major themes of this thesis, and how these themes relate to their corresponding problems in soft matter science.

the soft matter world as the flow of complex fluids in confinement.

These 'translations' of terminology used in membrane technology to the terminology found in soft matter science leads us to the central aim that has guided the work in this thesis:

In this thesis, we aim to understand the microscopic processes near, at, and within filtration membranes. In particular we address the question how can we design clever experiments to probe, quantify, visualize and disentangle i) the structure and dynamics of dense and non-ideal particle packings, ii) confined flows of complex fluids and iii) the mechanisms of pore clogging due to flow-induced aggregation.

A schematic representation of these three major themes in the context of a membrane system is given in Fig.1.2. In the following sections we will focus on each theme separately; dense colloidal packings as a model for filter cakes in section 1.2, the flow of complex fluids in confinement as a way to describe flow

across a membrane in section 1.3 and flow-induced aggregation to understand pore clogging behavior in section 1.4.

1.2 Colloidal glasses

As membranes start to foul a filter cake builds up on top of the membrane. Particulates are deposited on the membrane, making the flow through the membrane pores more and more restricted. These deposited filter cakes are densely packed solids of particles that are often difficult to remove due to their high density and ability to stick to the membrane surface. In soft matter terms, such a dense packing of colloidal particles is often studied in the context of dense liquids and/or glasses. To this end, we study a few selected topics in the field of colloidal glasses of non-hard sphere systems to gain insight into how various particle properties influence such densely packed systems.

Colloidal suspensions of small (0.01-10 μm) particles in a suspending fluid exhibit a rich phase behavior[17], showing e.g. fluid, liquid, crystalline, gel-like and glassy states (see Fig.1.3), depending on the particle volume fraction ϕ, interparticle interactions, external fields (gravity, electrical), polydispersity, particle softness, etc[18]. We first consider the simplest case of colloidal particles in suspension; a suspension of purely repulsive particles, interacting by volume exclusion alone, known as hard-spheres[19]. A suspensions of colloidal hard spheres behaves as a fluid at low ϕ and can become solid upon increasing ϕ, either by crystallizing at $\phi = 0.545$, where the system forms a highly ordered, regular structure (see Fig.1.3 for a schematic example) if the particles are sufficiently monodispersed. Or by forming a disordered solid, known as a glass above $\phi_g \simeq 0.58$, when crystallization is suppressed, usually by increasing the particle polydispersity. In most practical situations, suspensions are polydisperse such that crystallization is unlikely; we thus focus here on the glassy state in the colloidal phase diagram.

As the glass transition volume fraction ϕ_g is approached in such a hard sphere suspension, the free volume surrounding each particle decreases and the particle motion becomes increasingly restricted by neighboring particles due to the formation of configurational cages[18, 19, 20]. While the particles exhibit small scale

vibrational motion within these geometric cages, known as cage rattling motion, these cages restrict the long-ranged motion of particles. Only at sufficiently long time-scales, collective particle motion reshapes the cages and allows particles to translate on much larger length scales. The emergence of this caging-uncaging behavior leads to a slowdown of relaxation dynamics of the suspension, making it behave as a solid at the appropriate time scales. Interestingly, this process is analogous to the glass transition in molecular glass formers, where the fluid transitions into a glass upon lowering the temperature due to the associated reduction in local free volume[21, 22]. We note, that in colloidal systems the natural control parameter to induce this fluid-solid transition is not temperature but the particle volume fraction ϕ.

A natural property to quantify slowing down of particle motion within the system is the macroscopic viscosity, which is directly related to the self-diffusion rate of the particles at the microscopic scale. As ϕ increases, the low viscosity fluid phase transforms into a phase with an exceedingly high viscosity, which appears solid within experimental time scales[23, 24]. We note that the question if the glass transition is the true solid-liquid transition or that a secondary jamming transition at slightly higher volume fractions is the liquid-solid point remains a topic of debate, and is outside of the scope of this thesis[25, 26].

For colloidal hard spheres, the growth of macroscopic viscosity is very weak at low volume fractions, but as the glass transition is approached at $\phi_g \approx 0.58$ the viscosity rapidly increases by many orders-of-magnitude with only moderate changes in ϕ (see Fig.1.4a), signaling a very steep slowdown in dynamics close to the glass transition point. The steepness of this slowing down close to ϕ_g can vary dramatically between different glass formers and is captured by the concept of fragility, as first proposed for molecular glass formers by Angell[27]. A glass is termed 'fragile' if the viscosity increase is very steep and superexponential. A glass is denoted 'strong' if the viscosity exhibits a simple exponential (Arrhenius) growth upon approach of the glass point. For colloidal hard spheres the behavior is superexponential and thus its glass transition can be classified as fragile. We note that the terminology 'fragile' and 'strong' evoke the notion of reflecting on the mechanical rigidity and toughness of the material, yet these are completely different and uncoupled properties; here these terms only bear an indication on

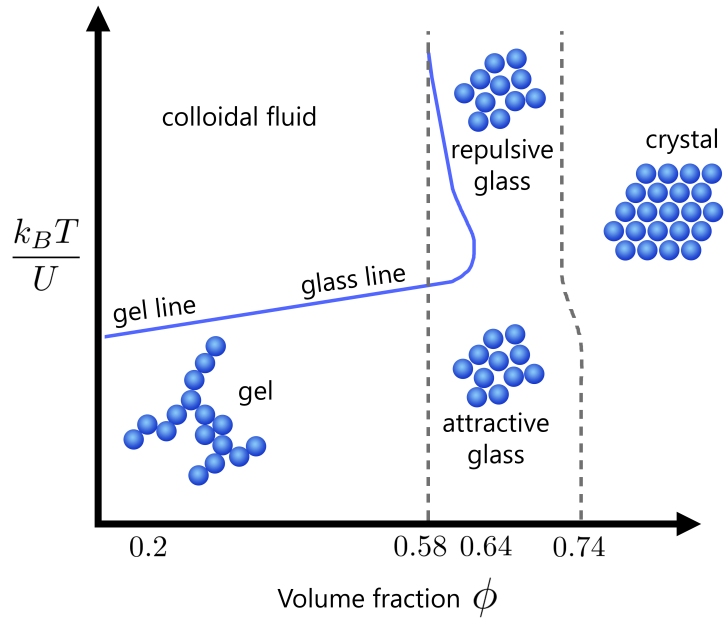

Figure 1.3: Phase diagram of colloidal particles as a function of volume fraction ϕ and inverse attraction strength k_BT/U. The blue line indicates the gel line, at which attraction strength colloidal gels (see schematic representation) start to form, and continues into the glass line, which shows at what attraction strengths and volume fraction glasses are formed (both attractive and repulsive glasses). Gray dashed lines show the volume fraction at which at zero attraction strength glasses are observed and which volume fraction is only accessible for crystals. Adapted by permission from Macmillan Publishers Ltd: Nature Materials[17], copyright 2002.

the steepness of the viscosity growth upon increasing the glass transition point.

Interestingly, it has been reported that the fragility of the hard sphere glass transition can be weakened and pushed to the strong glass limit by introducing softness to the colloidal particles. The growth in structural relaxation time τ, which is proportional to the viscosity, becomes increasingly gradual as the particles become softer, as previously explored by others for microgel colloids with different degrees of internal crosslinking[28]. For sufficiently soft particles an exponential viscosity growth is found (see Fig.1.4b, leading to the classification of a strong colloidal glass. These results are evocative for two reaons: i) the

fact that the entire range of fragilities can be explored in a colloidal system with a single tuning parameter gives rise to the possibility to study the origins of fragility at the microscopic scale, for which colloidal glasses are ideally suited, ii) since fragility is relevant for the processing properties of glasses, and thus the behavior of colloidal glasses in a filter cake, this may imply that colloidal engineering can be used to change filtration behavior. However, while these observations of fragility changes as a result of softness are interesting, so far it has remained unclear what the mechanisms are in which softness influences the colloidal glass transition. As a result, the underlying physics and universal description of the colloidal glass transition that captures fragility remains elusive.

In *Chapter 4* we solve this outstanding challenge by deriving a microscopic theory to explain the mechanisms of fragility in glasses of soft and compressible colloids, and use this to explain the mechanisms that control the nature of the glass transition in a variety of soft colloidal systems. To explore this topic in more detail, we then continued to investigate what happens when such deformable, soft, particles are highly compressed, and show that not only compressibility but also the propensity for shape changes must be taken into account for a completely quantitative description, as discussed in *Chapter 5*.

So far, we only considered systems interacting by purely repulsive potentials. Another very important factor, especially in practical situations, is the presence of (weak) attractive forces between the paricles in the fluid stream. Attractions can completely change the behavior of colloidal suspensions[29, 30, 31, 32], both at low and high ϕ. At low ϕ and high values of the attraction energy U ($U > 10k_BT$) a colloidal suspension forms a kinetically-arrested low density solid by forming a space-spanning percolated network, known as a colloidal gel[32] (Fig.1.3). In contrast, at high ϕ, i.e. for samples in proximity of the repulsive glass transition, even low attraction strengths ($U \geq 1k_BT$) can drastically alter the behavior of the colloidal glass. As illustrated in Fig.1.3, introducing weak attractions can drive the repulsive glass into a fluid, by increasing the local free volume[29], followed by the formation of a new glass phase bonded by attractive forces if the attraction strength is further increased[30].

To understand the effects of attractive forces on the transition from a repulsive to an attractive glass we can again start by probing the dynamical slowing

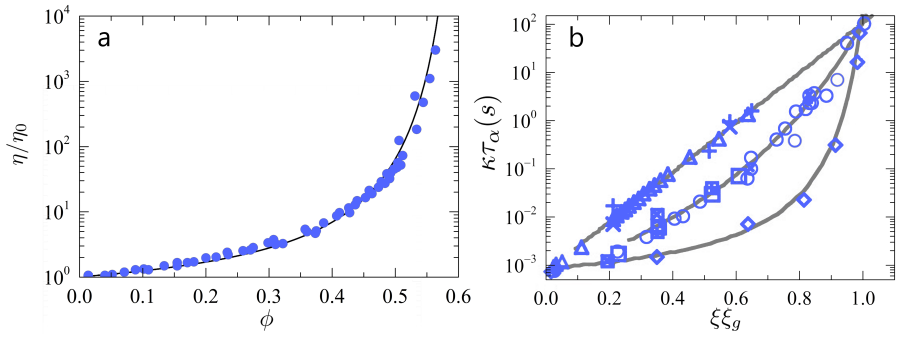

Figure 1.4: (a) Viscosity of colloidal suspensions as a function of volume fraction ϕ (blue circles), viscosities η are normalized to that of the pure solvent η_0. Black line shows a fit to a modified Doolittle equation, describing the increase in viscosity as a function of volume fraction; adapted from[18, 23], reproduced with permission of IOP Publishing. (b) Scaled relaxation time $\kappa\tau_\alpha$ as a function of effective volume fraction ξ normalized to ξ_g, where $\xi(\kappa\tau_\alpha = 100\text{s})$. The three different curves show particles with varying softness; stiff particles (diamonds), intermediate soft particles (circles and squares) and soft particles (triangles, crosses and pluses); adapted by permission from Macmillan Publishers Ltd: Nature[28], copyright 2009.

down, this time at the microscopic scale. A natural starting point is the mean-squared displacement $\langle \Delta x^2(\Delta t) \rangle$, a measure for time- and ensemble-averaged mobility of particles in the suspension. At low ϕ the mean-squared displacement increases linearly as a function of the lag time Δt, obeying the Einstein diffusion equation[33, 34]:

$$\langle \Delta x^2(\Delta t) \rangle = 6Dt \tag{1.2}$$

where D is the diffusion coefficient. As the diffusion constant, within the context of the Stokes-Einstein relation, is inversely proportional to the sample viscosity, also this is a probe for the macroscopic sample properties. However, as the volume fraction is increased the simple diffusive behavior gives way to more complex dynamics, which no longer obey the Stokes-Einstein law. As the sample becomes glassy, a plateau appears in the mean-squared displacement, indicative of the caging behavior described earlier, where particles are trapped in configurational cages and exhibit only localized thermal motion (cage rattling). Only

rarely, does a cage break open and allows a particle to move away from its previous averaged position; this results in a cage-to-cage hopping motion represented by long time diffusive behavior as evident from the eventual upturn observed in $\langle \Delta x^2(\Delta t) \rangle$ at high ϕ[36] (Fig.1.5a). The ensemble- and time-averaged mean-squared displacement probes the average dynamics of the sample, and thus does not reveal if the dynamics are temporally and spatially (in)homogeneous. If the coordinates and trajectories of all particles are explicitly known, for example in computer simulations or by employing particle-tracking algorithms on confocal microscopy data of colloidal glasses imaged at the single-particle scale, the mean-squared displacement can also be calculated for every particle in the glass separately. Interestingly, this approach also directly reveals the caging-uncaging motion described above[36] (Fig.1.5d).

Such investigations at the single particle level reveal another striking feature of colloidal glasses; dynamical heterogeneity. Some regions of particles may show very different dynamics as compared to others parts of the same sample, even though they are spatially very close together[35]. Clearly, probing only the macroscopic sample dynamics cannot capture the full complexity that emerges when a suspension enters a glassy phase. These dynamical heterogeneities become stronger as one approaches ϕ_g. Dynamical heterogeneity is typically associated with cooperative motion. As the glass transition is approached, the timescale for relaxation is coupled to that of growing length scales of particle clusters which must move in sync in order to accommodate any motion. As the size of these cooperative clusters grows, the barrier for relaxation grows and the sample dynamics slow down[36, 37, 38]. See Fig.1.5 for a visualization of a cluster of cooperative motion in a suspension of repulsive hard spheres close to (b) and over ϕ_g (c).

The addition of weak attractive forces greatly influences the way these dynamical heterogeneities manifest[39], as explored in two-dimensional systems exclusively to date. For a repulsive glass in 2D, the cooperative clusters are small and string-like (see Fig.1.5e) while for an attractive glass in 2D the clusters become much larger and condensed (see Fig.1.5f). This illustrates just one example of the large differences between these two solid states of repulsive and attractive glasses. However, several key questions remain unanswered about the difference

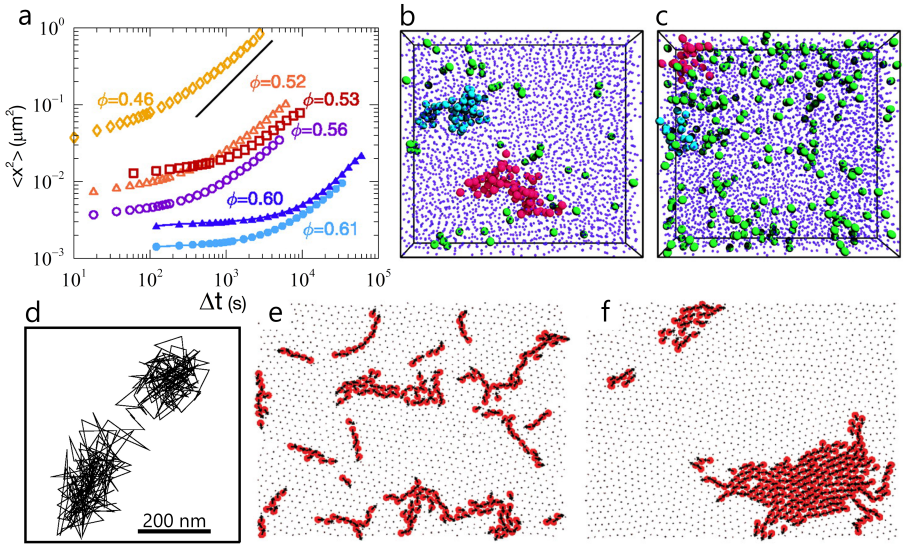

Figure 1.5: (a) Mean square displacement, $\langle \Delta x^2(\Delta t) \rangle$, for hard sphere suspensions at various volume fractions ϕ, as indicated in the figure, open symbols show supercooled liquids ($\phi = 0.46$ remains a fluid), closed symbols show glasses. Cooperative clusters showing a strong dynamical heterogeneity for two different samples, (b) shows a supercooled liquid at $\phi = 0.56$, while (c) shows a glass at $\phi = 0.61$. The 5% fastest particles are shown at true size, while all other particles are reduced in size for clarity. (d) Trajectory of a single particle moving for 100 minutes, shows how a particle is trapped in a configurational cage and occasionally hops and shows a quick cage rearrangement. Cooperative clusters illustrating the difference between a repulsive 2D glass (e) and an attractive 2D glass (f), the 10% fastest particles are colored in red and shown at their true size. Data and figures from (a-d) are adapted and reprinted from[36]. Reprinted with permission from the AAAS. Data for (e-f) are reprinted with permission from[39]. Copyright 2011 by the American Physical Society.

between the repulsive and weakly attractive glass. For instance, are attractive bonds alone sufficient to explain dynamical arrest at the attractive glass transition, and can this be extrapolated from the arrest found at much lower ϕ at the fluid-gel transition? And how do attractive forces effect the local dynamics in glasses in 3 dimensions, which are known to differ fundamentally from glasses in two dimensions[40, 41]?

In *Chapter 3* we provide a detailed experimental investigation at the single-particle scale of this solid-solid transition from repulsive to attractive glasses

in 3D. Interestingly, we find a distinct discontinuity in the length scales associated with heterogeneous dynamics, confirming the discontinuous nature of this transition as predicted by theory[31]. Moreover, we provide tentative evidence that the attractive glass transition is a continuous extension of the gel line that starts at lower volume fractions and higher attraction strengths.

1.3 Confined flow of complex fluids

A membrane filtration module consists of many narrow channels, which introduces a complexity beyond the macroscopic level captured by simple fluid dynamic considerations. Thus also here, we adopt a soft matter approach to explore how confinement affects the flow of complex fluids.

Confinement effects can alter the flow behavior of suspensions dramatically. At the macroscopic scale we are used to think about complexity in fluid flows within the framework of turbulence. While turbulence is far from understood[42, 43], it sets the scene for our innate feeling of how fluids should behave. At the microscopic scale, confined flows behave very differently however. First of all, almost always, the flow conditions will meet the laminarity conditions set by a low Reynolds number[44, 45], Re:

$$Re = \frac{\rho v L}{\eta} \equiv \frac{f_i}{f_v} \tag{1.3}$$

where ρ is the fluid density, v the fluid velocity, L the typical length scale in the system and η the viscosity of the fluid. The Reynolds number gives a balance between inertial (f_i) and viscous forces (f_v) and dictates when laminar flow conditions break down. As a rule of thumb, if $Re \leq 2000$ flow is considered laminar. Typical flow conditions in strongly confined flows lead to fluid Re numbers as low as 10^{-6} to ~ 10 in special cases[45], thus always well below the laminar-turbulence transition point. From a macroscopic perspective, the absence of turbulence leads to a 'simpler' problem with very well-defined and predictable flow fields. However, as we will also show in *Chapter 6*, this is not the case when particles in the fluid stream introduce complexity, originating from particle-particle and particle-fluid interactions.

For instance, the introduction of a single constriction in an already narrow

microchannel can have an enormous effect[46]. Even weak filtration at the constriction, biasing the passage of fluid with respect to that of particles, leads to a density gradient in the channel enabling structure formation upstream (see Fig.1.6a, top), and subsequent shear melting at the constriction (see Fig.1.6a, bottom). In this particular experiment carried out in earlier work, the transition from crystalline to glassy phases strongly influences the flow behavior of the suspension, as evidenced by the large changes in velocity profiles (v_x as a function of y, the width of the channel) found in different parts of the confined geometry (see Fig.1.6b-d). The flow goes from almost pure plug-flow (Fig.1.6b), to almost ideal Poiseuille flow in the constriction (red line, Fig.1.6c) to a typical blunted velocity profile often found for shear-thinning systems such as highly concentrated glassy flows (Fig.1.6d).

In addition to distinct deviations of the average flow profile away from the predictions of fluid dynamics, complexity is also observed in the stability of the flow in time[47]. Increasing the confinement ratio, defined as the ratio of channel width to particle size, transforms the stable flow, which exhibits a constant $\langle v \rangle$ in time, to an unstable one in which the velocity exhibits very large fluctuations, with amplitudes that can be as large as the mean $\langle v \rangle$ (Fig.1.6e). These large velocity fluctuations are directly correlated to the local particle volume fraction[46] and attributed to the local caging-uncaging of the glassy state and the creation of shear-jammed configurations which can completely block the flow[48]. This also causes the formation of distinct flow vortices by the collective rotation of large particle clusters[49]. The forces created during confined flows thus act on the natural dynamical heterogeneity of these suspensions at rest, and introduce a complexity akin to turbulence while the fluid flow conditions are strictly laminar.

In the previous section on colloidal glasses (section 1.2) we discussed how, as the glass transition is approached, larger regions of particles must cooperatively move together. Such cooperative motion is exacerbated in confined flows[49]. As the volume fraction of the dispersed phase is increased these regions of cooperative motion, their size here denoted as ξ, grow strongly as a function of volume fraction (see Fig.1.6f).

These complex phenomena encountered in the flow of dispersions in strong

confinement can sometimes be used advantageously in separation processes[50]. If the flow conditions ensure a gradient in the shear rate, i.e. the flow conditions deviate from linear simple shear, particle-particle collisions can lead to migration away from the wall[51]. This lateral displacement is ultimately a balance between the randomizing effects of Brownian motion of the particles, such that particle size plays an important role, and the forced migration by shear and can be captured by the dimensionless Péclet number (Pe), defined as[45]:

$$Pe = \frac{\dot{\gamma} a^2}{D_0} = \frac{6\pi\eta\dot{\gamma} a^3}{k_B T} \tag{1.4}$$

with $\dot{\gamma}$ the shear rate, a particle radius and D_0 the particle self-diffusion coefficient at rest. For $Pe > 1$, which is strongly dependent on the particle size, and in the presence of a shear rate gradient lateral displacement can occur. This type of hydrodynamic particle migration is often denoted as shear-induced diffusion[51, 50].

Hydrodynamic particle migration can be used to separate particles that are relatively close in size (size difference of approximately 1 μm) by establishing a concentration gradient in a confined geometry[52]. Typically, a shear gradient applied to a polydisperse or bidisperse suspension leads to an enrichment of larger particles in the center of the channel, where the shear rate is minimal, and the smaller particles enrich to the sides where the shear gradients are stronger (see Fig.1.6g). Such a concentration gradient needs time to develop once the flow is confined (see Fig.1.6h-i), where there is no size segregation at the start of confinement, but a strong concentration gradient develops further downstream[53]. Understanding how the kinetics of this process occur is one of the open challenges in designing migration-based separation processes. To date, the research on shear-induced diffusion has focused on suspensions at relatively low volume fractions (maximum $\phi \approx 0.38$), where strong effects due to particle caging are negligible. However, for reasons of energy efficiency it is of great interest to work at as high volume fractions as possible and feasible.

In *Chapter 6* we investigate the limits of such shear-induced fractionation by studying highly concentrated suspensions of soft particles, with $\phi >> 0.64$. We use confocal microscopy to directly visualize the flow of these highly concentrated suspensions and show that even in such concentrated systems fractiona-

tion is still possible and is mediated by the large collective motions of particle clusters described above. This opens the way for large improvements in process efficiency based on shear-gradient particle separation techniques.

The visualization of confined flows is important, as direct microscopic visualization allows us to study these flows at the microscopic scale and gain quantitative understanding of the processes that govern confined flows[54, 55]. Besides dense particle suspensions, another classical example of confined flow of complex fluids involves the flow of two immiscible phases (i.e. water and oil) in a complex geometry. This is encountered during oil recovery, where water is pumped into porous bedrock to displace oil[56], or during washing, where laundry detergent needs to permeate into the fibers of clothes to displace oily stains[57]. How such displacement occurs, especially in the random structures often encountered in real-world situations is a complex problem that currently is incompletely understood.

In *Chapter 7* we establish a microfluidic design to enable the direct visualization of two phase flows in random network geometries at the microscopic scale. We show that by understanding the mechanisms underlying the complex displacement cascade, we can tailor the properties of the displacement phase to result in a much more efficient displacement process.

The visualization of flow fields is vital to understand the underlying mechanisms of the flow of dispersions through complex structures, which will exhibit strong deviations from the Navier-Stokes equations. Flow field mapping is typically performed by adding tracer particles to a fluid stream and the use of particle tracking or velocimetry algorithms to extract local fluid velocities from images recorded of these flows. However, this approach has an evident limitation as the flow geometry must always be much larger than the particles used to visualize the flows. The minimum size of tracer particles for accurate flow imaging is $\approx$ 200 nm, the Abbe diffraction limit[58], thus placing strict limits on the size of the flow geometry in which flow fields can still be measured.

To break through this barrier, we take the first steps in developing molecular flow tracers, whose inherently small dimensions (of order nm's) would allow the study of flows even in extreme nanometric confinement. In *Chapter 8* we make the first steps towards such a molecular flow sensor based on mechanically-

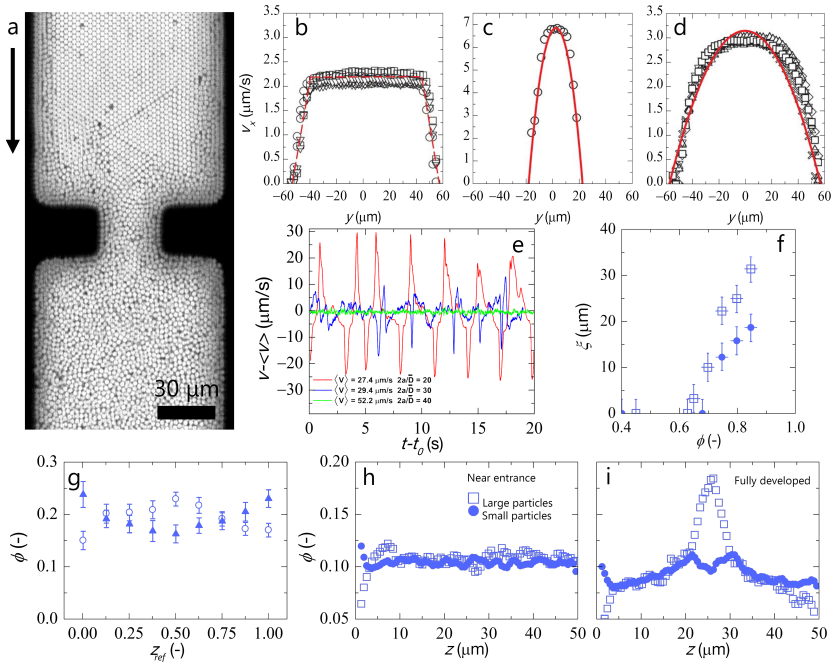

Figure 1.6: (a) Confocal image of a dense suspension flowing through a constriction. (b-d) Velocity profiles (v_x, along the flow direction) as a function of channel width y, (a) v_x before the constriction, (b) v_x in the constriction and (c) v_x after the constriction, see text for drawn lines. (e) Velocity, v, differences compared to the long-time average velocity $\langle v \rangle$ as a function of time $(t - t_0)$ for three different confinement ratios, green is lightly confined, blue intermediately and red is strongly confined. (f) Flow cooperativity length ξ as a function of volume fraction ϕ of an emulsion. Squares show a monodisperse emulsion, circles show a polydisperse emulsion. (g) Concentration profile for large particles (circles, 2.65μm) and small particles (triangles, 1.53μm) as a function of distance z_{ref} from wall to wall. Development of a concentration gradient in confinement over the height z of a channel, at the start of confinement there is no concentration difference (h), further downstream the gradient becomes fully developed (i) and an enrichment of large particles is evident. Data in (b-d) adapted from[46] with permission of The Royal Society of Chemistry, data in (e) adapted with permission from[47] Copyright 2009 by the American Physical Society, data in (f) adapted by permission from Macmillan Publishers Ltd: Nature[49], copyright 2008, data in (g) from[52], with permission from Springer, data in (h-i) reprinted from[53] with the permission of AIP Publishing.

responsive luminescence, and use single molecule spectroscopy to test and calibrate their functioning. Finally, we provide the first preliminary proof of their

use as molecular flow sensors in the *General Discussion* chapter that concludes this thesis.

1.4 Pore clogging

So far we have shown how the concept of filter cake and the flow behavior of particles within membrane modules can be mapped onto corresponding soft matter problems. In this section, these two aspects will come together to explore another challenging membrane problem: clogging. Clogging of individual pores is the singular event in which the free passage through a narrow membrane pore becomes blocked. As individual pores clog, the fluid can still pass but additional particles cannot; as a result, particles will accumulate within the pore and spill over onto the membrane surface where they may form a cake as detailed in section 1.2. In the previous section (section 1.3) we showed how the flow of a suspension within membrane modules can be mapped onto the soft matter problem of confined flow of complex fluids, and how such confinement introduces considerable complexity in the flow of dispersions. Once such a dispersion reaches the membrane surface the case becomes even more complex. Depending on their size, particles can agglomerate at the confinement walls, which leads to clogging (Fig.1.7a and b). Clogging is the primary process that underlies the failure of membranes and is thus of large relevance, but is also crucial in many emerging microfluidic technologies, where the inherently small scales lead to devices prone to clogging.

There are three main mechanisms of clogging, depending on the size of the particle, a, the size of the constriction, W, and the volume fraction ϕ of the particles in the fluid stream[59]. In the situation where $a > W$, such that a single particle will completely block a pore, a process called sieving (Fig.1.8a). When $a < W$ there are two possible mechanisms that can lead to pore clogging. This can either be due to arching, in which multiple particles arrive at a constriction simultaneously and form a configurational arch that blocks further particles from passing (Fig.1.8b). Such arching is mostly observed during flow of granular material or highly concentrated hard sphere suspensions, and these arches often break and reform intermittently causing fluctuations in the flow[61]. Since the

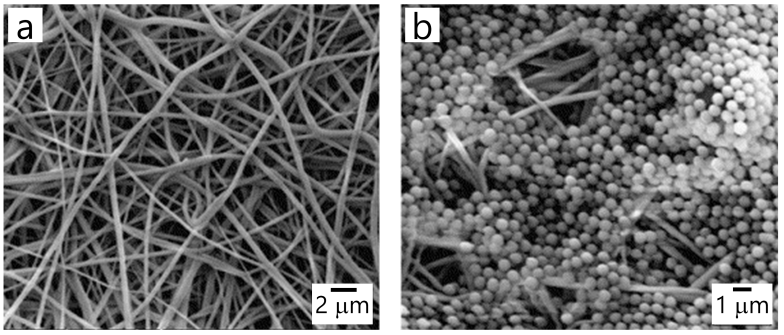

Figure 1.7: SEM images of a fibrous membrane structure before (a) and after filtration of a suspension with 1 μm colloidal particles. Adapted from[60], copyright 2006, with permission from Elsevier.

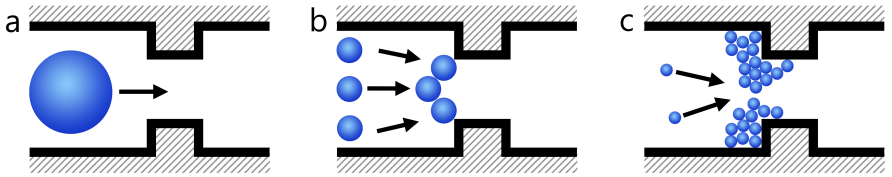

Figure 1.8: Schematic representation of the different mechanisms that can lead to clogging of microchannels, (a) sieving, where a particle larger than the pore causes blockage, (b) bridging, where multiple particles arrive at a constriction and form an arch and (c) aggregation, in which multiple particles stick to each other and the channel wall which eventually causes blockage. Adapted from[59] with permission of The Royal Society of Chemistry.

propensity of arch formation by local density fluctuations decreases rapidly with decreasing particle volume fraction, this scenario is only relevant for dense suspensions. However, clogging can still occur when $a < W$ and for more dilute flows due to flow-induced particle-wall and particle-particle aggregation. Where multiple particles adhere to a wall and each other, eventually causing a complete blockade of the flow through a pore (Fig.1.8c).

Flow-induced aggregation involves different factors contributing to the final, clogged state. Particles need to come in close enough contact with each other or the pore wall such that they will stick and aggregate. This probability depends

not only on the hydrodynamic conditions but also strongly on the interactions between particles and the confining walls. How all these factors are interrelated has proven difficult to disentangle and it remains unclear if a generic and scale-bridging approach exists to unify the description of clogging in various scenarios, a topic of active research in the soft matter community[48, 59, 62]. Understanding clogging is made easier by the development of membrane micromodels in microfluidic devices that offer a unique way to study flow-induced aggregation under very well defined conditions[59, 63]. Moreover, such micro-engineered devices also offer a new and quick way to prototype possible new designs which may delay or prevent clogging.

Some examples of microfluidic devices that have been used to study clogging are shown in Fig.1.9a-d[63, 64]. Such devices typically consist of multiple channels in parallel with several constrictions in series along the length of each pore channel. These devices enable a large degree of control for specific parameters and are thus well suited to isolate variables influences clogging. For instance, increasing the particle flux (by increasing the pressure) has been shown to lead to faster clogging[63]. As the pressure increases, the amount of time it takes for the entire device to clog, with α the ratio of clogged channels, decreases, as shown in Fig.1.9e, where the blue circles are at higher pressures (and thus fluxes) compared to the red diamonds. Based on these results the authors[63] postulate that clogging depends linearly on the flux, since they assume that a critical number of particles N^* must pass a constriction for clogging to occur. This approach however ignores that shear forces may enhance the aggregation rate, possibly leading to a much steeper dependency on flux.

In *Chapters 9 and 10* we verify this hypothesis, derive a theory to explain it and explain how the apparent contradictions across different experimental studies can be understood. Moreover, we show how the geometry of the pores makes a considerable difference in the time to clogging, which we introduce as a geometric consideration into our transition-state theory for clogging.

These microfluidic devices have also been used by others to investigate the effects of larger contaminants on clogging[64]. If these contaminants are much larger than the average particle size, and larger than the pore size, two competing clogging processes are present, i.e. sieving and flow-induced aggregation (see

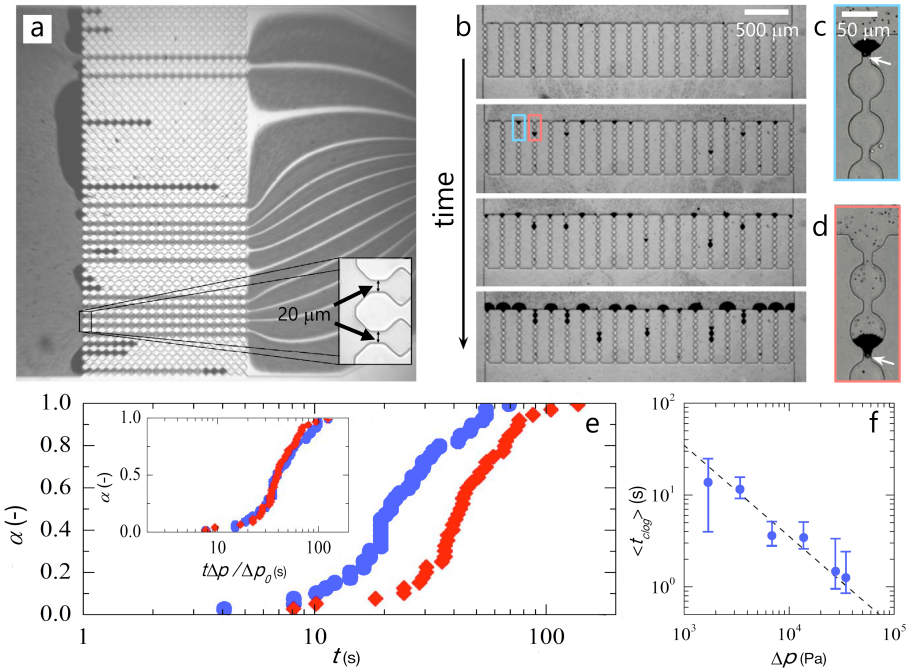

Figure 1.9: (a-d) Microscopic images of microfluidic devices used for clogging experiments; (a) shows a particle suspension flowing from left to right, causing particles to clog in the narrow constrictions (see inset, 20 μm minimum width), particle size is 2.9 μm with $\phi = 0.04$, (b) shows a time series of images where the amount of clogged channels increases in time, in this case larger contaminants are present that can cause clogging by sieving, (c-d) show close-ups of such a large contaminant causing a clog at the start of a channel (c) or further inside the microfluidic device (d). (e) The ratio of clogged channels α as a function of time for two different applied pressures ($\Delta p = 14$ kPa for the red diamonds, and $\Delta p = 28$ kPa for the blue circles), the inset shows how the data collapses onto the same curve when normalized by the relative pressure difference. (f) Mean time between two clogging events $\langle t_{clog} \rangle$ as a function of the applied pressure difference, dashed line has a slope of $1/\Delta p$. Data in (a) and (e) are adapted and reprinted with permission from[63], copyright 2006 by the American Physical Society, data in (b-d) and (f) are adapted and reprinted from[64] with the permission of AIP Publishing.

Fig.1.9b for an overview of the microfluidic device, with different pores clogging at different times, and Fig.1.9c-d for two close-ups of large contaminants blocking a pore). Such large contaminants dominate the clogging process, and result in a linear dependence of the time between clogs, t_{clog} and the pressure, which

highlights the complex interplay of many factors influencing clogging behavior.

So far, in almost all microfluidic clogging studies, a so-called dead-end configuration was used, which implies that the entire particle flow passes through the membrane structure. However, in industry, most membrane processes are operated in a cross-flow configuration, where there is an additional flow across the membrane structure to a secondary outlet. A cross-flow configuration is used to promote mass transfer from the membrane surface back into the feed solution in order to extend the operation time of a membrane. Despite its widespread use, the physical mechanisms remain largely unclear.

In *Chapter 10* we develop the first cross-flow filtration micromodel, which allows us to investigate the physical mechanisms by which the application of cross-flow reduces the propensity to clogging. Interestingly, we find that the primary rate of clogging of individual pores only depends on the flux through the membrane. The cross-flow however effects the pore-pore communication and leads to a transition from membrane failure by the uncorrelated clogging of individual pores to a cooperative clogging process; we capture this transition by deriving a new dimensionless clogging number that captures the essential physics at a qualitative level.

1.5 Outline

The content of this thesis is schematically illustrated in the overview in Fig.1.2 and Fig.1.10. Here we show how each Chapter is related and how we investigate the three separate themes in this thesis. Below we provide a short summary for each Chapter.

In Chapter 2 we provide a technical overview of the synthesis recipes and strategies used throughout this thesis for the synthesis of colloidal model systems. Concise recipes are provided, along with the design considerations for each of these model systems.

Quantitative, 4D confocal microscopy is used in Chapter 3 to investigate the repulsive-to-attractive colloidal glass transition, and we show the first experimental evidence of a discontinuity in the transition from repulsive to attractive glasses.

In Chapter 4 we develop a simple model that provides a microscopic explanation for the fragility of colloidal glasses and show how we can use it to describe a wide variety of experimental data from various soft colloidal systems. Our results show how the elastic energy per particle acts as a fragility order parameter, which leads to a universal description of the colloidal glass transition.

Chapter 5 focuses on how soft particles deform in highly concentrated packings. We show that there is a transition where at low packing pressures shape changes dominate the elastic response, where volume changes dominate the response above a critical osmotic pressure. Our results show that both types of deformation (deswelling and facetting) must be considered for an accurate description of concentrated suspensions of soft spheres.

Chapter 6 shows how shear-induced diffusion can still occur in soft particle suspensions that are well above their glass transition and how these are mediated by non-affine flow vortices in a strictly laminar hydrodynamic flow. These results evoke the possibility to design a more efficient separation process by utilising fractionation at very high concentration.

A microchip design to investigate oil displacement in a random porous network structure is presented in Chapter 7. Combined with quantitative, high-speed microscopic imaging we show that by changing the properties of the displacing fluid we can greatly increase the efficiency of the overall displacement.

In Chapter 8 we develop the first molecular flow sensor by combining single-molecule hyperspectral imaging and simulations to show how our molecular force sensors based on semiconducting and luminescent polymers are able to sense stretching forces as low as 100 fN. These results pave the way to visualize flow fields at extreme confinement and the smallest scales.

Membrane pore geometry is the focal point of attention in Chapter 9, in which we show experimentally how the exact geometry of a membrane pore has an enormous influence on the clogging behavior of membrane micromodels. We quantitatively explain our results by developing a model based on transition-state theory, which allows us to predict the geometry dependence, as well as the effect of slight attractive forces.

Chapter 10 expands on the previous chapter, where we investigate the effect of cross-flow, as commonly found in industry, on the clogging rate. We

extend existing models to take into account flow-enhanced agglomeration and show how the primary clogging rate only depends on the flux through the membrane, while cross-flow reduces the effect of communication between neighboring pores.

Finally, in the General Discussion we discuss the implications of this work in a broader context, where we discuss all three major themes separately. We also provide future routes to further develop the work done in this thesis, and wrap up with a final conclusion reflecting on how to move forward.

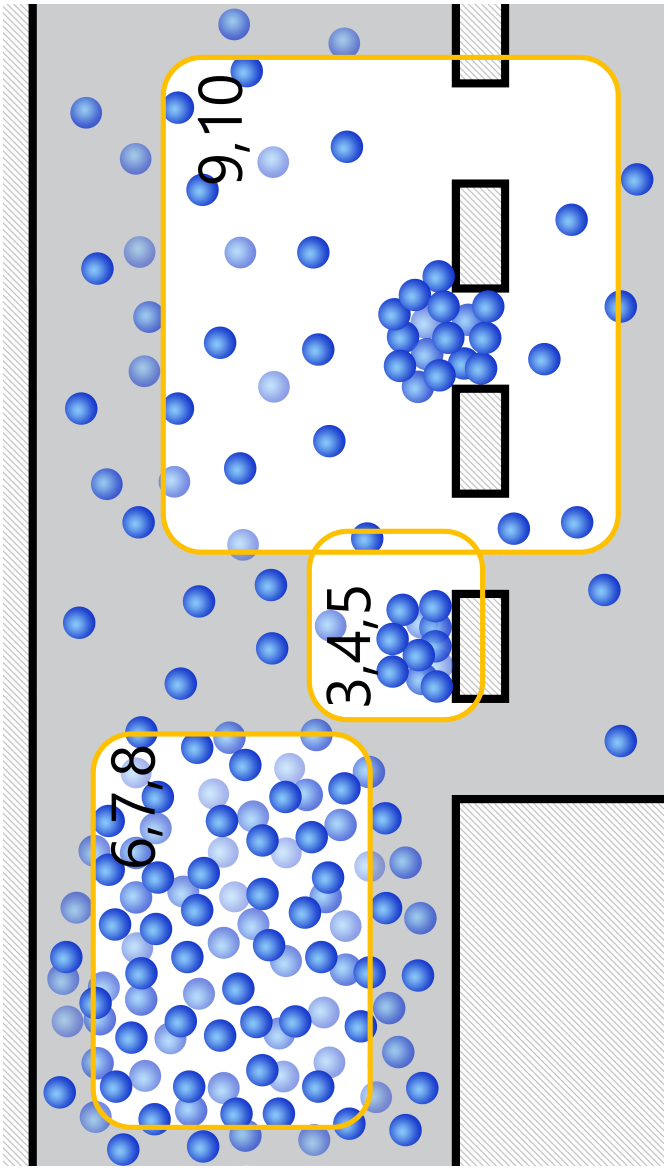

Figure 1.10: Overview of the different chapters in this thesis.

References

[1] Lee, K. P., Arnot, T. C. & Mattia, D. A review of reverse osmosis membrane materials for desalination: development to date and future potential. *Journal of Membrane Science* **370**, 1–22 (2011).

[2] Charcosset, C. A review of membrane processes and renewable energies for desalination. *Desalination* **245**, 214–231 (2009).

[3] Van der Bruggen, B., Vandecasteele, C., Van Gestel, T., Doyen, W. & Leysen, R. A review of pressure-driven membrane processes in wastewater treatment and drinking water production. *Environmental Progress & Sustainable Energy* **22**, 46–56 (2003).

[4] Shannon, M. A. *et al.* Science and technology for water purification in the coming decades. *Nature* **452**, 301–310 (2008).

[5] Girard, B., Fukumoto, L. & Sefa Koseoglu, S. Membrane processing of fruit juices and beverages: a review. *Critical reviews in biotechnology* **20**, 109–175 (2000).

[6] D'souza, N. & Mawson, A. Membrane cleaning in the dairy industry: a review. *Critical reviews in food science and nutrition* **45**, 125–134 (2005).

[7] Daufin, G. *et al.* Recent and emerging applications of membrane processes in the food and dairy industry. *Food and Bioproducts Processing* **79**, 89–102 (2001).

[8] Saxena, A., Tripathi, B. P., Kumar, M. & Shahi, V. K. Membrane-based techniques for the separation and purification of proteins: an overview. *Advances in Colloid and Interface Science* **145**, 1–22 (2009).

[9] Rodrigues, T., Carrondo, M. J., Alves, P. M. & Cruz, P. E. Purification of retroviral vectors for clinical application: biological implications and technological challenges. *Journal of biotechnology* **127**, 520–541 (2007).

[10] Eknoyan, G. *et al.* Effect of dialysis dose and membrane flux in maintenance hemodialysis. *New England Journal of Medicine* **347**, 2010–2019 (2002).

[11] Locatelli, F. *et al.* Effect of membrane permeability on survival of hemodialysis patients. *Journal of the American Society of Nephrology* **20**, 645–654 (2009).

[12] Baker, R. W. *Overview of Membrane Science and Technology*, 1–14 (John Wiley & Sons, Ltd, 2004).

[13] Mulder, J. *Basic principles of membrane technology* (Springer Science & Business Media, 2012).

[14] Van der Bruggen, B. *Membrane Technology* (John Wiley & Sons, Inc., 2000).

[15] Darcy, H. *Les fontaines publiques de la ville de Dijon: exposition et application...* (Victor Dalmont, 1856).

[16] Whitaker, S. Flow in porous media i: A theoretical derivation of darcy's law. *Transport in porous media* **1**, 3–25 (1986).

[17] Sciortino, F. Disordered materials: One liquid, two glasses. *Nature materials* **1**, 145–146 (2002).

[18] Hunter, G. L. & Weeks, E. R. The physics of the colloidal glass transition. *Reports on Progress in Physics* **75**, 066501 (2012).

[19] Pusey, P. *et al.* Hard spheres: crystallization and glass formation. *Philosophical Transactions of the Royal Society of London A: Mathematical, Physical and Engineering Sciences* **367**, 4993–5011

(2009).

[20] Van Megen, W. & Underwood, S. Glass transition in colloidal hard spheres: Mode-coupling theory analysis. *Physical review letters* **70**, 2766 (1993).

[21] Van Megen, W., Underwood, S. & Pusey, P. Nonergodicity parameters of colloidal glasses. *Physical review letters* **67**, 1586 (1991).

[22] Pusey, P. N. & Van Megen, W. Phase behaviour of concentrated suspensions of nearly hard colloidal spheres. *Nature* **320**, 340–342 (1986).

[23] Cheng, Z., Zhu, J., Chaikin, P. M., Phan, S.-E. & Russel, W. B. Nature of the divergence in low shear viscosity of colloidal hard-sphere dispersions. *Phys. Rev. E* **65**, 041405 (2002).

[24] de Kruif, C. d., Van Iersel, E., Vrij, A. & Russel, W. Hard sphere colloidal dispersions: Viscosity as a function of shear rate and volume fraction. *The Journal of chemical physics* **83**, 4717–4725 (1985).

[25] Brambilla, G. *et al.* Probing the equilibrium dynamics of colloidal hard spheres above the mode-coupling glass transition. *Physical review letters* **102**, 085703 (2009).

[26] Zhang, Z. *et al.* Thermal vestige of the zero-temperature jamming transition. *Nature* **459**, 230–233 (2009).

[27] Angell, C. A. *et al.* Formation of glasses from liquids and biopolymers. *Science* **267**, 1924–1935 (1995).

[28] Mattsson, J. *et al.* Soft colloids make strong glasses. *Nature* **462**, 83–86 (2009).

[29] Eckert, T. & Bartsch, E. Re-entrant glass transition in a colloid-polymer mixture with depletion attractions. *Phys. Rev. Lett.* **89**, 125701 (2002).

[30] Pham, K. N., Egelhaaf, S. U., Pusey, P. N. & Poon, W. C. K. Glasses in hard spheres with short-range attraction. *Phys. Rev. E* **69**, 011503 (2004).

[31] Dawson, K. *et al.* Higher-order glass-transition singularities in colloidal systems with attractive interactions. *Phys. Rev. E* **63**, 011401 (2000).

[32] Zaccarelli, E. Colloidal gels: equilibrium and non-equilibrium routes. *Journal of Physics: Condensed Matter* **19**, 323101 (2007).

[33] Einstein, A. Über die von der molekularkinetischen theorie der wärme geforderte bewegung von in ruhenden flüssigkeiten suspendierten teilchen. *Annalen der physik* **322**, 549–560 (1905).

[34] Mason, T. G. Estimating the viscoelastic moduli of complex fluids using the generalized stokes–einstein equation. *Rheologica Acta* **39**, 371–378 (2000).

[35] Berthier, L., Biroli, G., Bouchaud, J.-P., Cipelletti, L. & van Saarloos, W. *Dynamical heterogeneities in glasses, colloids, and granular media*, vol. 150 (OUP Oxford, 2011).

[36] Weeks, E. R., Crocker, J. C., Levitt, A. C., Schofield, A. & Weitz, D. A. Three-dimensional direct imaging of structural relaxation near the colloidal glass transition. *Science* **287**, 627–631 (2000).

[37] Weeks, E. R., Crocker, J. C. & Weitz, D. A. Short-and long-range correlated motion observed in colloidal glasses and liquids. *Journal of Physics: Condensed Matter* **19**, 205131 (2007).

[38] Kegel, W. K. & van Blaaderen, A. Direct observation of dynamical heterogeneities in colloidal hard-sphere suspensions. *Science* **287**, 290–293 (2000).

[39] Zhang, Z., Yunker, P. J., Habdas, P. & Yodh, A. Cooperative rearrangement regions and dynamical heterogeneities in colloidal glasses with attractive versus repulsive interactions. *Physical review letters* **107**, 208303 (2011).

[40] Flenner, E. & Szamel, G. Fundamental differences between glassy dynamics in two and three dimensions. *Nature communications* **6** (2015).

[41] Vivek, S., Kelleher, C. P., Chaikin, P. M. & Weeks, E. R. Long-wavelength fluctuations and the glass transition in two dimensions and three dimensions. *Proceedings of the National Academy of Sciences* **114**, 1850–1855 (2017).

[42] Feynman, R. P., Leighton, R. B. & Sands, M. *The Feynman lectures on physics, Vol. I: The new millennium edition: mainly mechanics, radiation, and heat*, vol. 1 (Basic books, 2011).

[43] Eames, I. & Flor, J. New developments in understanding interfacial processes in turbulent flows (2011).

[44] Reynolds, O. Xxix. an experimental investigation of the circumstances which determine whether the motion of water shall he direct or sinuous, and of the law of resistance in parallel channels. *Philosophical Transactions of the Royal Society of London* **174**, 935–982 (1884).

[45] Squires, T. M. & Quake, S. R. Microfluidics: Fluid physics at the nanoliter scale. *Reviews of modern physics* **77**, 977 (2005).

[46] Genovese, D. & Sprakel, J. Crystallization and intermittent dynamics in constricted microfluidic flows of dense suspensions. *Soft Matter* **7**, 3889–3896 (2011).

[47] Isa, L., Besseling, R., Morozov, A. N. & Poon, W. C. Velocity oscillations in microfluidic flows of concentrated colloidal suspensions. *Physical review letters* **102**, 058302 (2009).

[48] Zuriguel, I. *et al.* Clogging transition of many-particle systems flowing through bottlenecks. *Scientific reports* **4**, 7324 (2014).

[49] Goyon, J., Colin, A., Ovarlez, G., Ajdari, A. & Bocquet, L. Spatial cooperativity in soft glassy flows. *Nature* **454**, 84–87 (2008).

[50] Schroën, K., van Dinther, A. & Stockmann, R. Particle migration in laminar shear fields: A new basis for large scale separation technology? *Separation and Purification Technology* **174**, 372–388 (2017).

[51] Eckstein, E. C., Bailey, D. G. & Shapiro, A. H. Self-diffusion of particles in shear flow of a suspension. *Journal of Fluid Mechanics* **79**, 191–208 (1977).

[52] Van Dinther, A., Schroën, C., Imhof, A., Vollebregt, H. & Boom, R. Flow-induced particle migration in microchannels for improved microfiltration processes. *Microfluidics and nanofluidics* **15**, 451–465 (2013).

[53] Semwogerere, D. & Weeks, E. R. Shear-induced particle migration in binary colloidal suspensions. *Physics of Fluids* **20**, 043306 (2008).

[54] Link, D., Anna, S. L., Weitz, D. & Stone, H. Geometrically mediated breakup of drops in microfluidic devices. *Physical review letters* **92**, 054503 (2004).

[55] Song, Y., Manneville, P. & Baroud, C. N. Local interactions and the global organization of a two-phase flow in a branching tree. *Physical review letters* **105**, 134501 (2010).

[56] Lake, L. W. *Enhanced oil recovery* (Prentice Hall Englewood Cliffs, NJ, 1989).

[57] Ingham, D. B. & Pop, I. *Transport phenomena in porous media* (Elsevier, 1998).

[58] Born, M. & Wolf, E. *Principles of optics: electromagnetic theory of propagation, interference and diffraction of light* (Elsevier, 2013).

[59] Dressaire, E. & Sauret, A. Clogging of microfluidic systems. *Soft matter* **13**, 37–48 (2017).

[60] Gopal, R. *et al.* Electrospun nanofibrous filtration membrane. *Journal of Membrane Science* **281**, 581–586 (2006).

[61] Campbell, A. I. & Haw, M. D. Jamming and unjamming of concentrated colloidal dispersions in channel flows. *Soft Matter* **6**, 4688–4693 (2010).

[62] Cates, M., Wittmer, J., Bouchaud, J.-P. & Claudin, P. Jamming, force chains, and fragile matter. *Physical review letters* **81**, 1841 (1998).

[63] Wyss, H. M., Blair, D. L., Morris, J. F., Stone, H. A. & Weitz, D. A. Mechanism for clogging of microchannels. *Physical review E* **74**, 061402 (2006).

[64] Sauret, A. *et al.* Clogging by sieving in microchannels: Application to the detection of contaminants in colloidal suspensions. *Applied Physics Letters* **105**, 074101 (2014).

Part I

Colloidal Glasses

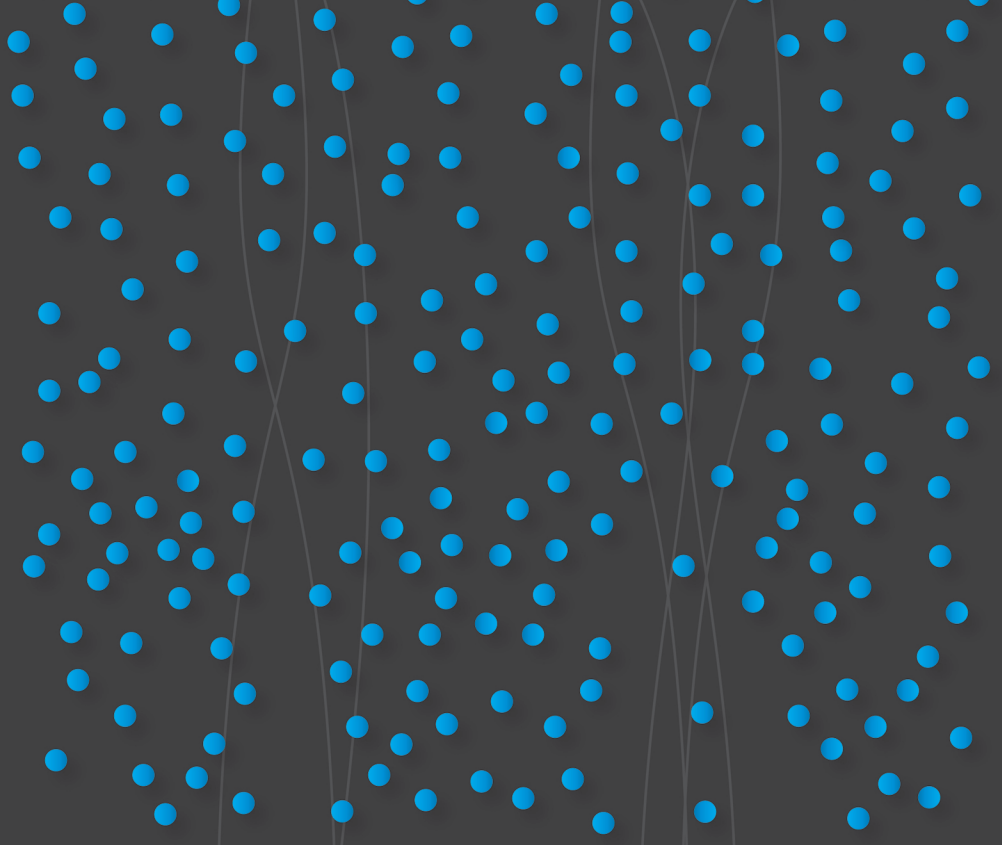

Sticky Squishy & Stuck

Chapter 2

Synthesis of Colloidal Systems

Studying the behavior of dense colloidal systems, both at rest and under flow benefits greatly from quantitative visualization. However, depending on the problem being studied, the requirements for a specific colloidal system can vary greatly. We highlight various synthetic routes towards monodisperse, well-defined colloidal particles which offer control over many important aspects, such as particle size and softness. We provide short recipes for each specific colloidal system and discuss the advantages and limitations of each system.

Manuscript in preparation as:

T. van de Laar, K. Schroën and J. Sprakel: *Synthesis of colloidal systems*

2.1 Introduction

In this thesis we study the behavior of dense colloidal systems in rest and under flow. To allow for quantitative visualization of these experiments, and to enable tuning of particle size, softness and interactions, synthetic protocols that give us control over these crucial properties are necessary. In this chapter we will detail these synthesis methods for the various colloidal systems used in this thesis.

All these systems have their own advantages and disadvantages, broadly speaking differences can be broken down depending on the technique used to visualize the system. For confocal microscopy refractive index matching between the colloidal particles and the surrounding fluid becomes vital. Differences in refractive index between particles and fluid lead to diffuse scattering, minimizing this difference leads to deeper penetration of light into a sample without optical blurring or loss of intensity, which will result in much higher quality images. In bright-field microscopy, image contrast results from the difference in refractive index between particle and fluid, and thus, a high mismatch is often desired. Matching of density between particles and fluid is important in both cases, as minimizing the effects of gravity is always desired. Tuning both refractive index and density simultaneously for a colloidal system usually requires the use of multiple solvents and a mix of monomers that make up the colloidal particles; and their choice another important parameter when designing a colloidal system. Besides, compatibility with elastomers such as PDMS is crucial when performing microfluidic experiments in such devices, which rules out most organic solvents and may require a different colloidal system to fulfil any index- and density-matching requirements. Finally we make the distinction between homogeneous colloids and core-shell colloids. The main difference between the two systems is the location of a fluorescent dye, while homogeneous colloids will be completely fluorescent, core-shell particles will have a non-fluorescent corona surrounding a fluorescent core. This core-shell architecture allows for even more precise imaging, as the separation distance between the various fluorescent centers is much larger. However, this may come at the expense of fluoresence intensity, as there is less fluorescent label present in such a smaller core, compared to a homogeneously dyed particle.

To achieve monodisperse colloidal particles we use three main routes of poly-

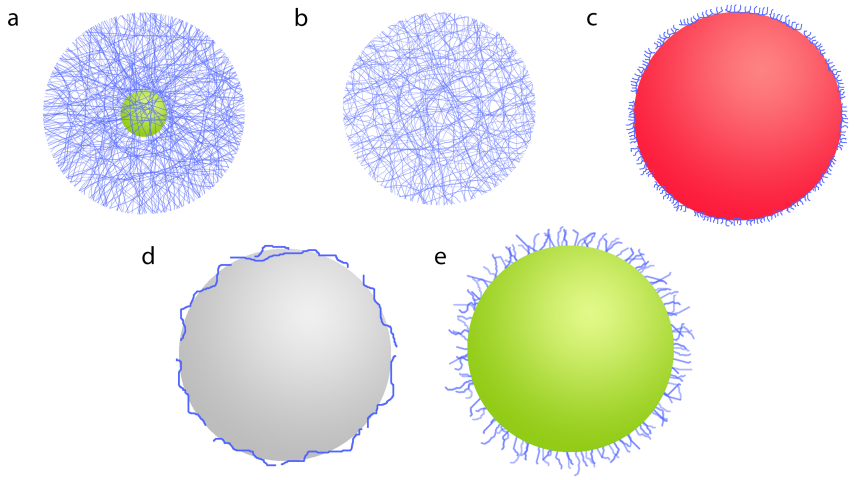

Figure 2.1: Schematic representations of the colloidal particles we use, a) core-shell NIPAm microgels, b) polystyrene microgels, c) PMMA-PHSA hard sphere colloids, d) polystyrene particles and e) tFEMA-tBMA inimer colloids.

merization that are described in more detail in the following sections. All these polymerization techniques are a form of free-radical polymerization, from which we produced the particles schematically depicted in Fig.2.1.

Emulsion Polymerization

Emulsion polymerization starts with an emulsion of monomer, a continuous phase in which the monomer is non-miscible (usually water) and surfactant. Upon injection of a water-soluble free radical agent polymerization is initiated. By contrast to what the name suggests polymerization does not occur in the emulsion droplets (except when talking about mini-emulsion polymerization), but in small micelles formed by the surfactant. Initially, particle nuclei form inside the micellar cores. Subsequently, additional monomer diffuses into these liquid nuclei leading to particle growth. The particle size is determined by the number of nuclei and the amount of monomer available for their growth; the former is controlled by the surfactant concentration, while in general total monomer concentration controls the latter. Emulsion polymerization is suitable for high volume fractions (up to 30 v%), and proceeds to complete conversion over the course of

several hours. In an emulsion polymerization, the particles are stabilized by a combination of the surfactant, adsorbed at the particle-fluid interface, and covalently linked charges resulting from the, often, charged free radical initiator.

Dispersion Polymerization and Precipitation Polymerization

Whereas an emulsion polymerization begins as and remains a two-phase system, the initial states of a dispersion and precipitation polymerization are a homogeneous solution of all necessary ingredients. The reaction is initiated by decomposition of the free radical initiator, often by heat, while light-triggered or redox-active initiators have also been used. Initially, the polymerization results in short oligomers that remain soluble. Once these growing chains reach a critical molecular weight, they become insoluble and precipitate to form the particle nuclei. In a dispersion polymerization, particle stability, which is crucial to avoid aggregation and to obtain well-defined and monodisperse colloids, is provided by the addition of a polymeric stabilizer, often poly(vinyl pyrollidone), which acts as a chain transfer agent and thus tethers covalently to the colloids. By contrast, in a precipitation polymerization, the stabilizer is formed in situ, e.g. through the addition of charged monomers that remain soluble in the continuous phase throughout the reaction. Since solubility plays such an important role the quality of the solvent is the main control parameter to tune particle size in dispersion- or precipitation polymerization.

2.2 Synthesis

Core-shell NIPAm microgels

Microgels are commonly used as model systems for deformable, soft particles. However, these microgels are usually difficult to visualize as it is challenging to incorporate fluorescent labels properly. We solve this issue by synthesizing microgels with a latex, fluorescent core. Due to their core-shell nature (Fig.2.1a), these microgels are well suited for confocal microscopy experiments. These particles readily form crystals, but due to the large separation distance between the fluorescent cores locating is very straightforward (Fig.2.2c). N-isopropyl-

acrylamide (NIPAm) only shows good solvency in pure water and while scattering from the shell is minimised by homogeneous cross-linking, the same cannot be done for the core. The resulting index-mismatch between solvent and core material can be decreased by switching to different monomers for these cores, i.e. 2,2,2-trifluoroethylmethacrylate (tFEMA) or mixtures including tFEMA, which are preferred since fluorescence performance for the latter particles is usually better. The fluor side groups heavily influence the way fluorescent molecules can stack within the core, the addition of other monomers besides tFEMA will make sure fluorescent molecules are incorporated normally. It is good to mention that this inherent index mis-match somewhat limits the use of these microgel particles, especially in experiments where 3D imaging is important.

Using emulsion polymerization we first synthesize small core particles from various monomers[1]; styrene, 2,2,2-trifluoroethylmethacrylate (tFEMA) or a combination of tFEMA and tert-butyl methacrylate (tBMA) mixed at a 1:1 volume-ratio. In a round bottom flask we mix 13.5 gr monomer, 1.5 gr N-isopropylacrylamide (NIPAm), 0.025 gr sodium dodecyl sulfate (SDS), 50 gr water and a fluorescent dye. We flush the solution with nitrogen for 15 minutes while heating to 75°C, after which we initiate the reaction by the addition of 0.15 gr potassium persulfate (KPS) dissolved in 2 ml water. We let the reaction proceed overnight after which we filter the particles and store them for further use.

We synthesize the microgel shell onto these core particles by seeded precipitation polymerization. This also allows for a direct size control, as the amount of cores will directly determine the size of the final core-shell microgel. To ensure a homogeneously cross-linked shell, which will reduce scattering and improve imaging, we create starved-feed reaction conditions by drip addition of monomers[2], as described below.

We mix 1.17 gr NIPAm, 20 ml water, 10 mg N,N-methylenebisacrylamide and 250 μl acrylic acid, this forms our monomer mix. Next we mix 25 ml water, 300 μl core solution (at 25 v%) and 5 ml of this monomer mix in a two-neck round bottom flask. We flush the solution with nitrogen while heating to 80°C under reflux. We initiate the reaction by the addition of 0.02 gr KPS dissolved in 1 ml water. After 4 minutes we start the drip addition of the remaining monomer mix, either from a dripping funnel or via syringe pump, at a rate of 0.35 ml/minute,

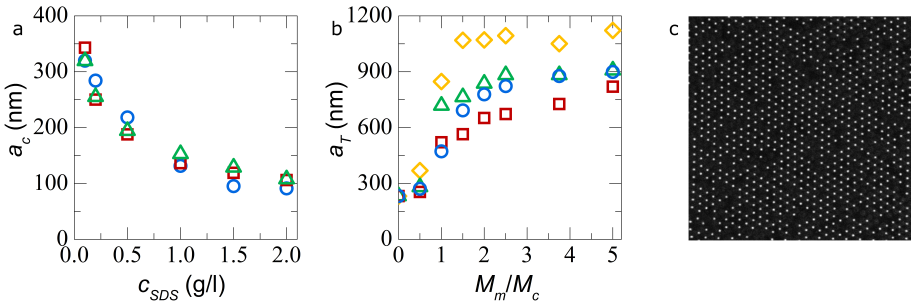

Figure 2.2: a) Latex core size a_c as a function of SDS concentration c_{SDS}, for styrene (circles), MMA (squares) and tFEMA (triangles). b) core-shell microgel size a_T as a function of the ratio of monomer to core material M_m/M_c, crosslinking density (circles, 1% crosslinker and squares 5% crosslinker) and presence of charged monomer (triangles and diamonds, both with 1% crosslinker and 10% charged monomer, in water and 1 mM NaOH respectively). c) confocal image of a microgel suspension, which shows the clear fluorescent separation. Data in a) and b) adapted from[1].

for 45 minutes. After complete monomer addition we allow the reaction to proceed for an additional 15 minutes. Finally we filter and store these particles at refrigerated conditions. We clean our particles by repeated centrifugation cycles, and suspend them in a 10 mM NaOH solution, to swell these microgels to their maximum degree, $\sim 2\mu$m when fully swollen by solvent.

To control the size of the latex core and the NIPAm shell individually we have two control parameters. In the core synthesis we can use the concentration of SDS as an effective way to tune the size of the core a_c, as shown in Fig.2.2a. By varying the ratio of monomer to core material (M_m/M_c) during the shell growth step we can tune the size of the shell, i.e. more cores will mean that on average less monomer is available per particle and that thus the shell will remain thinner. Varying the amount of crosslinker in the shell also changes the size (circles and squares, Fig.2.2b), along with the stiffness of the microgel; more crosslinker means a more dense microgel that is generally smaller. A final way to increase the shell size is by the addition of charged monomers like methacrylic acid or acrylic acid, as these groups will cause large electrostatic repulsions when incorporated into the microgel shell (in the presence of 10 mM NaOH to deprotonate the carboxylic acid groups), which will in turn increase the swelling ratio of the shell further (triangles and diamonds, Fig.2.2b).

Polystyrene microgels

Unlike their NIPAm counterparts, polystyrene microgels (Fig.2.1b) show good solvency in a range of organic solvents, which makes them useful as depletants to study the effect of attractive forces on for instance colloidal glasses. Another advantage is that polystyrene microgels can be synthesized in such a way that they contain no residual charges, which eliminates problems due to charge interaction. The microgels can also be completely index matched in a mixture of bromobenzene and iodobenzene, which makes this a suitable system for light scattering experiments. To synthesize polystyrene microgels[3] we dissolve 12 gr of hexadecyltrimethylammonium bromide (CTAB) in 138 gr deionized water. Seperately we prepare a mixture of 15 ml styrene, 75 μl divinylbenzene and 225 mg 2,2-azobis(2-methylpropionitrile) (AIBN). Which is subsequently emulsified in the surfactant solution, aided by high-intensity ultrasonic treatment to create a stable microemulsion. After mixing we purge the reaction mixture with nitrogen and initiate the polymerisation by heating to 65 $^{\circ}$C. The reaction is allowed to proceed overnight. The particles are purified by precipitation in cold methanol and redissolution in tetrahydrofuran; we repeat this procedure 3 times to ensure complete removal of impurities. The particles are then dried in vacuo. This synthesis results in particles of roughly 10 to 20 nm in diameter, depending on the amount of CTAB added.

Polystyrene particles

Colloidal polystyrene is useful for studies that involve brightfield microscopy and microfluidics, due to the ease of density matching in solvents (a mixture of water and deuterated water) that work well with microfluidic devices made from PDMS. Thanks to the high refractive index-mismatch of polystyrene and these density matching solvents identification of changes in local volume fraction, for instance when a clog forms, are relatively easy. The high refractive index-mismatch is also this systems biggest weakness, as it is almost impossible to simultaneously index and density-match polystyrene, and this severly limits the use in anything besides brightfield imaging.

We synthesize polystyrene particles (Fig.2.1c) by dispersion polymerisation

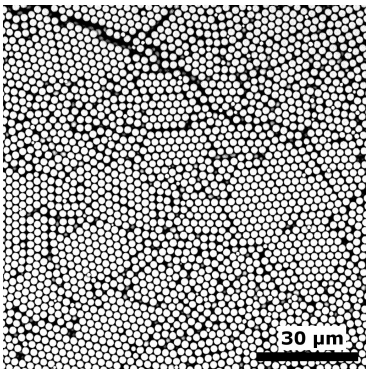

Figure 2.3: Scanning Electron Microscope (SEM) image of polystyrene particles synthesized by dispersion polymerisation, scale bar indicates 30 μm.

[8]. In 150 ml butanol we dissolve 17 ml styrene monomer, 2.34 gr poly(vinylpyrrolidinone)-k30 (PVP-k30), 0.64 gr dioctyl sulfosuccinate sodium salt (AOT) and 0.170 gr 2,2-azobis(2-methylpropionitrile) (AIBN). After mixing we purge the solution with nitrogen for 20 minutes and subsequently evacuate the round bottom flask. We allow the reaction to proceed overnight at 70°C while tumbling. We clean our particles by repeated centrifugation, draining and resuspension. Finally we can suspend our particles in a density-matching mixture of water and deuterated water. Typical particle sizes for this synthesis are around 3 μm, as shown in Fig.2.3.

The particle size can be easily tuned by selecting a different continuous phase, as the alkane part of the alcohol gets longer (up till pentanol) the solvency of the monomer decreases which will result in larger particles. Changing the solvent from methanol to pentanol results in a factor two increase in size, from 2 μm to 4 μm[8].

PMMA-PHSA hard sphere colloids

PMMA-PHSA hard spheres(Fig.2.1d) can be index- and density-matched simultaneously (in a mixture of cyclohexabromide (CXB), tetralin and decalin), making this system particularly well-suited for 3D confocal microscopy. An additional advantage is that it is extremely well studied and the closest approximation to a

true hard sphere system. However, the solvents needed for index- and density-matching can only be used in combination with glass, which prevents their use in for instance microfluidics made from PDMS. Another problem is that CXB is volatile, which makes sample preparation more complex because CXB evaporation needs to be prevented in order to not change the index- and density-match and possibly the volume fraction.

The crucial first step in synthesizing PMMA-PHSA hard spheres is the correct synthesis of the PHSA comb stabiliser[4]. We start by polymerizing 12-hydrostearic acid (HSA) which forms short chains of poly-(12-hydrostearic acid) (PHSA), by azeotropic condensation of HSA in toluene. A typical reaction starts by refluxing 47.9 gr HSA (technical grade), 0.12 gr methane sulfonic acid and 8.6 gr toluene at 150°C overnight. To collect the condensation water, and thereby follow the condensation reaction we use a Dean-Stark apparatus (15 ml size), to which an additional 12 ml toluene is added in the Dean-Stark leg. To achieve typical chain lengths of 4 to 5 monomers, which leads to optimal stability in subsequent steps [4], we collect ∼1.5 ml of water for a reaction of this size. To remove all water we add 20 ml toluene at the end of the reaction and azeotropically distill 15 ml of the added volume.

To functionalize the PHSA from step 1 we react it with glycidyl methacrylate (GMA) to form a methacrylated end-group on the PHSA. We take 49.5 gr PHSA from the previous step and mix this with 46.7 gr toluene, 0.054 gr tert-butyl catechol, 0.134 gr N,N-dimethyldodecylamine and 5.871 gr GMA. We reflux this mixture at 150°C for 7 hours.

In the final step of the stabilizer synthesis we graft these short PHSA chains to a polymethacrylate backbone. First we mix 49.2 gr functionalised PHSA from step 2 with 22.44 gr methyl methacrylate (MMA), 2.50 gr GMA and 0.4 gr 2,2-azobis(2-methylpropionitrile) (AIBN). We add this mixture to a refluxing mixture, at 110°C, of ethyl acetate (EA, 17 gr) and butyl acetate (BA, 8.5 gr) using a syringe pump, at 0.45ml/min for a total addition time of 3 hours. We allow the reaction to proceed for an additional 2 hours, after which we add 0.19 gr AIBN in 2 gr EA and 1 gr BA. After another 2 hours we inject a similar portion of AIBN. Finally we dilute with 26.56 gr EA and 13.28 gr BA and allow the reaction to proceed for another 15 hours. After cooling, the mixture is used directly as a

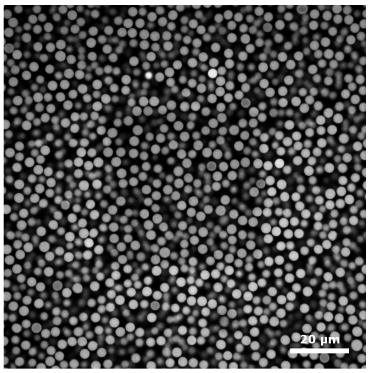

Figure 2.4: Confocal Laser Scanning Microscopy (CSLM) image of fluorescently dyed PMMA-PHSA particles, scale bar indicates 20 μm.

stabiliser during the synthesis of PMMA-PHSA hard spheres.

To synthesize colloidal PMMA particles we mix 49 gr MMA, 1 gr methacrylic acid, 29.8 gr hexane, 14.3 gr mineral oil and 10 mg Nile Red dye in a 250 ml round bottom flask. We add a magnetic stir bar and stir untill the dye has dissolved. Finally we add 5 gr of the stabiliser, 0.39 gr AIBN and 0.3 gr 1-octanethiol. We allow the reaction to proceed under reflux at 80°C for 2 hours while stirring slowly. We filter the resulting particle suspension and wash the particles by repeated centrifugation. To index and density match our particles we suspend them in a mixture of cyclohexyl bromide (CXB), decalin and tetralin (roughly 80/5/15 vol%) and add 200 nM tetrabutylammonium bromide to ensure hard-sphere interactions[4, 5, 6, 7].

The major advantage of this synthesis method is that it yields highly monodisperse particles (Fig.2.4) if the stabiliser is synthesized well. Sizes can be controlled directly by varying the amount of monomer added in the final step, going from 35% to 55% monomer leads to particles ranging between 200 nm to just under 3 μm respectively[6]. However, the stabiliser synthesis itself is non-trivial and while a proper stabiliser will yield highly monodisperse particles, a poor stabiliser will only yield undesired highly polydisperse particles.

tFEMA-tBMA-inimer colloids

As an alternative to the hard sphere PMMA system that is compatible with PDMS microfluidics we synthesize particles (Fig.2.1e) by copolymerizing two monomers, tBMA and tFEMA at a volume ratio of 72:28, by dispersion polymerization[9]. These particles can be index- and density-matched in solvents compatible with PDMS (mixtures of both water and 2,2,-thiodiethanol and sulfonone and formamide work very well), the solvents are also non-volatile, which simplifies sample handling. By incorporating a reactive group for Atom Transfer Radical Polymerization (ATRP) we can modify the surface of our particles after the initial synthesis, which allows us to greatly increase the stability and tune any desired surface interactions[9]. It is possible to synthesize these particles in two ways; homogeneously fluorescently labeled and with a core-shell architecture. We first describe the homogeneous case, as the core-shell version of these particles only requires a small variation of this standard recipe.

A typical synthesis proceeds as follows: we mix 90 ml MeOH, 10 ml water, 2.8 ml tFEMA, 7.2 ml tBMA, 4 gr PVP-k30, 100 mg AIBN and 250 μl PEG-inimer (a low molecular weight PEG chain with a methacrylate on one end and a 2-(2-bromoisobutyryloxy) ethyl group for ATRP synthesis on the other side) in a round bottom flask and purge with nitrogen for 20 minutes. We evacuate the flask before tumbling the solution overnight at 55°C.

To modify the surface of our particles using ATRP we add to a round bottom flask 67 ml water, 67 ml formamide, 5 gr 3-sulfopropyl methacrylate potassium salt (SPMA), 2.5 gr N,N-dimethylacrylamide (DMA), 245 μl 1,1,4,7,10,10-hexamethyltriethylenetetramine (HMTETA), 50 mg Cu(II)Cl_2 and 100 μl methyl 2-bromopropionate, which acts as a sacrificial initiator during the ATRP reaction to control the chain lengths of polymer created on the surface of a particle. To this mixture we add the unwashed particle suspension from the previous step. We purge the entire mixture while stirring for several hours to completely remove any oxygen. We initiate the ATRP reaction by adding 45 mg Cu(I)Cl and allow the reaction to proceed overnight at room temperature.

After surface modification we add a fluorophore to the particles by swelling. We create a mini-emulsion of 3.5 gr toluene (with 10 mg fluorophore) in 32 gr of water using 700 mg Pluronic F127 by high-shear mixing and ultrasonic

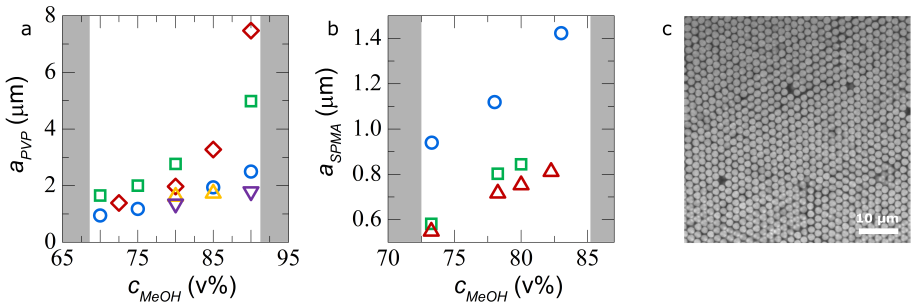

Figure 2.5: a) effect of co-solvent and inimer type on the diameter of PVP stabilized particles; (circles) water and no inimer, (up-triangles) water and acrylate inimer, (down-triangles) water and methacrylate inimer, (squares) formamide and acrylate inimer, (diamonds) formamide and methacrylate inimer. b) effect of monomer concentraiton on particle size for SPMA stabilized particles, (circles) 15 v% monomer, (squares) 10 v% monomer, (triangles) 5 v% monomer. Shaded areas in both a) and b) show areas where the synthesis only yields polydisperse, coagulated samples. c) CLSM image of homogeneously fluorescently labeled tFEMA-tBMA-inimer particles, scale bar indicates 10 μm. Data in a) and b) adapted from [9].

treatment. We add this mini-emulsion to the particle suspension and allow the particles to swell and take up flourophore for 5 hours. We flush the suspension with nitrogen at 50°C overnight to completely remove all toluene.

Particle sizes can be tuned by changing the ratio between solvents or changing the solvent type during synthesis, as shown in Fig.2.5a. This synthesis method yields highly monodisperse and highly fluorescent particles, as shown in Fig.2.5c.

To synthesize core-shell particles we first synthesize particles using SPMA as a stabilizer instead of PVP. In this case we control particle size by changing the amount of monomer present, instead of varying the co-solvent ratios, as shown in Fig.2.5b. A typical core synthesis proceeds as follows: we mix 80 ml MeOH, 22 ml water, 2.8 ml tFEMA, 7.2 ml tBMA, 0.11 g of SPMA, 0.1 ml of inimer, 0.1 ml of ethylene glycol dimethacrylate (EGDMA), a fluorescent monomer, like rhodamine B-methacrylate and 0.1 g AIBN. We heat the mixture to 80°C and reflux the mixture for 5 hours. We can than use these fluorescent cores for a seeded dispersion polymerization step, using the recipe described earlier for our homogeneously fluorescent particles with PVP. The thickness of the shell can be precisely controlled by the amount of cores added to the shell growth step[9].

To simultaneously index- and density-match these particles we suspend them in a 30/70 v% mixture of water and 2,2,-thiodiethanol. To screen electrostatic interactions we add 10 mM NaCl.

Conclusion

By having a broad spectrum of synthesis methods available we can make a wide range of colloidal particles. This gives us a versatile toolbox to study various problems in soft matter physics while utilising a range of different techniques. In the following chapters all of the mentioned colloidal systems are utilised, by fine-tuning them to the specific experiment. Creating a working experimental system however, is only the first step and the following chapters will focus on the scientific questions that these experimental systems help to answer.

References

[1] Appel, J. *et al.* Temperature Controlled Sequential Gelation in Composite Microgel Suspensions. *Particle and Particle Systems Characterization* **32**, 764–770 (2015).

[2] Still, T., Chen, K., Alsayed, A. M., Aptowicz, K. B. & Yodh, A. G. Synthesis of micrometer-size poly(N-isopropylacrylamide) microgel particles with homogeneous crosslinker density and diameter control. *Journal of Colloid and Interface Science* **405**, 96–102 (2013).

[3] Antonietti, M. *et al.* Synthesis and size control of polystyrene latices via polymerization in microemulsion. *Macromolecules* **24**, 6636–6643 (1991).

[4] Elsesser, M. T. & Hollingsworth, A. D. Revisiting the Synthesis of a Well-Known Comb-Graft Copolymer Stabilizer and Its Application to the Dispersion Polymerization of Poly(methyl methacrylate) in Organic Media. *Langmuir* **26**, 17989–17996 (2010).

[5] Klein, M. K., Zumbusch, A. & Pfleiderer, P. Photo-crosslinkable, deformable PMMA colloids. *Journal of Materials Chemistry C* **1**, 7228 (2013).

[6] Antl, L. *et al.* The preparation of poly(methyl methacrylate) latices in non-aqueous media. *Colloids and Surfaces* **17**, 67–78 (1986).

[7] Royall, C. P., Poon, W. C. K. & Weeks, E. R. In search of colloidal hard spheres. *Soft Matter* **9**, 17–27 (2013).

[8] Paine, A. J., Luymes, W. & McNulty, J. Dispersion polymerization of styrene in polar solvents. 6. Influence of reaction parameters on particle size and molecular weight in poly(N-vinylpyrrolidone)-stabilized reactions. *Macromolecules* **23**, 3104–3109 (1990).

[9] Kodger, T. E., Guerra, R. E. & Sprakel, J. Precise colloids with tunable interactions for confocal microscopy. *Scientific Reports* **5**, 14635 (2015).

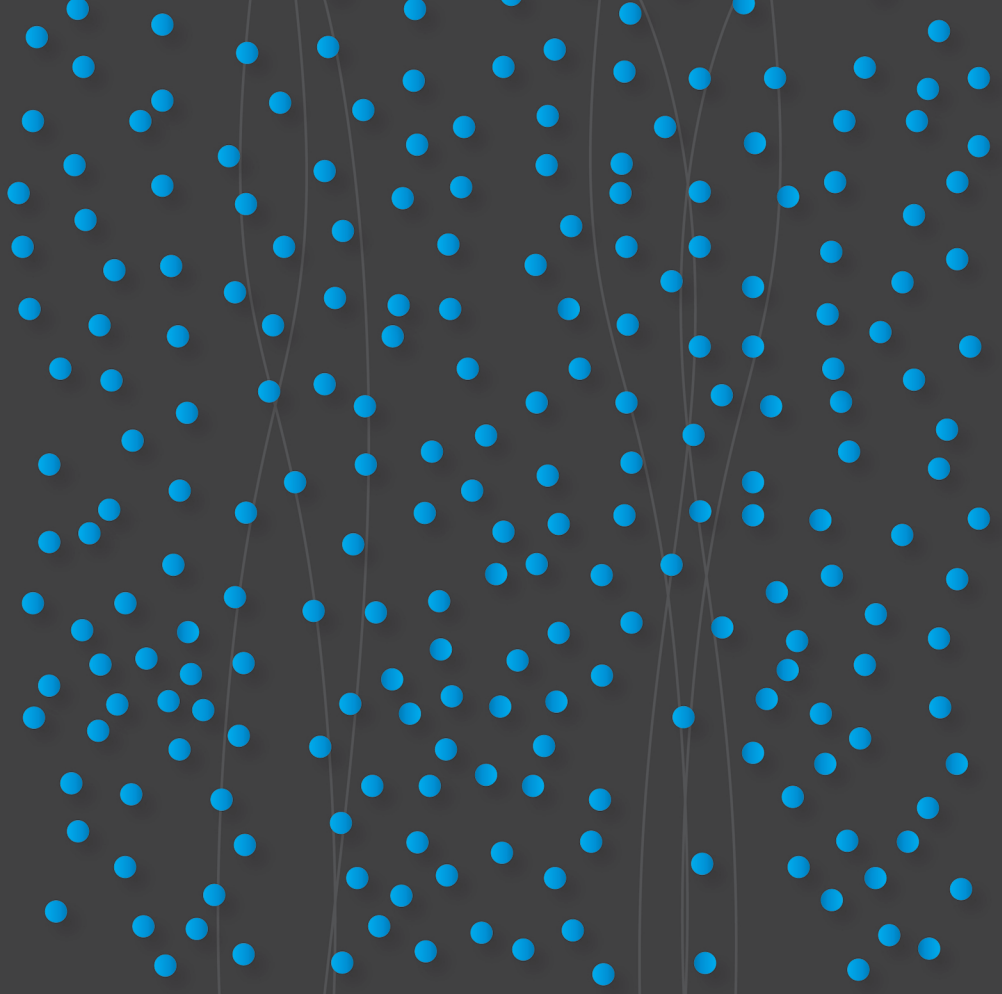

Sticky Squishy & Stuck

Chapter 3

Discontinuous Nature of the Repulsive-to-Attractive Colloidal Glass Transition

In purely repulsive colloidal systems a glass transition can be reached by increasing the particle volume fraction beyond a certain threshold. The resulting glassy state is governed by configurational cages which confine particles and restrict their motion. A colloidal glass may also be formed by inducing attractive interactions between the particles. When attraction is turned on in a repulsive colloidal glass a re-entrant solidification ensues. Initially, the repulsive glass melts as free volume in the system increases. As the attraction strength is increased further, this weakened configurational glass gives way to to an attractive glass in which motion is hindered by the formation of physical bonds between neighboring particles. In this Chapter, we study the transition from repulsive-to-attractive glasses using three-dimensional imaging at the single-particle level. We show how the onset of cage weakening and bond formation is signalled by subtle changes in local structure. We then demonstrate the discontinuous nature of the solid-solid transition, which is marked by a critical onset at a threshold bonding energy. Finally, we highlight how the interplay between bonding and caging leads to complex and heterogeneous dynamics at the microscale.

This chapter was published as:

T. van de Laar, R. Higler, K. Schroën and J. Sprakel: *Discontinuous Nature of the Repulsive-to-Attractive Colloidal Glass Transition*, Sci. Rep. *6* (**2016**), 22725.

3.1 Introduction

The vitrification of colloidal hard spheres is accompanied by a rapid rise in structural relaxation time when the particle volume fraction ϕ is increased in proximity of the glass transition at $\phi_g \approx 0.58$. The reduction in free volume at these densities leads to the emergence of configurational cages in which particle motion is restricted by neighbouring particles [1, 2, 3]. The introduction of short-ranged attractive interactions to a hard sphere suspension in the supercooled regime leads to a departure from this well-established caging picture [4, 5, 6]. Low attraction strengths, $U \approx k_B T$, give rise to weak clustering which increases the local free volume and melts the glass [7, 4]. Upon increasing the strength of attractive interactions, physical bonds between neighboring particles form, whose lifetime grows with attraction strength [8]. This causes a re-entrance into a bonding-dominated glassy state whose properties are distinctly different from the repulsive glass [9, 10].

In dilute suspensions of colloids, short-ranged attractions lead to phase separation and kinetic arrest. This result in the formation of a highly heterogeneous solid state; the colloidal gel [11, 12, 10]. It has been proposed that the gel line in the (U, ϕ)-plane of the suspension phase diagram extends to the supercooled regime and causes the re-entrant transition to an attractive glass[7, 4, 6, 13]. Nonetheless, several key questions about the nature of this solid-solid transition between two very different amorphous states remain unanswered.

For example, what is the nature of dynamical arrest at the onset of the attractive glass transition? In repulsive systems arrest occurs by the formation of confining cages which slow down particle self-diffusion in proximity of the glass transition ϕ_g. Even though the decrease of particle mobility is steep, the transition is continuous as the system remains ergodic up to, and beyond, ϕ_g[14]. By contrast, the gel point in dilute suspensions of attractive colloids is characterised by both structural and dynamical signs of a critical percolation transition[15, 11, 12]. Finally, in colloids which bond with a well-defined valency, yet another scenario is reported, where the glass transition exhibits Arrhenius behavior with a relaxation time $\tau \propto \exp(U/k_B T)$ and no critical onset[16]. This raises the question how a dense suspension of particles undergoes a transition to an attractive glass, where bonding forces rule, but remnants of configurational cages

persist. Moreover, our understanding of how interactions influence the spatial homogeneity of local dynamics in three-dimensional glasses is incomplete. For purely repulsive system the length scale associated with dynamical heterogeneity is known to grow strongly upon increasing the particle volume fraction[17]. For two-dimensional glasses, experiments have shown a transition from string-like cooperative motion for repulsive particles, to condensed islands of larger mobility at moderate attractions[8]. However, it was recently established that there are distinct differences in the glass transition in two and in three dimensions [18]. It thus remains a challenge to establish the transitions in global and local dynamics occurring during the attractive glass transition in three dimensions.

In this Chapter we use three-dimensional confocal fluorescence imaging to explore the nature of the transition from repulsive to attractive colloidal glasses upon introducing weak bonding interactions. We show how small changes in local structure signal the onset of bond formation. This results in a critical onset for the attractive glass. At the edges of the intermediate supercooled liquid state, we find a distinct discontinuity in the length scale associated with heterogeneous dynamics. Our results evidence the proposed connection between gels and attractive glasses[10, 13], and shed new light on this transition between two disordered solids governed by different microscopic physics.

3.2 Results & Discussion

We study a glass of colloidal hard spheres in a solvent mixture that closely matches the density of the particles; this allows us to study equilibrium bulk behavior in absence of gravitational stresses. In this solvent mixture, also the refractive index of the fluorescent colloids is matched, enabling us to look deep inside the suspension with confocal fluorescence microscopy. The suspensions consists of a bidisperse mixture, with particles of $a_A = 0.89$ and $a_B = 1.23$ μm, to avoid crystallisation even after prolonged equilibration. We note that we do not observe decoupling between the diffusivity of the two sizes for this size ratio [19]. The sample bidispersity completely prevents local crystalline order. To introduce attractive interactions we add polystyrene microgels to the suspension ($a_{\mu g} = 21$ nm), which induce a depletion attraction between the larger

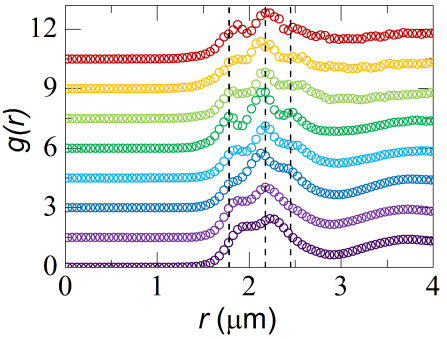

Figure 3.1: Pair correlation functions as a function of attraction strength, with (bottom to top): $U/k_BT = 0$, 0.8, 2.5, 3.1, 4.6, 5.2, 6.7 and 8.3. Curves have been offset vertically for clarity. Dotted lines indicate bonding distances between AA, AB and BB pairs in the bidisperse glass.

colloidal hard spheres[20]. The depth of the attractive minimum due to the depletion of the larger hard spheres by the smaller microgels is approximated as $U/k_BT \approx \frac{3}{2}\frac{a_L}{a_S}\phi_S$[20], where $\frac{a_L}{a_S} = \frac{\frac{1}{2}(a_A+a_B)}{a_S} \approx 50$ is the size ratio of hard spheres to depletant and ϕ_S the volume fraction of polystyrene microgels, which we determine by capillary viscosimetry.

Structure

The purely repulsive glass exhibits a liquid-like pair correlation function $g(r)$ that is devoid of any signs of long- or medium-ranged order (Fig.3.1). This illustrates how the binary size ratio we use here thus frustrates the system such that ordering is prevented completely. The global shape of the pair correlation function is unaffected by increasing the interparticle attraction energy (Fig.3.1). However a subtle change in the nearest-neighbor peak is observed when interparticle attractions become significant. As U increases, bonds between neighboring particles form, which gives rise to a distinct fine-structure in the first peak of $g(r)$. Since the sample is composed of two distinct populations, three sub-peaks emerge indicative of AA, AB and BB bonds (dotted lines Fig.3.1). Thus, while weak attraction does not change the global structure of the glass, subtle changes

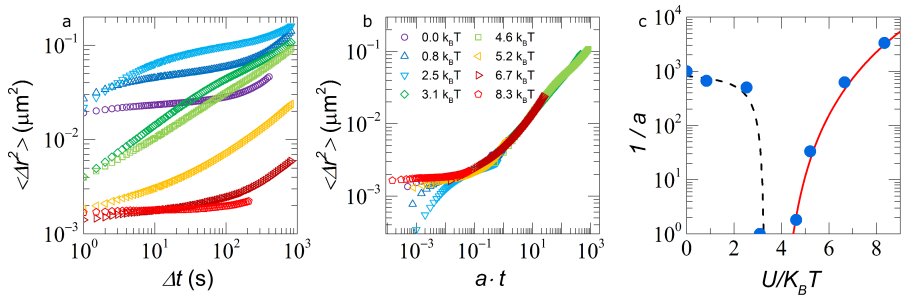

Figure 3.2: Mean-squared displacements $\langle \Delta r^2(\Delta t) \rangle$ for all attraction strengths and b) The same mean-squared displacements superposed onto a single master curve, symbols and colors are similar for both figures. c) Shows shift factor $1/a$ as a function of U: solid line is a fit to the data with $1/a \propto (U - U_c)^v$, dotted line is a guide to the eye.

occur at the nearest-neighbor level.

Global dynamics

To explore how these changes in local structure affect the global dynamics of the glass we calculate the ensemble-averaged mean-squared displacement $\langle \Delta r^2 \rangle$. For the repulsive glass we find the characteristic short-time cage rattling motion leading into a caging plateau and the subsequent upturn towards long-time diffusion at longer times due to cage breaking (Fig.3.2a). For weak attractions, $U < 3$ k_BT, $\langle \Delta r^2 \rangle$ shifts upwards signaling the gradual "melting" of the glass. Upon crossing a threshold attraction strength $U \approx 3$ k_BT, corresponding to where bonding peaks emerged in the $g(r)$, $\langle \Delta r^2 \rangle$ strongly decreases with increasing attraction strength as the system enters the attractive glassy state (Fig.3.2a). This re-entrance was observed previously in both hard spheres[7, 8, 21] and microgels [4].

The structural relaxation time cannot be easily extracted directly from confocal microscopy experiments as we only have access to a limited range of lag times. We therefore rescale the mean-square displacements to a master curve, in analogy to the time-temperature superposition principle used for the rheology of molecular and polymeric glass formers[22].

We find a good collapse of the mean-squared displacements for time scales

which are associated with cage- or bond-breaking and translational diffusion (Fig.3.2b). This suggests a universal shape of the mean-squared displacements for these processes, with an observation window depending only on the ratio of experimental time versus the characteristic time scale for a particle to escape its neighbors. However, the rescaling does not collapse the short time dynamics. In this regime particles perform vibrations within a repulsive cage, or confined by attractive bonds; these dynamics depend mainly on the curvature of the confining potential rather than its absolute depth, and on the number of bonded neighbors.

We can now evaluate the attraction strength dependence of the shift factor a for the lag time axis, which relates to the structural relaxation time of the sample as $\tau \sim 1/a$ (Fig.3.2c). The liquefaction of the repulsive glass, which results from a rise in free volume due to clustering, can be clearly observed at low U. The relaxation time decreases very strongly close to an attraction strength $U \approx 3.5 k_B T$ where the glass melts, suggesting a steep dependence of particle diffusivity on free volume in proximity to the glass transition. This is also manifested by the fragility of the hard sphere glass transition along the ϕ axis[14].

On the attractive side of the re-entrance $U > 4\ k_B T$, we see a strong rise in relaxation time, increasing by more than 3 orders of magnitude over a small range of U (Fig.3.2c). In dilute suspensions, the dynamics and mechanics are established to exhibit a critical scaling at the onset of gelation. Also for the attractive glass transition we study, this scenario holds: our data is well described by the critical power-law $\frac{1}{a} \propto (U - U_c)^v$, with $U_c = 3.9\ k_B T$ the critical attraction strength for the onset of bonding-dominated arrest and $v = 4$ the critical exponent. This provides direct experimental evidence for the theoretical prediction that bonding-dominated arrests, whether it is gelation at low volume fractions or vitrification at high volume fractions, occurs by crossing a universal gel line that traverses the (U, ϕ)-plane of the suspension phase diagram.

Local & heterogeneous dynamics

Both the average global structure and dynamics display a distinct transition from a caging-dominated glass to a solid state governed by particle bond formation. We proceed by investigating dynamics at the local, single-particle, scale. We com-

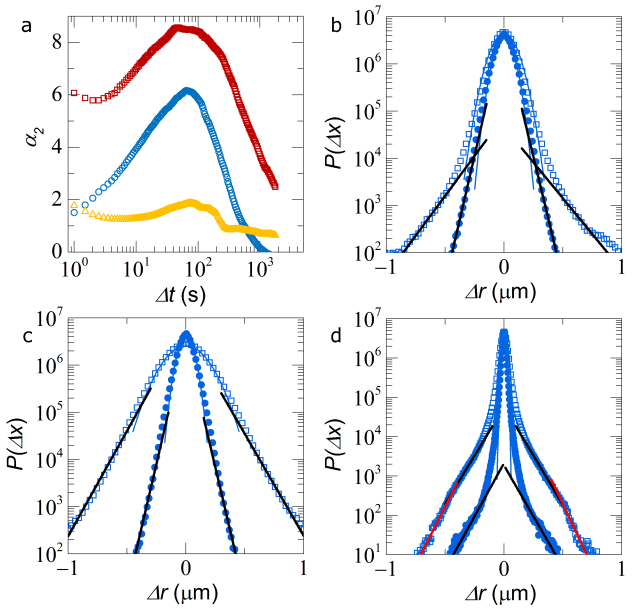

Figure 3.3: a) Non-gaussian parameter $\alpha_2(\Delta t)$ for the repulsive glass (U =0 k_BT, circles), the supercooled liquid (U =2.5 K_BT, triangles) and attractive glass (U =8.3 k_BT, squares), b-d) show corresponding particles displacement probabilities $P(\Delta r, \Delta t)$ for Δt = 0.5 s (circles) and $t = t^*$ (squares). Lines are fits to Gaussian (blue) and exponential distributions (red and black) as discussed in the text.

pute the Gaussianity of the particle displacements Δr by means of the often used non-Gaussian parameter $\alpha_2 = \langle \Delta r^4 \rangle / (3\langle \Delta r^2 \rangle^2) - 1$. For the repulsive glass $U = 0$, we find strongly heterogeneous dynamics peaking at a characteristic time t^* ≈66s (Fig.3.3a). The corresponding displacement distributions $P(\Delta r)$ show largely Gaussian behavior for short times $t \ll t^*$ and a characteristic Gaussian distribution with exponential tails at t^* (Fig.3.3b)[17]. As the glass melts, the dynamics become significantly more homogeneous, with α_2 becoming much smaller over the entire range of time scales explored (Fig.3.3a). Also the displacement distributions become more Gaussian, while exponential tails persist at the largest Δr (Fig.3.3c); indicating that due to the high ϕ in our experiments, the glass melts into the strongly supercooled regime, which still exhibits signatures of glassy dynamics.

In the attractive glass, the heterogeneous dynamics are most pronounced; α_2 is finite and large across the entire spectrum, even for the shortest lag times we explore (Fig.3.3a). Inspection of $P(\Delta r)$ shows two distinct populations at the shortest lag times $t = 0.5s$. We observe a narrow Gaussian mode of small displacements, which we attribute to bond vibrations, and an exponential relaxation mode, due to intermittent debonding-induced local translation within configurational cages. These motions extend to somewhat larger distances, but do not exceed the typical size of the cages (Fig.3.3d). As thermally-activated bond breaking is a Poisson process, even at the short times both bonded particles and those that have debonded and diffuse within a configurational cage must be present. At larger times $t = t^*$, a second exponential relaxation mode becomes apparent, which results from particles which both debond and escape their configurational cages, which eventually leads to long-time translational motion. While the attractive glass transition is dominated by attractive bonds, the remnant of cages remain noticeable in the local glass dynamics, giving rise to complex relaxation dynamics. This is also reflected in the non-linear rheology of attractive glasses, which exhibit two distinct yielding processes associated with bond- and cage-breaking[9, 10].

Finally, we evaluate the spatial homogeneity of these multiple populations which coexist within the glass adopting the approach described previously [17]. We first identify the particles with the largest displacements at t^*. We select the 10% fastest particles, averaged over the entire length of the experimental observation. This means, that within each frame the number of fast particles can vary substantially. Clusters of these "fast" particles are determined based on proximity, allowing us to measure their size N. In all cases, a large amount of isolated fast particles, N =1 are observed. To visualise the extent of clustering, we reconstruct our three-dimensional experimental data by showing "fast" particles part of a cluster with $N > 2$ at true size and all others at reduced size for visibility.

While the purely repulsive glass displays several large, spatially extended clusters (Fig.3.4c), particle dynamics appear more homogeneous for systems deep within the attractive glass regime (Fig.3.4d). Indeed, the cluster size distributions $P(N)$ show a subtle change in the probability of finding large clusters; with the repulsive glass being more prone to exhibiting spatial heterogeneity involving

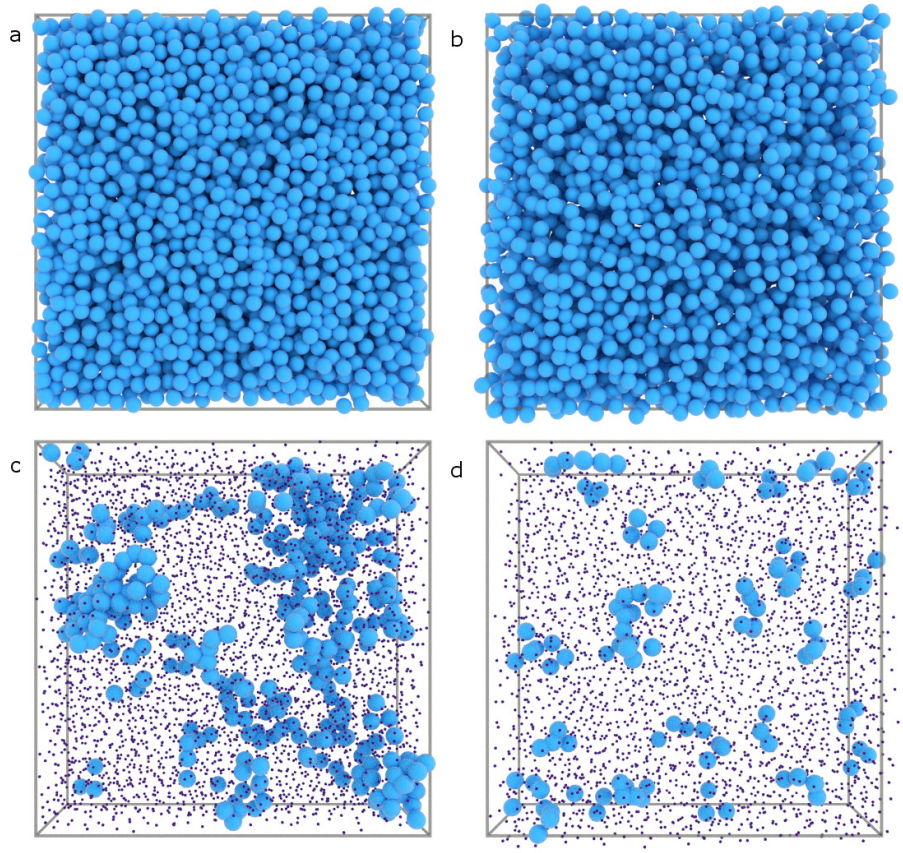

Figure 3.4: Computer-generated renderings of the experimental system for $U = 0$ k_BT (a,c) and $U = 8.3\ k_BT$ (b,d). Top row: all particles in the glass at approximately their real size, bottom row: highlighting the location of the fastest particles part of clusters with $N_c > 2$ in the glass, all others shown at reduced size for clarity.

many particles (Fig.3.4c). We note that, $P(N > 2)$ at all attraction strengths, is well described by an exponential decay (dotted lines in Fig.3.5a), indicative of a characteristic length scale associated with these heterogeneous dynamics.

As a measure for the spatial extent of clustering we measure the time-averaged size of the largest cluster in our field of view $\langle N_{max} \rangle$. This clearly reveals a discontinuity, as predicted by mode-coupling theory, at the transition from repulsive to attractive glass[6]. The characteristic cluster size vanishes as the re-

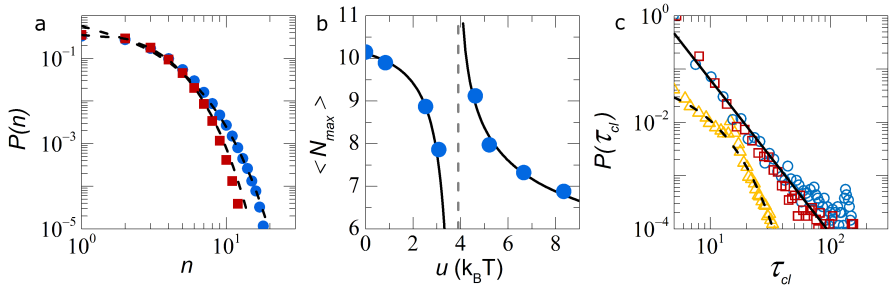

Figure 3.5: a) Probability distributions of cluster sizes $P(N)$ for the repulsive (circles) and attractive glass (squares), corresponding lines show fits to an exponential distribution. b) Maximum average cluster size $\langle N_{max} \rangle$ as a function of U. Solid lines indicate the discontinuity at U_c (dotted line). c) Distribution of the lifetime of a particle in a connected cluster of fast particles $P(\tau_{cl})$, for repulsive (circles) and attractive glasses (squares) and the re-entrant liquid (triangles). Solid line is a powerlaw fit, dotted line an exponential distribution.

pulsive glass melts towards U_c, whereas the same measure diverges when U_c is approached from the attractive side (Fig.3.5b).

These clusters of fast particles that are characteristic of heterogeneous dynamics in supercooled liquids emerge within the amorphous solid due to subtle differences in local structure. As collective thermal fluctuations continuously randomize the local surroundings of each particle, we may expect these clusters to be transient and dissolve and emerge throughout the solid as time proceeds. We compute the average life time τ_{cl} that a single particle is connected to a cluster as a proxy for the cluster dynamics. Interestingly, we find a distinctly different behavior in the re-entrant liquid as compared to the glassy phases. In the liquid, the cluster lifetime decays exponentially, with a characteristic decay time $\tau^*_{cl} \approx 5$ s, which corresponds roughly to the Brownian time scale of the particles (triangles in Fig.3.5c). Simple diffusion thus governs the cluster dynamics in the liquid as expected. However, in the glassy state, the exponential decay gives way to a powerlaw probability distribution (circles and squares in Fig.3.5c). This indicates that there is no longer a characteristic time scale for transient cluster dynamics. This suggests that not only the structure of these clusters is fractal[17] but that their scale-free nature extends to their dynamics. Surprisingly, this met-

ric does not show any difference between the repulsive and attractive glasses. We speculate that the emergence and dissolution of the "fast" clusters is governed by very small and local positional fluctuations of the particles. The short-time dynamics of the colloids in the glass are relatively unaffected by attraction strength, as compared to the long-time diffusive behavior which shows a strong dependence on the particle interactions (Fig.3.2).

Conclusion

These results show how small changes in local structure, signalling the onset of bond formation, give rise to large changes in global and local particle dynamics when a repulsive glass transforms into an attractive glass. The attraction-induced melting of the repulsive glass shows strong similarities to its behavior at $U = 0$ with changing ϕ. By contrast, the emergence of the attractive glass is strongly bonding-driven, exhibiting a distinct critical onset as the suspension crosses the gel line. Within the attractive glass dynamics are revealed to be complex, with different modes of relaxation acting simultaneously. Our results highlight the different microscopic physics which govern repulsive and attractive glasses and shed new light on the competition between bonding and caging at the boundary between these two different amorphous solids.

Methods

Colloidal glasses

We study a colloidal glass of fluorescent poly(methyl methacrylate) particles, stabilised by poly(hydroxy-stearic acid). The particles are synthesized following established protocols[23, 24] and labelled with the dye Nile Red. After cleaning by repeated washing against hexanes, the particles are suspended and equilibrated in an index- and density-matching mixture of cyclohexyl bromide, decaline and tetralin. To ensure hard-sphere like interactions, we add 260 nM tetrabutylammonium bromide to screen residual charge interactions[25]. We use a bidisperse mixture of particles with radii $a_A = 0.89$ and $a_B = 1.23$ μm radius to avoid crystallisation even after prolonged equilibration. At this size ratio we do not observe decoupling between the diffusivity of the two sizes[19]. Quantifying the

exact value of the volume fraction of concentrated suspensions is notoriously difficult especially for bidisperse mixtures[26]; we determine the effective volume fraction at $\phi \approx 0.57$ by sedimenting a diluted stock and assuming a random close packed sediment at $\phi \approx 0.65$. In all our experiments ϕ is kept strictly constant such that errors in determining ϕ do not lead to systematic error in our analysis.

Depletion interactions are induced by addition of polystyrene microgels, synthesized as following[27]. In brief: 12 gr of hexadecyltrimethylammonium bromide (CTAB) is dissolved in 138 gr deionized water. In a separate flask, we prepare a mixture of 15 ml styrene, 75 μl divinylbenzene and 225 mg 2,2-azobis(2-methylpropionitrile) (AIBN). We subsequently emulsify the styrene mixture in the surfactant solution, aided by high-intensity ultrasonic treatment to create a stable microemulsion. After mixing we purge the reaction mixture with nitrogen and initiate the polymerisation by heating to 65 °C. The reaction is allowed to proceed overnight. The particles are purified by precipitation in cold methanol and redissolution in tetrahydrofuran; we repeat this procedure 3 times to ensure complete removal of impurities. The particles are then dried in vacuo. The resulting polystyrene microgels exhibit a hydrodynamic radius of $a_{\mu g} = 21$ nm in the solvent mixture described above.

Confocal microscopy

The samples are loaded into hermetically sealed glass sample chambers; after equilibration for at least several hours, images are recorded using a Visitech VT-infinity3 equipped with a Hamamatsu ORCA Flash 4.0 camera. For each sample we acquire 5000 three-dimensional image volumes of 52x52x22 μm at 2 stacks/s. From these data, particle coordinates are extracted in three-dimensions and time using established routines[28] with a spatial resolution of 30 nm in xy and 60 nm in z.

References

[1] Hunter, G. L. & Weeks, E. R. The physics of the colloidal glass transition. *Rep. Prog. Phys.* **75**, 66501 (2012).

[2] Pusey, P. N. *et al.* Hard spheres: crystallization and glass formation. *Phil. Trans. R. Soc. A* **367**, 4993–5011 (2009).

[3] van Megen, W. & Underwood, S. M. Glass transition in colloidal hard spheres: Mode-coupling theory analysis. *Phys. Rev. Lett.* **70**, 2766–2769 (1993).

[4] Eckert, T. & Bartsch, E. Re-entrant Glass Transition in a Colloid-Polymer Mixture with Depletion Attractions. *Phys. Rev. Lett.* **89**, 125701 (2002).

[5] Pham, K. N., Egelhaaf, S. U., Pusey, P. N. & Poon, W. C. K. Glasses in hard spheres with short-range attraction. *Phys. Rev. E* **69**, 11503 (2004).

[6] Dawson, K. *et al.* Higher-order glass-transition singularities in colloidal systems with attractive interactions. *Phys. Rev. E* **63**, 11401 (2000).

[7] Pham, K. N. *et al.* Multiple Glassy States in a Simple Model System. *Science* **296**, 104–106 (2002).

[8] Zhang, Z., Yunker, P. J., Habdas, P. & Yodh, a. G. Cooperative Rearrangement Regions and Dynamical Heterogeneities in Colloidal Glasses with Attractive Versus Repulsive Interactions. *Phys. Rev. Lett.* **107**, 208303 (2011).

[9] Pham, K. N. *et al.* Yielding behavior of repulsion- and attraction-dominated colloidal glasses. *J. Rheol.* **52**, 649–676 (2008).

[10] Koumakis, N. & Petekidis, G. Two step yielding in attractive colloids: transition from gels to attractive glasses. *Soft Matter* **7**, 2456–2470 (2011).

[11] Lu, P. J. *et al.* Gelation of particles with short-range attraction. *Nature* **453**, 499–503 (2008).

[12] Trappe, V., Prasad, V., Cipelletti, L., Segre, P. N. & Weitz, D. A. Jamming phase diagram for attractive particles. *Nature* **411**, 772–775 (2001).

[13] Bergenholtz, J. & Fuchs, M. Nonergodicity transitions in colloidal suspensions with attractive interactions. *Phys. Rev. E* **59**, 5706–5715 (1999).

[14] Brambilla, G. *et al.* Probing the Equilibrium Dynamics of Colloidal Hard Spheres above the Mode-Coupling Glass Transition. *Phys. Rev. Lett.* **102**, 85703 (2009).

[15] Patrick Royall, C., Williams, S. R., Ohtsuka, T. & Tanaka, H. Direct observation of a local structural mechanism for dynamic arrest. *Nat. Mater.* **7**, 556–561 (2008).

[16] Biffi, S. *et al.* Equilibrium gels of low-valence DNA nanostars: a colloidal model for strong glass formers. *Soft Matter* **11**, 3132–3138 (2015).

[17] Weeks, E., Crocker, J., Levitt, A., Schofield, A. & Weitz, D. A. Three-Dimensional Direct Imaging of Structural Relaxation Near the Colloidal Glass Transition. *Science* **287**, 627–631 (2000).

[18] Flenner, E. & Szamel, G. Fundamental differences between glassy dynamics in two and three dimensions. *Nat. Commun.* **6**, 7392 (2015).

[19] Zaccarelli, E., Liddle, S. M. & Poon, W. C. K. On polydispersity and the hard sphere glass transition. *Soft Matter* **11**, 324–330 (2015).

[20] Yodh, A. *et al.* Entropically driven selfâĂŞassembly and interaction in suspension. *Phil. Trans. R. Soc. A* **359**, 921–937 (2001).

[21] Simeonova, N. B. *et al.* Devitrification of colloidal glasses in real space. *Phys. Rev. E* **73**, 1–5 (2006).

[22] Olsen, N. B., Christensen, T. & Dyre, J. C. Time-Temperature Superposition in Viscous Liquids. *Phys. Rev. Lett.* **86**, 1271–1274 (2001).

[23] Antl, L. *et al.* The preparation of poly(methyl methacrylate) latices in non-aqueous media. *Colloid and Surfaces* **17**, 67–78 (1986).

[24] Elsesser, M. T. & Hollingsworth, A. D. Revisiting the Synthesis of a Well-Known Comb-Graft Copolymer Stabilizer and Its Application to the Dispersion Polymerization of Poly(methyl methacrylate) in Organic Media. *Langmuir* **26**, 17989–17996 (2010).

[25] Royall, C. P., Poon, W. C. K. & Weeks, E. R. In search of colloidal hard spheres. *Soft Matter* **9**, 17–27 (2013).

[26] Poon, W. C. K., Weeks, E. R. & Royall, C. P. On measuring colloidal volume fractions. *Soft Matter* **8**, 21–30 (2012).

[27] Antonietti, M. *et al.* Synthesis and size control of polystyrene latices via polymerization in microemulsion. *Macromolecules* **24**, 6636–6643 (1991).

[28] Gao, Y. & Kilfoil, M. L. Accurate detection and complete tracking of large populations of featuresin three dimensions. *Opt. Express* **17**, 4685–4704 (2009).

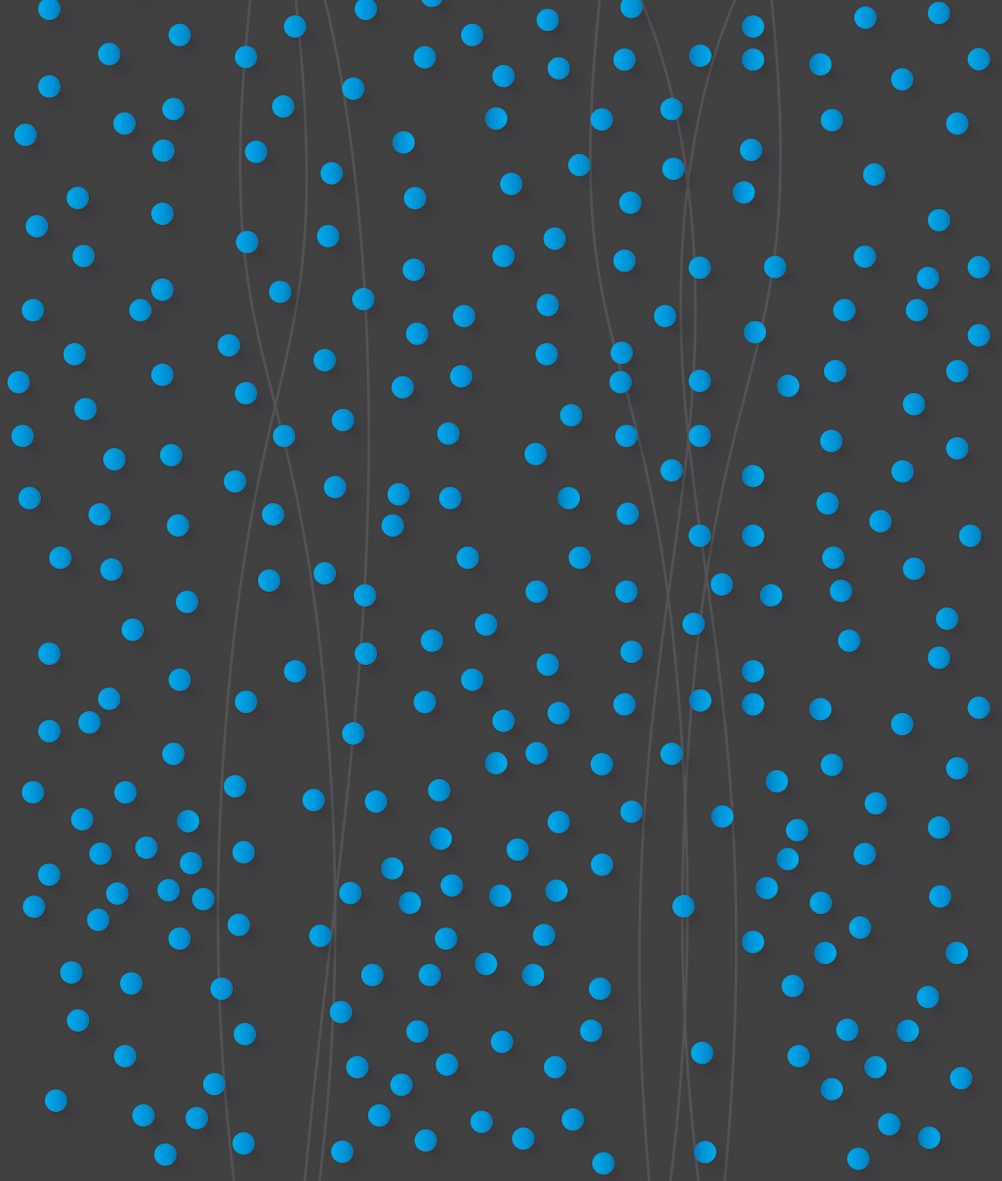

Sticky Squishy & Stuck

Chapter 4

Fragility and Strength in Nanoparticle Glasses

Glasses formed from nano- and microparticles form a fascinating testing ground to explore and understand the origins of vitrification. For atomic and molecular glasses, a wide range of fragilities have been observed; in colloidal systems these effects can be emulated by adjusting the particle softness. The colloidal glass transition can range from a super-exponential, fragile, increase in viscosity with increasing density for hard spheres to a strong, Arrhenius-like, transition for compressible particles. However, the microscopic origin of fragility and strength remain elusive, both in the colloidal and the atomic domain. In this Chapter, we propose a simple model that explains fragility changes in colloidal glasses by describing the volume regulation of compressible colloids in order to maintain osmotic equilibrium. Our simple model not only provides a microscopic explanation for fragility, but we show that it can describe experimental data for a variety of soft colloidal systems, ranging from microgels to star polymers and proteins. Our results highlight that the elastic energy per particle acts as an effective fragility order parameter, leading to a universal description of the colloidal glass transition.

This chapter was published as:

P. van der Scheer, T. van de Laar, J. van der Gucht, D. Vlassopoulos and J. Sprakel: *Fragility and Strength in Nanoparticle Glasses*, ACS Nano. *11 (7)* (**2017**), 6755-6763.

4.1 Introduction

Suspensions of colloidal hard spheres vitrify when the particle volume fraction ϕ is increased beyond the colloidal glass transition, often identified to occur at $\phi_g \approx 0.59$ [1, 2]. Upon approaching the glass transition, the structural relaxation time of the suspension τ grows rapidly and fingerprints of the glassy state emerge, such as heterogeneous dynamics[3, 4, 5], long-lived local structures[6, 7] and percolating networks of mechanically bonded neighbors[8, 9]. Mode coupling theory (MCT) [10] has been successfully used to demarcate the transition from freely flowing fluid to a glassy state at ϕ_g. On the other hand, experiments suggest that this colloidal glass transition does not involve ergodicity breaking as predicted by MCT, but that this occurs only at slightly higher volume fractions[11].

For molecular and polymeric glasses, Angell proposed a classification scheme depending on how steeply the liquid viscosity η rises as the glass transition temperature T_g is approached [12]. When η shows a very steep, super-exponential increase with T/T_g, the glass is denoted as "fragile". By contrast, when η grows more gradually, following an exponential Arrhenius-law, the glass is classified as "strong". In other words, in a fragile glass former, even small changes in temperature can have dramatic effects on the liquid viscosity; the viscosity is more robust to small temperature fluctuations in a strong glass.

In suspensions of nanoparticles or colloids, the phase behavior of the system is governed by the volume fraction rather than temperature. For hard spheres, the structural relaxation time τ, which is proportional to the suspension viscosity, rises superexponentially as the volume fraction approaches its glass transition point ϕ_g. As a result, the hard-sphere glass can be classified as fragile, in analogy with the concept of fragility and strength for glasses formed by atomic, molecular or polymeric building blocks [12].

Also soft and compressible particles, such as microgels [13, 14, 15], star polymers [16, 17] and even globular proteins [18, 19] and cells[20, 21], exhibit a glass transition when their packing fraction approaches a critical value. However, for many of these soft systems, the fragile transition gradually gives way to a much weaker and exponential growth of the relaxation time $\tau \propto e^{\phi/\phi_g}$ [13, 20], resembling strong, Arrhenius, glasses in the molecular realm [12]. In particular

for sufficiently soft microgels, ultrasoft polymer stars and suspensions of cells, a pure Arrhenius behavior has been observed experimentally [13, 16, 17, 20].

This raises the intriguing possibility that the entire range of fragility and strength known to exist for molecular systems, may be explored by studying glasses of colloids with varying softness. For example, for microgel suspensions it has been demonstrated that a transition from fragile to strong glass forming behavior could be induced solely by changing the elasticity of the individual particles. Clearly, a connection must exist between the elasticity at the scale of a single particle, and the nature of the glass transition at the macroscopic scale. For metallic glasses, such a connection was recently established quantitatively in which the "softness" of the interatomic repulsions acts as a tuning fork for fragility [22, 23]. However, such a framework does not yet exist for glasses formed from nanoparticles and colloids. As a result, a universal description of the glass transition that explains the origins of fragility and strength has to date remained unavailable.

In this chapter we propose a description for the microscopic mechanism of fragility transitions in glasses of compressible colloids, based on the regulation of osmotic equilibrium. Using a simple phenomenological model we show how apparent changes in fragility can arise when the particle softness is varied. We find that the elastic energy per particle acts as an effective order parameter for the fragility of the glass transition. A qualitative comparison of our model with experimental data suggests that a fragile-to-strong transition can be induced not only by increasing particle softness, but also by decreasing the particle size. Our results provide a framework to explain the underlying mechanisms that control the nature of the glass transition in a variety of colloidal systems.

4.2 Theoretical framework

In most experiments with purely repulsive colloidal suspensions, the phase behavior is controlled by the particle volume fraction ϕ. For hard and incompressible colloids, the state parameter is unambiguously defined as $\phi = n\frac{4}{3}\pi a^3$, where n is the number concentration of particles with radius a. For compressible particles however, defining the real particle volume fraction is more difficult. As n in-

creases, the osmotic pressure of the bath, comprised of all particles immersed in their solvent, grows. To maintain osmotic equilibrium, compressible particles, which are equilibrated with their surroundings, must increase the pressure in the particle interior. This is accomplished by their deswelling, which increases the internal osmotic pressure of the polymer network.

Due to this osmotic equilibrium, the volume of compressible particles is not constant but becomes a function of n and as such the linear relation between number density and volume fraction is lost. The osmotic deswelling of individual compressible nano- and microparticles has been studied in detail previously[24, 25, 26, 27, 28, 29]. In experiments on microgels, the particle volume fraction is typically measured in dilute conditions and extrapolated to the concentrated regime. This extrapolated packing fraction, which is the experimental control parameter being used, is defined as $\zeta = n\frac{4}{3}\pi a_0^3$, with a_0 the particle size at infinite dilution $\phi \to 0$.

Notably, ζ is linear in n, but not in ϕ[30]; for highly compressible particles, such as soft microgels, ζ may thus increase well beyond unity when $a \ll a_0$. Due to the non-linearity between ζ and ϕ, this discrepancy cannot be resolved by normalising ζ to a characteristic state point in the particle phase diagram, for example the freezing point or glass transition. To resolve this, we propose a simple qualitative model that accounts for osmotic shrinkage of compressible particles upon approaching their glass transition. Previously, osmotic shrinkage of compressible spheres has been postulated to lead to the lack of a glassy state all together[31] but a direct link to changes in glass fragility has not been established.

We model colloidal spheres, with equilibrium radius $a(\phi \to 0) = a_0$, where the internal volume fraction of osmolyte $\phi_p = \phi_{p,0}$. For example for microgel colloids, or polymer stars, ϕ_p represents the volume fraction of polymer segments within the particle. The microscopic details of the internal equation of state, which governs the balance between osmotic and elastic pressure within a particle,Π_{in}, vary greatly among different experimental systems. Yet, all systems in osmotic equilibrium with a bath of pure solvent must satisfy: $\Pi_{in}\left(\phi_{p,0}\right) \equiv 0$. For microgels, this is achieved by balancing a positive contribution to the internal pressure due to mixing of chains and solvent with a negative contribution resulting from entropic chain elasticity, commonly expressed within the Flory-

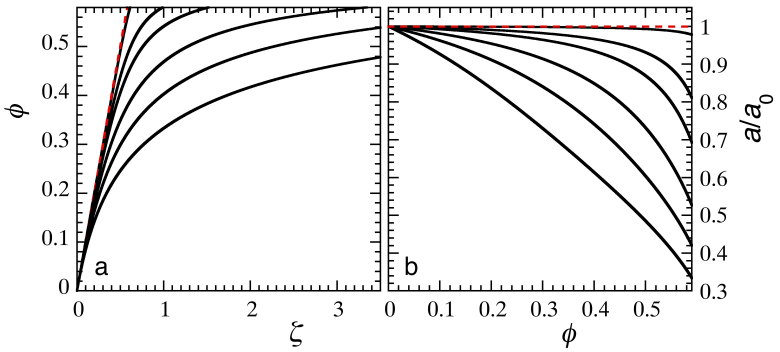

Figure 4.1: a) Real volume fraction ϕ *versus* experimental control parameter ζ as a function of particle elasticity, for (top to bottom) $k = 1 \cdot 10^4$, $1 \cdot 10^3$, $5 \cdot 10^2$, $2 \cdot 10^2$, $1 \cdot 10^2$ and $5 \cdot 10^1$ Pa, with $a_0 = 50$ nm and $\phi_{p,0} = 0.1$ b) Extent of osmotic deswelling a/a_0 with increasing particle volume fraction for the same settings as in a).

Rehner theory for gels [32].

Rather than using a microscopic theory, such as the Flory-Rehner theory for hydrogels or the elastic description of single particle micromechanics proposed recently by Riest *et al.*[29], to describe a specific type of compressible spheres, here we start with a phenomenological description of the internal equation of state at a qualitative level such that analytical results can be obtained. The aim of this paper is to arrive at a conceptual understanding of fragility in compressible sphere packings; of course, for specific systems a more quantitative description can be derived if the internal equation-of-state, and that of the suspension bath, are known a-priori.

Here we use a phenomenological form for the sake of simplicity, inspired by the mean-field description of polymers in the marginal (*i.e.* theta-solvent conditions) and semi-dilute regime $\Pi \propto \phi_p^2$ [33]. Given the additional constraint that Π_{in} must be equal to the external pressure at equilibrium, which is zero for very dilute suspensions, we use the functional form:

$$\Pi_{in} = k\left(\phi_p^2 - \phi_{p,0}^2\right) \tag{4.1}$$

where k is an effective stiffness of the particles. We note that this can be easily changed to good-solvent conditions by changing to a power of $\frac{9}{4}$ instead of 2. Since $\phi_p/\phi_{p,0} = a_0^3/a^3$, the internal pressure can be rewritten as

$$\Pi_{in} = k\phi_{p,0}^2 \left(\frac{a_0^6}{a^6} - 1 \right) \tag{4.2}$$

As the overal particle concentration n increases, a significant colloidal osmotic pressure Π_{out} will develop in the bath, which we describe with the empirical equation of state proposed by Speedy [34]:

$$\Pi_{out} = \frac{s_1 n k_B T}{1 - s_2 \phi} \tag{4.3}$$

in which $k_B T$ is the thermal energy and s_1 and s_2 are numerical constants. For hard spheres, it can be parametrized with $s_1 \approx 2.55$ and $s_2 = 1/\phi_{rcp} \approx 1.55$, in which ϕ_{rcp} is the random close packing fraction. Here we choose this description for the equation-of-state of the bath as it describes the pressure at finite volume fractions reasonably well and its simple form allows solving the equations analytically. The Speedy equation-of-state does not accurately represent the limit of $\phi \to 0$; however, this limit is not considered in the present work, hence we do not pursue this point further.

The underlying assumption in choosing this form is that in the limit of full deswelling of the particles, when $\phi_p \to 1$ and all solvent is expelled from the particle interior, the initially soft particles become incompressible which must lead to a divergence of the bath pressure. Moreover, this implies that at equilibrium, the bulk modulus K of the particles must be a function of its degree of deswelling. Within our approximate and phenomenological approach, the bulk modulus of the particles is indeed density-dependent and can be defined as $K = \phi_p d\Pi_{in}/d\phi_p = 2k\phi_p^2$. We note that, also here, for a quantitative description, the bath equation-of-state of the specific system must be known; for example in experiments on microgels, such as those revealing the fragility transitions with softness[13], charged residues on the particles will significantly alter the magnitude of the bath osmotic pressure. In fact, it is the ratio of the intrinsic particle softness k to the bath pressure that governs the behavior.

Using $\phi = a^3\zeta/a_0^3$, we find:

$$\Pi_{out} = \frac{3k_B T s_1 \zeta}{4\pi \left(a_0^3 - s_2 a^3 \zeta \right)} \tag{4.4}$$

At each ζ, a new equilibrium is established by reducing the particle size $a < a_0$, simultaneously increasing Π_{in} and reducing the bath pressure until $\Pi_{in} = \Pi_{out}$. With

$$\lambda = \left(\frac{a}{a_0}\right)^3 \tag{4.5}$$

and

$$A = \frac{3s_1}{4\pi s_2}\frac{k_BT}{k\phi_{p,0}^2 a_0^3} \tag{4.6}$$

we can define the equilibrium condition as:

$$\zeta = \frac{1-\lambda^2}{s_2\left(A\lambda^2 - \lambda^3 + \lambda\right)} \tag{4.7}$$

which gives direct access to the relationship between number density and volume fraction . Interestingly, the extent to which osmotic balance creates a non-linearity between ϕ and ζ is governed solely by the normalised elastic energy per particle $\bar{k}a_0^3/k_BT$, with $\bar{k} = k\phi_{p,0}^2$ the intrinsic particle elasticity. The elastic energy per particle is directly coupled to the external equation-of-state, since $3s_1/4\pi s_2 A = \bar{k}a_0^3/k_BT$, such that 'softness' can be defined as the relative resistance to volume changes of the particles as compared to how steep the osmotic pressure in the bath grows with ϕ.

In the limit of very soft particles $\bar{k}a_0^3 \ll k_BT$, so that osmotic shrinkage is strong $\lambda \ll 1$. In this limit Eq.4.7 is approximated as

$$\zeta \approx 1/s_2\left(A\lambda^2 + \lambda\right) \tag{4.8}$$

which yields

$$\lambda \approx \frac{1}{2A}\left(\sqrt{1 + \frac{4A}{s_2\zeta}} - 1\right) \tag{4.9}$$

At high number densities, $\zeta \gg A$, this leads to $\lambda \approx 1/s_2\zeta$. With $\phi = \zeta\lambda$, we find $\phi \approx 1/s_2 = \phi_{rcp}$. This implies that for very soft particles at sufficiently high number concentrations, the system equilibrates at random close packing;

addition of more particles results in a proportional isotropic compression of the system such that the volume fraction remains constant; this could explain the lack of a glassy state in certain cases[31]. We finally note that in this derivation we assume that the particles respond to increasing particle density by osmotic deswelling only, and thus that particle deformation can be ignored. This implies that the particles we describe have a Poisson's ratio $\nu < 0.5$, which is a reasonable assumption for hydrogel systems under the appropriate conditions[35].

4.3 Results & Discussion

We first evaluate the effect of particle softness, regulated by k, on the relationship between real volume fraction ϕ and extrapolated packing parameter ζ. For small colloids, $a_0 = 50$ nm, a significant bath pressure develops already at moderate volume fractions. When the particles are stiff, the hard sphere limit $\bar{k} = \infty$ is approached for which $\phi \equiv \zeta$ (dotted line Fig.4.1a). When the effective particle elasticity is reduced, and osmotic regulation effects become pronounced, the non-linearity between ζ and the real volume fraction ϕ grows. The corresponding osmotic shrinkage of the particles, expressed here by the deswelling ratio a/a_0, as shown in Fig.4.1b, can be very strong for the softest particles, with actual radii $a(\phi)$ more than a factor of 3 smaller than their fully swollen dimension a_0, at reasonable volume fractions; this is in direct agreement with experiments on microgel particles[36, 30].

To explore the implications this pronounced osmotic shrinkage has on the apparent fragility of the glass transition we adopt the ansatz that structural relaxation slows down universally with ϕ below the ideal mode-coupling glass transition. The structural relaxation time, normalised to the characteristic time of unhindered Brownian diffusion, τ/τ_0 is thus assumed to be described by a single equation as a function of ϕ. To this end, we use an equivalent of the classical VFT equation in which particle volume fraction governs the dynamics[37, 11]:

$$\log\left(\frac{\tau}{\tau_0}\right) = \frac{C}{\frac{\phi_c}{\phi} - 1} \tag{4.10}$$

where C is a numerical constant and ϕ_c is a critical volume fraction at which

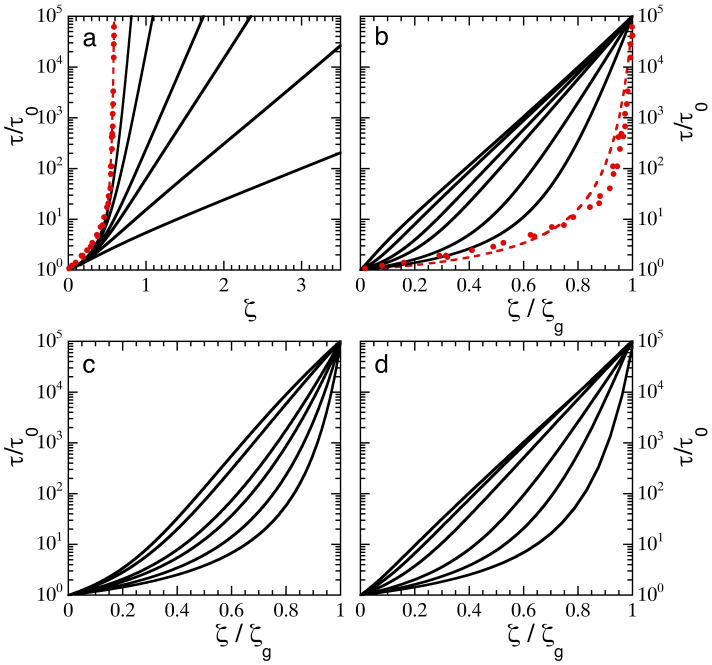

Figure 4.2: a) Structural relaxation time τ, normalised to the Brownian time scale τ_0, as a function of extrapolated particle packing fraction ζ for (solid lines, top to bottom) $\bar{k} = 20$, 10, 5, 3.5, 2 and 1 Pa, with $a_0 = 50$ nm, using Eq.4.7. Symbols: experimental data for colloidal hard spheres from [11] fitted to the VFT equation as described in the text (dotted line). b) Same data as in a) in the so-called Angell representation where the packing fraction is normalised to the glass transition ζ_g. c) Angell plot for theoretical predictions using the harmonic approximation for Π_{in} (Eq.4.11) for $\kappa = 350, 400, 500, 600, 1000$ and 5000 J/m^2. d) Angell plot for theoretical predictions using the Flory-Rehner equation of state (Eq.4.12) for $N_x = 100, 500, 1000, 2000, 3000$ and 4000.

the system becomes non-ergodic. According to extensive light scattering experiments on colloidal hard spheres [11], the point of ergodicity breaking lies above the MCT glass transition $\phi_c > \phi_g$. For the purposes of this manuscript, we parameterise the VFT law by fitting it to experimental data for hard spheres ($\bar{k} \approx \infty$) as reported by Brambilla *et al.* [11] (symbols Fig.4.2); these experimental data are well fitted by $C = 0.7$ and $\phi_c = 0.625$ (dotted line Fig.4.2).

Having expressions for both $\tau(\phi)$ and $\phi(\zeta)$, we can now explore how suspensions of compressible colloids vitrify by reconstructing $\tau(\zeta)$, which is typ-

ically measured in experiments. Our simple model qualitatively reproduces the results observed experimentally for microgel colloids[13], where τ/τ_0 grows more slowly for softer particles, and extrapolated packing fractions of well over unity are required to reach the glassy state (Fig.4.2a).

To evaluate the fragility of these predicted glass transitions, we first define the glass transition as the packing fraction where $\tau/\tau_0 \equiv 10^5$, following Mattsson *et al.* [13]. For the hard sphere data of Brambilla *et al.* [11], this yields $\phi_g \approx 0.59$, in agreement with MCT predictions and experimental findings[10, 2]. Having defined ϕ_g we can replot our predictions in the Angell representation [12, 38], where the relaxation time is plotted as a function of the rescaled packing fraction ζ/ζ_g; indeed our model reproduces the experimentally observed fragility transition[13] with decreasing $\bar{k}$ (Fig.4.2b).

One may wonder if the observed fragility change as a function of particle softness is a robust feature of any system which exhibits osmotic regulation, many of which will have a different form of their internal or external equation-of-state as compared to the choices above. For example, we can argue that close to their equilibrium size a_0, for small degrees of deswelling $a/a_0 \approx 1$, the free energy of a single compressible particle may be considered to be parabolic: $\Delta G = \kappa(a - a_0)^2$, in which κ is the spring constant, a related measure for the particle softness as compared to k, but with different dimensions. Since $\Pi_{in} = -d\Delta G/dV$ and the particle volume $V = \frac{4}{3}\pi a^3$, we have:

$$\Pi_{in} = \frac{-3d\Delta G}{4\pi a^2 da} = \frac{-3\kappa(a - a_0)}{2\pi a^2} \tag{4.11}$$

Also for this form of the internal pressure, using the Speedy equation-of-state for the bath, we can predict how the relaxation time grows with ζ. We solve these equations numerically, and find that also for this different shape of the internal equation-of-state, a fragile-to-strong transition emerges upon changing the spring constant κ (Fig.4.2c). This highlights how the conceptual idea that osmotic equilibrium governs the fragility of the colloidal glass transition is not sensitive to the exact choice for the internal pressure. It is interesting to note that the "strong" limit of our model does not produce a true Arrhenius curve, since some curvature remains at low values of ζ where the efects of osmotic regulation are weak and the inherent curvature in $\tau(\phi)$ of the VFT equation remains.

Thus, the analogy with Arrhenius behavior is only an apparent one and not truly reflective of a pure exponential decay of relaxation rates with ζ/ζ_g.

For certain specific soft sphere systems, more precise and microscopic descriptions of the internal equation-of-state exist. One particular example is the Flory-Rehner swelling theory that describes the internal pressure of uncharged microgel particles as a balance between a mixing term to promote swelling and the entropic elasticity of the polymer segments between crosslinks that counteracts swelling. Within this framework the internal equation of state can be written as [39]:

$$\Pi_{in} = \frac{k_B T}{l_k^3}\left(\left[\phi_p + \ln(1-\phi_p) + \chi\phi_p^2\right] - \frac{\phi_{p,c}}{N_x}\left[\frac{\phi_p}{\phi_{p,c}} - \left(\frac{\phi_p}{\phi_{p,c}}\right)^{1/3}\right]\right) \tag{4.12}$$

which is governed by microscopic properties such as the monomer dimension l_k and the solvent-polymer interaction parameter χ and the polymer volume fraction of the collapsed particle $\phi_{p,c}$ where the elastic contribution to the internal pressure vanishes. Softness is controlled by the crosslinking density, which determines the number of monomer repeat units between crosslinks N_x, which is thus an inverse softness parameter within this model.

Aiming to describe for example pNIPAM microgels, we choose $l_k = 1$ nm, $\phi_{p,c} = 0.5$ and good solvency such that $\chi = 0$. Indeed, also for this microscopic internal equation-of-state, an apparent fragility transition emerges upon changing the crosslinking density N_x (Fig.4.2d). We note that the values of N_x required to induce fragility changes are somewhat higher than those expected in experiments [13]; we attribute this to the fact that we assume a hard-sphere equation of state for the bath, while these experiments worked with partially charged microgels, in which the bath pressure rises much more steeply thus resulting in effectively softer particles, as discussed in more detail below. Finally, we observe that the exact line shape of τ *versus* ζ/ζ_g differs depending on the choice of the internal equation of state. This may hold the promise of deducing the internal equation-of-state of compressible particles from high-resolution measurements of the structural relaxation time and to quantify their softness directly.

To further validate the predictions of our model, we collect published data

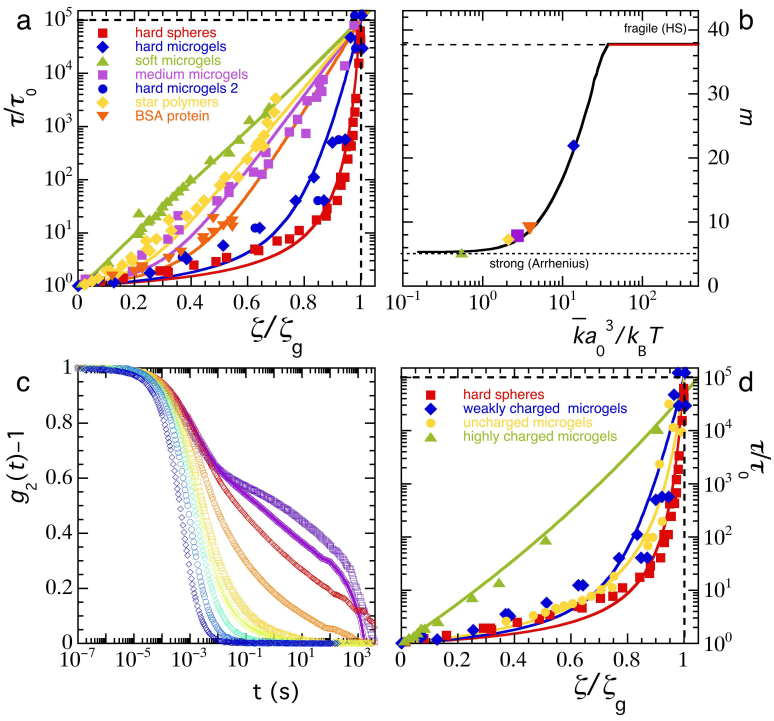

Figure 4.3: a) Angell plot for various systems of compressible spheres, symbols (defined in legend): experimental data for hard spheres ($a_0 \sim 130$ nm) [11], various microgels ($a_0 \sim 90$ nm)[13, 40], star polymers ($a_0 \sim 20$ nm) [37] and the globular protein bovine serum albumin ($a_0 \sim 5$ nm) [41], drawn lines: predictions from the model as outlined in the text with $\bar{k}$ as the adjustable parameter, b) fragility index m as a function of $\bar{k}a_0^3$ as predicted by the model (line) and for the data sets in a) (symbols), c) intensity correlation functions from dynamic light scattering for uncharged polystyrene microgels with (from left to right) $\zeta = 0.64, 0.88, 1.02, 1.03, 1.19, 1.25, 1.30, 1.35$, d) Angell plot for compressible colloids of varying charge density: hard spheres [11], weakly charged microgels [13, 40], uncharged microgels from c), and highly charged microgels [36], drawn lines: predictions from the model.

for particle self-diffusion in a variety of systems composed of compressible spherical objects, ranging from microgels of different softness [13, 40], star polymers [37] and globular proteins [41] (symbols in Fig.4.3). While the microscopic mechanisms with which osmotic equilibrium is regulated differ between these systems, as does the exact form of the equation-of-state, we fit all these data with the analytical form of our model (Eq.4.5-4.7). Since a_0 is known from the ex-

periments this leaves $\bar{k}$ as the only adjustable parameter. We note explicitly, that a comparison of the absolute values of $\bar{k}$ are meaningless, since the underlying equations-of-state for these different systems are not the same; hence the value of $\bar{k}$ needed to fit the data is the effective softness of these particles with the Speedy equation-of-state as an internal standard.

Nonetheless, the line shape, and entire range of experimentally observed fragilities in these soft colloidal systems can be qualitatively reproduced with a simple phenomenological model (drawn lines Fig.4.3a). This highlights how fragility transitions in colloidal systems can be the direct result of osmotic regulation of particle size, providing a mechanism of feedback between number density, particle size and thus volume fraction and the macroscopic structural relaxation time. This provides a theoretical foundation to the idea put forth by Mattsson *et al.* that the fragility changes in microgel suspensions are directly related to local elasticity [13]. Above we have shown how the steepness with which the structural relaxations slow down as the particle concentration is increased are governed by the parameter $\bar{k}a_0^3$. This implies that not only the particle softness, expressed by $\bar{k}$, but also the particle size has an effect on the fragility of the glass. In other words, hard colloids may make strong glasses if the particles are small enough, and soft colloids may make fragile glasses if they are sufficiently large. To make this idea more quantitative, we can compute the kinetic fragility index from the data for $\tau(\zeta)$ as:

$$m = \left. \frac{d \log(\tau/\tau_0)}{d(\zeta/\zeta_g)} \right|_{\zeta=\zeta_g} \tag{4.13}$$

We note that this is an approximation to the kinetic fragility index that is defined as the local slope of the viscosity with temperature in atomic and molecular glass formers. While a more proper analogy would use the pressure rather than packing fraction[42], this is experimentally intractable and beyond the scope of this paper. Thus, to allow for a comparison to experimental data we use the slope of relaxation time *versus* packing fraction as a proxy for the kinetic fragility index of the colloidal glass.

The lower limit of m, for strong glasses that exhibit ideal Arrhenius behavior, is set at m =5, by our definition of the glass transition at $\log(\tau/\tau_0) = 5$. At the other extreme we have the hard sphere glass transition, as the most fragile case

of fully incompressible particles, which has $m \approx 37$ based on experimental data [11].

Interestingly, when the elastic energy per particle is $\bar{k}a_0^3 \ll k_BT$, osmotic shrinkage is pronounced, which results in strong glasses, such as for the softest microgels (Fig.4.3b). When $\bar{k}a_0^3$ becomes of the order of the thermal energy, the intrinsic particle elasticity effectively competes with the pressure which develops in the bath, and the transition becomes increasingly fragile until the hard-sphere limit is reached when $\bar{k}a_0^3 \gg k_BT$ (Fig.4.3b). The bulk elastic energy per particle thus acts as an order parameter for the fragility of the colloidal glass transition. Indeed, the experimental data can be collapsed onto the predicted relation between the fragility index m and the normalised particle elasticity when the experimentally-determined fragility is plotted against $\bar{k}a_0/k_BT$, with $\bar{k}$ determined from the fits shown in Fig.4.3a, and a_0 taken from the experimental publications as indicated in the figure caption.

Our phenomenological model does not take the microscopic origins of internal and external pressures into account. For example the Speedy equation-of-state is only valid for particles interacting by volume exclusion alone. Additional contributions, for example due to charges, will affect the osmotic balance both inside the particles and in the bath. This can have significant effects on the phase behavior of soft particle suspensions, *e.g.* leading to the absence of a solid phase in fully ionic microgels even at very high densities[31, 43]. For a comprehensive description of the swelling behavior of ionic microgels which accounts for both polymeric and ionic terms, we refer to Colla *et al.* [44].

To illustrate the effects of charges we start from published experimental data for strongly crosslinked microgels, both for systems that are highly charged [36] and microgels that carry a small amount of charges due to the ionic initiator used during particle synthesis [40, 13]. As no experimental data is available for microgels which carry absolutely zero charges, we synthesize polystyrene microgels using a non-ionic initiator resulting in particles free of ionic groups [45] (see also the Materials & Methods section). These particles are suspended in a mixture of bromo- and iodobenzene which is both a good solvent for the polystyrene gel network and matches their refractive index. We determine the structural relaxation of suspensions of these uncharged microgels with dynamic light scattering

(DLS), as a function of ζ, which is determined by capillary viscosimetry in the dilute limit.

With increasing particle concentration, the autocorrelation curves $g_2(t) - 1$ obtained from DLS experiments, show both the slowing down of particle diffusion and the emergence of a plateau at intermediate times, indicative of the formation of repulsive cages which hinder particle motion (Fig.4.3c). These data are consistent with DLS experiments on aqueous, and slightly charged, microgels [40, 13]. We note that at very long lag times $t > 500$ s, a lack of statistics, due to the experimental aqcuisition time leads to an artifical superexponential decay of the correlation function. Nonetheless, the data clearly show the glass transition as the particle concentration is increased. We do not use the data beyond > 500s to extract the characteristic structural relaxation time such that this does not effect our results. For these uncharged microgels, the glass transition is very fragile and virtually traces the hard sphere line with $m = 37$ (Fig.4.3d). For the weakly charged microgels a small decrease in fragility can be seen, whereas a nearly exponential, Arrhenius, behaviour results for highly charged microgels (Fig.4.3d). This, surprisingly, suggests that a high concentration of charges, which increases the internal osmotic pressure and thus provides additional resistance to deswelling, effectively "softens" the particles by reducing the effective value of $\bar{k}a_0^3$ required to describe the vitrification with our phenomenological model (lines Fig.4.3d).

The counter-intuitive observation that charged microgels act "softer" than uncharged particles at the same crosslinking density, is in agreement with the observation that the osmotic deswelling of ionic microgels can be so severe that the volume fraction at which a liquid-solid transition must occur is not reached, even at exceedingly high values of the extrapolated packing fraction $\zeta > 35$ [31, 43]. This emergent softness was attributed to the high osmotic pressure of the bath, governed by mobile ions unbound to the microgel particles[46], which result in strong compression of the particles as the solid-liquid transition is approached. This argument, and its experimental proof [31], underpins the concept we have raised above, that rather than particle softness alone, as hypothesized previously [13], it is in fact the balance between the osmotic pressure of the bath and the intrinsic softness of the particle that governs the solid-liquid transition and its

fragility. Even when the single-particle mechanics indicate a relatively high bulk modulus, if the bath osmotic pressure is high enough, for example due to the presence of ions or for sufficiently small particles, osmotic deswelling may be significant, resulting in a strong rather than a fragile glass. The unusually strong deswelling of ionic microgels furthermore leads to unexpected behavior, such as the strong shrinkage of large microgels in a crystal of smaller particles to accomodate to the lattice and minimize the energy penalty associated with defect formation[47, 48].

4.4 Conclusion

We have presented a simple model, based on the osmotic deswelling of compressible colloids, which qualitatively captures fragility changes observed in colloidal glasses. The change from a fragile to a strong glass transition can be explained by a non-linear relation between the experimental control parameter ζ and the real particle volume fraction which dictates the dynamics of the suspension. The degree of non-linearity depends only on the elastic energy per particle, which thus serves as an effective order parameter for fragility. As the elastic energy per particle scales inversely with particle volume, hard colloids may make strong glasses and soft colloids may make fragile glasses depending on nominal particle size, the particle softness and the equation-of-state of the bath. While the phenomenological description we present provides new insight into the nature of the colloidal glass transition at the macroscopic scale, it does not yet account for spatial heterogeneity at microscopic length scales. Experiments and simulations have shown that softness reduces both the magnitude and spatial extent of dynamical heterogeneities [49] and extends the validity range of the Stokes-Einstein relation to higher packing densities [50, 51]. Perhaps this can be explained by the weaker dependence of relaxation time on local density for softer particles due to osmotic regulation. Extending the simple model proposed here to account for such local effects could aid in elucidating the intriguing connection between glass fragility and dynamical heterogeneity[52, 53, 54].

4.5 Materials & Methods

We prepared stricktly uncharged microgels using a method described in detail elsewhere [45]. Briefly, we dissolved 2 g sodium dodecyl sulfate in 320 ml deionized water in a round bottom flask. Seperately, we prepared a solution of 96 g styrene, 6 g of the crosslinker divinylbenzene, 5 ml hexadecane and 1 g of the radical initiator 2,2-azobis(2-methylpropionitrile). We mix the aqueous and monomer phase and first created a coarse pre-emulsion by using a high-shear rotor-stator mixer. We subsequently formed a stable mini-emulsion using high-intensity ultrasonication. After purging the reaction flask with nitrogen, we allowed the mixture to react overnight at 65°C. The microgel particles were purified by precipitation in cold methanol, filtration and drying in vacuo, followed by resuspension in THF and precipitation in methanol. This is repeated 3x to ensure complete removal of surfactant and reaction byproducts. Finally we resuspend the microgels in THF to swell the microgels completely, which allows any linear polystyrene to diffuse out of the microgels, which we remove by centrifugation at 30000 g and removal of the supernatant. This was repeated three times to ensure complete removal of all linear polystyrene as confirmed by gel permeation chromatography. We then dried the microgels in vacuo. The resulting particles have a hydrodynamic radius in the dilute limit of $a_0 = 93$ nm, measured in the index-matching solvent.

Samples are prepared by suspending a known weight of dried microgels in an index-matching mixture of iodobenze and bromobenzene (70:30 by volume). Samples are mixed extensively by vortexing and repeated centrifugation for the most viscous samples; in all cases, the sample was centrifuged at 1500 g in the sample tube prior to measurement to remove any air bubbles and dust from the scattering volume. Samples were equilibrated for at least 1 hour in the thermostated sample bath at 21°C to ensure a homogeneous temperature within the sample. Measurements were performed using a dynamic light scattering (DLS) setup based on an ALV/CGS-3 goniometer, equipped with an avalanche photon detector, 633 nm diode laser (JDSU) and dual ALV LSE-5004 hardware correlators for cross-correlation. All measurements were performed at a scattering angle of 150°, which gives a scattering vector $q = \frac{4\pi}{\lambda} sin\frac{\theta}{2} = 0.02$ nm^{-1}. We note that to measure true self-diffusion, measurements should be performed at scat-

tering vectors $qa \leq 2\pi$, with a the particle radius. For the polystyrene microgels we study here, this implies a minimum scattering vector of $q = \frac{2\pi}{a} \approx 0.07$ nm^{-1} which is not attainable in this set-up. Since our scattering vector was below this value, we probed dynamics on somewhat larger characteristic length scales, which we took as a measure of the sample's viscosity or long-time particle self-diffusivity.

References

[1] Pusey, P. N. Colloidal Suspensions. In Hansen, J. P., Levesque, D. & Zinn-Justin, J. (eds.) *Liquids, Freezing and the Glass Transition*, 765–942 (Elsevier, Amsterdam, 1991).

[2] Hunter, G. L. & Weeks, E. R. The Physics of the Colloidal Glass Transition. *Rep. Prog. Phys.* **75**, 66501 (2012).

[3] Kegel, W. K., van Blaaderen & Alfons. Direct Observation of Dynamical Heterogeneities in Colloidal Hard-Sphere Suspensions. *Science* **287**, 290 – 293 (2000).

[4] van de Laar, T., Higler, R., Schroën, K. & Sprakel, J. Discontinuous Nature of the Repulsive-to-Attractive Colloidal Glass Transition. *Sci. Rep.* **6**, 22725 (2016).

[5] Weeks, E., Crocker, J., Levitt, A., Schofield, A. & Weitz, D. A. Three-Dimensional Direct Imaging of Structural Relaxation Near the Colloidal Glass Transition. *Science* **287**, 627–631 (2000).

[6] Malins, A., Eggers, J., Royall, C. P., Williams, S. R. & Tanaka, H. Identification of Long-Lived Clusters and Their Link to Slow Dynamics in a Model Glass Former. *J. Chem. Phys.* **138**, 12A535 (2013).

[7] Patrick Royall, C., Williams, S. R., Ohtsuka, T. & Tanaka, H. Direct Observation of a Local Structural Mechanism for Dynamic Arrest. *Nat. Mater* **7**, 556–561 (2008).

[8] Laurati, M., Maßhoff, P., Mutch, K. J., Egelhaaf, S. U. & Zaccone, A. Long-Lived Neighbors Determine the Rheological Response of Glasses. *Phys. Rev. Lett.* **118**, 18002 (2017).

[9] Conrad, J. C., Dhillon, P. P., Weeks, E. R., Reichman, D. R. & Weitz, D. A. Contribution of Slow Clusters to the Bulk Elasticity Near the Colloidal Glass Transition. *Phys. Rev. Lett.* **97**, 265701 (2006).

[10] Götze, W. Recent Tests of the Mode-Coupling Theory for Glassy Dynamics. *J. Phys.: Condens. Matter* **11**, A1 (1999).

[11] Brambilla, G. *et al.* Probing the Equilibrium Dynamics of Colloidal Hard Spheres Above the Mode-Coupling Glass Transition. *Phys. Rev. Lett.* **102**, 85703 (2009).

[12] Angell, C. A. Formation of Glasses from Liquids and Biopolymers. *Science* **267**, 1924–1935 (1995).

[13] Mattsson, J. *et al.* Soft Colloids Make Strong Glasses. *Nature* **462**, 83–86 (2009).

[14] Liu, Y. H. *et al.* Characterization of Nanoscale Mechanical Heterogeneity in a Metallic Glass by Dynamic Force Microscopy. *Phys. Rev. Lett.* **106**, 125504 (2011).

[15] McKenna, G. B., Narita, T. & Lequeux, F. Soft Colloidal Matter: A Phenomenological Com-

parison of the Aging and Mechanical Responses With Those of Molecular Glasses. *J. Rheol.* **53**, 489–516 (2009).

[16] Mayer, C. *et al.* Asymmetric Caging in Soft Colloidal Mixtures. *Nat. Mater* **7**, 780–784 (2008).

[17] Roovers, D. V., Fytas, G., Pakula, T. & Jacques. Multiarm Star Polymers Dynamics. *J. Phys.: Condens. Matter* **13**, R855 (2001).

[18] Vitkup, D., Ringe, D., Petsko, G. A. & Karplus, M. Solvent Mobility and the Protein 'Glass' Transition. *Nat. Struct. Mol. Biol.* **7**, 34–38 (2000).

[19] Lee, A. L. & Wand, A. J. Microscopic Origins of Entropy, Heat Capacity and the Glass Transition in Proteins. *Nature* **411**, 501–504 (2001).

[20] Zhou, E. H. *et al.* Universal Behavior of the Osmotically Compressed Cell and its Analogy to the Colloidal Glass Transition. *Proc. Natl. Acad. Sci.* **106**, 10632–10637 (2009).

[21] Angelini, T. E. *et al.* Glass-like Dynamics of Collective Cell Migration. *Proc. Natl. Acad. Sci.* **108**, 4714–4719 (2011).

[22] Krausser, J., Samwer, K. H. & Zaccone, A. Interatomic Repulsion Softness Directly Controls the Fragility of Supercooled Metallic Melts. *Proc. Natl. Acad. Sci.* **112**, 13762–13767 (2015).

[23] Zaccone, A. E. L., Krausser, J., Evenson, Z., Samwer, K. & A. Unifying Interatomic Potential, g (r), Elasticity, Viscosity, and Fragility of Metallic Glasses: Analytical model, Simulations, and Experiments. *J. Stat. Mech.: Theory Exp.* **2016**, 84001 (2016).

[24] Fernández-Nieves, A., Fernández-Barbero, A., Vincent, B. & de las Nieves, F. J. Osmotic De-Swelling of Ionic Microgel Particles. *J. Chem. Phys.* **119**, 10383–10388 (2003).

[25] Saunders, B. R. & Vincent, B. Osmotic De-Swelling of Polystyrene Microgel Particles. *Colloid Polym. Sci.* **275**, 9–17 (1997).

[26] Saunders, B. R., Crowther, H. M. & Vincent, B. Poly[(methyl methacrylate)-co-(methacrylic acid)] Microgel Particles: Swelling Control Using pH, Cononsolvency, and Osmotic Deswelling. *Macromolecules* **30**, 482–487 (1997).

[27] Evans, I. D. & Lips, A. Concentration Dependence of the Linear Elastic Behaviour of Model Microgel Dispersions. *J. Chem. Soc., Faraday Trans.* **86**, 3413–3417 (1990).

[28] Hashmi, S. M. & Dufresne, E. R. Mechanical Properties of Individual Microgel Particles Through the Deswelling Transition. *Soft Matter* **5**, 3682–3688 (2009).

[29] Riest, J., Athanasopoulou, L., Egorov, S. A., Likos, C. N. & Ziherl, P. Elasticity of Polymeric Nanocolloidal Particles. *Sci. Rep.* **5**, 15854 (2015).

[30] Pellet, C. & Cloitre, M. The glass and jamming transitions of soft polyelectrolyte microgel suspensions. *Soft matter* **12**, 3710–3720 (2016).

[31] Pelaez-Fernandez, M., Souslov, A., Lyon, L. A., Goldbart, P. M. & Fernandez-Nieves, A. Impact of Single-Particle Compressibility on the Fluid-Solid Phase Transition for Ionic Microgel Suspensions. *Phys. Rev. Lett.* **114**, 98303 (2015).

[32] Flory, P. J. & Rehner, J. Statistical Mechanics of CrossåĂŘLinked Polymer Networks II. Swelling. *J. Chem. Phys.* **11** (1943).

[33] Flory, P. J. *Principles of Polymer Chemistry: Paul J. Flory*. The George Fisher Baker Non-Resident Lectureship in Chemistry At Cornell University (Cornell University, 1953).

[34] Speedy, R. J. The Equation of State for the Hard Sphere Fluid at High Density. The Glass

Transition. *Physica B+C* **121**, 153–161 (1983).

[35] Li, Y., Hu, Z. & Li, C. New Method for Measuring Poisson's Ratio in Polymer Gels. *J. Appl. Polym. Sci.* **50**, 1107–1111 (1993).

[36] Romeo, G., Imperiali, L., Kim, J.-W., Fernández-Nieves, A. & Weitz, D. A. Origin of De-Swelling and Dynamics of Dense Ionic Microgel Suspensions. *J. Chem. Phys.* **136**, 124905 (2012).

[37] Fleischer, G., Fytas, G., Vlassopoulos, D., Roovers, J. & Hadjichristidis, N. Self-Diffusion of Multiarm Star Polymers in Solution Far From and Near the Ordering Transition. *Phys. A* **280**, 266–278 (2000).

[38] Angell, C. A. The Old Problems of Glass and the Glass Transition, and the Many New Twists. *Proc. Natl. Acad. Sci.* **92**, 6675–6682 (1995).

[39] Voudouris, P., Florea, D., van der Schoot, P. & Wyss, H. M. Micromechanics of temperature sensitive microgels: Dip in the poisson ratio near the lcst. *Soft Matter* **9**, 7158–7166 (2013).

[40] Kasper, A., Bartsch, E. & Sillescu, H. Self-Diffusion in Concentrated Colloid Suspensions Studied By Digital Video Microscopy of Core-Shell Tracer Particles. *Langmuir* **14**, 5004–5010 (1998).

[41] Roosen-Runge, F. *et al.* Protein Self-Diffusion in Crowded Solutions. *Proc. Natl. Acad. Sci.* **108**, 11815–11820 (2011).

[42] Berthier, L. & Witten, T. A. Glass transition of dense fluids of hard and compressible spheres. *Phys. Rev. E* **80**, 021502 (2009).

[43] Sierra-Martin, B. & Fernandez-Nieves, A. Phase and Non-Equilibrium Behaviour of Microgel Suspensions as a Function of Particle Stiffness. *Soft Matter* **8**, 4141–4150 (2012).

[44] Colla, T., Likos, C. N. & Levin, Y. Equilibrium properties of charged microgels: A poisson-boltzmann-flory approach. *J. Chem. Phys.* **141**, 234902 (2014).

[45] Antonietti, M., Pakula, T. & Bremser, W. Rheology of Small Spherical Polystyrene Microgels: A Direct Proof for a New Transport Mechanism in Bulk Polymers besides Reptation. *Macromolecules* **28**, 4227–4233 (1995).

[46] Levin, Y., Diehl, A., Fernández-Nieves, A. & Fernández-Barbero, A. Thermodynamics of Ionic Microgels. *Phys. Rev. E* **65**, 36143 (2002).

[47] Scotti, A. *et al.* The Role of Ions in the Self-Healing Behavior of Soft Particle Suspensions. *Proc. Natl. Acad. Sci.* **113**, 5576–5581 (2016).

[48] Iyer, A. S. & Lyon, L. Self-Healing Colloidal Crystals. *Angew. Chem., Int. Ed.* **48**, 4562–4566 (2009).

[49] Rahmani, Y. *et al.* Dynamic Heterogeneity in Hard and Soft Sphere Colloidal Glasses. *Soft Matter* **8**, 4264–4270 (2012).

[50] Ikeda, A. & Miyazaki, K. Glass transition of the monodisperse gaussian core model. *Phys. Rev. Lett.* **106**, 015701 (2011).

[51] Gupta, S. *et al.* Validity of the stokes-einstein relation in soft colloids up to the glass transition. *Phys. Rev. Lett.* **115**, 128302 (2015).

[52] Debenedetti, P. G. & Stillinger, F. H. Supercooled Liquids and the Glass Transition. *Nature* **410**, 259–267 (2001).

[53] Kanaya, T., Tsukushi, I., Kaji, K., Gabrys, B. & Bennington, S. M. Heterogeneity of Amorphous Polymers With Various Fragility Indices as Studied in Terms of Non-Gaussian Parameter. *J. Non-Cryst. Solids* **235âĂŞ237**, 212–218 (1998).

[54] Starr, F. W., Douglas, J. F. & Sastry, S. The Relationship of Dynamical Heterogeneity to the Adam-Gibbs and Random First-Order Transition Theories of Glass Formation. *J. Chem. Phys.* **138**, 12A541 (2013).

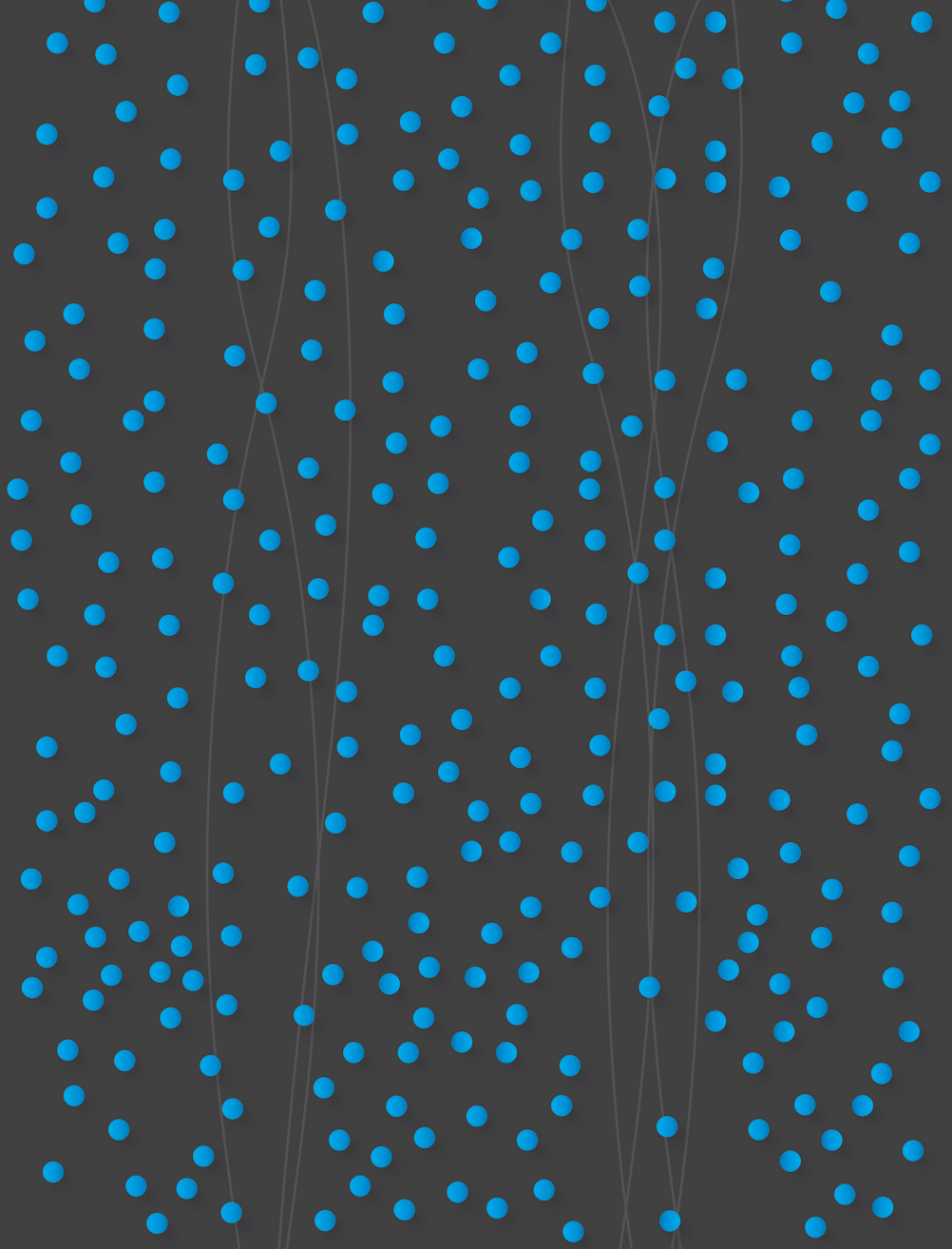

Sticky Squishy & Stuck

Chapter 5

Deswelling and Deformation of Microgels in Concentrated Packings

Increasing the particle density of a suspension of microgel colloids above the point of random-close packing, must involve deformations of the particle to accommodate the increase in volume fraction. By contrast to the isotropic osmotic deswelling of soft particles, the particle-particle contacts give rise to a non-homogeneous pressure, raising the question if these deformations occur through homogeneous deswelling or by the formation of facets. In this Chapter we aim to answer this question through a combination of imaging of individual microgels in dense packings and a simple model to describe the balance between shape versus volume changes. We find a transition from shape changes at low pressures to volume changes at high pressures, which can be explained qualitatively with our model. Whereas contact mechanics govern at low pressures giving rise to facets, osmotic effects govern at higher pressures, which leads to a more homogeneous deswelling. Our results show that both types of deformation play a large role in highly concentrated microgel suspensions and thus must be taken into account to arrive at an accurate description of the structure, dynamics and mechanics of concentrated suspensions of soft spheres.

This chapter was published as:

I. Bouhid de Aguiar, T. van de Laar, M. Meireles, A. Bouchoux, J. Sprakel and K. Schroën: *Deswelling and Deformation of Microgels in Concentrated Packings*, Sci. Rep. *7* (**2017**), 10223.

5.1 Introduction

Microgels are colloidal particles made from a solvent-swollen crosslinked polymer network[1, 2], whose softness can be tuned with the crosslink density[3]. These microgels are commonly used as a well-defined experimental model system to explore the phase behavior, dynamics and mechanics of soft particle suspensions [4, 5]. Their softness, which entails both a low resistance to shape and to volume changes, has a large effect on the properties of dense suspensions of these particles. For example, they can be compressed to packing density in excess of random close packing and their increase in viscosity as they approach the liquid-solid boundary shows significant deviations from the behavior of hard spheres[6, 7]. Moreover, microgels exhibit a rich phase behavior [8, 9, 10], which can be tailored by their degree of crosslinking[11], the presence of charges[12] or inherent network inhomogeneities[13].

To achieve effective packing densities of well above the random close packing limit for hard spheres, the reduction in available volume must be accommodated by either shape or volume changes in the constituent particles. This can occur either by forming facets at the contact points with the surrounding particles[14, 15, 8] and by the expulsion of solvent from the particle, leading to homogeneous deswelling and volume reduction[16, 17]. Recent work has highlighted how the latter can have pronounced effects on the interpretation of experiments on microgels, since osmotic deswelling can lead to substantial deviations between the apparent and real particle volume fraction[18].

It is most likely that facetting and homogeneous deswelling are relevant to some extent; however, this remains relatively unexplored. Recent contrast-variation scattering experiments have shed light on this complexity for the first time, showing an interplay of deformations, deswelling and even interpenetration of surface-dangling chains as the particle concentration is varied[19]. Yet, our quantitative understanding of particle deswelling and deformation remains incomplete.

The isotropic compression of individual microgels subjected to a homogeneous osmotic force has been studied in detail previously. For example, microgels suspended in solutions of a polymeric osmolyte, such as dextran which is excluded from the microgel network, exhibit a homogeneous osmotic deswell-

ing consistent with polymer swelling theory[6], from which the bulk modulus K of the individual microgels could be determined. Squeezing a single microgel between two sapphire plates, yielding two discrete contact points, has shown that this is a controlled way of probing deformations of single particles, but the possibility of an interplay between shape and volume changes was not discussed[17]. In this last case, the microgel is under non-homogeneous pressure. This implies that contact deformations cannot be ignored as it is also the case for shape or volume changes, dictated by the Poisson ratio, which is typically between 0.4-0.45 for hydrogel particles[20]. Of course, the same argument holds for particles with more than two contact points, as would be the case in a dense packing of particles, contacting multiple neighbors. The fact that both effects contribute to microgel shape and size in non-homogeneous pressure fields is illustrated by the capillary micromechanics work of Guo and Wyss[5] where individual soft particles are brought into a tapered confinement, which induced both shape and size changes, that can be quantified accurately, for example to derive the full linear mechanics of single particles.

So while it is clear that the mechanical response of compressible and deformable microgels to complex pressure fields involves both shape and size changes, these effects remain to be explored in dense packings of many microgels in close contact. Understanding these effects is an important step towards a more comprehensive description of the combined effects of single-particle mechanics and osmotic equilibrium on the properties of highly concentrated suspensions of soft particles.

In this Chapter we explore the deformation and deswelling mechanisms of microgels in compressed microgel packings and provide a framework to understand their behaviour. We osmotically stress mixtures of fluorescent and non-fluorescent microgels and image the shape and size of single microgels with high resolution using confocal microscopy and quantitative analysis algorithms. We find that the ratio of shape to volume changes, evolves non-monotonically with applied pressure; at low pressures shape changes are pronounced, in the form of facets, while at larger pressure the facets disappear and the microgels assume a spherical shape by deswelling homogeneously. We qualitatively explain these results using a simple mechanical model, which combines the osmotic pressure

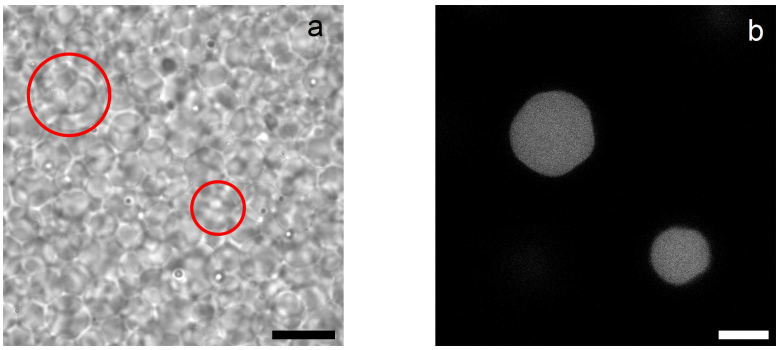

Figure 5.1: Compressed microgel packing composed of a mixture of fluorescent and non-fluorescent microgels. (a) Bright field image. Scale bar denotes 20 μm. (b) CLSM image. Scale bar denotes 10 μm. The images were made at the same region of the sample. Red circles in the bright field image indicate the position of the fluorescent particles but are not to scale.

of the gel network with contact mechanics.

5.2 Results & Discussion

We study microgels made from poly(acrylamide) (pAAm) prepared by emulsion templating. The particles are crosslinked with 1%wt of crosslinker with respect to the total monomer content, resulting in reasonably soft microgels. Here we aim to prepare microgels with sizes larger than 10 μm such that their shape and size can be carefully deduced from confocal fluorescence microscopy experiments. Although our microgels are large enough to be imaged by brightfield microscopy, it remains challenging to obtain the entire shape and size due to significant artefacts that arise due to the high particle concentration. Rather, we choose to use confocal microscopy to vizualize a few labelled microgels in a large excess of undyed particles. This enables us to resolve the microgel shape and size with high resolution and without being hindered by the high particle density. To concentrate the microgel suspensions to a well-defined macroscopic osmotic pressure, we stress the suspensions by placing them in a dialysis membrane and equilibrating them against poly(ethylene glycol) (PEG) as an osmolyte, which leads to a homogeneous compression of the suspension to osmotic pres-

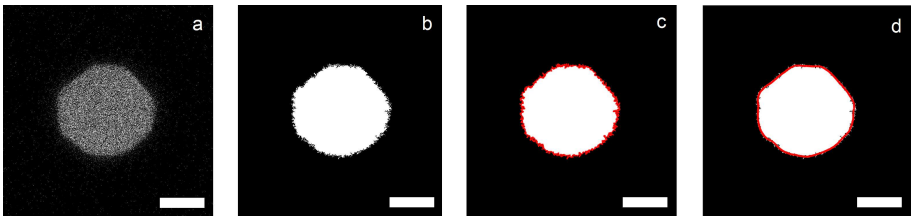

Figure 5.2: Steps during image treatment, (a) shows the raw microscopy data, (b) shows the binary version of this image, generated to most closely preserve the microgel shape, (c) shows a simple edge trace of this binary image, resulting in many artifacts, (d) shows the much smoother tracing after fitting this boundary with a Savitzky-Golay filter, which results in a smooth boundary while preserving the overall microgel shape. Scale bars denote 5 μm.

sure differences between 10^3-10^6 Pa.

If all the microgels are fluorescently labelled, observing the boundaries of a single particle at its contacts with neighbors becomes highly inaccurate. To end this, we use a mixture of fluorescent and non-fluorescent microgels in our experiments. This allows us to accurately observe a single fluorescent microgel that is surrounded by non-fluorescent microgels. While identification of single particles is difficult in bright-field microscopy images (Figure 5.1a) where all particles provide contrast, well-defined images of single fluorescent particles can be made using confocal microscopy, as shown in Figure 5.1b.

To quantify changes in size and shape of the individual microgels in the packings, we image at least twenty separate microgels in three-dimensions using confocal microscopy for each compression pressure. From these images, we can calculate the microgel volume and shape. In order to calculate an accurate perimeter and area for each slice in the three-dimensional image stacks, we first convert our images (Figure 5.2a) to binary black and white (Figure 5.2b). During this thresholding, pixelation at the background-particle edge results in jagged edges in an edge-detection algorithm (Figure 5.2c). Such roughness on the perceived perimeter would overestimate the particle contour. This discretization effect can be minimized by recording high-resolution confocal images, but some boundary effects remain. To solve this issue we first trace this perimeter using a Savitsky-Golay (SG) filter[21] to smooth the boundary (Figure 5.2d). From these

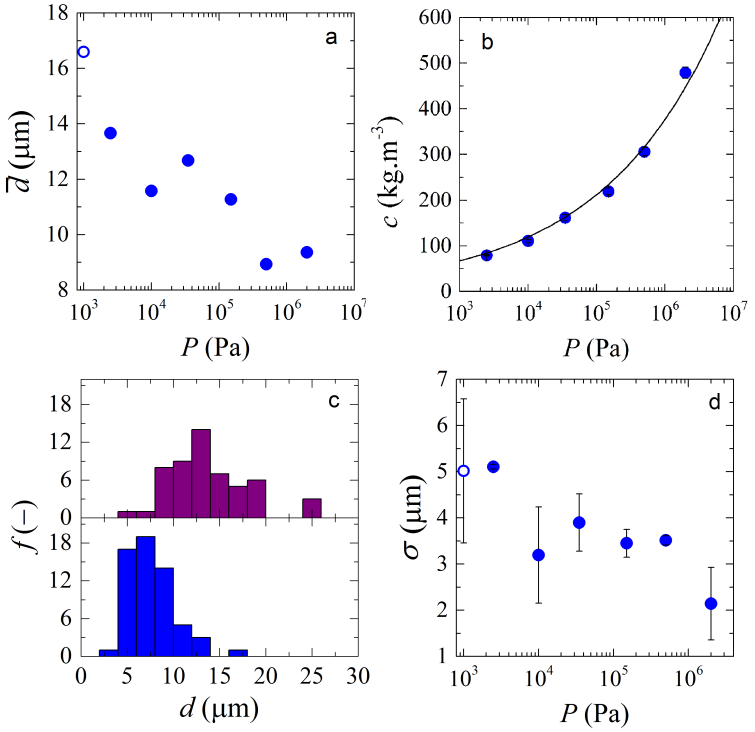

Figure 5.3: (a) Average microgel diameter ($\overline{d}$) as a function of compression pressure, (b) microgel packing polymer concentrations c as a function of pressure P. Solid line describes the $P \propto c^4$ scaling. (c) size distributions of microgel diameter (d) for two compression pressures (2.5 kPa - top and 2 MPa - bottom), which shows a narrowing of the size distribution at increased compression and (d) width of fitted Gaussian functions (σ) for each size distribution as a function of compression pressure. Open symbols are values obtained at zero pressure (P).

smoothed traces we then reconstruct the image, which allows us to calculate the perimeter and area much more accurately, while still having access to the overall microgel shape without blunting due to the filtering.

We first probe the changes in particle volume, as a way to evaluate their osmotic deswelling in response to the contact pressure of neighboring particles. We deduce the particle volume from the equivalent sphere diameter $\overline{d}$ fitted to

the three-dimensional image stacks of thresholded and filtered images of single particles (more details in the Material and Methods section). As expected, we observe that the average size of the microgels decreases with increasing compression pressure, as a result of solvent expulsion by the microgels (Figure 5.3a). The average values were obtained by averaging over multiple particles in a polydisperse population; nevertheless, we see a clear monotonic trend of deswelling with increasing pressure P, consistent with previous reports[17, 22].

For each compression pressure P, we also determine the polymer concentration in the compressed microgel packings by dehydrating the particle pastes and measuring the dry weight (Figure 5.3b). We find that the osmotic pressure increases steeply with increasing polymer concentration. The data is well described by a scaling $P \propto c^4$, which is significantly higher than the scaling prediction for the osmotic pressure of a semi-dilute polymer solution within the blob model of $P \propto c^{9/4}$[23]. We attribute this to the additional contribution of network elasticity to the osmotic pressure, as described by the Flory-Rehner theory[24], where the rise in osmotic pressure with concentration, in particular close to the equilibrium swelling state of the particles, is much steeper than that of a simple solution of linear chains [25].

From our experimental observations, we do not only have access to the average particle size as a function of compression, but also the size distribution. Interestingly, we see how the size distribution shifts as the compression increases (Figure 5.3c). This is likely due to the fact that larger microgels will be more compressed in the packings, whereas small particles can reside in interstitial spaces and thus experience smaller contact pressures on average. As a consequence, larger particles will deswell more than smaller ones, thus narrowing the size distribution of the sample. To quantify the change in size distribution, we measure the width of the particle size distributions σ as the full width at half maximum (FWHM) by fitting the experimental data to a normal distribution at all compression pressures. Indeed, the width of the distribution decreases with increasing pressure (Figure 5.3d). We also plotted (results not shown) the ratio between the gaussian width and the mean with varying pressure and obtained the same decreasing trend. The fact that we obtained the same trend shows that the decrease in size of the particles is not the reason for the narrowing of the size dis-

tribution. This observation of a narrowing particle size distribution is consistent with earlier reports of a co-crystallisation of large microgels in a bath of smaller particles as the pressure increased, leading to shrinkage of the larger particles to fit into the microgel lattice[26].

Clearly, increasing the particle density leads to pronounced osmotic deswelling of the particles. However, visual inspection of the confocal microscopy images shows also how distinct facets develop at the particle-particle contact points (Figure 5.2). While most previous studies have studied in-depth the changes in volume associated with osmotic compression of microgel packings, these shape changes have received much less attention so far, but may be crucial to understand the rheology and dynamics of microgel pastes.

To evaluate the extent of shape changes, we determine to what extent the particle shape deviates from a perfect sphere. Due to the preparation templated in emulsion droplets, the rest shape of the microgels is a near-perfect sphere. We define the sphericity, extracted from our two-dimensional confocal images as:

$$\Psi = \frac{2\sqrt{\pi N_a}}{N_{circ}} \tag{5.1}$$

where N_a is the number of pixels in the area enclosed by the SG filtered boundary (red line in Figure 5.2d) and N_{circ} is the number of pixels along the boundary contour. For a perfect circle $\Psi \equiv 1$, while any asphericity, e.g. due to facetting, will result in $\Psi < 1$.

Samples at zero pressure $P = 0$, exhibit an almost perfect spherical geometry with $\Psi \approx 0.99 \pm 0.1$ (Figure 5.4c); the small deviation from $\Psi = 1$ is caused by the inevitable discretization of the images at the scale of a pixel, which cannot be completely circumvented by the SG filtering of the particle contour.

At finite pressure, the sphericity, averaged over at least twenty particles at each pressure, initially decreases. This indicates that the microgels become deformed by the formation of facets at contact points with neighboring particles (Figure 5.4d). As the compression pressures P increase, the average sphericity of the microgels increases again, which indicates that the particles regain their spherical shape (Figure 5.4e). For comparison, we evaluated images containing polygons and obtained sphericity values for an hexagon and a square of 0.97 and 0.91, respectively. We also evaluated images of spheres of different sizes to rule

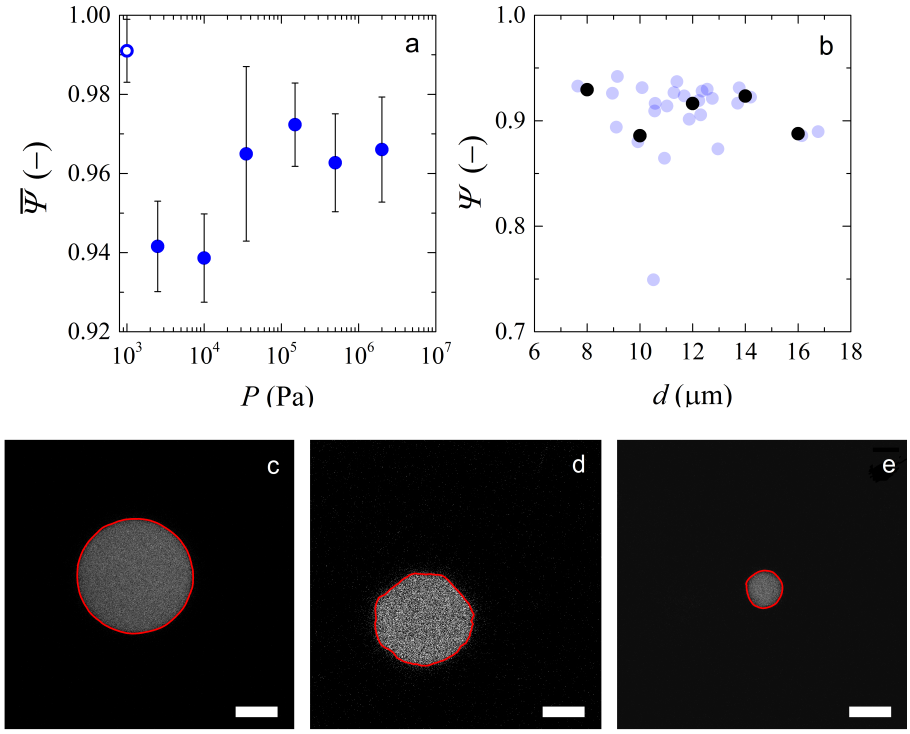

Figure 5.4: a) Average sphericity $\left(\overline{\Psi}\right)$ as a function of compression pressure. The open symbol is a value obtained at zero pressure $P = 0$. (b) Microgel sphericity $\left(\Psi\right)$ as a function of microgel diameter (d) for a single compression pressure (10 kPa). Black circles are binned data. Bin width is 2 and the values within each bin were averaged. Confocal images of a single microgel at (c) zero pressure, (d) at P =10 kPa and (e) 2 MPa. Red outlines correspond to the edges of the particle after image analysis. Scale bars denote 5 μm.

out the effect of the amount of pixels constituting the sphere in the sphericity values. We found that for the size of images used (1000x1000 pixels), or the size of the sphere did not interfere in the sphericity results. Finally, to investigate whether the size polydispersity of the microgels has an influence on their degree of deformation, we plot the sphericity Ψ as a function of the diameter of the microgels d (Figure 5.4b) for a certain compression pressure (10 kPa). We find no statistically significant trend, indicating that there is no significant effect of size

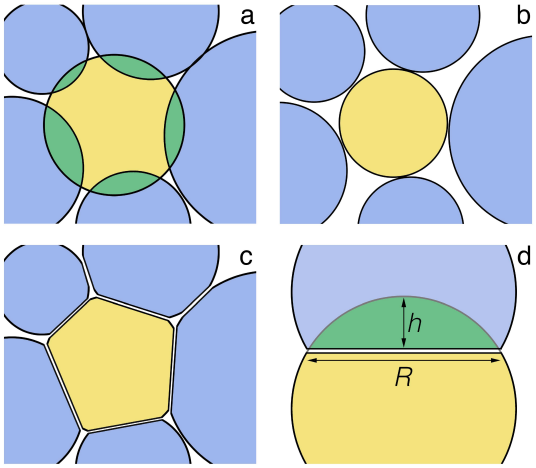

Figure 5.5: Osmotic compression of a microgel suspension leads to unphysical overlap between neighbours (a), which is resolved either by deswelling the particles (b) or through particle deformation in the form of contact facets (c). In the calculation of the energy of deformation by facet formation U_f we use a Hertzian contact model in which the deformation is approximated by the overlap with penetration depth h leading to facets of size R (d).

polydispersity on the particle deformations, within the statistical noise of our experiment.

Our experimental results show that both faceting and deswelling happen, depending on the applied pressure, in a distinctly non-monotonic way. As the pressure increases, facets first become more pronounced, until they start to become less noticeable and the particle appears to homogeneously deswell to a (smaller) spherical configuration. This counterintuitive observation triggers the question if these are equilibrium effects, or wether non-equilibrium aspects may be important. First, we note that the samples are equilibrated for 14 days at a given osmotic pressure. The timescales for poroelastic relaxation, i.e. the solvent flow within the porous polymer particles required to achieve shape and size changes, occurs on much smaller time scales, and are thus not likely to contribute. Moreover, experiments conducted at different times give identical results, suggesting time-dependencies not to be of significant influence.

To confirm that the change from facetting at low pressure to osmotic deswell-

ing at higher pressures is an equilibrium effect, we derive a simple equilibrium model that is capable of reproducing the observed behavior by balancing contact mechanics versus osmotic effects upon creating particle-particle contacts.

Since the experimental microgel particles of polyacrylamide are under good solvency conditions, we derive an extension on the classical description of Flory and Rehner [27, 28], which assumes ideal chains between nodes that are marginally stretched, to account for large chain extensions. The osmotic pressure within a microgel particle results from two opposing terms. The first is a mixing term, describing the mixing entropy and the enthalpy of solvent-monomer interactions, which promotes swelling. Within the mean-field Flory-Rehner approach this can be written as:

$$\Pi_{mix} = \frac{k_B T}{a^3} \left(-\varphi - \ln(1-\varphi) - \chi \varphi^2 \right) \tag{5.2}$$

where $k_B T$ is the thermal energy, a the size of a statistical chain segment, χ the Flory interaction parameter and φ the monomer volume fraction, which is the main control parameter. This term is always positive and as such promotes the uptake of solvent within the microgel particle.

The mixing pressure is balanced by the elasticity of chain segments between crosslinks. Swelling stretches the chains between crosslinks which reduces their conformational entropy. Traditionally, within the Flory-Rehner description, this entropic elasticity is estimated within the Gaussian approximation, which assumes that chains obey a Hookean force law. However, this is only valid when the distance between two crosslinks ξ is close to the relaxed dimension of the chains R_g. For strongly swollen microgels however, chain extension between nodes may be strong, where large deviations from Hookean behaviour may be expected.

To capture this limit as well, we use the freely-jointed chain (FJC) model, which describes the elastic force F on a polymer chain extended to length ξ as:

$$F = \frac{\beta k_B T}{a} \tag{5.3}$$

in which β is the inverse Langevin function, that can be expanded as:

$$\beta = 3\left(\frac{\xi}{N_x a}\right) + \frac{9}{5}\left(\frac{\xi}{N_x a}\right)^3 + \frac{297}{175}\left(\frac{\xi}{N_x a}\right)^5 + \dots \tag{5.4}$$

where N_x is the number of statistical segments between crosslinks. In the limit of small chain extensions this returns to the Gaussian result for which the Hookean spring constant $k = k_B T / N_x a^2$ is valid. Particle swelling, thereby increasing ξ, leads to an effective elastic pressure to counteract swelling:

$$\Pi_{el} = \frac{F}{\xi^2} = \frac{\beta k_B T}{a\xi^2} = \frac{k_B T}{a}\left(\frac{3}{\xi N_x a} + \frac{9\xi}{5(N_x a)^3} + \frac{297\xi^3}{175(N_x a)^5} + \dots\right) \tag{5.5}$$

where the monomer volume fraction is related to the characteristic mesh size as $\varphi = N_x a^3/\xi^3$.

As the microgel is dissolved in a solvent, thermodynamic equilibrium requires the balancing of the pressure within the particle Π_{in}, by swelling or deswelling, with the external osmotic pressure Π_{ex}:

$$\Pi_{in} = \Pi_{mix} - \Pi_{el} = \Pi_{ex} \tag{5.6}$$

We define the relaxed reference state of the microgel as $\Pi_{in} = \Pi_{ex} = 0$, where the polymer volume fraction within the particles $\varphi = \varphi_0$ The bulk modulus K is defined as:

$$K = \varphi \frac{\mathrm{d}\Pi_{in}}{\mathrm{d}\varphi} \tag{5.7}$$

The resistance of the same particle against shape changing deformations, typically by the formation of facets at the contacts of a particle with its neighbours, can be defined by its Young's modulus E, defined as:

$$E = 3K\left(1 - 2\nu\right) \tag{5.8}$$

with ν the Poisson's ratio of the hydrogel particles. More comprehensive micromechanical mean-field approaches to explore the effect of particle elasticity and compressibility on microgel glasses both at rest and under shear have been reported recently [29, 18].

Upon increasing the pressure of a microgel suspension, any physical overlap between the particles (Figure 5.5a) must be avoided, either by shrinking or the formation of facets (Figure 5.5b,c). To evaluate the extent of both of these modes of response to compression we consider the work of deformation due to faceting W_d and the work of shrinkage W_s; both of these represent the reversible (thermodynamic) work performed on a central particle at a given number of particles, total volume of the system and temperature.

The overlap h between two neighboring particles is defined in Figure 5.5d, which can be resolved by a linear combination of contributions due to deformation h_d and shrinking h_s: $h = h_s + h_d$. The fraction of the response attributed to faceting-type deformations can thus be formulated as: $\alpha_d = \frac{h_d}{h_d + h_s}$, and the fraction contributed to shrinking as $(1 - \alpha_d)$.

The work of shrinkage is given by:

$$W_s = \Pi_{in} \Delta V = \frac{4\pi}{3} \Pi_{in} \left({R_0}^3 - (R_0 - h_s)^3 \right) \tag{5.9}$$

with R_0 the radius of the microgel in dilute conditions, where $\Pi_{in} = 0$.

The work of deformation by forming facets is gauged by using the Hertzian model for the elastic contact between two spheres of equal size R_0. The force required to form an indentation of depth h is given by:

$$F = \frac{4}{3} E {R_0}^{1/2} h^{3/2} \tag{5.10}$$

such that the work required to perform a deformation of depth h_d between two spheres becomes:

$$W_d = \int_0^{h_d} F(h) dh = \frac{8}{15} E {R_0}^{1/2} {h_d}^{5/2} \tag{5.11}$$

Since each microgel particles has Z neighbours, the total work associated with deformations becomes:

$$W_d = \frac{8}{15} E {R_0}^{1/2} {h_d}^{5/2} Z \tag{5.12}$$

The total mechanical work can now be defined as:

$$W = \alpha_d W_d + (1 - \alpha_d) W_s \tag{5.13}$$

These two contributions need to be balanced to minimize the overall mechanical work. Thus to find the relative amounts of deformation and shrinkage, we must solve:

$$\frac{dW}{d\alpha} = 0 \tag{5.14}$$

This allows us to evaluate for each pressure, given our expressions for the microgel elasticity and the mechanical work upon compression to what extent a particle will deform and shrink, as expressed by the parameter α_d. If $\alpha_d \approx 1$ the particle will solely deform and shrinkage is negligible; by contrast if $\alpha_d \approx 0$, only isotropic shrinkage occurs while the particles maintain their spherical shape.

To compute the elastic properties of the microgels, we need to choose values for the three independent parameters which govern the microgel properties: i) N: the number of statistical segments between crosslinks, for which we use $N = 250$ (note that the behaviour we observe is robust to the choice of the crosslinking density and is mostly sensitive to the Poisson ratio of the hydrogel). ii) a: the size of a statistical unit, for polyacrylamide microgels as the experimental example, we use the Kuhn length of polyacrylamide as $a \sim 0.4$ nm[30], iii) χ: the Flory interaction parameter describing the interactions between polymer and solvent, for polyacrylamide in water at room temperature $\chi = 0.48$[31]. For the equilibrium particle size at rest R_0 we take 5 μm as also used in our experiments. Even though the coordination number is known to vary with particle concentration[32], for the sake of simplicity we assume $Z = 12$, corresponding to the close-packed limit for monodisperse spheres; also here we find that the results are robust to the choice of Z.

Indeed we see that the mechanical work W has a minimum when plotted as a function of α, the fraction of the overlap h mitigated by means of faceting (Figure 5.6a). By finding this minimum, we can now assess the relative contributions of shrinkage and deformation as a function of the applied pressure.

Interestingly, the experimental behaviour is qualitatively reproduced within our approximate theory. When we plot the amount of overlap h that is mitig-

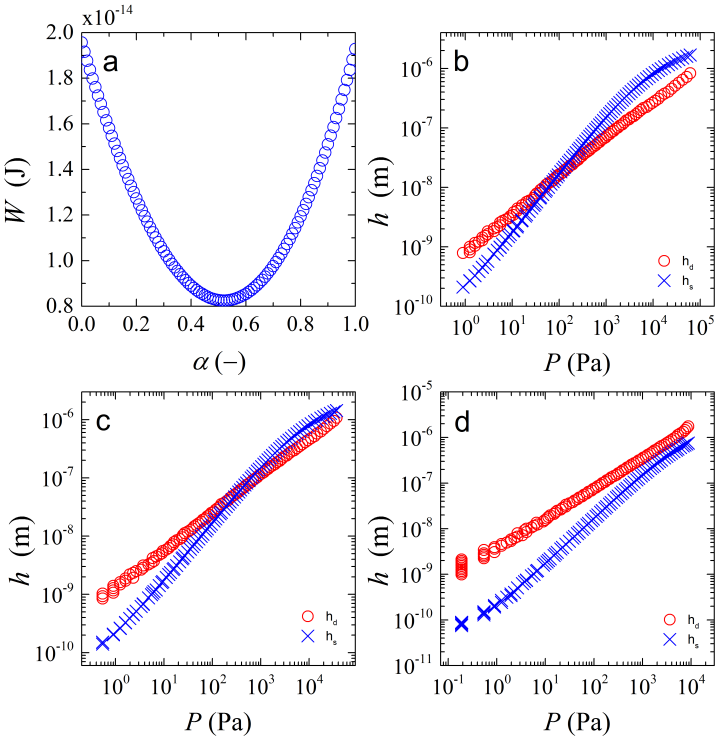

Figure 5.6: (a) Mechanical work W as a function of the fraction of the overlap that is mitigated through deformation $\alpha = h_d/(h_s + h_d)$, showing a clear minimum where $dW/d\alpha = 0$, signalling the equilibrium condition (for: $\nu = 0.40$ and $h_s + h_d = 100$nm), b-d) Contributions of shrinkage h_s and deformation h_d to the total particle response as a function of the total pressure P for three different values of the Poisson's ratio $\nu = 0.3$ (b), 0.4 (c) and 0.48 (d).

ated by faceting h_d and shrinking h_s as a function of the overall pressure Π, we see a crossover in the response. At low pressures, h_d is dominant, indicating a response governed by faceting (Figure 5.6b-d). As the pressure is increased, we see a transition in the behaviour, as a crossing point of h_s and h_d, to a response governed by isotropic shrinkage. This is in qualitative agreement with our experimental observations. These results can seem counterintuitive from the point of view of classical contact mechanics, where the contact between two spheres would always increase its facets if they are more compressed. However, here we

are dealing with a particle compressed and surrounded by other particles. As such, both contact mechanics and osmotic effects come into play.

The crossover pressure at which $h_s > h_d$ thus signals the point at which the osmotic effects of the particle suspension as a whole begin to dominate over the contact mechanics at the particle-particle contacts. At pressures beyond this crossover point, the high osmotic pressure of the particle 'bath' leads to a homogeneous deswelling of the particles.

Within the model we have choosen here, the ratio of shrinkage versus deformation depends strongly on the Poisson ratio of the microgels. For low Poisson's ratios, indicative of compressible solids, shrinkage begins to dominate at relatively low pressures. By contrast, when we choose a high Poisson's ratio, close to that for an incompressible solid, a response governed by deformation is observed. In fact, in the limit of $\nu \to 0.5$, h_s goes to zero and $h \approx h_d$.

Experimentally, we find a crossover in the sphericity at approximately 10 kPa. While the model is approximate, e.g. by the choice of a mean-field approach for the osmotic pressure and ignoring the molecular details of the particle surface, comparing this value to the theoretical cross-over pressures, indicates that the Poisson ratio of our experimental system is between 0.43-0.45. This is in the correct order of magnitude for swollen polyacrylamide hydrogels, for which $\nu = 0.457$, as determined independently previously[33].

At this time, the agreement between theory and experiments is qualitative, since the exact equation of state is not known for these particles. While the Flory-Rehner form (Eqs.5.2-5.5) is a common starting point, it does not take microscopic details, such as crosslinking inhomogeneities, the effects of charges, etc. into account. It may be expected that changing the exact nature of the equation of state, or of the expressions used to related the network structure to the shear rigidity, will change the crossover pressure at which osmotic effects begin to govern over contact mechanics. However, the general notion that at low overal osmotic pressure the particle-particle contacts themself dominate the particle deformation, while the bath pressure takes over when it becomes sufficiently large, is expected to hold irrespective of the choices for the equation of state. In fact, since the facetting is most sensitive to the Young's modulus of the particles, while homogeneous deswelling is governed by their bulk modulus, we may speculate

that the Poisson ratio of the particle is the governing metric for if and when a crossover in behavior may be expected.

Depending on the manner in which microgels are prepared, the surface structure of the polymer chains may be different, leading to significant variations in the length and grafting density of the dangling surface polymers. Also this can have an effect that is currently not accounted for, e.g. by the creation or suppression of lubrication layers and the establishment of a significant disjoining pressure to break these layers during compression.

Finally, recent work from our group has suggested an approach to treat the real volume fraction in systems of compressible colloids but taking osmotic deswelling into account[18], where we assumed that only deswelling occurs while facetting was presumed to be negligible. The results in the current study highlight that this approximation fails especially close to the jamming transition where facetting is severe. Interestingly, since facetting does not lead to a reduction in the real particle volume fraction with compression while deswelling does, the crossover in behavior we find indicates an even steeper effect of compression on the real versus apparent volume fraction than that predicted previously[18]. Moreover, the purpose of the previous study was to explore the effect of osmotic deswelling in absence of facets, on the slowing down of structural relaxations in microgel glasses. We may expect that facets, and the lubrication layers between the two interfaces across a facet, could alter the diffusion rate of particles with respect to their neighbors, and thus have a pronounced effect on the nature of the colloidal glass transition. In principle, this could be tested by comparing the behavior of particles with identical stiffness but different Poisson ratios, through which the balance between osmotic versus contact effect can be tuned.

5.3 Conclusion

In this Chapter, we investigated the behaviour of individual microgels in microgel packings under compression considering simultaneous deswelling and deformation mechanisms. Our experiments show that microgels initially facet under compression and that at higher compression pressures, they regain their spherical shape. To explain this behaviour, we propose a model that balances

the work of osmotic deswelling, within the Flory-Rehner picture of gel swelling, versus facet formation in the Herzian contact model. Numerical solutions of the model predict behavior qualitatively consistent with our experimental observations with a crossover from contact mechanics dominated response at low pressures to an osmotically governed response at high pressures. These results imply that treatments of the dynamics and mechanics of packings of soft particles, that account only for facetting or deswelling, are approximate, and that a full description requires taking both effects into account. This is particularly important at low pressures, close to the jamming and/or glass transition, where deformations are significant. These results also have important implications for the flow behavior of soft particles, e.g. in complex geometries such as membrane pores or constrictions[34, 35, 36, 37], where deswelling and/or deformation plays an important role in pore passage and mitigation of clogs.

5.4 Material and Methods

Microgel synthesis

We synthesise polyacrylamide microgels by polymerization of monomer solutions in emulsion droplets as a template. In a round bottom flask, we mix 100 ml kerosene with 1%wt of the surfactant polyglycerol polyricinoleate (PGPR90). In a separate flask we prepare our monomer solution with 10 ml of water, 0.1M sodium hydroxide solution to set the pH at 8.5, 2.5 g of acrylamide, 50 mg of potassium persulfate (KPS) and 25 mg of N,N'-methylenebisacrylamide (BIS) as the crosslinker at 1%wt as compared to the total monomer content. For fluorescent microgels, we include 25 mg of fluorescein methacrylate at this stage. We add our monomer solution to the content of the round bottom flask and emulsify the aqueous phase into the oil phase under high shear with a rotor-stator mixer for three minutes. We then close the round bottom flask with a rubber septum and bubble the emulsion with nitrogen for 20 minutes to remove oxygen. We subsequently place the round bottom flask on a stirring plate on ice and we inject 1 ml N,N,N',N'-tetramethylethylenediamine (TEMED) to trigger the polymerization. We allow the system to react for 2-3 hours and precipitate the microgels in cold methanol. We clean our microgels by repeated centrifu-

gation and resuspension steps, first in methanol to remove excess kerosene and surfactant, and finally in water, after which the microgel suspension is stored at 4°C.

Osmotic stress

We use a mixture of fluorescent and non-fluorescent microgel suspensions at a number ratio of 1:20 to allow observation of individual microgels in the packing using confocal fluorescence microscopy. We compress the microgel suspension using the osmotic stress technique. We place the suspension of microgels in dialysis bags that we then place in a solution of polyethylene glycol (PEG) with known concentration. The concentration of a PEG solution can be correlated to its osmotic pressure through empirical equations available in the literature[38]. We use a range of PEG concentrations corresponding to osmotic pressures between 2.5 kPa and 2 MPa. The volume of dialysate is at least 100 times larger than the sample volume. The system is allowed to equilibrate for two weeks to ensure the desired compression pressure P is achieved. The dialysate is renewed in the middle of this process, after one week.

Confocal microscopy

To determine how the microgels deform we use confocal fluorescence microscopy to record three-dimensional image stacks of individual, fluorescently labelled microgels. As we only have a small amount of fluorescently labelled microgels in each sample we can visualize single microgels as they deform and shrink at varying osmotic pressure. These experiments are performed on a Zeiss microscope, equipped with a 488 nm laser line and imaged using a x100 oil-immersion objective. The resolution of the images is 1000x1000 pixels. To measure the type and degree of deformation of a microgel at different compression pressures we analyse the confocal image stacks using custom Matlab routines (available upon request). To accurately determine the surface area and circumference of a microgel in each confocal slice we trace the boundary of every microgel and fit a polynomial function to this shape using Savitsky-Goley smoothing. We calculate the surface area for each slice in our three-dimensional image stack and determine the total volume of each microgel in our field of view.

References

[1] Fernández-Nieves, A., Fernández-Barbero, A., Vincent, B. & De Las Nieves, F. J. Charge controlled swelling of microgel particles. *Macromolecules* **33**, 2114–2118 (2000).

[2] Han, K., Tiwari, R., Heuser, T. & Walther, A. Simple Platform Method for the Synthesis of Densely Functionalized Microgels by Modification of Active Ester Latex Particles. *Macromolecular Rapid Communications* **37**, 1323–1330 (2016).

[3] Destribats, M. *et al.* Soft microgels as Pickering emulsion stabilisers: role of particle deformability. *Soft Matter* **7**, 7689–7698 (2011).

[4] Sung, B., Kim, C. & Kim, M. H. Biodegradable colloidal microgels with tunable thermosensitive volume phase transitions for controllable drug delivery. *Journal of Colloid and Interface Science* **450**, 26–33 (2015).

[5] Guo, M. & Wyss, H. M. Micromechanics of Soft Particles. *Macromolecular Materials and Engineering* **296**, 223–229 (2011).

[6] Sierra-Martin, B. *et al.* Determination of the bulk modulus of microgel particles. *Colloid and Polymer Science* **289**, 721–728 (2011).

[7] Mattsson, J. *et al.* Soft colloids make strong glasses. *Nature* **462**, 83–86 (2009).

[8] Meeker, S. P., Bonnecaze, R. T. & Cloitre, M. Slip and flow in soft particle pastes. *Physical Review Letters* **92**, 198302–1 (2004).

[9] Di Lorenzo, F. & Seiffert, S. Particulate and continuum mechanics of microgel pastes: Effect and non-effect of compositional heterogeneity. *Colloid and Polymer Science* **291**, 2927–2933 (2013).

[10] Habicht, A. *et al.* Critical fluctuations and static inhomogeneities in polymer gel volume phase transitions. *Journal of Polymer Science, Part B: Polymer Physics* **53**, 1112–1122 (2015).

[11] Nolan, C. M., Reyes, C. D., Debord, J. D., García, A. J. & Lyon, L. A. Phase transition behavior, protein adsorption, and cell adhesion resistance of poly(ethylene glycol) cross-linked microgel particles. *Biomacromolecules* **6**, 2032–2039 (2005).

[12] Su, W., Yang, M., Zhao, K. & Ngai, T. Influence of Charged Groups on the Structure of Microgel and Volume Phase Transition by Dielectric Analysis (2016).

[13] Habicht, A., Schmolke, W., Lange, F., Saalwächter, K. & Seiffert, S. The non-effect of polymer-network inhomogeneities in microgel volume phase transitions: Support for the mean-field perspective. *Macromolecular Chemistry and Physics* **215**, 1116–1133 (2014).

[14] Nyström, L. *et al.* Electrostatic Swelling Transitions in Surface-Bound Microgels. *ACS Applied Materials and Interfaces* **8**, 27129–27139 (2016).

[15] Maldonado-Valderrama, J., del Castillo-Santaella, T., Adroher-Benítez, I., Moncho-Jordá, A. & Martín-Molina, A. Thermoresponsive microgels at the airâĂŞwater interface: the impact of the swelling state on interfacial conformation. *Soft Matter* **8**, 6416 (2016).

[16] Pellet, C. & Cloitre, M. The glass and jamming transitions of soft polyelectrolyte microgel suspensions. *Soft Matter* **12**, 3710–3720 (2016).

[17] Lietor-Santos, J. J. *et al.* Deswelling microgel particles using hydrostatic pressure. *Macromolecules* **42**, 6225–6230 (2009).

[18] van der Scheer, P., van de Laar, T., van der Gucht, J., Vlassopoulos, D. & Sprakel, J. Fragility

and strength in nanoparticle glasses. *ACS nano* (2017).

[19] Mohanty, P. S. *et al.* Interpenetration of polymeric microgels at ultrahigh densities. *Scientific Reports* **7** (2017).

[20] Hashmi, S. M. & Dufresne, E. R. Mechanical properties of individual microgel particles through the deswelling transition. *Soft Matter* **5**, 3682–3688 (2009).

[21] Savitzky, A. & Golay, M. J. E. Smoothing and Differentiation of Data by Simplified Least Squares Procedures. *Analytical Chemistry* **36**, 1627–1639 (1964).

[22] Liétor-Santos, J. J., Sierra-Martín, B. & Fernández-Nieves, A. Bulk and shear moduli of compressed microgel suspensions. *Physical Review E - Statistical, Nonlinear, and Soft Matter Physics* **84**, 1–4 (2011).

[23] de Gennes, P. *Scaling Concepts in Polymer Physics* (Cornell University Press, 1979).

[24] Flory, P. *Principles of Polymer Chemistry*. Baker lectures 1948 (Cornell University Press, 1953).

[25] Menut, P., Seiffert, S., Sprakel, J. & Weitz, D. A. Does size matter? Elasticity of compressed suspensions of colloidal- and granular-scale microgels. *Soft Matter* **8**, 156 (2012).

[26] Scotti, A. *et al.* The role of ions in the self-healing behavior of soft particle suspensions. *Proceedings of the National Academy of Sciences* **113**, 5576–5581 (2016).

[27] Flory, P. J. & Rehner, J. Statistical Mechanics of Cross-Linked Polymer Networks I. Rubberlike Elasticity. *The Journal of Chemical Physics* **11**, 512 (1943).

[28] Flory, P. J. & Rehner, J. Statistical Mechanics of CrossâĂŘLinked Polymer Networks II. Swelling. *The Journal of Chemical Physics* **11**, 521–526 (1943).

[29] Seth, J. R., Mohan, L., Locatelli-Champagne, C., Cloitre, M. & Bonnecaze, R. T. A micromechanical model to predict the flow of soft particle glasses. *Nature materials* **10**, 838 (2011).

[30] Kundu, S. & Crosby, A. J. Cavitation and fracture behavior of polyacrylamide hydrogels. *Soft Matter* **5**, 3963 (2009).

[31] Kayaman, N., Okay, O. & Baysal, B. M. Swelling of polyacrylamide gels in polyacrylamide solutions. *Journal of Polymer Science Part B: Polymer Physics* **36**, 1313–1320 (1998).

[32] van Hecke, M. Jamming of soft particles: geometry, mechanics, scaling and isostaticity. *Journal of Physics: Condensed Matter* **22**, 33101 (2010).

[33] Takigawa, T., Morino, Y., Urayama, K. & Masuda, T. Poisson's ratio of polyacrylamide (paam) gels. *Polymer Gels and Networks* **4**, 1–5 (1996).

[34] Linkhorst, J., Beckmann, T., Go, D., Kuehne, A. & Wessling, M. Microfluidic colloid filtration. *Scientific Reports* **6** (2016).

[35] Hendrickson, G. & Andrew Lyon, L. Microgel translocation through pores under confinement. *Angewandte Chemie - International Edition* **49**, 2193–2197 (2010). Cited By 38.

[36] Nir, O., Trieu, T., Bannwarth, S. & Wessling, M. Microfiltration of deformable microgels. *Soft Matter* **12**, 6512–6517 (2016).

[37] Roa, R., Zholkovskiy, E. K. & Nagele, G. Ultrafiltration modeling of non-ionic microgels. *Soft Matter* **11**, 4106–4122 (2015).

[38] Bouchoux, A., Cayemitte, P.-E., Jardin, J., Gésan-Guiziou, G. & Cabane, B. Casein Micelle Dispersions under Osmotic Stress. *Biophysical Journal* **96**, 693–706 (2009).

Part II

Confined Flow of Complex Fluids

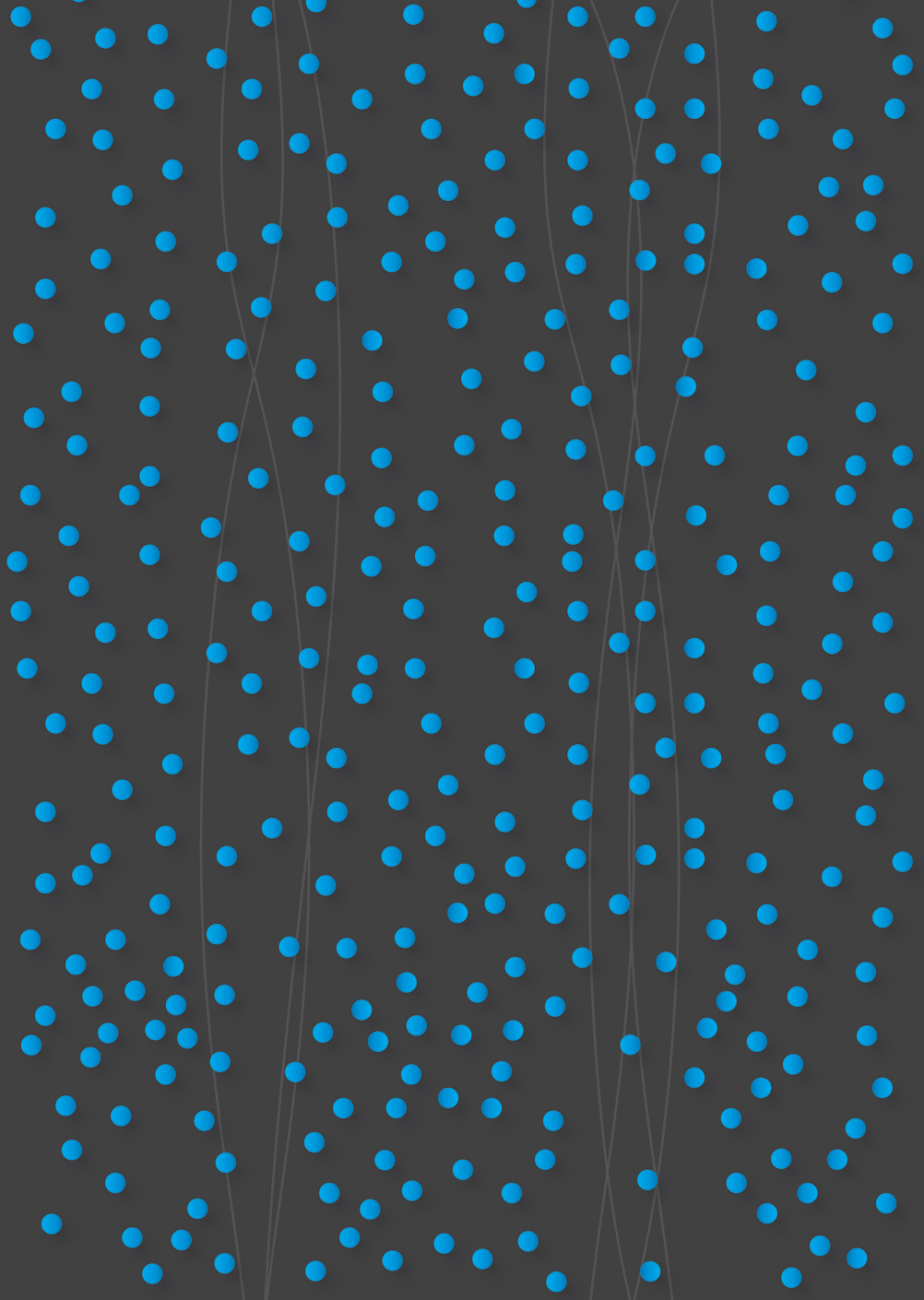

Sticky Squishy & Stuck

Chapter 6

Cooperativity and Segregation in Confined Flows of Soft Binary Glasses

When a suspension containing particles of different sizes flows through a confined geometry a size gradient can be established with large particles accumulating in the channel centre. Such size separation driven by hydrodynamic interactions is expected to facilitate membrane filtration, and may lead to the design of novel and innovative separation techniques. For this, a wide range of particle concentrations has to be investigated, in order to clarify whether shear-induced migration can be utilised at concentrations close to or above the colloidal glass transition, where particle motion is severely hindered and hydrodynamic interactions are screened. We explore this scenario by studying the flow of binary mixtures of soft colloidal microgels, well above their liquid-solid transition, through narrow microchannels. We find that, even though the flow becomes strongly heterogeneous, both in space and time, characterised by a large cooperativity length, size segregation still occurs. This suggests that even above the glass transition shear-induced diffusion could still be used as a fractionation mechanism, which is of great relevance for process intensification purposes.

This chapter was published as:

T. van de Laar, K. Schroën and J. Sprakel: *Cooperativity and Segregation in Confined Flows of Soft Binary Glasses*, Phys. Rev. E *92* (**2015**), 022308.

6.1 Introduction

Membrane filtration is one of the most prevalent unit operations encountered in a wide variety of industrial processes for size-based particle separation. One of the major problems during membrane filtration is the accumulation of particles on the membrane, leading to reduced cross-membrane fluxes[1], and in the worst case, complete clogging of the pores[2]. This necessitates time- and energy-consuming cleaning steps in order to remove the accumulated particles[1]. The design of membrane systems in which particle accumulation can be delayed or avoided thus presents one of the major challenges in membrane technology. In recent years, it has been established that shear-induced diffusion and migration may be used to establish a size- and concentration gradient in a suspension prior to its arrival at the membrane pores. This can lead to innovative solutions to prevent or reduce particle accumulation and pore clogging[3, 4, 5].

In relatively dilute suspensions of particles undergoing shear flow, hydrodynamic interactions between particles, which collide due to velocity differences when they advect along different fluid streamlines, causes them to perform erratic motion, in analogy to the thermal diffusion of Brownian particles at rest[6, 7]. From dimensional analysis it is expected that the resulting shear-induced diffusion coefficient $D \propto \dot{\gamma} a^2$, increases linearly with shear rate $\dot{\gamma}$ and quadratic with particle radius a. For small colloids, which diffuse due to thermal motion at rest, the effects of shear-induced diffusion become noticeable only at sufficiently large shear rates. This can be evaluated with the dimensionless Péclet number, which balances the relative importance of thermal and advective motion.

$$Pe = \frac{\dot{\gamma} a^2}{D_0} = \frac{6\pi\eta\dot{\gamma} a^3}{k_B T} \tag{6.1}$$

where D_0 is the self-diffusion coefficient of particles at rest, η is the viscosity of the suspending fluid and $k_B T$ the thermal energy[8]. For $Pe > 1$ shear-induced diffusion can result in the formation of both a concentration gradient, where particles accumulate at locations of low shear rate[9, 10], and a size gradient, where larger particles move faster towards lower $\dot{\gamma}$ therewith excluding small particles from the central region on the channel [4, 3].

Efficient use of these effects in the design of microfiltration devices, for in-

stance maximizing velocity gradients by confinement, makes it possible to perform separations at much higher volume fractions, $\phi \approx 0.4$, than what is believed achievable in conventional membrane filtration. However, at these concentrations, the particles remain diffusive even at rest.

When the volume fraction ϕ of a suspension is increased further, the zero-shear viscosity grows steeply and the particle self-diffusion coefficient D_0 decreases[11]. Until, at some volume fraction $D_0 \rightarrow 0$, beyond which the suspensions exists in a glassy state. For hard spheres this glass transition occurs at $\phi_g \approx 0.58$. For soft particles, which are deformable, e.g. emulsions, or compressible, such as microgels, the volume fraction can be increased significantly above ϕ_g[12]. For these soft colloidal glasses $Pe \propto 1/D_0$ becomes infinitely large, such that shear-induced diffusion becomes the only mechanism of particle mobility even at very low rates of deformation.

In this soft glassy state, where the constituent particles are in direct contact with several neighbors, hydrodynamic interactions are largely screened and the bulk rheology of the suspension is governed by the elastic interactions between the particles and the local microstructure[13, 14]. This raises the intriguing question how the phenomena so well-established at dilute and intermediate packing fractions, manifest at volume $\phi > \phi_g$. For hard sphere glasses, it has been shown that the linear relation between shear rate and shear-induced diffusion coefficient breaks down; at $\phi = 0.62$, $D \propto \dot{\gamma}^{0.8}$[15]. This suggests that the purely hydrodynamic descriptions, well established and confirmed for $\phi < \phi_g$, no longer hold. Especially for soft colloidal particles, the mechanisms that govern shear fluidization, and the resulting migration and segregation effects, remain largely unclear. Understanding these effects is important to extend the range of concentrations where membrane filtration may be applied, which in turn could significantly reduce the environmental and economic footprint of such processing steps and other separation processes.

In this Chapter we explore the confined flow of dense binary suspensions of soft colloidal particles. The bulk rheology of these suspensions exhibits a distinct transition from fluid to jammed solid above a critical volume fraction ϕ_c. When suspensions at $\phi \gg \phi_c$ are flown through narrow microchannels at constant pressure we observe strong velocity fluctuations, both in time and space.

The spatial heterogeneities are characterised by highly cooperative zones of non-affine displacements, which grow in size with increasing pressure differential. We show that even in highly jammed suspensions, where motion at rest is virtually absent, shear fluidization can give rise to lateral separation of small and large particles. These results suggest that suspensions of soft Brownian colloids at sufficient packing fractions exhibit global and local flow behavior very similar to that found in athermal jammed systems.

6.2 Materials and Methods

Binary microgel system

Soft, fluorescently labelled core-shell microgel particles are synthesised as described in detail elsewhere[16] and in Chapter2. We first synthesise fluorescently-labelled solid core particles, with $d = 300$nm, of polystyrene by emulsion polymerisation; we prepare red-labelled cores (Pyromethene 605) for the small microgels and green-labelled cores (Pyromethene 546) for the large microgels. A soft microgel shell is grown around these cores as follows: in 300 ml DI water we dissolve 160 mg N-N-methylene bisacrylamide and 400 μl methacrylic acid. To vary the size of the PNIPAm shell we vary both the amount of NIPAm added and the number of cores added. For the larger microgels we add 4 ml of the cores (30% wt) and 7.8 grams of NIPAm. For the smaller microgels we use 11 ml cores (30% wt) and 5 grams of NIPAm. Reaction mixtures are degassed with nitrogen for 20 minutes, and initiated with 500 mg of potassium persulfate dissolved in 15 ml DI water. The reaction is allowed to proceed overnight at 70 °C or 80 °C for the large and small particles, respectively. After filtration, the particles are cleaned by repeated centrifugation and redispersion in 0.1 mM NaOH. At this high pH all carboxylic acid groups are deprotonated, rendering the microgels insensitive to small variations in temperature[17]. We measure the hydrodynamic particle size with multi-angle dynamic light scattering and find $d_s = 0.97$ and $d_l = 1.36$ μm for small and large particles, respectively, with a polydispersity less than 5% for both samples. This gives a size ratio of $d_s/d_l = 0.71$; this size ratio effectively suppresses crystallisation at most mixing ratios[17]. For the experiments reported here, we mix small and large particles at 1:1 by volume.

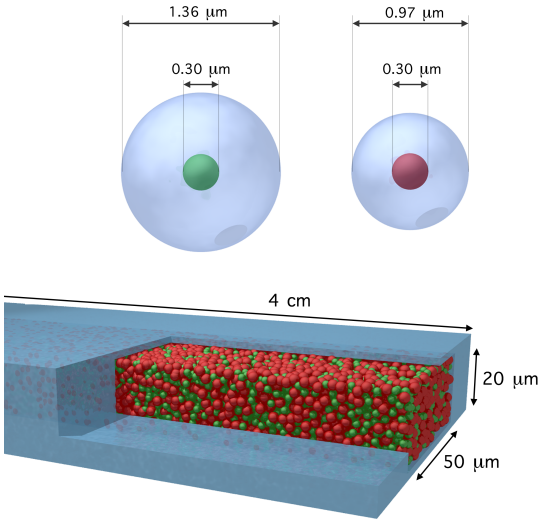

Figure 6.1: Illustration of the experimental system: indicating the dimensions of the core-shell microgel particles and microfluidic channels.

Rheometry

Rheological characterisation of the microgel suspensions, at varying volume fractions, are performed in a 40 mm parallel plate geometry with roughened surfaces to prevent slip, on a Discovery Hybrid rheometer (TA Instruments). The linear viscoelasticity of the suspensions is characterised by frequency sweeps, recorded in a frequency range $\omega = 10^{-1}$ - 10^{2} rad/s, at a fixed strain amplitude of $\gamma = 0.01$. The flow behavior is evaluated from flow curves, where the steady-state shear stress σ is measured as a function of shear rate between $\dot{\gamma} = 10^{-3}$ - 10^{2} s^{-1}.

Microchannel flow

Microfluidic flow experiments are conducted in glass microchannels (Micronit Microfluidics) with a rectangular cross-section of 20 x 50 μm, with a total length of 4 cm (Fig.6.1). Flow is induced by feeding the suspension, through a silica capillary (I.D. 150 μm), into the device at constant pressure, applied with a dif-

ferential pressure transducer (Bronkhorst Nederland), with a control stability of ± 0.5 mbar.

We use an open-source PIV algorithm (JPIV) to measure spatially- and temporally-resolved flow fields from time-lapse sequences recorded with microscopy. For high flow velocities we record image sequences with a high-speed camera (Phantom v9.1) at an acquisition rate of 3125 Hz, while confocal fluorescence microscopy (Zeiss Axiovert 200M with a LSM 5 exciter) is used, at 3.5 Hz, for slow-flowing samples. As small and large particles are labelled with two spectrally-separated fluorophores, we can detect the local concentration of both small and large species from their relative fluorescence intensities across the channel width. Fluorescence intensity profiles represent the average over at least 120 independent frames. Once the suspension enters the confined microchannel, shear-induced migration, diffusion and size-segregation begin to occur. For dilute suspensions, this leads to the establishment of a new steady-state, which is estimated to be fully developed at a distance L_e away from the entrance. For suspensions at volume fractions in excess of 0.3, this entrance length can be estimated as $L_e \sim R^3/d^2$, where R is the characteristic dimension of the flow channel[18]. Taking $R = 20$ μm, the smallest channel dimension, we find for our experiments $L_e \approx 4$ mm. While it is not clear if this expression for L_e holds for the high volume fractions we explore here, all experiments are performed at 2 cm away from the channel orifice, to minimize entrance effects. We acquire images at the channel midplane, 10 μm from the bottom of the channel, to minimise wall effects. In all our experiments we operate at low Reynolds numbers. The upper bound (at highest speeds of 8000 μm/s) for the fluid Reynolds number in our measurements is $Re \leq 10^{-3}$, and that for the particles $Re_p \leq 10^{-2}$. This ensures that viscous forces 'overwhelm' inertial forces and the resulting flows are laminar[8].

6.3 Results and Discussion

Mixtures of small and large soft microgel particles efficiently form glasses, and crystallisation is almost completely suppressed at the size and mixing ratio we employ[17]. Suspensions of soft colloids undergo a liquid-solid transition at some critical volume fraction ϕ_c; this point is typically identified as the random

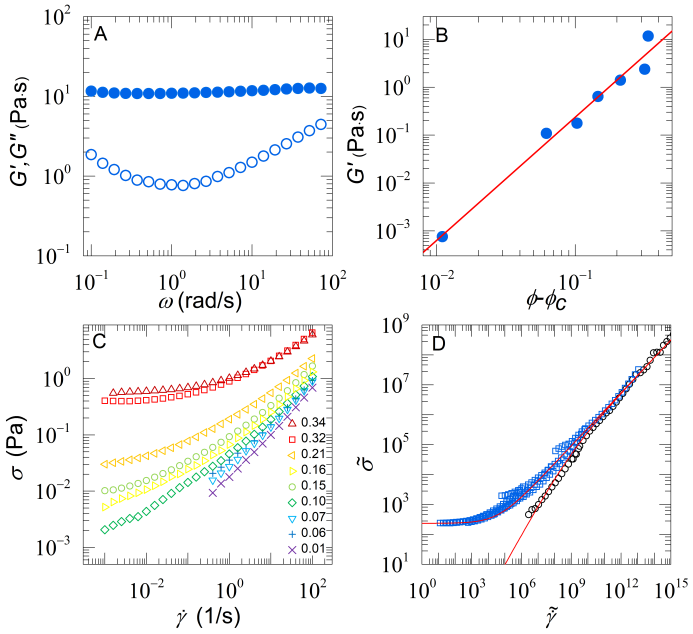

Figure 6.2: (A) Storage (closed symbols) and loss moduli (open symbols) as a function of angular frequency for a typical sample above ϕ_c ($\phi - \phi_c = 0.336$), (B) Storage modulus, at fixed $\omega = 10$ rad/s, versus $\phi - \phi_c$. Drawn line is a power-law fit with characteristic exponent $a = 2.5$, (C) Flow curves for various volume fractions, legend indicates concentrations of measured suspensions relative to ϕ_c, (D) collapse of all flow curves onto two distinct branches, above and below ϕ_c. Drawn lines are fits as described in the text.

close packing limit $\phi_c \approx 0.64$. For hard, incompressible spheres, the volume fraction ϕ is defined as $\phi = nV$, where n is the number concentration of particles and V the volume of a single particle. However, for microgels, which are compressible, V is not a constant; as the concentration increases and the ensemble osmotic pressure rises, the microgels shrink to maintain equilibrium[19, 20]. As a result, volume fraction is no longer a well-defined quantity. We therefore define the volume fraction of each sample relative to ϕ_c.

We first measure the frequency-dependent linear storage, G', and loss moduli G''. At $\phi < \phi_c$, no elastic modulus exists and the sample behaves as a viscous liquid. For samples at $\phi > \phi_c$, we observe a shear elastic modulus G' which

is nearly independent of frequency (Fig.6.2A). Moreover, these samples exhibit a minimum in the viscous dissipation, measured as G'', at a frequency which corresponds to the β-relaxation of the particles which form the glass[21]. This frequency response is characteristic for soft glassy solids.

To find ϕ_c we assume that the shear elasticity vanishes critically at this volume fraction. We therefore plot G', at a fixed frequency $\omega = 10$ rad/s, versus $\Delta\phi = \phi - \phi_c$, and minimize the deviation of the data to a power-law $G \propto (\phi - \phi_c)^a$; this allows us to find, from the limited number of experimental data points, a reasonable estimate of the volume fraction where the shear elasticity vanishes. For these systems we find $a = 2.5$; this is significantly larger than that expected for jammed packings of soft, frictionless, spheres[13], likely due to electrostatic repulsion between the particles, as the screening length in these experiments is relatively large at $\sim$30 nm.

The flow behavior of these binary glassy suspensions is first investigated using conventional rheometry. We measure the steady state stress σ as a function of applied rotational shear rate $\dot{\gamma}$. The flow curves for $\phi < \phi_c$ exhibit a Newtonian regime at low shear rates ($Pe < 1$), thermal motion governs particle displacements, and a shear thinning regime at high rates ($Pe > 1$), where advective motion dominates and the shear flow may induce structural transformations[22]. Also here, ϕ_c marks a distinct transition, as the flow behavior of samples in the solid regime are characterised by a distinct yield stress plateau at low deformation rates, and shear thinning at higher $\dot{\gamma}$ (Fig.6.2C).

Microgel particles are known to undergo a stiffness-dependent glass transition, where the Brownian relaxation time of the suspension grows steeply[12]. It has been argued that the same system undergoes a second transition, at higher packing fractions, akin to the jamming transition for athermal systems. This second transition is characterised by the emergence of a zero-frequency shear modulus when the coordination number exceeds a critical value[23]. The exact connection between these two phenomena remains a topic of ongoing research and exploration[24, 25, 26].

To assess if the systems we investigate here show the characteristics of a jammed solid, we adopt the approach recently described by Paredes *et al.* for emulsions and by Nordstrom *et al.* for microgel glasses. We rescale the flow

curves for various volume fractions using the rescaled shear stress $\tilde{\sigma} = \sigma/|\Delta\phi|^{\alpha}$ and shear rate $\tilde{\dot{\gamma}} = \dot{\gamma} \cdot |\Delta\phi|^{\beta}$. We find, for $\alpha = 4.4$ and $\beta = 6.5$, that the flow curves collapse reasonably onto a single mastercurve with two distinct branches, one for the fluid and one for the jammed solid, separated at $\phi \sim \phi_c$. This is in direct agreement with previous results[27, 28]. We note that the collapse of the solid branch fails at the lowest lowest shear rates, which we ascribe to the difficulty in measuring the true yield stress of a soft solid as discussed extensively in literature e.g. by Moeller *et al.*[29]. The reasonable collapse at higher shear rates suggests that the microgel glass behaves akin to a wider class of materials in which such universality is observed, such as emulsions. Also here, the flow behavior of the solid branch is well described by the classical Herschel-Bulkley constitutive equation for yield stress fluids:

$$\tilde{\sigma} = \tilde{\sigma_0} + K\tilde{\dot{\gamma}}^{n} \tag{6.2}$$

$\tilde{\sigma_0}$ is the rescaled yield stress and the exponent $n \approx \alpha/\beta$ the slope of the shear-thinning regime in the flow curve and $K = 0.45$ is a fitting parameter (drawn line Fig.6.2D).

By contrast, the fluid branch exhibits no yield stress and is characterised by Newtonian flow at low rates followed by weak shear thinning at higher $\dot{\gamma}$ when $Pe > 1$. This branch can be well described by the Cross equation for shear thinning of viscoelastic fluids, combined with the Krieger-Dougherty equation for the volume-fraction dependence of the zero-shear viscosity:

$$\tilde{\sigma} = \frac{\eta_s \phi_c^m \tilde{\dot{\gamma}}}{\left(1 + \left(\frac{\eta_s \phi_c^m}{K}\right)\tilde{\dot{\gamma}}^{1-n}\right)} \tag{6.3}$$

where η_s is the viscosity of the suspending fluid and $m \approx \alpha - \beta$ is the Krieger-Dougherty exponent (drawn line Fig. 6.2D). These results suggest that ϕ_c, determined above as the volume fraction where the shear rigidity vanishes, indeed represents the volume fraction at which the suspension undergoes a rigidity transition from a fluid to a jammed solid.

At rest, or low deformation rates, these two branches represent two distinct phases, with a discontinuous transition. At sufficiently large deformation rates,

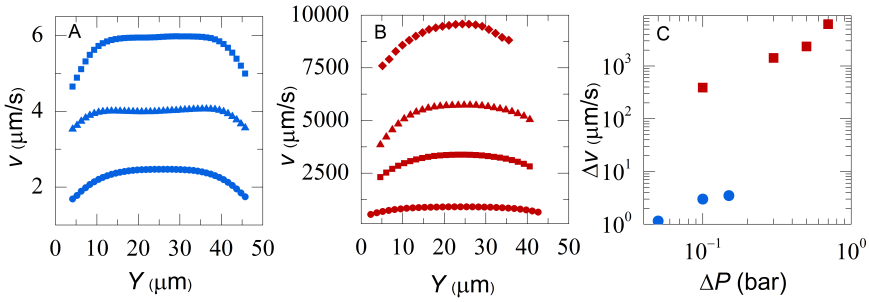

Figure 6.3: Velocity profiles for $\Delta\phi = 0.317$ at $\Delta P = 0.05$, 0.1 and 0.15 bar (circles, triangles and squares in A) and for $\Delta\phi = 0.158$ at 0.1, 0.3, 0.5 and 0.7 bar (circles, squares, triangles and diamonds in B), (C) slip velocity as a function of ΔP for $\Delta\phi = 0.158$ (squares) and $\Delta\phi = 0.317$ (circles).

the two branches converge, and the transition from fluidized solid to fluid becomes continuous. We note that recent computer simulations have suggested that, while the glass transition of soft spheres and their jamming transition give rise to a similar progression of the macroscopic flow curves with packing fraction, the microscopic physics underlying these two phenomena are distinctly different[25]. Further in-depth study is required to disentangle these two phenomena with accuracy in these systems.

We now proceed to flow the same dense binary suspensions through narrow microchannels, with a confinement ratio $R/a \approx 15$. In this geometry we can measure the local flow fields using particle imaging velocimetry (PIV) using the particles themselves as the tracers, without the need to add additional components to the system. For a very dense suspension, $\Delta\phi = 0.317$, we observe that the time- and spatially-averaged flow profiles deviate strongly from classical Poiseuille flow, expected for Newtonian fluids. Rather, a plug-like flow is observed in the centre of the channel where $\dot{\gamma}$ becomes very small, and shear-bands, in which most of the deformation is localised, close to the channel walls (Fig.6.3A). This is consistent with the expected channel flow profiles for yield stress fluids. Increasing the pressure leads to a distinct broadening of the shear bands, and narrowing of the central, unsheared, zone; a similar growth of the shear localisation zones with overall applied shear rate is observed for yield stress fluids in Couette flow[30].

When the packing fraction is decreased to $\Delta\phi = 0.158$, the distinct separation into a central unsheared zone, lined by shear bands, weakens and a gradual transition from shear zones, to weakly sheared central zone is observed (Fig.6.3B). Fully parabolic profiles are not expected to be observed until $\phi \ll \phi_c$. Unfortunately, the refractive index mismatch between glass walls ($n_d \approx 1.48$) and aqueous suspension ($n_d = 1.33$) causes optical aberrations at the fluid-wall interface. Due to the resulting lensing, reliable flow velocities can only be measured some distance away from the walls. Due to the high flow rates this effect is most pronounced for the lower packing fraction shown in Fig.6.3B, which are recorded with brightfield microscopy and a high-speed camera. By contrast, the data obtained with confocal microscopy (Fig.6.3A), suitable only for slow flows, suffers much less from these optical artefacts. Even though one or two layers of microgel particles line the channel walls by physical adsorption, rendering the channel walls rough on the order of the particle diameter, this is not sufficient to suppress wall slip. A significant slip velocity is observed at the channel walls, which increases strongly with packing fraction and applied pressure (Fig.6.3C)[31]. These velocity profiles represent the time- and spatial-average from the 2D flow fields obtained by PIV. Interestingly, we find that for high packing fractions the flow becomes strongly heterogeneous both in space and time.

For packing densities relatively close to ϕ_c, the spatially-averaged velocity at fixed applied pressure is virtually constant in time. Note that we can observe a small regular oscillation, with an amplitude of only 1 % of the mean velocity. This is caused by the electronic feedback mechanism of the pressure transducer, operating at 50 Hz (Fig.6.4A). By contrast, the average velocity shows strong fluctuations for more concentrated samples, which range from periodic at low pressure (Fig.6.4B) to intermittent at high pressures (Fig.6.4C). The periodic fluctuations in velocity at low pressures occur with a characteristic frequency of 2.2 mHz, measured from the power spectrum of the $V(t)$ trace, which cannot be explained by the fast feedback rate of the transducer. Rather, such slow feedback processes must represent some internal mechanism in the suspension.

For hard sphere glasses, it is known that under strong confinement, regular and erratic velocity fluctuations may emerge at $\phi \sim \phi_c$ due to transient and localised jamming and unjamming events, caused by local density fluctuations

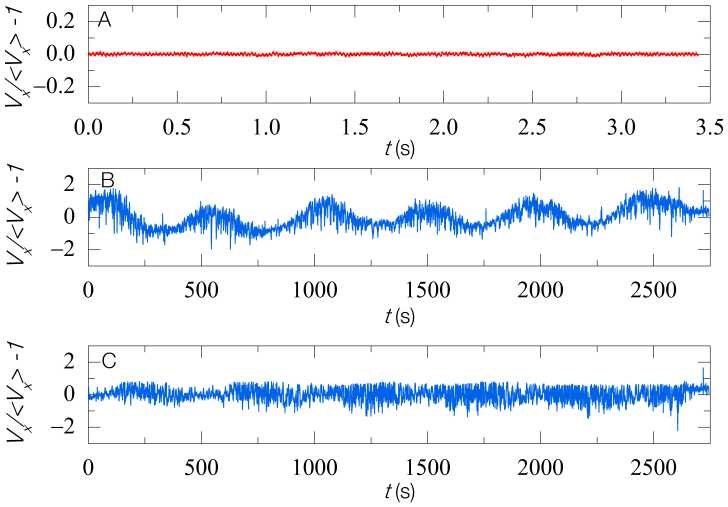

Figure 6.4: Velocity in the centre of the channel V_x, normalised by the time-average velocity $\langle V_x \rangle$, as a function of time for $\Delta\phi = 0.158$ at $\Delta P = 0.1$ bar (A) and $\Delta\phi = 0.317$ at $\Delta P = 0.05$ (B) & 0.1 bar (C).

which are enhanced by the velocity gradient across the channel[32, 33]. While we also observe strong intermittency in our soft glassy systems, with amplitudes several times the mean velocity, it only emerges at packing fractions $\phi \gg \phi_c$. This may be related to the fact that for hard spheres in a glassy state, small transient and localised densifications can lead to orders of magnitude increase in local viscosity and rigidity[21], while these effects are much weaker for soft particle glasses close to ϕ_c[12]. We thus speculate that the coupling between density and mechanics needs to be sufficiently steep to provide the internal feedback required to generate intermittency. For soft particle packings this only occurs when the ensemble is compressed strongly, depending on the initial softness of the particles.

In the intermittent flow regime, where the velocity fluctuates strongly in time, we also observe large spatial heterogeneities, evident in the full two-dimensional flow fields (Fig.6.5A). These spatial heterogeneities are more clearly visible when the affine component of the flow is subtracted. This leaves the non-affine component of the flow which exhibits distinct zones of collective reorganisa-

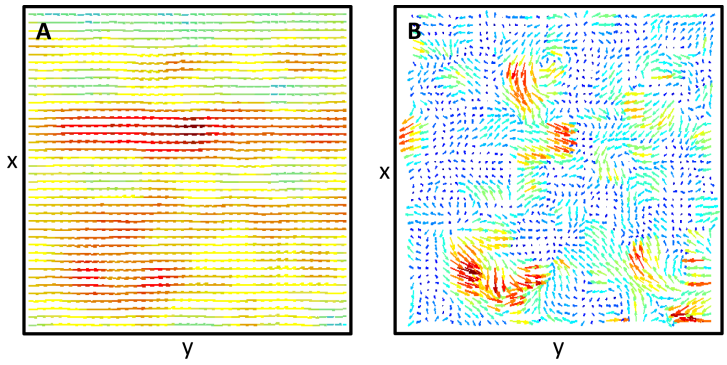

Figure 6.5: Spatially-resolved flow field for $\Delta\phi = 0.317$ at $\Delta P = 0.05$, (A) shows full velocity field (B) shows the corresponding non-affine velocity, in which the affine flow field, obtained from the time-average, is subtracted. Flow is from left to right, total size of the field-of-view is $\approx$ 50 x 50 μm, with a voxel size for the PIV analysis of $1.08\mu m^2$.

tions (Fig.6.5B). In this highly jammed state, particle motion is strongly hindered by elastic contacts with many neighbors; for a single particle to advect along a streamline, many of its neighboring particles must rearrange.

To evaluate the spatial distribution of these collective rearrangements, we first select only those vectors whose magnitude is 1.5 times larger then the mean velocity for each frame. This thresholding separates clusters of co-moving fluid elements which exhibit correlated motion, whose size can then be determined. While the exact numerical value of the threshold velocity is arbitrary, we verify that the results are qualitatively robust to changes in this parameter. For both volume fractions and all pressures, these distributions are well described by a power-law distribution with exponential cut-off (drawn lines in Fig.6.6A&B). These scale-invariant distributions, with a cut-off which is bounded by the finite size of the microchannel, are characteristic for driven systems which exhibit intermittency, and suggest a strong coupling between local collective phenomena and the global response to flow. From these distributions we can measure both the mean size of cooperatively flowing non-affine fluid clusters, and a measure for their upper bound from the exponential cut-off. We observe how the spatial cooperativity length increases with volume fraction (Fig.6.6C), as observed for emulsions in confined flows previously[34].

Interestingly, Goyon *et al.* described how the flow of concentrated emulsions through microchannels can be described using a single spatial cooperativity length which appears independent of flow velocity[34]; in our experiments we observe that increasing the pressure differential leads to a strong increase in the size of cooperatively reorganising clusters. As the dimensions of spatial cooperativity reach the order of magnitude of the channel size, which is only 20 μm here, strong non-local effects come into play [34, 35]. As a consequence, the local velocity profiles measured in strong confinement cannot be mapped onto the macroscopic flow profiles as done successfully for flow through wider microchannels for similar suspensions of microgel colloids [27]. This is exacerbated by the strong shear banding we observe here, where distinct zones with different properties appear.

In dilute suspensions comprised of particles of different size the strong shear field that develops in confined flow leads to distinct segregation of large and small particles across the channel. Typically, large particles will localise at the centre of the channel, where the shear rate is minimal, displacing the smaller particles towards the channel walls[9, 10]. This effect can be used efficiently in filtration processes to prevent the proximity of larger objects near to the pores through which a fluid stream enriched in small particles can be separated from one enriched in large colloids. This decreases the probability for clogging, thereby extending the life time of membranes and increasing separation efficiency[3, 4]. Such shear-induced segregation however requires individual particles to migrate. Obviously, single particle migration is strongly hindered in a glassy suspension.

This raises the intriguing question whether shear fluidization of a soft glass is sufficient to induce these effects at $\phi \gg \phi_c$. To determine if size segregation occurs we utilise the fact that our small and large particles are fluorescently dyed with different fluorophores. By averaging the fluorescence intensity as a function of position across the channel over at least 120 frames, we can construct a fluorescence intensity profile for both small (red) and large particles (green), as shown in Fig.6.7. As a first order approximation, since the fluorescent cores of the particles show no overlap, the average fluorescence intensity is linearly proportional to the local volume fraction of particles.

Surprisingly we find that indeed, even at $\Delta\phi = 0.317$ segregation still oc-

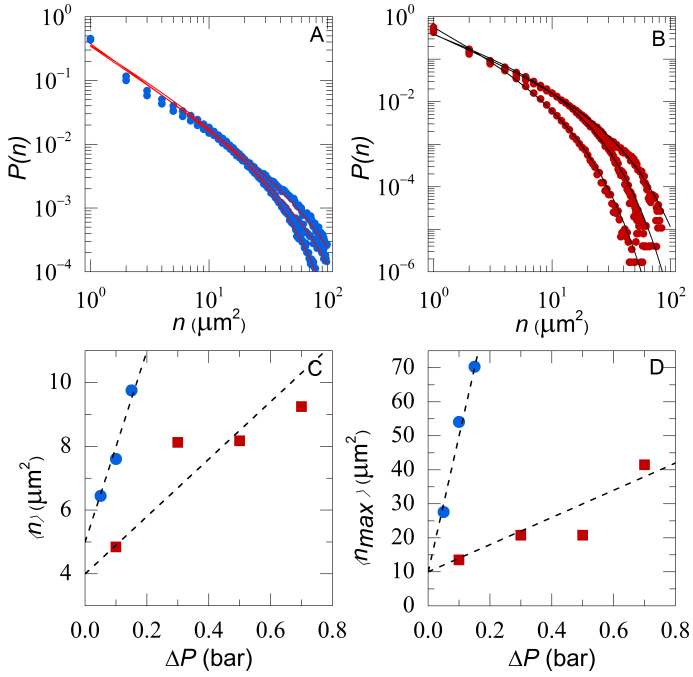

Figure 6.6: Probability distributions of cooperative cluster sizes in μm^2 for $\Delta\phi = 0.317$ at $\Delta P = 0.05$, 0.1 & 0.15 bar (A) and $\Delta\phi = 0.158$ at $\Delta P = 0.1$, 0.3, 0.5 & 0.7 bar (B). Drawn lines represent fits to a power-law distribution with an exponential cut-off. Mean cluster size (C) and maximum cluster size (D) in μm^2 as a function of pressure for $\phi = 0.317$ (circles) and $\phi = 0.158$ (squares). Dotted lines are a guide to the eye.

curs. Apparently, despite the large hindrance in such a glassy suspension, the strongly collective shear fluidization can still lead to the development of distinct segregation patterns. To evaluate if the measurements performed at 2 cm from the channel entrance represent a fully-developed profile, we also record data at 1 and 3 cm away from the orifice. Indeed, no significant changes occur, verifying that the entrance length $L_e < 1$ cm (Fig.6.7A-C).

At low pressures we observe strong localisation of the large particles in the centre of the channel, where the small particles are depleted (Fig.6.7D). At higher pressures we observe multiple bands of size segregated particles (Fig.6.7E&F). For the size ratio of microgel particles we study here, we previously showed that

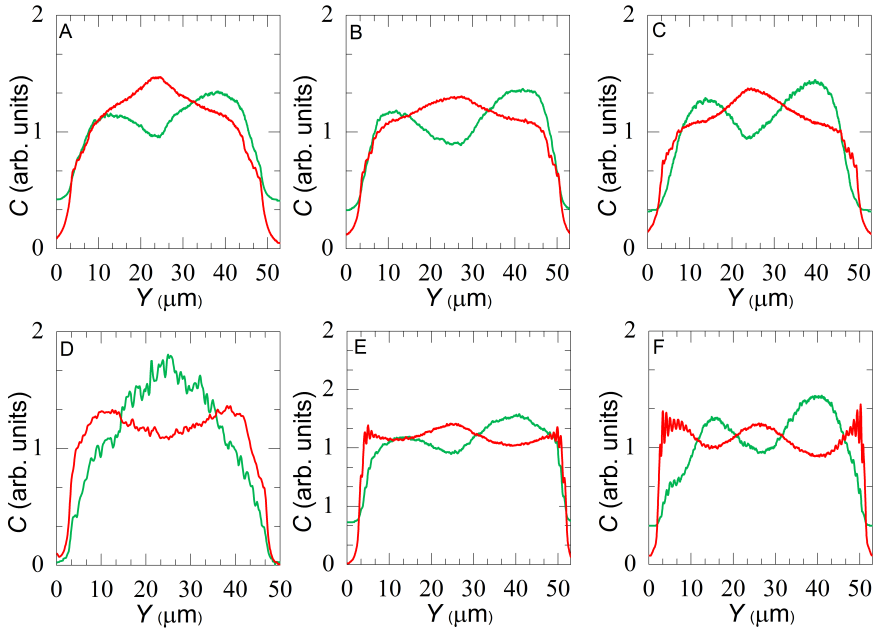

Figure 6.7: Normalised fluorescence intensity profiles for $\Delta\phi = 0.317$ at $\Delta P = 0.7$ for three different positions in the channel, at 1 (A), 2 (B) and 3 cm (C) from the channel entrance and for three different pressures at 2 cm with $\Delta P = 0.05$ (D), 0.5 (E) and 0.8 bar (F) as a function of channel width. Green and red lines show the measured fluorescence intensity, which is proportional to the local concentration, of the large and small microgel colloids, respectively.

addition of only 10 % of the large spheres is sufficient to completely frustrate crystallisation[17]. The size segregation which occurs in these dense suspensions is complete enough to observe crystallisation of the small particles close to the channel walls, seen from the distinct oscillations in fluorescence intensity at the channel boundaries (Fig.6.7F).

The development of multiple bands, rather than a single band of large spheres in the centre, most likely is a kinetically trapped state which develops during segregation. Ultimately, we would expect all large particles to tend to the centre of the channel where they experience minimal shear. Also for size segregation in strongly driven granular packings, the separation into multiple bands enriched in particles of different sizes has been observed[36].

This surprising result shows how size segregation can also occur in the flow

of suspensions which are well above their liquid-solid transition. At rest, translational diffusion in these suspensions is absent, rendering the system effectively athermal; moreover, the hydrodynamic interactions, generally considered to drive shear-induced migration, are most likely to be highly screened at these concentrations. It thus appears that the strong intermittency and spatial cooperativity and non-local effects we observe for these systems of highly packed small colloidal particles are more akin to those effects observed in dry granular media[37, 38, 34, 36].

Our results strongly hint at the possibility to use confined flows to pre-sort polydisperse particles even at very high volume fractions in the design of new and improved microfiltration and separation devices. However, the exact nature of size segregation, in conjunction with the large spatial cooperativity we observe, remains unclear. If many particles move in sync, how can this random and intermittent motion result in the sorting of particles along the channel based on size; these questions may be answered using slower flows and high-speed confocal imaging in which the trajectories of individual particles can be followed. Moreover, how the flow profiles in these yield stress fluids are affected by the presence of pores in the side walls of the channel, required for separation purposes, is unclear but may be expected to lead to additional non-linearities and strong shear localisation at the pore walls, indicating that if a process is to be based on these effects, understanding shear induced diffusivity effects in relation to pore phenomena is of key importance.

References

[1] Belfort, G., Davis, R. H. & Zydney, A. L. The behavior of suspensions and macromolecular solutions in crossflow microfiltration. *Journal of Membrane Science* **96**, 1–58 (1994).

[2] Wyss, H. M., Blair, D. L., Morris, J. F., Stone, H. A. & Weitz, D. A. Mechanism for clogging of microchannels. *Phys. Rev. E* **74**, 61402 (2006).

[3] van Dinther, A. M. C., Schroën, C., Imhof, A., Vollebregt, H. M. & Boom, R. M. Flow-induced particle migration in microchannels for improved microfiltration processes. *Microfluidics and Nanofluidics* **15**, 451–465 (2013).

[4] Kromkamp, J., Faber, F., Schroen, K. & Boom, R. Effects of particle size segregation on crossflow microfiltration performance: Control mechanism for concentration polarisation and particle fractionation. *Journal of Membrane Science* **268**, 189–197 (2006).

[5] van Dinther, A., Schroën, C. & Boom, R. Particle migration leads to deposition-free fractionation. *Journal of Membrane Science* **440**, 58–66 (2013).

[6] Leighton, D. & Acrivos, A. The shear-induced migration of particles in concentrated suspensions. *Journal of Fluid Mechanics* **181**, 415–439 (1987).

[7] Leighton, D. & Acrivos, A. Measurement of shear-induced self-diffusion in concentrated suspensions of spheres. *Journal of Fluid Mechanics* **177**, 109–131 (1987).

[8] Squires, T. M. & Quake, S. R. Microfluidics: Fluid physics at the nanoliter scale. *Rev. Mod. Phys.* **77**, 977–1026 (2005).

[9] Semwogerere, D. & Weeks, E. R. Shear-induced particle migration in binary colloidal suspensions. *Physics of Fluids* **20**, – (2008).

[10] Koh, C. J., Hookham, P. & Leal, L. G. An experimental investigation of concentrated suspension flows in a rectangular channel. *Journal of Fluid Mechanics* **266**, 1–32 (1994).

[11] Hunter, G. L. & Weeks, E. R. The physics of the colloidal glass transition. *Reports on Progress in Physics* **75**, 66501 (2012).

[12] Mattsson, J. *et al.* Soft colloids make strong glasses. *Nature* **462**, 83–86 (2009).

[13] van Hecke, M. Jamming of soft particles: geometry, mechanics, scaling and isostaticity. *Journal of Physics: Condensed Matter* **22**, 33101 (2010).

[14] Koumakis, N., Pamvouxoglou, A., Poulos, A. S. & Petekidis, G. Direct comparison of the rheology of model hard and soft particle glasses. *Soft Matter* **8**, 4271–4284 (2012).

[15] Besseling, R., Weeks, E., Schofield, A. & Poon, W. Three-Dimensional Imaging of Colloidal Glasses under Steady Shear. *Physical Review Letters* **99**, 028301 (2007).

[16] Appel, J. *et al.* Temperature Controlled Sequential Gelation in Composite Microgel Suspensions. *Particle and Particle Systems Characterization* **32**, 764–770 (2015).

[17] Higler, R., Appel, J. & Sprakel, J. Substitutional impurity-induced vitrification in microgel crystals. *Soft Matter* **9**, 5372–5379 (2013).

[18] Butler, J. E., Majors, P. D. & Bonnecaze, R. T. Observations of shear-induced particle migration for oscillatory flow of a suspension within a tube. *Physics of Fluids (1994-present)* **11** (1999).

[19] Muluneh, M. & Weitz, D. A. Direct visualization of three-dimensional crystallization behavior in microgels. *Phys. Rev. E* **85**, 21405 (2012).

[20] Fernández-Nieves, A., Fernández-Barbero, A., Vincent, B. & de las Nieves, F. J. Charge Controlled Swelling of Microgel Particles. *Macromolecules* **33**, 2114–2118 (2000).

[21] Mason, T. G. & Weitz, D. A. Linear Viscoelasticity of Colloidal Hard Sphere Suspensions near the Glass Transition. *Phys. Rev. Lett.* **75**, 2770–2773 (1995).

[22] Cheng, X., Xu, X., Rice, S. A., Dinner, A. R. & Cohen, I. Assembly of vorticity-aligned hard-sphere colloidal strings in a simple shear flow. *Proceedings of the National Academy of Sciences* **109**, 63–67 (2012).

[23] Zhang, Z. *et al.* Thermal vestige of the zero-temperature jamming transition. *Nature* **459**, 230–233 (2009).

[24] Silbert, L. E. *et al.* Granular flow down an inclined plane: Bagnold scaling and rheology. *Phys. Rev. E* **64**, 51302 (2001).

[25] Ikeda, A., Berthier, L. & Sollich, P. Unified study of glass and jamming rheology in soft particle systems. *Phys. Rev. Lett.* **109**, 18301 (2012).

[26] Mari, R., Krzakala, F. & Kurchan, J. Jamming versus Glass Transitions. *Phys. Rev. Lett.* **103**, 25701 (2009).

[27] Nordstrom, K. N. *et al.* Microfluidic rheology of soft colloids above and below jamming. *Physical Review Letters* **105** (2010).

[28] Paredes, J., Michels, M. a. J. & Bonn, D. Rheology across the zero-temperature jamming transition. *Physical Review Letters* **111** (2013).

[29] Moller, P. C. F., Mewis, J. & Bonn, D. Yield stress and thixotropy: on the difficulty of measuring yield stresses in practice. *Soft Matter* **2**, 274–283 (2006).

[30] Moller, P. C. F., Rodts, S., Michels, M. A. J. & Bonn, D. Shear banding and yield stress in soft glassy materials. *Phys. Rev. E* **77**, 41507 (2008).

[31] Isa, L., Besseling, R. & Poon, W. C. K. Shear Zones and Wall Slip in the Capillary Flow of Concentrated Colloidal Suspensions. *Phys. Rev. Lett.* **98**, 198305 (2007).

[32] Isa, L., Besseling, R., Morozov, A. N. & Poon, W. C. K. Velocity Oscillations in Microfluidic Flows of Concentrated Colloidal Suspensions. *Phys. Rev. Lett.* **102**, 58302 (2009).

[33] Genovese, D. & Sprakel, J. Crystallization and intermittent dynamics in constricted microfluidic flows of dense suspensions. *Soft Matter* **7**, 3889–3896 (2011).

[34] Goyon, J., Colin, A., Ovarlez, G., Ajdari, A. & Bocquet, L. Spatial cooperativity in soft glassy flows. *Nature* **454**, 84–87 (2008).

[35] Nicolas, A. & Barrat, J.-L. Spatial Cooperativity in Microchannel Flows of Soft Jammed Materials: A Mesoscopic Approach. *Phys. Rev. Lett.* **110**, 138304 (2013).

[36] Moakher, M., Shinbrot, T. & Muzzio, F. J. Experimentally validated computations of flow, mixing and segregation of non-cohesive grains in 3D tumbling blenders. *Powder Technology* **109**, 58–71 (2000).

[37] Schall, P. & van Hecke, M. Shear Bands in Matter with Granularity. *Annual Review of Fluid Mechanics* **42**, 67–88 (2010).

[38] Wandersman, E., Dijksman, J. A. & van Hecke, M. Particle diffusion in slow granular bulk flows. *EPL (Europhysics Letters)* **100**, 38006 (2012).

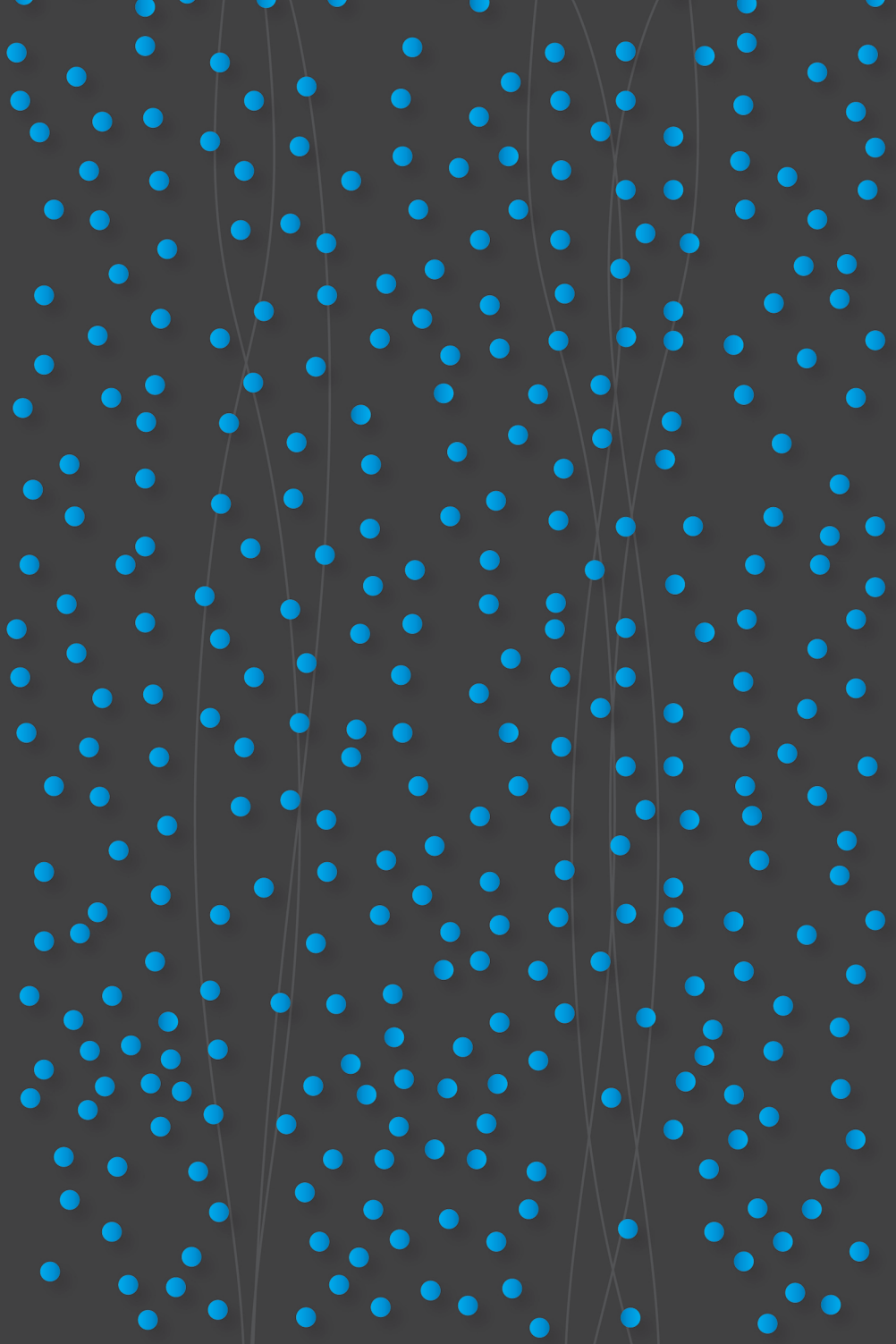

Sticky Squishy & Stuck

Chapter 7

Oil Displacement by Visco-Elastic Fluids in a Disordered Micromodel

Disordered porous media are found commonly in both nature and industry. Flow through such disordered structures is a common but complex phenomenon, with many different factors interacting at different length scales. A classical example of a major problem encountered with flow through porous media is that of non-complete displacement, where a displacing phase flows through a porous structure, but large pockets of the to-be-displaced phase remain. Structure of the porous system, flow rates, and the different length scales all influence the effectiveness of such displacement. Non-complete displacement has a major impact on for instance the efficiency of oil recovery processes. Here we present a microfluidic model to study two-phase flow through a disordered micromodel using high-speed quantitative microscopic imaging. We investigate the effect of visco-elasticity on the displacing fluid and show that by changing the visco-elastic behavior of the displacing fluid we can greatly increase the efficiency of the overall displacement process.

This chapter was submitted as:

T. van de Laar, K. Remmers, K. Schroën and J. Sprakel: *Oil Displacement by Visco-elastic Fluids in a Disordered Micromodel*

7.1 Introduction

Porous media are present all over this planet and at various scales, both as manufactured structures and as natural occurances. Most of these porous structures are random orientated, where textile, paper and sand are classical examples[1]. Flow through these porous media is ubiquitous in everyday life; when printing inks, doing laundry, but also when water flows through treeroots[2, 3, 4, 5]. Another common example is found in oil recovery, where water is used to displace oil from porous bedrock. This two-phase flow through porous media is a complex problem, involving phenomena that are not well understood[3, 6]. One major problem is non-complete displacement, where pockets of the to-be-displaced phase remain. This lowers e.g. the efficiency of oil recovery processes, hampers the efficiency of detergents and leads to an improper printing process[7, 8].

Various factors contribute to such non-complete displacement; wettability differences between the two phases, as often a non-wetting phase will displace a wetting phase[9, 10], the viscosity ratio between the fluids, the surface tension, and possible interactions between the liquids and the wall which may be strongly influenced by the presence of surface active components[11]. The structure of the porous network, along with the flow rates and length scales all influence the displacement process, and could lead to (stronger) non-complete displacement[12, 13].

Studying how all these factors contribute to the displacement process is difficult, complicated further by the inability to see what happens inside a porous rock (or other similar porous materials). Micromodels offer a usual alternative way to study this problem, as these micromodels allow direct visualization of the displacement process when manufactured from PDMS or glass[3, 14, 15, 16, 17]. These micro-engineered structures also open up the possibility to study the various factors that lead to a non-complete displacement in a systematic way[3, 12, 18]. Most micromodels use ordered structures to investigate how displacement can be improved. However, most natural porous systems are highly disordered, and how this disorder and differences in structure contribute to a non-complete displacement remains poorly understood.

In this chapter we focus on a random approach to model a porous structure, inspired by the approach of Wu *et al.*[3, 19]. Instead of using series of connected

channels we introduce nodes (or pores) that connect these channels of varying length and under varying angles to more accurately mimic natural porous structures, and fabricate these channels out of PDMS. We use high-speed brightfield microscopy to visualize and study the displacement process, and investigate how the random structure influences the displacement in our micromodel. We observe a strong effect of the network geometry, where channels not aligned in the general flow direction will replace with much more difficulty. We also look at the effects of changing the viscosity of the displacing phase, and how this might lead to a more complete displacement. We show that by increasing the viscosity of the displacing phase we achieve a much more complete, and thus efficient, displacement. We attribute this increase in efficiency to the slowing down of the displacement process, which prevents trapping of pockets of the to-be-displaced phase.

7.2 Materials and Methods

We create random porous micromodels by taking inspiration from the approach of Wu *et al.*[3, 19] Our micromodel features large pores connected by narrow channels to emulate the porous structure present in rock. We start by randomly placing a fixed number of circles (250 in total) on a fixed surface area (tailored such that it matches the maximum field of view for our microscope system) using a custom Matlab routine. We make sure that none of these circles touch (see Fig.7.1a), we then connect all circles using Delaunay triangulation[20], this ensures that there is no physical overlap between the channels (Fig.7.1b). We tailor the Matlab output to automatically generate circles of a fixed size and channels of a fixed width in AutoCAD (Fig.7.1c). During the conversion from Matlab to AutoCAD all channels are given a fixed finite width, which leads to some overlap in channels close to the edge. In a Delaunay triangulation any line cannot overlap, but the same does not go for lines of fixed finite width. We manually remove these overlapping channels to prevent the formation of a wide, easily accessible channel that would dominate the displacement process. The final design can be seen in Fig.7.1d, with a close-up of the porous structure shown in Fig.7.1e. We use this design to create a photolitographic mask and fabricate our micromodel out

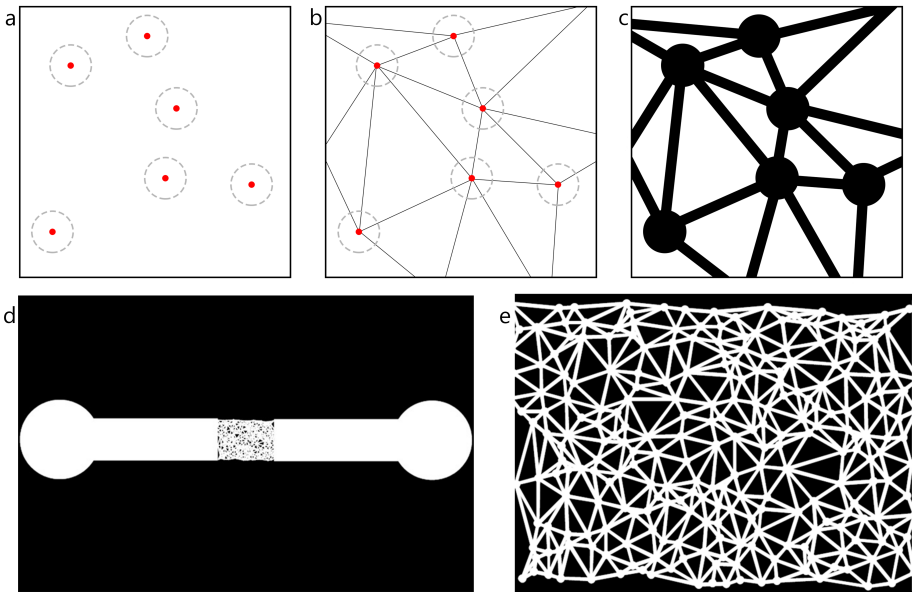

Figure 7.1: (a-c) Schematic showing how circles are randomly placed (a), connected using Delaunay triangulation (b) and finally filled in to form our micromodel (c). (d) Overview of our micromodel, including inlet and outlet for tubing, white shows all areas open to flow, (e) shows the porous structure in more detail.

of PDMS using standard soft lithography techniques[21]. After plasma-bonding a PDMS device will initially be hydrophillic, and turn hydrophobic over time[22]. To ensure that each of our devices has the same wetting properties and is hydrophobic we place each device in an oven at 120°C for 36 hours[22] after plasma bonding.

To simulate two-phase flow through porous media we first fill our disordered micromodel with oil (perfluorodecalin, our wetting phase) with a syringe pump. We use two three-way valves (both at the inlet and outlet) to ensure complete removal of air from the system. Once all air has been removed we switch our three-way valves and turn on the water flow (10 μl/min) which will displace the oil in our porous micromodel. We add a colorant (Brilliant Blue) to the water phase to create a large contrast difference between the two phases. We follow the displacement process at the single pore scale, using high-speed brightfield

microscopy (utilizing a Phantom v9.1 camera at 500 fps, mounted on a Zeiss microscope equipped with a 2.5x magnification objective). We note that while we use syringe pumps to move the fluid, all experiments are actually quasi-pressure driven, as due to the extraordinarily high capillary pressures in our porous micromodel our syringe pump actually runs at the stall pressure. A pressure-driven process mimics displacement as it occurs in larger porous structures, where pressure gradients are common[19].

We measure the effect of viscoelastic behaviour on the displacement efficiency in our porous micromodel by the addition of different concentrations of polyacrylic acid (PAA) to the water phase (1.250.000 MW, Sigma-Aldrich). To avoid differences in wetting behavior between the water phases containing PAA and the experiments not containing PAA we add a very low amount (0.001 wt%) PAA, which we verify does not induce any viscoelastic behaviour to the water phase. We verify the viscoelastic properties of these various concentrations of PAA by rheology (performed on an Anton Paar MCR 301 rheometer).

We compare the amount of displaced oil for all experiments to the maximum possible amount of water in the micromodel. To obtain an accurate determination of this number we perform an experiment in which we render our device completely hydrophilic before we fill it with water. We first flush the device with a polydiallyldimethylammonium chloride (pDADMAC) solution to ensure maximum hydrophilicity. We subsequently fill the micromodel with our colored water solution and ensure that every part of the device is filled. This image is used as the standard to calculate and compare the the amount of displacement for all experiments. All analysis of images and data is done using custom Matlab routines.

7.3 Results and Discussion

Microscopic images of the micromodel can be seen in Fig.7.2, where for clarity the background (PDMS) is colored in light gray. Figure 7.2 shows a series of images with a 0.2 second interval where we can see the water (black) replacing the oil (white). We can see that displacement occurs as an invasion-percolation process[23], where there is no preferred path for the water to take through the

porous micromodel. We can also see that once the water reaches the end of the micromodel, which we define as the moment of breakthrough[3], there is still a significant amount of oil in the micromodel, so called residual-oil-in-place (ROIP) or residual oil saturation[24, 25, 26]. We can see that the first step in the displacement process occurs on the timescale of seconds, but the time needed to displace the ROIP happens on a much slower timescale. In oil recovery a wide variety of processing aids are used to help displace this ROIP, for example surfactants and polymeric thickeners. The usage of any of these processing aids is referred to as Enhanced Oil Recovery (EOR)[27, 28, 29], all in an effort to reduce the time needed to displace the ROIP and increase the efficiency with which it is displaced.

We can quantify this displacement process and these two different timescales by analyzing every frame and counting the amount of dark pixels (i.e. all parts of the micromodel where water is present) and dividing this by the total area of the micromodel, such that the replaced fraction, defined as X_R is 0 when no oil has been displaced and 1 when the entire micromodel is filled with water. We can calculate X_R over the entire time range of our experiment, and see how we go from an almost linear increase on a short timescale, (Fig.7.3a), to a much more erratic displacement of the ROIP at a much longer timescale (Fig.7.3b). During the initial displacement, which we will refer to as stage 1, we see that roughly 65% of the oil gets replaced. Once breakthrough has occurred the ROIP gets displaced much more slowly, we refer to the displacement of ROIP after breakthrough as stage 2. Displacement during stage 2 occurs logarithmically, such that $X_R \sim \log(t)$, and the limit of $X_R \sim 1$ is only reached at $t \sim \infty$.

To understand where the ROIP remains during both stage 1 and stage 2 in this complex geometry we look at how the oil is displaced spatially. From our microscopy data we can analyze when water reaches any part of the micromodel for the first time, for instance when the oil in a pore is initially displaced by water, this would be seen as the first time water reaches that specific part of the micromodel. We record at what time this initial displacement occurs and in this way calculate for every location in the micromodel at what time the first displacement occurs in said location. Based on this time-location data we can color code our entire micromodel to see at what time every location in the micromodel is

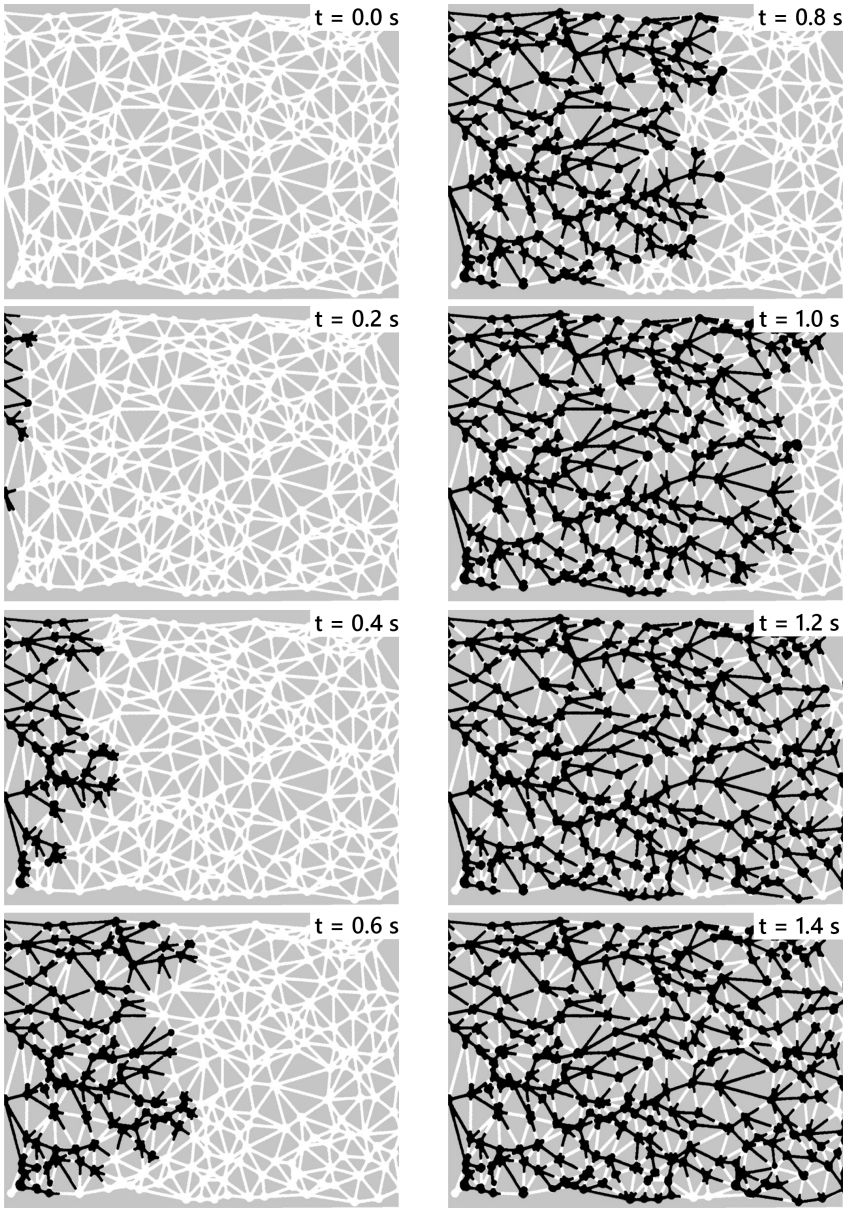

Figure 7.2: experimental time series with $\Delta t = 0.2s$, all images show raw microscopy data where the background PDMS is colored light gray for increased clarity.

displaced by water, and where oil tends to remain.

These color-coded maps of our microchannel give us insight into how the various pores and channels are displaced during invasion percolation, and how the ROIP is displaced during stage 2. We can see that initially the water is indeed displacing oil in a percolation process, often observed for flow in porous media (see Fig. 7.3c). It is also clear that the displacing water does not reach every channel or pore in the micromodel: e.g. in Fig. 7.3c we can see where the ROIP remains after stage 1 (all dark red parts are locations in the micromodel where oil remains). Once water reaches the end of the porous structure for the first time the slow, erratic displacement from stage 2 begins. Once stage 2 starts we see that the oil in channels that was not displaced during stage 1 is displaced in an almost step-like fashion. The ROIP in a single channel gets displaced, after which the flow stabilizes for some time before oil in another channel gets displaced. Due to experimental constraints we only observe the first 1000 seconds of stage 2 and see that in this time frame of 1000 seconds roughly 10% of the total amount of oil is displaced, while approximately 25% remains.

During large scale oil recovery changes in productivity are common[30, 29], and the natural productivity of a well decreases with time. These changes in productivity can be linked to our observations in the micromodel. Our first phase is marked by high productivity and removal of easily accessible oil. After phase 1 a significant fraction of oil still remains, which takes much more time to remove, usually requiring the help of multiple processing aids in an industrial setting[27, 28, 29]. In our experiments the actual timescales are very different from those encountered in the oil industry. We observe displacement in seconds and displacement of ROIP in thousands of seconds, while during large scale oil recovery initial displacement takes months, but a well can remain active for decades. Even though our actual times for displacement differ tremendously, the differences in time scales between the two stages are comparable[31]. By understanding what causes these large differences in displacement efficiency during the two different stages we might be able to improve the oil recovery process.

To investigate the apparent differences between the two displacement stages we first take a closer look at how oil displacement occurs during stage 1 and 2. We see that during stage 1 predominantly the oil in pores, and in channels parallel

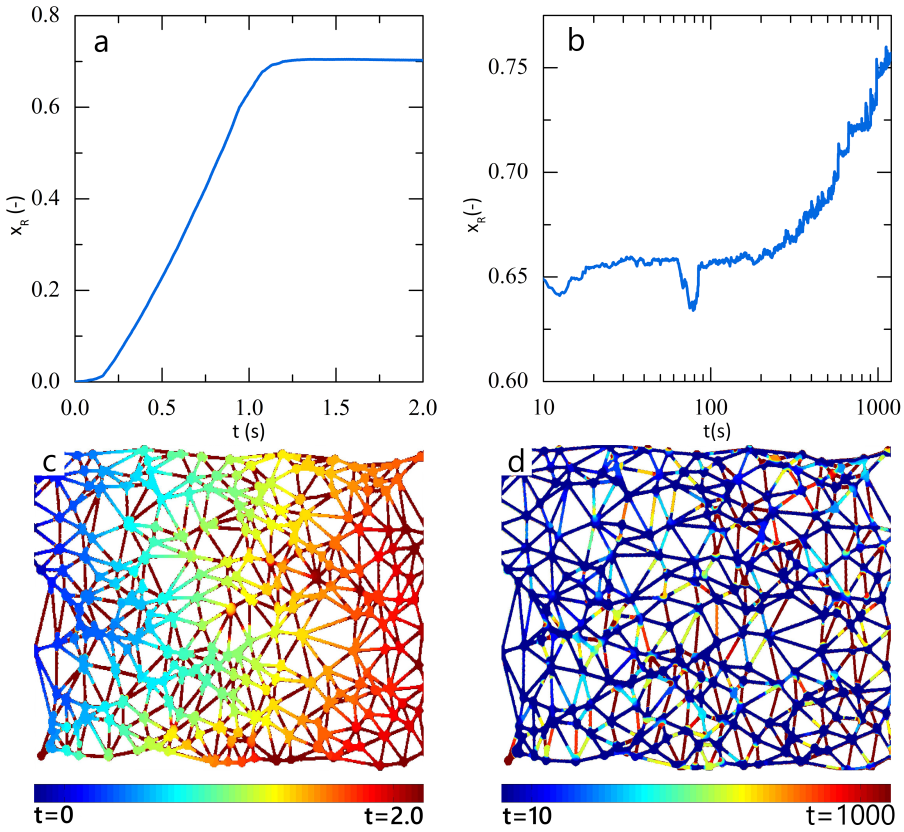

Figure 7.3: Replaced fraction X_R on the short timescale (a) and on the longer timescale (b). Corresponding replacement paths for this short time scale (c) and long time scale (d). Blue indicates replacement early on in the time range, while red indicates late or no replacement of oil with water.

to the inlet-outlet axis, is displaced. After breakthrough, oil in channels that are oriented away from this inlet-outlet axis starts to be displaced. To quantify this we can define an angle, α, for every channel to determine how close to parallel it is in the major flow axis of the microchannel. A channel that is perfectly aligned along the inlet-outlet axis has an angle $\alpha = 0$, while a channel that is completely perpendicular to this major flow axis has an angle $\alpha = 90$.

We can calculate α for every channel in our porous micromodel and combine this information with the displacement maps in Fig.7.3c-d, and correlate the

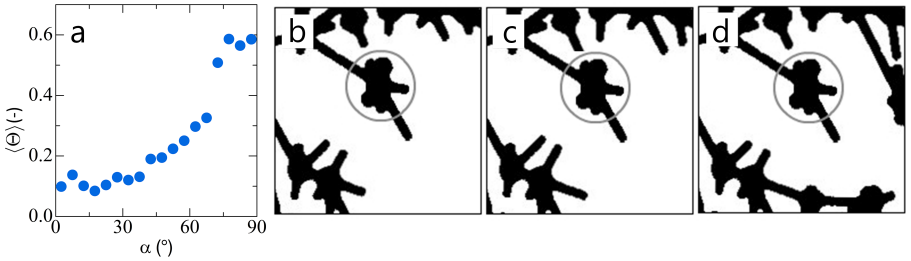

Figure 7.4: (a) Correlation between the angle of a channel α, with $\alpha = 0$ parallel with the flow direction and the normalized time of displacement Θ. All angles are binned together per 5°, with the replacement time the average for that angle group. (b-d) Time sequence of a single pore filling up (gray circle), shows how oil can get trapped in a single channel (red square) by the displacing water phase.

time at which the oil in a channel is displaced with the angle α of that specific channel. We define the normalized time of displacement as Θ, where $\Theta = 0$ corresponds to the earliest displacement, and $\Theta = 1$ to the last observed displacement that occurs, note that this means that $X_R \neq 1$ for $\Theta = 1$, as we do not observe complete oil displacement. We calculate the average displacement time, $\langle\Theta\rangle$ as a function of α, where all values for α are grouped in bins of 5°. We see that oil in channels with $\alpha \leq 45°$ are displaced early on, mostly during stage 1 in the displacement process. For angles with an α larger than 45° we find on average a much later replacement time, as shown in Fig. 7.4a. We note that the average displacement time $\langle\Theta\rangle$ does not go to 1, not even for $\alpha = 90°$, due to the randomness of our micromodel, i.e. while displacing oil in channels with $\alpha \approx 90$ might not be favorable during stage 1, it does happen as these channels might randomly be in the path the water is taking during this percolation phase.

What causes this preference for channels that align more with the flow direction? We start by looking at the pressure drop over our entire micromodel, ΔP, defined as:

$$\Delta P = \frac{Q\eta L}{\kappa A} \tag{7.1}$$

where Q is the volumetric flow rate, κ the permeability of the micromodel, A the total cross-sectional area where fluid can flow, η the viscosity and L the length

of the total connected path the fluid travels. We see that the pressure drop depends on the cross-sectional area and the length of the path that the fluid needs to travel. To minimize ΔP any path the displacing water will take will thus contain as much pores as possible (due to their larger cross-sectional area compared to a channel), and preferably channels that are along the major flow axis, as this will result in the shortest total length that the displacing water needs to travel. A lower value of ΔP in this case indicates that if the displacing water follows such a path it encounters less flow resistance, and thus such a path is more likely to displace early. We see this preference for pores and parallel channels in Fig. 7.3c, where indeed, mostly pores and channels parallel to inlet-outlet axis are displaced during stage 1.

During stage 1 a lot of oil becomes trapped in channels between pores where water is present, forming trapped pockets of oil that are slowly displaced during stage 2. If we look at a close-up of a single pore filling up, we see that the displacing water moves towards a pore from various channels (Fig. 7.4b). Once the water from a single channel reaches the pore the remaining oil is blocked off by the water (Fig. 7.4c), which causes oil to be trapped in the other channels, forming the ROIP (Fig. 7.4d).

These observations give us a starting point to try and improve the displacement efficiency. If we can limit the number of trapped oil pockets, we could reduce the amount of ROIP and thus vastly increase the efficiency of the displacement process. One way to achieve this would be to reduce the variation in times at which water arrives at the pores, such that less oil becomes trapped. We could do this by slowing down the overall time it takes for breakthrough to occur, as that would slow down the water moving through the porous structure. However, simply reducing the water flow rate would not work, to understand why we can look at two dimensionless quantities that play an important role in porous media flows[32]. The capillary number (Ca) which describes the effect of capillary forces due to the creation of interface between two fluids, and the viscosity ratio (M) of the two fluids. These numbers are defined as:[12, 33, 34]

$$Ca = v\frac{\eta_w}{\gamma} \qquad\qquad M = \frac{\eta_w}{\eta_o} \tag{7.2}$$

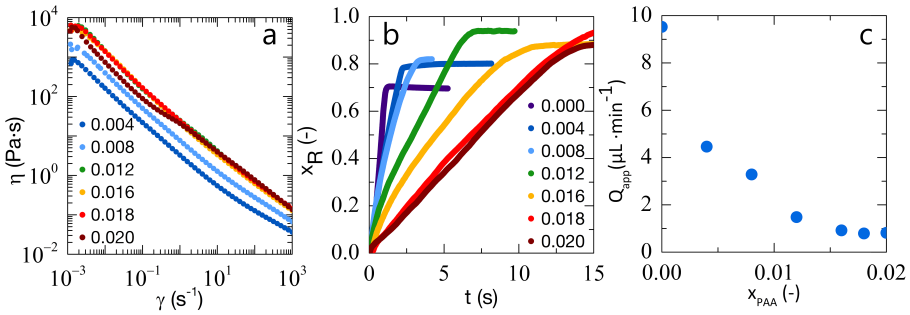

Figure 7.5: (a) effect of shear rate on the viscosity for different fractions of PAA (X_{PAA}, wt% given in legend), (b) replaced fraction X_R as a function of time for different fractions of PAA and (c) apparent filling rate Q_{app} as a function of PAA weight fraction X_{PAA}.

Where v is the flow velocity, η_w is the viscosity of the water phase, γ is the interfacial tension between the fluids and η_o the viscosity of the oil phase. When both Ca and M are sufficiently high a stable displacement will occur[34]. If we would simply decrease the flow rate Ca would decrease, while M stays constant, which would still not result in a stable displacement.

We can increase both Ca and M at the same time by increasing the viscosity of the water phase η_w. We increase the viscosity in our system by adding high molecular weight polyacrylic acid (PAA). PAA offers some additional advantages; it will also decrease γ as PAA can act as an emulsifier to reduce the interfacial tension between the two phases, addition of PAA also leads to shear thinning behavior, which can help displace oil in porous media[6]. We characterize the viscoelastic behavior using rheology, and see that the viscosity increases by multiple orders of magnitude compared to pure water ($\eta \approx 10^{-4}$ Pa s) when PAA is added (Fig.7.5a). We estimate that Ca varies between 10^{-4} and 10^{-2} as we go from pure water to the highest viscosity for the water phase. For pure water we find $M \approx 0.1$, M goes to values > 1 as the viscosity of the water phase increases. We expect a more stable displacement once $M \geq 1$, thus we should observe a transition as we go from pure water to an increased viscosity fluid.

We now use water with various concentrations of PAA (X_{PAA}) to displace oil in our micromodel. We focus on the displacement in stage 1 to see if we can increase the initial displacement of oil prior to breakthrough. We again calculate

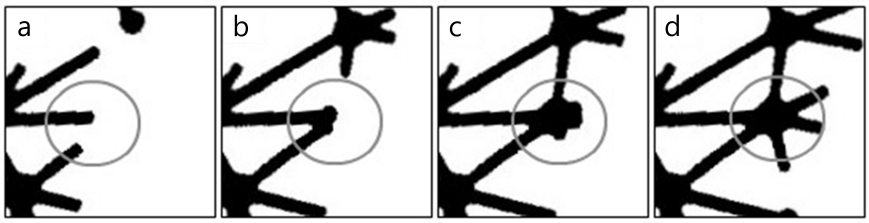

Figure 7.6: Time sequence of oil in a single pore being displaced, $X_{PAA} = 0.02$, the higher viscosity leads to a more even displacement, where every channel leading up to the pore contributes to the displacement process (a-c), leading to no residual oil in the channels (d) and thus a higher displaced fraction X_R.

X_R for every timestep and see a clear increase in both the total amount of oil displaced (i.e. X_R increases) prior to breakthrough albeit at the expense of an increase in time it takes for breakthrough to occur as the viscosity increases, as shown in Fig. 7.5b.

We are able to remove almost 90% of all oil present, therewith vastly reducing the amount of ROIP. We also observe a plateau, implying that increased viscosity will not lead to a complete removal of oil, suggesting that there is an optimum value for the viscosity that balances oil removed with time till breakthrough. The increase in time till breakthrough can be quantified using the slopes of the replacement curves, that are a measure of the apparent flow rate through our porous system, Q_{app}. We see that Q_{app} decreases as X_{PAA} increases. We see that by increasing the viscosity we have increased the time till breakthrough, while making the overall displacement more efficient. All experiments are quasi-pressure driven such that a decrease in the apparent flow rate is expected. However, by only reducing the flow rate we would not expect the same result, as this would actually decrease Ca while keeping M constant. We verify that lower flow rates in the absence of PAA indeed yield similar displacement efficiencies as the data shown for $X_{PAA} = 0$ in Fig.7.5b. This means that the increase in efficiency we observe must be a combination of not only a decrease in flow rate but also an effect of the increased viscosity, and most likely the shear-thinning behavior of PAA and the lowered interfacial tension.

We now take a closer look at what exactly changes once we increase the

viscosity of the displacing phase. We hypothesize that the increased viscosity delays breakthrough, and thus the displacing water reaches the various pores more evenly which leads to less trapped oil. If we look closely at what happens when water reaches a single pore from multiple channels (Fig.7.6a) we see that indeed, as the displacing water reaches the pore (Fig.7.6b-c) no oil is trapped, and every channel contributes to the displacement and ensures a complete displacement (Fig.7.6d). In general, it seems that the increased viscosity helps to slow down the overall flow (as indicated in Fig.7.5c) and contributes to a much higher displaced fraction X_R by causing a more even displacement over the entire porous network. A slower phase 1 will thus result in much less ROIP, which results in an overall more efficient process, as displacement of oil during stage 2 is a much slower affair, even compared to the longer time till breakthrough due to the increased viscosity.

Finally, we investigate what locations in our micromodel are now displaced during stage 1, compared to the displacement in stage 1 for pure water. Again we can generate a displacement map (similar to Fig.7.3c-d), but now we look at what concentration of PAA, X_{PAA}, leads to displacement of oil in a certain location. We compare each displacement experiment to the experiment with $X_{PAA} = 0$ and see in which additional locations oil is displaced as X_{PAA} goes up. We account for the randomness in our displacement process and micromodel by using the average value, $\langle X_{PAA} \rangle$ at which we expect, on average, oil in a certain channel to displace. We then generate a displacement map where we color code every location based on the average concentration of PAA, $\langle X_{PAA} \rangle$ required to displace oil in that location during stage 1.

When $\langle X_{PAA} \rangle \approx 0$ we see that oil most pores and the channels mostly aligned in the major flow axis are displaced (Fig.7.7a, dark blue areas), similar to the case where $X_{PAA} = 0$ (Fig.7.3d). Once we increase the concentration of PAA we see that oil in channels not parallel with the major flow axis is displaced as well (light blue to green areas in Fig.7.7a). Finally, at a high enough value for $\langle X_{PAA} \rangle$ we see the channels and pores that remain filled with oil at low concentrations are now displaced as well (red areas in Fig.7.7a). To check whether there is a relation between $\langle X_{PAA} \rangle$ and the angle of the channels, α, we can calculate the angle that corresponds to each channel where additional oil is displaced (in similar fashion

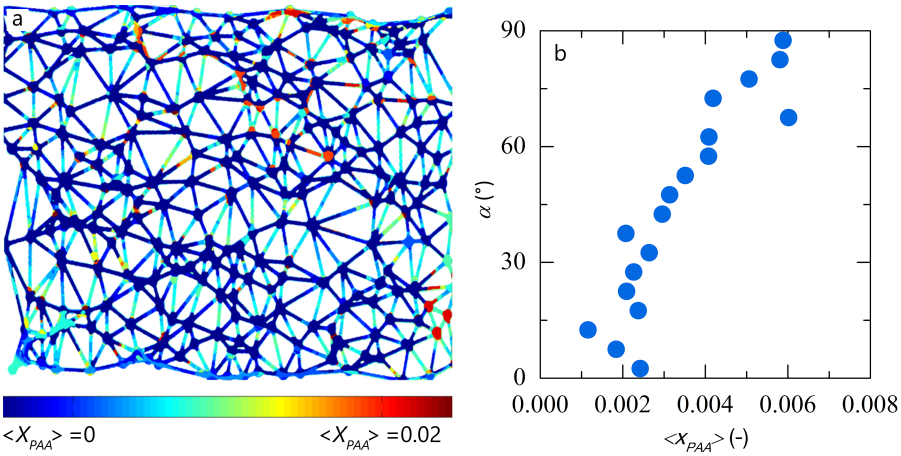

Figure 7.7: (a) Average fraction of PAA ($\langle X_{PAA} \rangle$) at which a pore or channel fills in the fast displacement regime, (b) correlation between the angle of a channel α with the flow direction and $\langle X_{PAA} \rangle$ at which that channel fills up during the fast displacement regime.

to Fig.7.4a). We use the displacement at $X_{PAA} = 0$ as a baseline, and look where any additional oil is displaced, and correlate any additional oil displacement to that channels value of α.

We see that as $\langle X_{PAA} \rangle$ increases the number of channels with a higher value of α where additional oil is displaced increases as well. This shows that a higher viscosity helps to displace oil in those channels that are less aligned with the inlet-outlet axis (see Fig.7.7b). This confirms that the additional oil displacement mainly comes from the areas of the porous microstructure that would normally be displaced during stage 2 (Fig.7.3b and d), thus vastly reducing the amount of ROIP.

Conclusion

In this Chapter we show a microfluidic approach to study a random microporous structure in which a wetting phase (oil) is displaced by a non-wetting phase (water). This yields interesting insights about the relation between the structure of the porous system and fluid behavior. We show that two stages exist on two very

different timescales for the displacement process. Until breakthrough occurs, the amount of oil displaced per unit time is practically linear. After breakthrough, the residual oil in place (ROIP) is displaced erratically as oil in separate channels is quickly displaced, followed by stabilization of the flow. This process repeats as more and more oil in various channels is displaced.

By tuning the viscoelastic properties of the displacing fluid we can change this behavior dramatically and ensure an almost complete displacement of oil during the short regime, with only a low fraction of ROIP. We attribute this effect to the slowing down of the linear regime till breakthrough, leading to less trapped oil in various side channels by the displacing water. These results give us new insights into the complex problem of two-phase flows in porous media and could help to improve efficiency in a wide range of processes, for instance more efficient oil recovery. These micromodels could also prove a valuable tool to investigate the effects of small contaminants in the displacing phase, which could lead to severe clogging of the entire porous structure.

References

[1] de Jong, J., Lammertink, R. G. H. & Wessling, M. Membranes and microfluidics: a review. *Lab Chip* **6**, 1125–1139 (2006).

[2] Ingham, D. B. & Pop, I. *Transport phenomena in porous media* (Elsevier, 1998).

[3] Wu, M. *et al.* Single- and two-phase flow in microfluidic porous media analogs based on Voronoi tessellation. *Lab Chip* **12**, 253–261 (2012).

[4] Perkins, T. K. & Johnston, O. C. A Review of Diffusion and Dispersion in Porous Media. *Society of Petroleum Engineers Journal* **3** (1963).

[5] Poulin, N., Tanguy, P., Aspler, J. & Larrondo, L. Numerical and physical modeling of the permeability of paper to cmc and coating liquids. *The Canadian Journal of Chemical Engineering* **75**, 949–955 (1997).

[6] Taylor, K. C. & Nasr-El-Din, H. A. Water-soluble hydrophobically associating polymers for improved oil recovery: A literature review. *Journal of Petroleum Science and Engineering* **19**, 265–280 (1998).

[7] Oh, S. G., Slattery, J. C. *et al.* Interfacial tension required for significant displacement of residual oil. *Society of Petroleum Engineers Journal* **19**, 83–96 (1979).

[8] Sohrabi, M., Danesh, A. & Jamiolahmady, M. Visualisation of residual oil recovery by near-miscible gas and swag injection using high-pressure micromodels. *Transport in Porous Media* **74**, 239–257 (2008).

[9] Joekar-Niasar, V., Hassanizadeh, S. M. & Leijnse, A. Insights into the Relationships

Among Capillary Pressure, Saturation, Interfacial Area and Relative Permeability Using Pore-Network Modeling. *Transport in Porous Media* **74**, 201–219 (2008).

[10] Joekar-Niasar, V., Hassanizadeh, S. M. & Dahle, H. K. Non-equilibrium effects in capillarity and interfacial area in two-phase flow: dynamic pore-network modelling. *Journal of Fluid Mechanics* **655**, 38–71 (2010).

[11] Keurentjes, J., Cohen-Stuart, M, Brinkman, D., Schroën, K. & Van't Riet, K. Surfactant-induced wetting transitions: role of surface hydrophobicity and effect on oil permeability of ultrafiltration membranes. *Colloids and surfaces* **51**, 189–205 (1990).

[12] Cottin, C., Bodiguel, H. & Colin, A. Drainage in two-dimensional porous media: From capillary fingering to viscous flow. *Phys. Rev. E* **82**, 46315 (2010).

[13] Stokes, J. P. *et al.* Interfacial stability of immiscible displacement in a porous medium. *Phys. Rev. Lett.* **57**, 1718–1721 (1986).

[14] Clotet, X., Ortín, J. & Santucci, S. Experimental study of stable imbibition displacements in a model open fracture. i. local avalanche dynamics. *Phys. Rev. E* **93**, 012149 (2016).

[15] Theodoropoulou, M., Sygouni, V., Karoutsos, V. & Tsakiroglou, C. Relative permeability and capillary pressure functions of porous media as related to the displacement growth pattern. *International journal of multiphase flow* **31**, 1155–1180 (2005).

[16] Berejnov, V., Djilali, N. & Sinton, D. Lab-on-chip methodologies for the study of transport in porous media: energy applications. *Lab Chip* **8**, 689–693 (2008).

[17] Lifton, V. A. Microfluidics: an enabling screening technology for enhanced oil recovery (eor). *Lab on a Chip* **16**, 1777–1796 (2016).

[18] Holtzman, R. Effects of pore-scale disorder on fluid displacement in partially-wettable porous media. *Scientific reports* **6**, 36221 (2016).

[19] Xu, W., Ok, J. T., Xiao, F., Neeves, K. B. & Yin, X. Effect of pore geometry and interfacial tension on water-oil displacement efficiency in oil-wet microfluidic porous media analogs. *Physics of Fluids* **26**, 093102 (2014).

[20] Delaunay, B. Sur la sphere vide. *Izv. Akad. Nauk SSSR, Otdelenie Matematicheskii i Estestvennyka Nauk* **7**, 1–2 (1934).

[21] Xia, Y. & Whitesides, G. M. Soft Lithography. *Angewandte Chemie International Edition* **37**, 550–575 (1998).

[22] Zhou, J., Ellis, A. V. & Voelcker, N. H. Recent developments in PDMS surface modification for microfluidic devices. *ELECTROPHORESIS* **31**, 2–16 (2010).

[23] Wilkinson, D. & Willemsen, J. F. Invasion percolation: a new form of percolation theory. *Journal of Physics A: Mathematical and General* **16**, 3365 (1983).

[24] Orr Jr, F. M., Dindoruk, B. & Johns, R. T. Theory of multicomponent gas/oil displacements. *Industrial & engineering chemistry research* **34**, 2661–2669 (1995).

[25] Dias, M. M. & Payatakes, A. C. Network models for two-phase flow in porous media part 1. immiscible microdisplacement of non-wetting fluids. *Journal of Fluid Mechanics* **164**, 305–336 (1986).

[26] Hunt, J. R., Sitar, N. & Udell, K. S. Nonaqueous phase liquid transport and cleanup: 1. analysis of mechanisms. *Water Resources Research* **24**, 1247–1258 (1988).

[27] Taylor, K. C. & Nasr-El-Din, H. A. Water-soluble hydrophobically associating polymers for improved oil recovery: A literature review. *Journal of Petroleum Science and Engineering* **19**, 265–280 (1998).

[28] Shah, D. O. *Improved oil recovery by surfactant and polymer flooding* (Elsevier, 2012).

[29] Lake, L. W. *Enhanced oil recovery* (Prentice Hall Englewood Cliffs, NJ, 1989).

[30] Barsky, R. B. & Kilian, L. Oil and the macroeconomy since the 1970s. *The Journal of Economic Perspectives* **18**, 115–134 (2004).

[31] Al-Hadhrami, H. S., Blunt, M. J. *et al.* Thermally induced wettability alteration to improve oil recovery in fractured reservoirs. In *SPE/DOE Improved Oil Recovery Symposium* (Society of Petroleum Engineers, 2000).

[32] Lenormand, R. Flow through porous media: Limits of fractal patterns. *Proceedings of the Royal Society of London A: Mathematical, Physical and Engineering Sciences* **423**, 159–168 (1989).

[33] Ferer, M., Bromhal, G. S. & Smith, D. H. Two-phase flow in porous media: Crossover from capillary fingering to compact invasion for drainage. *Phys. Rev. E* **71**, 26303 (2005).

[34] Joekar-Niasar, V. & Hassanizadeh, S. M. Analysis of Fundamentals of Two-Phase Flow in Porous Media Using Dynamic Pore-Network Models: A Review. *Critical Reviews in Environmental Science and Technology* **42**, 1895–1976 (2012).

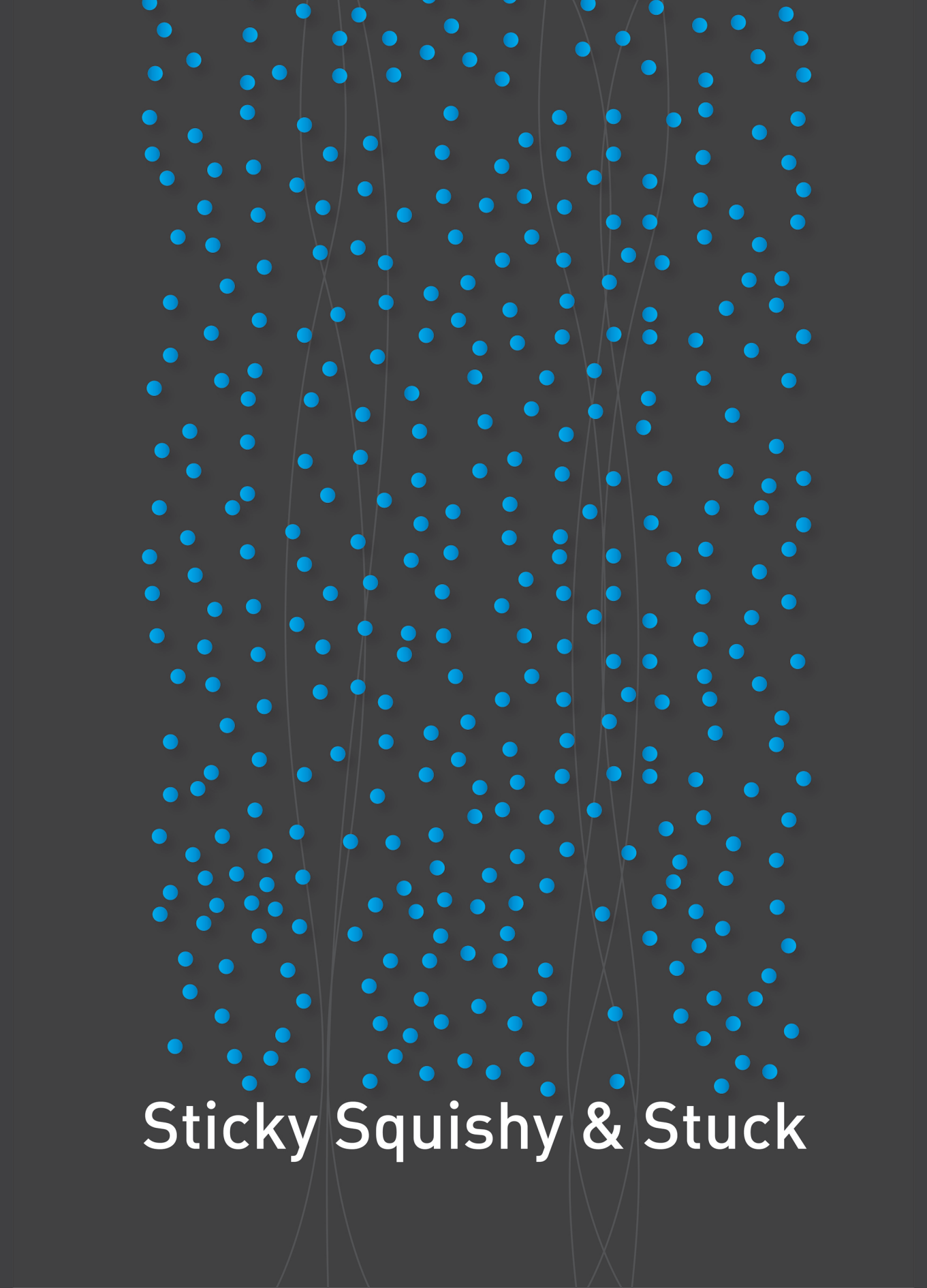
Sticky Squishy & Stuck

Chapter 8

Light from Within; Sensing Weak Strains and femtoNewton Forces in Single Molecules

Weak mechanical forces acting on individual molecules are in control of a wide variety of (bio)chemical and physical processes. The spatially inhomogeneous nature of these forces has a profound effect on the structure and mechanics of soft and biological materials. Yet, the lack of methods to probe sub-picoNewton forces at high resolution leaves our understanding of these effects incomplete. Here, we solve this challenge by demonstrating macromolecular strain sensors that are capable, after suitable conversion of the strain-optical signal, of reporting forces as low as 300 femtoNewtons in grayscale and at the scale of single molecules. Our approach breaks existing molecular force detection thresholds by a factor of 100. This approach opens the way to illuminate very weak and inhomogeneous forces in materials from within.

This chapter was published as:

T. van de Laar, H. Schuurman, P. van der Scheer, J.M. van Doorn, J. van der Gucht and J. Sprakel: *Light from Within; Sensing Weak Strains and femtoNewton Forces in Single Molecules*, Chem *4* (**2018**), 269-284.

8.1 Introduction

Mechanochromic molecules, which produce an optical signal in response to a mechanical stress, hold the promise to act as molecular mechanosensors for the non-invasive visualization of molecular mechanics deep within complex materials. This would ultimately enable a deep insight into the mechanisms by which mechanical cues at the molecular scale, e.g., govern biological mechanotransduction[1, 2], control structure formation in supramolecular self-assembly[3, 4, 5] and dictate how solids deform and ultimately fail[6, 7]. Many of the existing molecular mechanosensors are based on small molecules with a binary on/off response, which is triggered by a change in chemical structure that is often irreversible[8, 9, 10]. The threshold forces required to provoke a significant change in optical signal are relatively large, in the range of hundreds of pNs to nNs [11, 12, 13]. Such mechanosensors have been successfully used to probe the large forces emerging during the failure of tough solids [10, 8, 14]. However, the governing forces in soft and biological materials, such as hydrogels, supramolecular nanostructures or cells and tissues, are orders-of-magnitude weaker, which means that other approaches are required. Advances to lower the force threshold and compatibilize molecular sensors with soft and biological matter have been made by the development of biomolecular force sensors[15, 16]. For example, dye-labelled DNA duplexes that de-hybridize beyond a critical tensile force can give rise to a binary response corresponding to the two states [17], with force thresholds in the tens of picoNewtons. In most soft materials and biological systems, the spatial inhomogeneity of weak forces down to the molecular scale is crucial in governing the complex behaviour that is observed at larger scales. Thus, ideally, molecular sensors should be operational and detectable at the scale of single molecules. Despite immense progress in mechanochemistry[14, 18], no approaches exist to date to probe forces at the scale of single molecules in the picoNewton range and below that produce not merely a binary signal but that can be read-out in grayscale, to enable a quantitative mapping of force inhomogeneities at the smallest scale.

In this Chapter, we demonstrate grayscale strain sensing in single mechanochromic conjugated polymers, which, after conversion of the strain-optical signal, gives rise to a force detection threshold of $\sim$ 300 fN. We use single-molecule

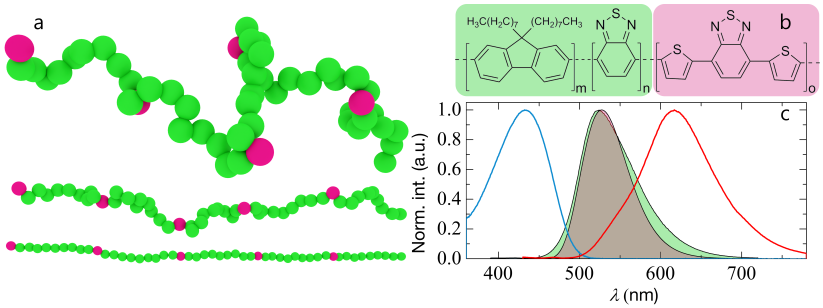

Figure 8.1: Schematic image of an acceptor-doped donor chain at different degrees of chain extension. b) Structure of the donor polymer poly(dioctylfluorene-alt-benzothiaziazole) (green), randomly doped with the acceptor DTBT (pink). Here, we use the same compound in polymeric (FS1) and oligomeric (FS2) form, with FS1: $M_w = 30.3$ kg/mol, PDI = 1.82, with on average $\langle m \rangle \approx 55$, $\langle n \rangle \approx 47$ and $\langle o \rangle \approx 8$ and FS2: $M_w = 1.9$ kg/mol, PDI = 1.12, with $\langle m \rangle \approx 4$, $\langle n \rangle \approx 3$ and $\langle o \rangle \approx 1$, c) absorption (blue line) and emission (filled green) spectra of the isolated donor F8BT and absorption (filled pink) and emission (red line) of the acceptor DTBT, showing the overlap between donor emission and acceptor absorption (shaded grey) where energy transfer occurs.

hyperspectral imaging to quantify the mechano-optical response of doped conjugated polymers within mechanically strained polymer solids down to the molecular scale, breaking the detection thresholds of existing mechanosensors by a hundredfold [11, 12, 13, 15, 16, 17]. Moreover, we combine our experiments with computer simulations to establish the design rules for single-polymer force sensors and to interpret our experimental data in terms of the strain-dependent segment density radial to the backbone. This results in a quantitative agreement between model and experiments without any adjustable parameters. Finally, we demonstrate how information on the distribution width in the energy transfer function in a population of single chains can be used to quantify the degree of mechanical inhomogeneity within a polymer solid. Our results establish the principle of single-molecule grayscale strain sensing at the sub-picoNewton scale and open the way to the non-invasive and high-resolution mapping of inhomogeneous strains deep within soft and biological matter.

8.2 Results

Designing a single-molecule grayscale mechanosensor

A molecular mechanosensor exhibits two features: i) a force-responsive element in the molecular design, capable of stress-induced conformational changes and ii) an optical read-out to probe the molecule's conformational state. Mechanosensors in which mechanical stress induces a binary conformational change will exhibit an on/off optical response. To achieve a grayscale mechano-optical response a continuous conformational change with increasing applied load is required; this is easily achieved using linear macromolecules that act as entropic springs. Polymer chains resist mechanical extension as a result of the associated reduction in their conformational entropy[6]. Thus, polymers are entropic springs whose conformation evolves continuously with the applied force (Fig.8.1a), from a coiled configuration at zero force to a linear string of monomers at larger forces.

Stretching a chain from a coiled to an elongated conformation leads to a reduction in the local monomer density radial to the backbone [19, 20]. In principle, chemically attaching donor-acceptor pairs for Förster resonant energy transfer (FRET) to an optically inert polymer chain, could convert this change in segmental density to a grayscale optical signal. This energy transfer mechanism operates through the transfer of excited state energy from a donor to an acceptor chromophore by means of a dipole-dipole coupling, which decays with the sixth power of distance between the acceptor and donor. However, small molecule fluorophores, which can be covalently tethered to a polymer backbone, suffer from sensitivity to photobleaching. This places limits on the time during which a single molecule can be observed, and thus on the accuracy with which optical signals can be detected.

We resolve this by using conjugated polymers, in which the semiconducting backbone acts as a string of donors, along which we place a small number of acceptor molecules as dopants, randomly positioned along the chain (Fig.8.1a). This approach offers two benefits: i) the entire chain is auto-fluorescent so that the total emission output of a single chain is large and ii) conjugated polymers are relatively photostable[21], enabling extended acquisition times. The combin-

ation of these effects accomplishes a high signal-to-noise ratio in single-molecule experiments[21]. While a coupling between chain conformation and optical response also exists in conjugated homopolymers[22, 23, 5], amplification of the mechano-optical response by means of acceptor doping enables a more accurate and quantitative read-out.

We use poly(fluorene-alt-benzothiadiazole) (F8BT) as the donor backbone, doped with dithienyl-benzothiadiazole (DTBT) monomers as acceptors, which have been copolymerized in the chain (see Fig.8.1b and *Appendix*). This design features a relatively low stiffness as compared to other semiconducting polymers, with Kuhn lengths of order 6-8 nm [10, 25, 26], making it suitable for use as an entropic spring. Absorption and emission spectra of the pure donor and acceptor chains illustrate their suitability as an energy transfer pair due to the overlap between donor emission and acceptor absorption (Fig.8.1c), with a Förster radius of $r_F = 4.9$ nm (see *Appendix*). While the donor chain F8BT is composed of an alternating backbone of two monomers, excitation of the fluorene subunits at λ_{ex} =405 nm leads to pure green emission from the benzothiadiazole chromophores. Copolymerization of donor and acceptor monomers within a single chain and subsequent Soxhlet fractionation leads to polymers (FS1, $M_w = 30.3$ kg/mol) that act as single-molecule strain sensors, as we will show below. In addition to energy transfer within the polymeric coil through the medium, excitonic energy transfer between donor and acceptor chromophores along the conjugated backbone also occurs [11]. This leads to a baseline of acceptor emission upon donor excitation, even when the chains are fully extended. As we probe relative changes in the overall energy transfer ratio, this does not affect our results.

Simulating molecular strain sensors

To explore how the mechano-optical response of these strain sensors depends on their chemical design, we perform highly coarse-grained Monte Carlo simulations of single chains (see Methods and *Appendix*). We note that in reality, quantum mechanical effects resulting from chain stretching, the alignment of transition dipoles of monomers within the chain and a modest increase in effective conjugation length may all play a role in governing the optical response of

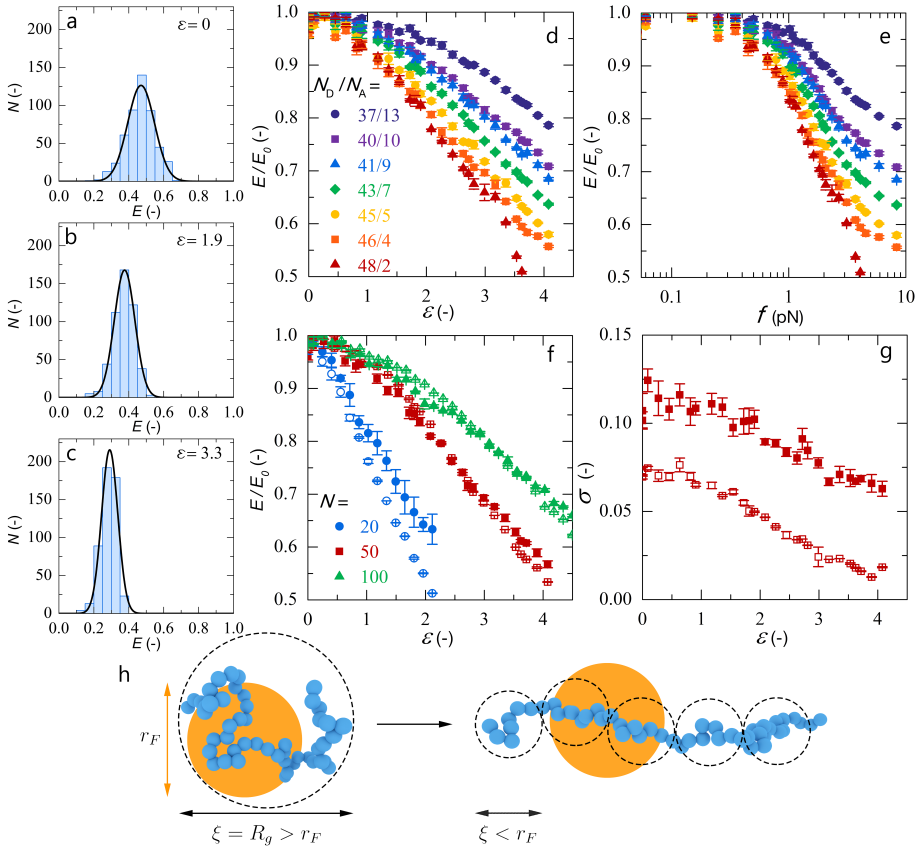

Figure 8.2: a-c) Histograms of energy transfer efficiency E for chains with $N_A = 5$ and $N_D = 45$, for 500 simulated chains per histogram, at different strains ϵ; solid lines are fits to a Gaussian distribution. d) Strain-sensing curve for randomly-doped chains with $N = 50$ at different degrees of acceptor-doping, as indicated. e) Converted force-optical response curve of E/E_0 as a function of the stretching force (legend as in d). f) Strain-optical response as a function of chain length N, for randomly doped chains (filled symbols) and sequence-controlled chains (open symbols) with a doping fraction of 0.1. g) Width σ of the energy transfer histogram for $N = 50$, for random (filled symbols) and sequence-controlled chains (open symbols). Error bars indicate the 95% confidence interval. h) Illustration of the blob-picture for chain stretching, modelling the chain as a string of blobs (dotted circles), where the energy transfer volume is indicated in orange.

our conjugated polymers to stretching; in our model, we only consider through-space energy transfer, and as we will show below, this provides a good quantitative, parameter-free, agreement with our data. Thus, while additional mechanisms cannot be ruled out, the energy transfer through the dielectric medium appears to be the dominating effect. A fully quantitative analysis of these strain sensors would require atomic-level resolution molecular dynamics simulations coupled to quantum mechanical orbital calculations, which is computationally expensive and thus prohibits the screening of a large parameter space, required to establish the chemical design rules. As this is our purpose here, we use a highly coarse-grained approach.

In short, the chains are modelled using the Kremer-Grest model [9], coarse-grained to the level of freely-jointed Kuhn segments with excluded volume and extended to different end-to-end distances L. The validity of the use of a freely-jointed chain (FJC) model to describe conjugated polymers based on polyfluorene was established in previous experiments, where the FJC model was shown to accurately capture the chain conformations[29]. We define an extensional strain as $\epsilon = L - < L_0 > / < L_0 >$, with $< L_0 >$ the root-mean-square end-to-end distance in the absence of a force. Intrachain energy transfer is described by a modified Förster equation which computes the chain-average energy transfer efficiency between all donor-acceptor pairs. We construct histograms of the energy transfer ratio E as a function of the strain ϵ imposed on the chain. We observe how the mean value of E shifts to lower values as ϵ increases (Fig.8.2a-c). This mechano-optical coupling is a direct manifestation of the reduction in monomer density in a volume around each donor group as the chain transforms from a coiled to an extended conformation. We fit the histograms to a Gaussian function (solid line in Fig.8.2a-c) to extract the mean, normalized to that at zero strain $\epsilon = 0$, to find the mechano-optical response curve $\frac{E}{E_0}(\epsilon)$.

Donor chains randomly doped with acceptors show the proposed grayscale force sensing, with an optical signal that decays gradually as the strain on the single chains is increased (Fig.8.2d). The sensitivity of the coupling depends on the extent of acceptor doping. For chains with few acceptors, the optical signal decays much more steeply than for chains highly doped with acceptors (Fig.8.2d). This allows tailoring of the sensitivity with which strains can be probed at the

single-molecule level. Using the freely-jointed chain model, previously shown to accurately capture the chain conformations of these polymers[29], and reported values for the stiffness of our experimental design[10, 25, 26], we convert ϵ to a force scale (Fig.8.2e). This calculation highlights the theoretical possibility of using acceptor-doped donor polymers to detect forces in the (sub-)pN range.

The energy transfer efficiency E is a direct probe for the local segmental density, which can be seen from an intuitive argument. Our chain consists of N segments, made of N_D donors and N_A acceptors. To first order we can separate the donor segments into a population which is within a Förster radius distance to an acceptor $n_{D>A}$ and thus transfer all of their energy to the acceptor and a population out of reach of acceptors n_D, such that $N_D = n_D + n_{D>A}$. To first order, the population n_D transfer none of their energy to acceptors and thus contribute $E = 0$ to the chain-mean and the segments $n_{D>A}$ transfer all of their energy and thus contribute $E = 1$ to the chain mean. The chain-averaged energy transfer efficiency, which is the quantity we measure, can thus be expressed as: $E \approx \frac{n_{D>A} \cdot N_A}{N_D} \cdot 1 + \frac{n_D \cdot N_A}{N_D} \cdot 0 = \frac{n_{D>A} \cdot N_A}{N_D}$. We can define a local segment density from the number of monomers with a volume with dimensions of the Förster radius r_F as $\rho = \frac{n_{D>A}}{r_F^3} = \frac{E \cdot N_D}{N_A \cdot r_F^3}$. Thus, the energy transfer efficiency we measure is a direct proxy for the local segmental density at a length scale r_F within the polymer chain.

The width σ of the energy transfer histograms is a manifestation of population heterogeneity, caused by three contributions. I) The conformational entropy of the chain gives rise, for a given strain, to a large number of possible conformations, which vary in their local segmental density. II) Random placement of acceptors leads to chemical heterogeneity that contributes to σ. III) Polydispersity could contribute to heterogeneity if the mechano-optical response depends on chain length N. To evaluate these effects, we compare chains with random and sequence-controlled placement of the acceptors as a function of overall chain length N. Indeed, we find a change in the strain-response curve with changes in chain length (Fig.8.2f), giving further handles to tailor the range and sensitivity of the mechano-optical coupling but also highlighting the adverse effect of polydispersity on the distribution width. While very long chains will have a relatively high force threshold to provoke a measurable optical response, too short

chains will no longer exhibit significant conformational degrees of freedom thus suppressing the mechanosensing effect.

Interestingly, random acceptor placement and sequence-controlled acceptor placement, at equidistant sites along the backbone, have the same effect on the mean energy transfer efficiency (Fig.8.2f). By contrast, the width σ decreases by a factor of 2 when sequence-controlled chains are used (Fig.8.2g). For chains with a sequence-controlled backbone at a given chain length, only the entropic contribution to population heterogeneity remains; in this case, the width directly reflects the conformational entropy S_c for the polymer. Indeed, we observe how the width decreases as the chains are stretched further (Fig.8.2g) evidencing the reduction in chain conformational entropy [6].

Experimental realisation of single-molecule grayscale strain detection

These simulation results suggest that very weak mechanical forces can be probed in single macromolecules. To establish this concept experimentally, we use sensor polymer FS1 (Fig.8.1b) that is fractionated using solvent-gradient Soxhlet extraction to reduce the polydispersity and obtain a high-molecular weight sensor. We optically probe individual chains using single-molecule emission spectroscopy. Single conjugated polymers are excited with a circularly polarised $\lambda_{ex} = 405$ nm laser and detected on a hyperspectral camera, consisting of an Andor Zyla sCMOS chip equipped with a tunable liquid crystal bandpass filter, as illustrated in Figure 8.3a. We record image hypercubes, each of which contains several diffraction-limited images of single conjugated molecules (Fig.8.3b). To probe the mechanical perturbation of single polymer chains within a solid material, we embed our sensor polymer in a cast polystyrene (PS) film at 0.83 ppm, which we subsequently strain in extension at a predefined extensional strain by placing the solid PS films in a home-built tensile stretcher. The entire device is heated to just above the glass transition temperature, $T_g = 105^\circ$ C, of PS to result in a stretchable film susceptible to extension at low stresses. Upon achieving the desired extensional strain, we rapidly cool the sample to below the matrix T_g to fix the strained chain conformations of the molecular sensors; since the experiments are conducted well below the glass transition point, $T_g - T = 80^\circ$ C, the sensor chains are expected to be completely frozen and represent a single

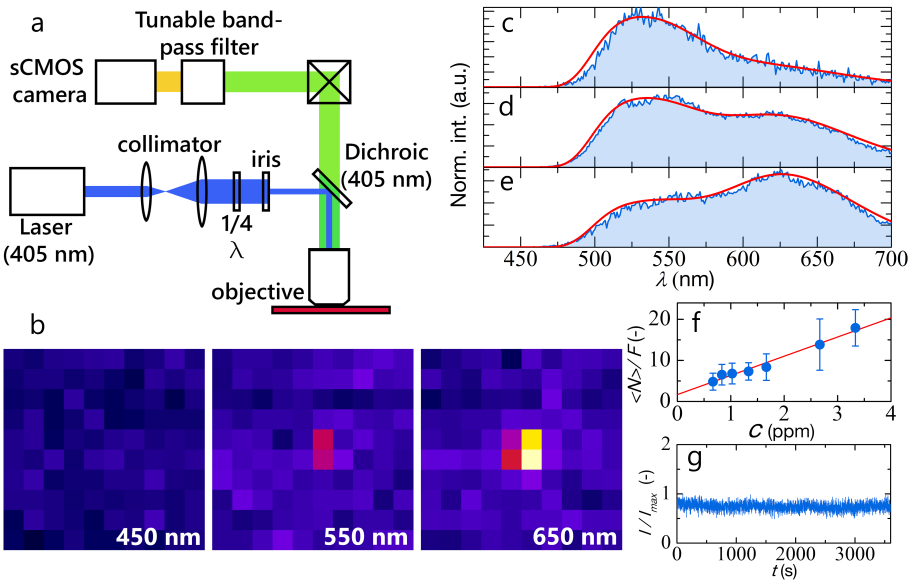

Figure 8.3: a) Experimental set-up for hyperspectral single-molecule imaging, with widefield illumination of a circularly polarised 405 nm (18 mW) laser beam and hyperspectral detection using a sCMOS camera connected to an electrically-tunable liquid crystal bandpass filter. b) Diffraction-limited image of a single mechanosensor molecule at different spectral slices as indicated. c-e) Example single-molecule fluorescence spectra (blue) showing the emission of individual chains exhibiting different degrees of energy transfer; red solid line is a fitted deconvolution to extract the energy transfer efficiency E. f) number of diffraction limited single-molecule images per frame as a function of polymer concentration c in the PS matrix. g) photoluminescence intensity time trace for a single conjugated polymer, indicating the absence of blinking or bleaching even during prolonged excitation.

static conformation. Thus, to achieve statistical insight, ensemble averaging is performed after the single-molecule measurements. For the experimental data, $\epsilon = h - h_0/h_0$ denotes the macroscopic strain imposed on the film, with h_0 and h the film dimension along the extension axis prior to and after stretching, respectively.

To confirm that we probe only single polymer chains, we first determine the linearity of the number of fluorescent objects per image as a function of dilution, as proposed previously[30]. We indeed find a linear relation up to concentrations of 3.5 ppm of molecular sensor with respect to the PS matrix (Fig.8.3f), indicating that aggregation or segregation of the sensor polymers within the transparent matrix is absent in this regime. We prepare our samples well within the linear regime at $c = 0.83$ ppm. Furthermore, for all of the diffraction-limited spots we analyse to extract single-molecule fluorescence spectra, we confirm that their absolute intensities are approximately equal.

The macromolecular strain sensors are remarkably photostable during prolonged illumination, without the necessity to remove oxygen from the sample or surroundings, add anti-fading agents or to work at low temperatures. We find that, even after > 3000 s of continuous excitation at 405 nm, we find no signs of photobleaching or blinking (Fig.8.3g). Thus, within the 60-100s interval required to record a single-molecule hyperspectral image cube, photo-oxidative processes can be ruled out.

Fluorescence spectra of single chains (Fig.8.3c-e) show distinct donor ($\lambda = 525$ nm) and acceptor ($\lambda = 625$ nm) peaks whose intensity ratio changes upon stretching. To determine the energy transfer ratio, we first deconvolve the experimental spectra using a Monte Carlo least-squares fitting algorithm (solid lines Fig.8.3c-e) and determine E as the ratio of acceptor emission to the total emitted intensity. Interestingly, the experimental histograms of E confirm the mechano-optical coupling proposed above, with the mean energy transfer ratio decreasing with tensile strain (Fig.8.4a-b).

Plotting the relative energy transfer efficiency E/E_0 from our experimental data as a function of strain for FS1 evidences their capability of reporting strains in grayscale at the molecular scale (Fig.8.4c). We observe an apparent plateau at low strains, as found also for the simulations, and discussed below. At strains of

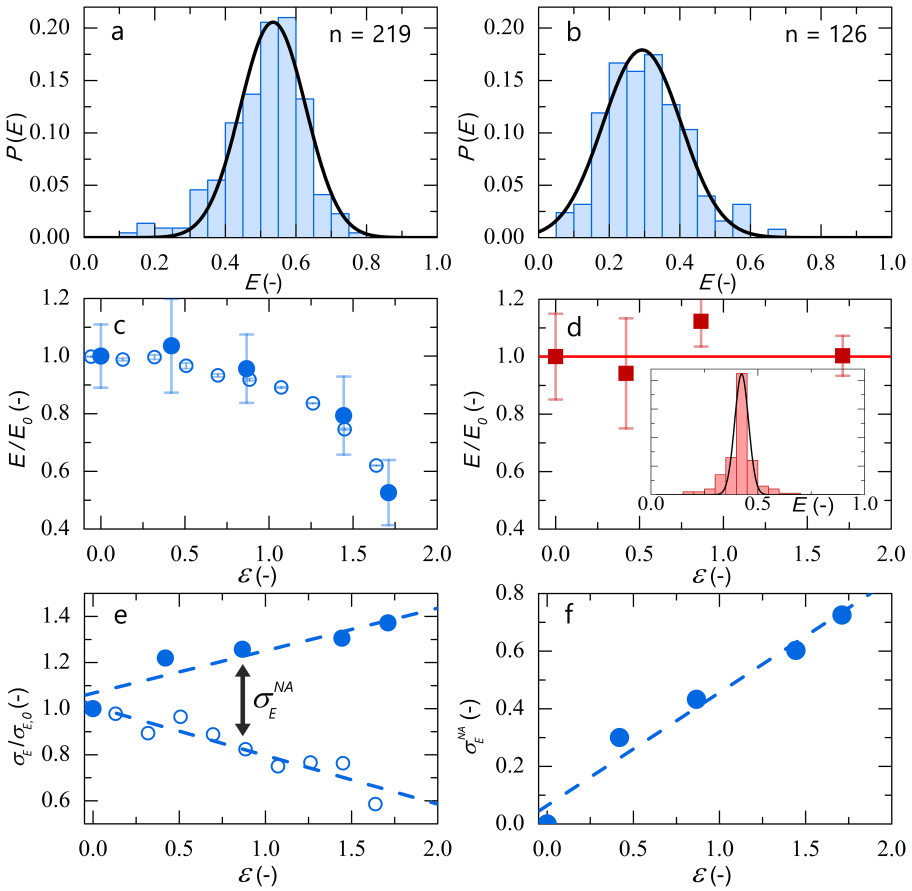

Figure 8.4: a-b) Histograms of energy transfer E from single-molecule experiments on n chains for FS1 in the unstrained ($\epsilon = 0$, a) and strained ($\epsilon = 1.71$, b) states. Solid lines are fits to a Gaussian distribution. c-d) Experimental strain-optical response curve for FS1 (closed circles,c) and FS2 (squares,d) and a comparison with simulations without adjustable parameters (open circles, c), inset in d) shows an energy transfer histogram for FS2 ($n = 169, \epsilon = 1.71$). Error bars indicate the standard deviation of the measured E over n samples. (e) Width of the distribution of donor-acceptor distances σ_E (see main text), normalized to the zero-strain case $\sigma_{E,0}$, for experimental data (FS1, closed symbols) and corresponding simulations (open symbols). Dashed lines are a guide to the eye. (f) Amplitude of non-affinity σ_E^{NA} as a function of strain, see text for definition. Line is a linear scaling as predicted theoretically.

$\epsilon > 0.5$, the mechano-optical signal becomes significant and measurable, with E/E_0 decreasing with increasing extensional strain.

Our experimental data can be quantitatively described by the simulations without any additional adjustable parameters. To do so, we determine the Förster radius for FRET between donor and acceptor to be $r_F \sim 4.9$ nm (see *Appendix*). For the polymer used here, the Kuhn length is 6-8 nm, found both in theoretical and experimental studies [10, 26, 25, 29], so that the number of Kuhn segments in FS1 is $N \approx 14$. While this is quite short within the coarse-grained Kremer-Grest approach, typically used to describe chains consisting of many Kuhn segments, we still find that, using independently-determined input values, that the MC simulations describe the experimental data quantitatively without free fitting parameters (Fig.8.4c). This quantitative agreement supports the validity of the FJC model for these polymers, as also established previously[29], and confirms that the strain sensing effect is caused predominantly by changes in intrachain FRET, attenuated by stretch-induced changes in local segment density radial to the polymer backbone.

We note that conjugated homopolymers also exhibit a coupling between optical signal and chain conformation. Depending on the type of polymer, its intrinsic stiffness, the presence of interchain energy transfer and its aggregation state, large spectral shifts have been identified. Here, we eliminate interchain communication by working in extremely dilute conditions (0.83 ppm). We also confirm that the chains in the PS matrix are not collapsed; collapsed chains, created by adding a non-solvent to a solution of these polymers, exhibit pure acceptor emission due to enhanced energy transfer. In our single-molecule experiments we have not observed any molecules which exhibit pure acceptor emission, indicative of a swollen conformation; indeed, previous studies have indicated that casting films from a good solvent (chloroform) retains the swollen native chain conformation in the solid film[22]. The mechano-optical response in conjugated homopolymers can also emerge from stretch- or aggregation-induced changes in the effective conjugation length, which results in significant, often bathochromic, spectral shifts[22, 31, 32, 33, 34, 35, 36]. These effects have previously been used for creating a wide variety of binding sensors[37, 38, 39, 5]. However, here we do not observe any bathochromic redshift, and the positions

of the two emission peaks remain constant at the exact position where we find emission of pure donor or pure acceptor polymer (Fig.8.1c). We observe the change in relative intensity of two emitting species (donor and acceptor) around an isosbestic point, further lending support to the idea that these effects are predominantly caused by through-space energy transfer. Finally, it is reported that for the specific backbone we employ here, poly(fluorene-co-benzothiadiazole), conformational changes result only in very minor spectral shifts if no acceptor moieties are present[40, 41]; the FRET-induced changes we observe in our experiments occur between two emission bands separated by 100 nm. Thus, the effects we observe can only be interpreted based on a FRET mechanism.

These single-molecule strain sensors based on entropic elasticity and intrachain energy transfer, offer significant advantages over existing strain and/or force-sensing molecules. For example, the threshold forces required to elicit an optical signal are very low. The sensitivity to weak forces derives from the purely entropic origin of the spring-like behaviour of polymer chains. In complement to the simulations (Fig.8.2e), an order-of-magnitude estimate of the force limits of these sensors can be derived from Gaussian polymer statistics. If we assume a linear response, a chain of N Kuhn segments of size a will have an entropic spring constant $k = k_BT/Na^2$. Without applied force, the chain adopts a coiled conformation with radius of gyration $R_g \sim \sqrt{N}a$. Stretching the chain to a new, elongated, dimension R, requires a force $f = k(R - R_g) \sim (R - \sqrt{N}a)K_BT/Na^2$. The spectral shifts saturate when the chain is stretched to its contour length $L_c = Na$. This gives a *maximum* measurable force $f_{max} = (Na - \sqrt{N}a)k_BT/Na^2 = k_BT/a(1 - 1/\sqrt{N})$. For our macromolecular sensor with $a = 5.9$ nm and $N = 14$, this yields $f_{max} = 1$ pN.

In reality, when the semiflexible sensor chain becomes significantly stretched, finite-extensibility and non-linearities become important, so that the real force range is larger. Due to the quantitative mapping onto the simulations (Fig.8.4c) we can calculate the force range corresponding to the strain axis in the experiments. For our experimental system, strains of $\epsilon = 0.7$ or larger give an optical signal in E/E_0 that can be measured with significance in a single chain (see Fig.8.4c). We thus compute our minimum force detection threshold to be as low as $\sim$*300 fN*. The force maximum when the chain is stretched to around its con-

tour length is $\sim$ 5 pN. This highlights how forces can be deduced in single macromolecular sensors across more than one decade in force due to the non-linear force-extension law, despite the limited range in ϵ.

Importantly, our semiconducting entropic spring approach increases the force resolution of existing molecular force sensors by almost a factor of 100, as compared to the most sensitive DNA-duplex based mechanosensors, which have threshold forces of around ten pN[17], and even more as compared to synthetic force sensors based on bond rupture, featuring threshold forces of > 100 pN extending to well into the nN range[11, 12, 13].

Both in simulations and experiments, we observe a strain-independent plateau at low ϵ (Fig.8.2f & Fig.8.4c). This can be explained by considering the stretching of a polymer chain within the Pincus blob description[19], in which the polymer is approximated as a chain of 'blobs' of size ξ, within which the chain configuration remains unperturbed. Thus, ξ sets a length scale below which the stretching has no effect on the chain conformation. In the unstretched state, $\xi = R_g$, the relaxed coil size of the chain, whereas ξ decreases as the chain is extended further (see illustration in Fig.8.2h). Energy transfer occurs in a volume around each donor monomer, whose size is set by the Förster radius r_F. For low strains, the blob size ξ is much larger than r_F, so that small increments in strain do not lead to significant changes in acceptor density around a donor, resulting in a strain-independent optical response. By contrast, when $\xi < r_F$, upon increasing the strain, each small increment in ϵ leads to a change in the local acceptor density and produces an optical signal. This explains the transition from a plateau at low strains to a decreasing E/E_0 at larger ϵ. The crossover strain thus marks the chain extension where the blob size becomes equal to the Förster radius.

Our approach relies on the conformational entropy of the chain to establish a mechano-optical coupling. This implies that chains whose contour length is of the order of the persistence length, so that the chain is already stretched in its unstrained conformation, should not exhibit any optical change in response to mechanical stress. To test this implication, we use oligomers with an identical chemical composition as the strain sensing polymers, which differ only in their molecular weight. This is accomplished by Soxhlet fractionation of the crude reaction product. The monodisperse oligomers (FS2, $M_w = 1.9$ kg/mol) are

obtained as the hexane fraction and have a contour length approximately equal to the Kuhn length [10], so that the effective chain length $N \approx 1$. We repeat the experiments described above, by encasing the oligomers in a PS film and stretching the film to a series of pre-defined extensional strains. Indeed, these rigid-rod molecules show no mechano-optical coupling indicated by the plateau in E/E_0 even at high strains $\epsilon > 1.5$ (Fig.8.4d), confirming the entropic origin of the mechano-optical coupling in these single-molecule macromolecular strain sensors.

Molecular non-affinity measurements

Finally, we explore the possibility that the stretching of a macroscopic piece of material may not lead to a uniform stretching of the molecules within this material. Descriptions of the mechanics of polymeric solids often assume that an applied deformation at the macroscopic scale, translates to a homogeneous deformation of each small element of that solid, down to the molecular scale; this is known as the assumption of affine deformation. However, in recent years it has become very clear that this is most often not the case. Rather, a homogeneous macroscopic strain is thought to lead to an inhomogeneous stretching of the polymer chains within the material, due to the spatial heterogeneity in the microstructure of such disordered solids[42]. In fact, this has also been predicted to occur specifically for the case of glassy polystyrene as used in our experiments[43]. Such a non-affine deformation would lead to a distribution of stretching degrees of the polymers within the material. This is now thought to play a crucial role in the mechanics of a wide variety of polymeric materials, ranging from biopolymer networks[44] to glassy polymers[45] and hydrogels[46].

As non-affinity leads to a heterogeneous distribution of stretching degrees, in our experiments this should lead to a broadening of the energy transfer histograms with increasing strain. To evaluate non-affinity quantitatively, we first extract the width σ_E of the $P(E)$ histograms; as described above, since E is proportional to the local segment density at a scale of the Förster radius, σ_E is a direct measure for the inhomogeneity in the segmental density across different chains in the ensemble.

The relative change in the distribution width $\sigma_E/\sigma_E(\epsilon = 0) = \sigma_E/\sigma_{E,0}$

contains two contributions: i) the affine part σ_E^A, which leads to a reduction in width as the local segmental density decreases with increasing extension and ii) the non-affine contribution σ_E^{NA}, the quantity of interest. In the simulations, we only have the affine contribution σ_E^A, as this condition is enforced. Indeed, the simulation data show a significant decay of $\sigma_E/\sigma_{E,0}$ (open symbols in Fig.8.4e). By contrast, the experiment contains both contributions, and shows a distinct broadening (closed symbols in Fig.8.4e), which thus must be due to non-affinity. To extract the contribution of non-affinity, as a direct measure for the amplitude of non-affine deformations, we can can extract σ_E^{NA} by comparing the affine limit of simulations with the experimental data: $\sigma_E^{NA} = \sigma_E - \sigma_E^A$.

Interestingly, we find that the amplitude of non-affinity increases linearly with the applied strain (Fig.8.4f). This is in direct agreement with theoretical predictions for glasses[47]. While such a linear scaling was recently confirmed in experiments on colloidal glasses[48, 49], direct measurements of non-affinity had remained intractable experimentally for (macro)molecular systems. This highlights how our approach is not only able to measure strains, and by suitable conversion very weak forces, but that it can also give direct insight into mechanical non-linearities such as non-affine deformations, at the molecular scale.

8.3 Discussion

Using a combination of simulations and single-molecule fluorescence spectroscopy experiments, we have demonstrated high-resolution single molecule strain sensing using doped semiconducting polymers as grayscale optomechanical sensors with threshold detection forces as low as ~ 0.3 pN. In direct analogy to most macroscopic force sensors, these molecular sensors are primarily strain sensors, and only become force sensors after suitable conversion of the force-extension behavior. In this Chapter, we have engineered a specific class of semiconducting polymers to perform this task. Semiconducting polymers are excellently suited due to their high photostability that enables the collection of single-molecule fluorescence spectra at a high signal-to-noise ratio. However, the concept we have demonstrated is not limited to this specific chemistry. For example, the attachment of multiple small molecule donor and acceptor dyes to the backbone

of an optically-inert flexible polymer would give a virtually identical approach, extending the possibilities to a much wider range of chemistries and possible applications. To highlight the broadness of our approach, we have performed additional MC simulations of such a dye-labelled flexible polymer in which the inert backbone is decorated with only a few donors and acceptors. Also for this scenario, a very similar strain-optical response curve is found, which can also be tailored by the number of donor and acceptors along the chain (see Fig.8.12 in the *Appendix*). We note however, that the use of semiconducting polymers, as we have done here, offers some strong advantages over the use of small molecule FRET pairs bound to an inert backbone; in particular their excellent photostability that enables extended observation of a single molecule, while the extent of a single-molecule FRET measurement is often restricted by their relatively rapid photobleaching.

The possibility of detecting such weak forces at the molecular scale using non-invasive hyperspectral imaging opens the way to the quantitative mapping of molecular mechanics within a wide variety of materials, for example to unravel the microscopic mechanisms of failure and repair. The chemical functionality of our conjugated molecular sensors can be readily tailored using the polymer side chains, for example to enable their covalent crosslinking within elastomers [50] or to render them watersoluble and biocompatible[51, 37, 5, 38, 52]. Recent advances in polymer chemistry have focused on methods for preparing well-defined sequence-controlled polymer architectures[53]; application of these methods to strain-sensing conjugated polymers could open the way to reduce population heterogeneity to further increase the fidelity and accuracy with which microscopic strains can be detected and visualized.

8.4 Materials and Methods

A detailed description of the synthesis protocols, experimental & theoretical methods and data analysis routines, including additional data, can be found in the *Appendix*. Simulation algorithms and analysis routines, implemented in Matlab, are available on request from the authors.

Macromolecular strain sensors.

The strain sensing polymer consists of poly(dioctyl fluorene-alt-(benzothiadiazole-co-dithienyl benzothiadiazole)) which is prepared using a standard Pd-catalysed Suzuki-Miyaura polycondensation [54]. Low molecular weight impurities and catalyst are removed from the reaction product by extensive Soxhlet extraction against methanol and acetone, yielding a crude yet purified product with $M_w = 24.5$ kg/mol and PDI = 2.08 at a yield of $\approx 80\%$. To obtain the oligomeric and polymeric strain sensors, we further fractionate the crude product using a sequential gradient from mediocre to good solvents. The oligomer FS2 is obtained as the hexane fraction with $M_w = 1.9$ kg/mol, PDI = 1.12 and yield = 76 mg, and the polymer FS1 as the chloroform fraction with $M_w = 30.3$ kg/mol, PDI = 1.82 and yield = 255 mg.

Single-molecule spectroscopy.

We perform single-molecule measurements on a home-built hyperspectral microscopy set-up constructed on a Nikon inverted microscope with a 100x oil immersion objective. Samples are excited using a circularly-polarised and expanded λ =405 nm (18 mW) laser diode (Thorlabs). The emission light is recorded on a hyperspectral camera consisting of a Kurios liquid-crystal tunable bandpass filter mounted onto an Andor Zyla 5.5 sCMOS camera. The tunable bandpass filter can be tuned at wavelengths between 420 and 730 nm. The optical response of the hyperspectral detection system is calibrated against a toluene-dissolved mixture of three different conjugated polymers to span the accessible spectral range, benchmarked onto spectra for identical solutions recorded on a conventional Cary Eclipse fluorescence spectrometer. Triggering between camera and tunable bandpass filter enables sequential acquisition of three-dimensional image hypercubes at typical exposure times of 200-400 ms/frame; giving a total acquisition time for each hyperspectral image cube of 60-100 s. Image data is processed using home-written Matlab analysis routines for spectral correction and background subtraction to establish a fluorescence spectrum for each single-molecule diffraction limited spot in the images. Samples are prepared by film casting polystyrene (PS, $M_w = 350$ kg/mol) solutions at 5% by weight in chloroform doped with 0.83 ppm of the conjugated polymer. Dried films are rapidly

stretched in a tensile stretcher brought to just above the glass transition point of the PS matrix and cooled to fix the strained chain conformations. Film segments are encased in optical-grade epoxy resin (Norland 68) and mounted onto microscope coverslips for use in the experiments. We ensure that only single molecules are observed by sufficient dilution to parts-per-millions level, further verified by measuring the linearity of spot number density versus concentration (see Fig.8.3f and *Appendix*) to confirm the absence of aggregation or segregation [30]

Monte Carlo simulations.

We simulate the stretching of individual chains of $N = N_A + N_D$ Kuhn segments, composed of N_D donors and N_A acceptors, using Monte Carlo simulations of the Kremer-Grest model [9], which combines weakly repulsive beads as coarse-grained monomers, connected along the linear polymer backbone by finitely-extensible springs (see Appendix for details). After extending and equilibrating the chain at a pre-defined end-to-end distance L, we generate 500 statistically-independent snapshots of equilibrium chain conformations for each given value of L. For the simulations, we adopt a microscopic definition of the extensional strain on a molecular basis as $\epsilon = (L - L_0)/L_0$, with L_0 the end-to-end distance in absence of mechanical stretching. For affine deformations, the experimental and microscopic strains are identical. From these snapshots of chain conformations, we compute the chain-average energy transfer efficiency, for a given ratio of donor and acceptor monomers, using a reformulated form of the Förster equation, whose derivation is given in the Appendix. Since each conjugated polymer chain is composed of multiple chromophores, the chain-averaged energy transfer efficiency can be expressed as the sum over all N_D donors and N_A acceptors:

$$E = \frac{1}{N_D} \sum_{j}^{N_D} \left[\frac{\sum_i^{N_A} \left(\frac{r_F}{r_{ij}} \right)^6}{1 + \sum_i^{N_A} \left(\frac{r_F}{r_{ij}} \right)^6} \right] \tag{8.1}$$

where r_{ij} is the Euclidian distance between the i-th acceptor and j-th donor moiety and r_F the Förster radius. For the donor backbone and acceptor dopant

we use in our experiments, we determine $r_F = 4.9$ nm, allowing us to compute E for each chain conformation as a function of extension ϵ and the chemical design parameters N_A, N_D and N.

References

[1] Ingber, D. E. Cellular mechanotransduction: putting all the pieces together again. *The FASEB journal* **20**, 811–827 (2006).

[2] Regul, N. I. C. G. Mechanotransduction across the cell surface and through the cytoskeleton. *Nat. Immun. Cell Growth Regul* **7**, 95 (1988).

[3] Whitesides, G. M. & Grzybowski, B. Self-assembly at all scales. *Science* **295**, 2418–2421 (2002).

[4] Korevaar, P. A. *et al.* Pathway complexity in supramolecular polymerization. *Nature* **481**, 492–496 (2012).

[5] Cingil, H. E. *et al.* Illuminating the reaction pathways of viromimetic assembly. *Journal of the American Chemical Society* **139**, 4962–4968 (2017).

[6] Rubinstein, M. & Colby, R. *Polymer Physics* (OUP Oxford, 2003).

[7] Grandbois, M., Beyer, M., Rief, M., Clausen-Schaumann, H. & Gaub, H. E. How strong is a covalent bond? *Science* **283**, 1727–1730 (1999).

[8] Davis, D. A. *et al.* Force-induced activation of covalent bonds in mechanoresponsive polymeric materials. *Nature* **459**, 68–72 (2009).

[9] Chen, Y. *et al.* Mechanically induced chemiluminescence from polymers incorporating a 1, 2-dioxetane unit in the main chain. *Nature chemistry* **4**, 559–562 (2012).

[10] Ducrot, E., Chen, Y., Bulters, M., Sijbesma, R. P. & Creton, C. Toughening elastomers with sacrificial bonds and watching them break. *Science* **344**, 186–189 (2014).

[11] Gossweiler, G. R., Kouznetsova, T. B. & Craig, S. L. Force-rate characterization of two spiropyran-based molecular force probes. *Journal of the American Chemical Society* **137**, 6148–6151 (2015).

[12] Dopieralski, P. *et al.* On the role of polymer chains in transducing external mechanical forces to benzocyclobutene mechanophores. *Journal of Materials Chemistry* **21**, 8309–8316 (2011).

[13] Ribas-Arino, J., Shiga, M. & Marx, D. Mechanochemical transduction of externally applied forces to mechanophores. *Journal of the American Chemical Society* **132**, 10609–10614 (2010).

[14] Black, A. L., Lenhardt, J. M. & Craig, S. L. From molecular mechanochemistry to stress-responsive materials. *Journal of Materials Chemistry* **21**, 1655–1663 (2011).

[15] Cost, A.-L., Ringer, P., Chrostek-Grashoff, A. & Grashoff, C. How to measure molecular forces in cells: a guide to evaluating genetically-encoded fret-based tension sensors. *Cellular and molecular bioengineering* **8**, 96–105 (2015).

[16] Goktas, M. & Blank, K. G. Molecular force sensors: From fundamental concepts toward applications in cell biology. *Advanced Materials Interfaces* **4** (2017).

[17] Albrecht, C. *et al.* Dna: a programmable force sensor. *Science* **301**, 367–370 (2003).

[18] Beyer, M. K. & Clausen-Schaumann, H. Mechanochemistry: the mechanical activation of covalent bonds. *Chemical Reviews* **105**, 2921–2948 (2005).

[19] Pincus, P. Excluded volume effects and stretched polymer chains. *Macromolecules* **9**, 386–388 (1976).

[20] de Gennes, P. *Scaling Concepts in Polymer Physics* (Cornell University Press, 1979).

[21] Barbara, P. F., Gesquiere, A. J., Park, S.-J. & Lee, Y. J. Single-molecule spectroscopy of conjugated polymers. *Accounts of Chemical Research* **38**, 602–610 (2005). PMID: 16028895.

[22] Huser, T., Yan, M. & Rothberg, L. J. Single chain spectroscopy of conformational dependence of conjugated polymer photophysics. *Proceedings of the National Academy of Sciences* **97**, 11187–11191 (2000).

[23] Zhou, Q. & Swager, T. M. Fluorescent chemosensors based on energy migration in conjugated polymers: The molecular wire approach to increased sensitivity. *Journal of the American Chemical Society* **117**, 12593–12602 (1995).

[24] Zhang, W., Gomez, E. D. & Milner, S. T. Predicting chain dimensions of semiflexible polymers from dihedral potentials. *Macromolecules* **47**, 6453–6461 (2014).

[25] Fytas, G., Nothofer, H., Scherf, U., Vlassopoulos, D. & Meier, G. Structure and dynamics of nondilute polyfluorene solutions. *Macromolecules* **35**, 481–488 (2002).

[26] Grell, M. *et al.* Chain geometry, solution aggregation and enhanced dichroism in the liquidcrystalline conjugated polymer poly (9, 9-dioctylfluorene). *Acta Polymerica* **49**, 439–444 (1998).

[27] Brédas, J.-L., Beljonne, D., Coropceanu, V. & Cornil, J. Charge-transfer and energy-transfer processes in π-conjugated oligomers and polymers: a molecular picture. *Chemical reviews* **104**, 4971–5004 (2004).

[28] Grest, G. S. & Kremer, K. Molecular dynamics simulation for polymers in the presence of a heat bath. *Phys. Rev. A* **33**, 3628–3631 (1986).

[29] Muls, B. *et al.* Direct measurement of the end-to-end distance of individual polyfluorene polymer chains. *ChemPhysChem* **6**, 2286–2294 (2005).

[30] Bout, D. A. V. *et al.* Discrete intensity jumps and intramolecular electronic energy transfer in the spectroscopy of single conjugated polymer molecules. *Science* **277**, 1074–1077 (1997).

[31] Barbara, P. F., Gesquiere, A. J., Park, S.-J. & Lee, Y. J. Single-molecule spectroscopy of conjugated polymers. *Accounts of chemical research* **38**, 602–610 (2005).

[32] Hu, D. *et al.* Collapse of stiff conjugated polymers with chemical defects into ordered, cylindrical conformations. *Nature* **405**, 1030 (2000).

[33] Kim, J. & Swager, T. Control of conformational and interpolymer effects in conjugated polymers. *Nature* **411**, 1030 (2001).

[34] Schindler, F., Lupton, J. M., Feldmann, J. & Scherf, U. A universal picture of chromophores in π-conjugated polymers derived from single-molecule spectroscopy. *Proceedings of the National Academy of Sciences of the United States of America* **101**, 14695–14700 (2004).

[35] Schwartz, B. J. Conjugated polymers as molecular materials: How chain conformation and film morphology influence energy transfer and interchain interactions. *Annual review of physical chemistry* **54**, 141–172 (2003).

[36] Zhu, Z. & Swager, T. M. Conjugated polymer liquid crystal solutions: control of conformation and alignment. *Journal of the American Chemical Society* **124**, 9670–9671 (2002).

[37] Thomas, S. W., Joly, G. D. & Swager, T. M. Chemical sensors based on amplifying fluorescent conjugated polymers. *Chemical Reviews* **107**, 1339–1386 (2007).

[38] Gaylord, B. S., Heeger, A. J. & Bazan, G. C. Dna detection using water-soluble conjugated polymers and peptide nucleic acid probes. *Proceedings of the National Academy of Sciences* **99**, 10954–10957 (2002).

[39] Liu, B. & Bazan, G. C. Homogeneous fluorescence-based dna detection with water-soluble conjugated polymers. *Chemistry of materials* **16**, 4467–4476 (2004).

[40] Zheng, Z. *et al.* Uniaxial alignment of liquid-crystalline conjugated polymers by nanoconfinement. *Nano letters* **7**, 987–992 (2007).

[41] Miller, W. L. *Single-molecule spectroscopic studies of conjugated polymers* (Ph.D. thesis: The University of Texas at Austin, 2007).

[42] Zaccone, A. Elastic deformations in covalent amorphous solids. *Modern Physics Letters B* **27**, 1330002 (2013).

[43] Zaccone, A. & Terentjev, E. M. Disorder-assisted melting and the glass transition in amorphous solids. *Physical review letters* **110**, 178002 (2013).

[44] Onck, P., Koeman, T., Van Dillen, T. & van der Giessen, E. Alternative explanation of stiffening in cross-linked semiflexible networks. *Physical review letters* **95**, 178102 (2005).

[45] Lappala, A., Zaccone, A. & Terentjev, E. M. Polymer glass transition occurs at the marginal rigidity point with connectivity z*= 4. *Soft matter* **12**, 7330–7337 (2016).

[46] Wen, Q., Basu, A., Janmey, P. A. & Yodh, A. G. Non-affine deformations in polymer hydrogels. *Soft matter* **8**, 8039–8049 (2012).

[47] DiDonna, B. & Lubensky, T. Nonaffine correlations in random elastic media. *Physical Review E* **72**, 066619 (2005).

[48] Denisov, D. V. *et al.* Sharp symmetry-change marks the mechanical failure transition of glasses. *Scientific reports* **5**, 14359–14359 (2015).

[49] Laurati, M., Maßhoff, P., Mutch, K. J., Egelhaaf, S. U. & Zaccone, A. Long-lived neighbors determine the rheological response of glasses. *Physical review letters* **118**, 018002 (2017).

[50] Kuehne, A. J. *et al.* Sub-micrometer patterning of amorphous-and β-phase in a crosslinkable poly (9, 9-dioctylfluorene): Dual-wavelength lasing from a mixed-morphology device. *Advanced Functional Materials* **21**, 2564–2570 (2011).

[51] Hong, J. W., Hemme, W. L., Keller, G. E., Rinke, M. T. & Bazan, G. C. Conjugated-polymer/dna interpolyelectrolyte complexes for accurate dna concentration determination. *Advanced Materials* **18**, 878–882 (2006).

[52] Cingil, H. E. *et al.* Monitoring protein capsid assembly with a conjugated polymer strain sensor. *Journal of the American Chemical Society* **137**, 9800–9803 (2015).

[53] Badi, N. & Lutz, J.-F. Sequence control in polymer synthesis. *Chemical Society Reviews* **38**, 3383–3390 (2009).

[54] Miyaura, N. & Suzuki, A. Palladium-catalyzed cross-coupling reactions of organoboron compounds. *Chemical reviews* **95**, 2457–2483 (1995).

8.5 Appendix

Polymer synthesis & characterisation

Synthesis

The strain sensors are prepared through conventional Suzuki-Miyaura polycondensation[1]. The reaction proceeded as follows: 10 g (17.90 mmol) 9,9-dioctylfluorene-2,7-diboronic acid bis (1,3-propanediol) ester, 1.1722 g (2.558 mmol) 4,7-Bis(5-bromo-2-thienyl)-2,1,3-benzothia-diazole and 4.51 g (15.34 mmol) 4,7-Dibromobenzo[c]-1,2,5-thiadiazole are charged into a 1L round bottom flask. The monomers are dissolved in 350 ml of toluene. Subsequently, 150 ml K2CO3 (2M aq.) is added and the mixture degassed by bubbling with dry N2 for 2.5 hours. The flask is fitted with a septum and placed under vacuum. The flask is degassed by 5 N2/vacuum cycles. Then, 524 mg (0.716 mmol) of [1,1'-Bis-(diphenylphosphino)ferrocene]-dichloropalladium(II) is added to the flask under N2. Another five vacuum/nitrogen cycles are performed and the flask is left under vacuum to react for 4 days at 100°C in the dark. The reaction mixture is then washed against 150 ml of brine. The organic phase containing the polymer is precipitated into cold methanol to yield a bright purple solid collected by centrifugation. The product is washed against methanol:water (1:1) by stirring the suspended solid overnight. The product is again collected by centrifugation and dried overnight under vacuum at 30°C.

To remove low molecular weight impurities and catalyst, the polymer was cleaned by Soxhlet extraction against methanol and acetone, extracted against chloroform and precipitated in MeOH. This yields a pure but polydisperse prefractionation product with $M_w = 24.5$ kg/mol and PDI = 2.08 at a yield of $\approx 80\%$.

The molecular weights and polydispersity index are determined by GPC, by dissolving 20mg of polymer in 2 ml of chloroform and dissolution for 4 days. The solutions are filtered over a 0.45 micron PTFE filter prior to injection on the GPC column with chloroform as the eluens. The molecular weights are calibrated against polystyrene standards and corrected with a factor of 2.7 to compensate for the more rigid backbone of the conjugated polymer compared to

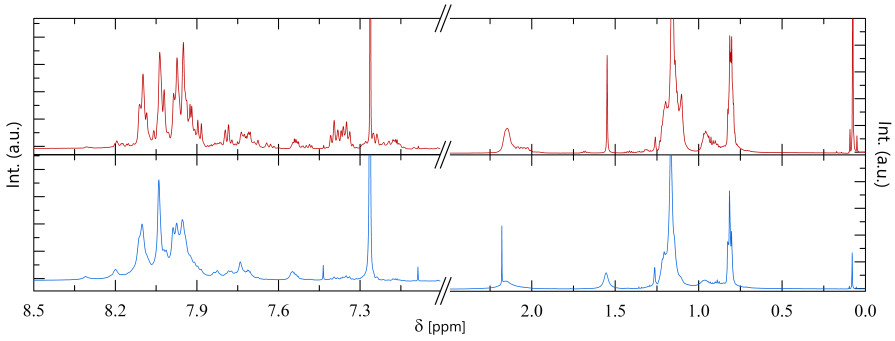

Figure 8.5: ^{1}H-NMR spectra of polymer FS1 (blue, bottom) and oligomer FS2 (red, top).

polystyrene[2].

To increase the monodispersity of the force sensors used in this study, and to obtain different molecular weight samples from the same polydisperse batch, we performed a fractionation by extracting the powder with a range of hexane:THF mixtures, THF:chloroform mixtures and finally extraction with pure chloroform.

In the experimental study we used short oligomers obtained from the pure hexane fraction, with $M_w = 1.9$ kg/mol and PDI = 1.12 (yield = 76 mg, denoted *FS2*), and long polymers from the pure chloroform fraction with $M_w = 30.3$ kg/mol and PDI = 1.82 (yield = 255 mg, *FS1*).

We further characterize the two fractions by NMR, see Fig.8.5 and Fig.8.6; we note that there is significant peak broadening for the long polymer (FS1) as compared to the oligomer (FS2) due to slow relaxations of the longer chains.
FS1: 1H NMR (600MHz, CDCl3) δ: 8.318(s), 8.106(s), 8.05(s), 8.006-7.886(m), 7.859-7.816(m), 7.804-7.666(m), 7.581-7.52(m), 2.161(s) 1.28-1.088(m), 1.012--0.872(m), 0.8430.782(t)
FS1: 13C NMR (600MHz, CDCl3) δ: 154.2, 151.69, 140.79, 136.34, 133.44, 128.29, 127.89, 123.88, 119.93, 76.8 (CHCl3), 55.46, 40.12, 31.76, 30.04, 29.22, 23.89, 22.58, 13.97
FS2: 1H NMR (600MHz, CDCl3) δ: 8.125-8.065(m), 8.061-7.994(m), 7.992 -7.863(m) 7.803-7.755(m), 7.742-7.6318(m), 7.568-7.473(m), 7.414-7.321(m)7.301-7.123(m),

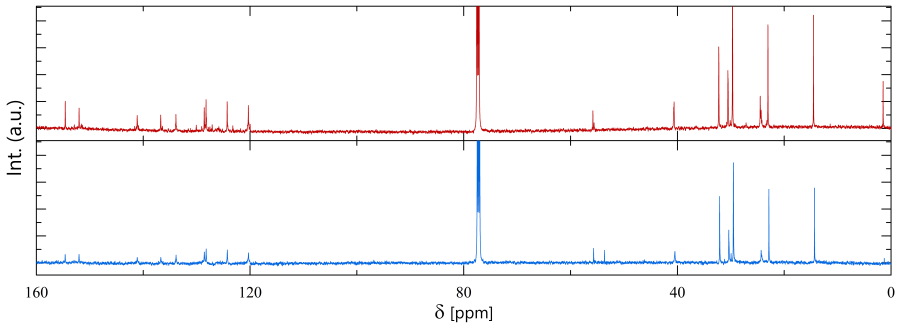

Figure 8.6: ^{13}C-NMR spectra of polymer FS1 (blue, bottom) and oligomer FS2 (red, top).

2.144(s) 1.243-1.066(m), 0.996-0.868(m), 0.8385-0.768(m)

FS2: 13C NMR (600MHz, CDCl3) δ: 154.3, 151.75, 140.82, 136.39, 133.55, 128.21, 127.92, 123.98, 119.98, 77.1 (CHCl3), 55.37, 40.02, 31.69, 29.98, 29.08, 23.94, 22.47, 13.90

Ensemble-averaged spectroscopy

We record ensemble-averaged absorption, emission and excitation spectra for both donor and acceptor emission by dissolving the conjugated polymers at very low concentrations in chloroform, on a conventional Cary Eclipse fluorescence spectrometer. These data are shown in Figure 8.7 below. We note that the acceptor peak in solution for the polymer is significantly higher than that of the oligomer; this is due to the coiled versus rod-like chain conformation of these two samples in solution, one well-above the persistence length (FS1) and one below (FS2). We also note that the ratio of donor and acceptor peaks of the same polymers embedded in a solid PS film are different from their spectra in chloroform solution as shown here. This is most likely due to changes in energy transfer efficiency, because of the different chain conformations in the solid film and in solution.

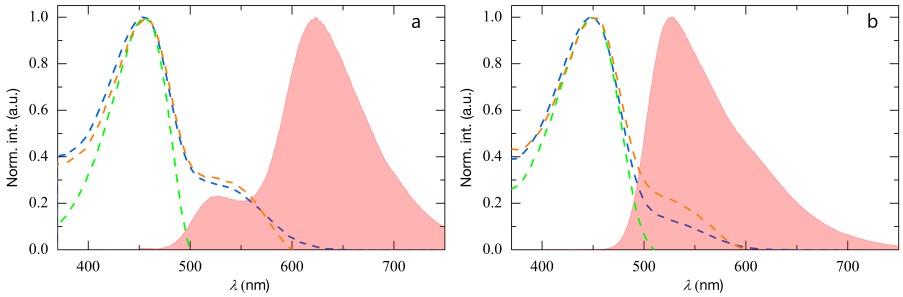

Figure 8.7: Ensemble-averaged spectroscopy of FS2 (a) and FS1 (b) in dilute chloroform solution, showing absorption (blue dashed), emission (red shaded) spectra and two excitation spectra for emission of the donor ($\lambda_{em} = 525$ nm, green dashed) and emission of the acceptor ($\lambda_{em} = 625$ nm, orange dashed), from which donor-acceptor energy transfer can be directly seen.

Excitation-emission spectra

We record a two-dimensional excitation-emission spectra for FS2 by dissolving the polymers in toluene at 5 μg/ml. Spectra are recorded on a Cary Eclipse fluorescence spectrometer. The two-dimensional excitation-emission spectra show a major peak at $\sim$ 550 nm, which is the donor emission, and a minor peak at $\sim$ 650 nm, which is the acceptor emission. For the acceptor emission we see both the direct excitation at $\lambda_{ex} = 525$-600 nm, and the emission upon energy transfer for $\lambda_{ex} = 390$-475 nm (see Fig.8.8).

Determination of Förster radius r_F

To determine the Förster radius of our donor-acceptor energy transfer pair we first synthesise two polymers, which have either pure donor (poly(dioctylfluorene-alt-benzothiadiazole)) or pure acceptor (poly(dioctylfluorene-alt-dithienylbenzothiadiazole) emission. The two polymers are synthesized using standard Suzuki-Miyaura polycondensations, and purified following the procedure described above. These alternating copolymers of fluorene and benzothiadiazole (donor) and dithienylbenzothiadiazole (acceptor) exhibit pure donor or acceptor emission due to efficient energy transfer within the chain. We note that it is essential to determ-

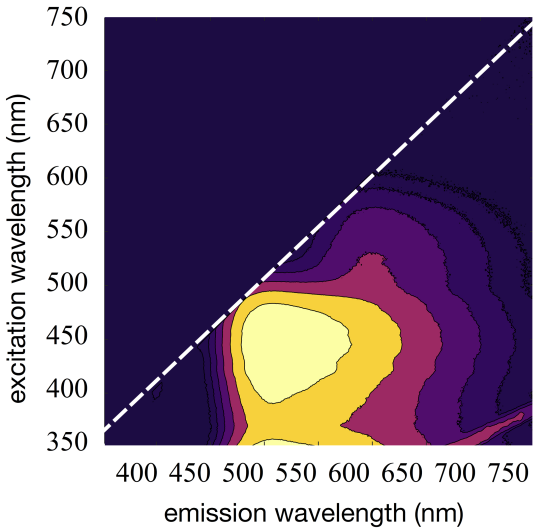

Figure 8.8: Excitation-emission spectrum for oligomer **FS2** dissolved in toluene. The diagonal intensity line starting at $\lambda_{em} = 700$ nm is due to second-order Rayleigh scattering.

ine the FRET efficiency of these chromophores embedded in a semiconducting polymer backbone, as the extended conjugation in these structures shifts their absorption and emission. Thus, measurements on the isolated monomers would not give a fair representation of the overlap integral required to compute r_F. To extract the absorption spectrum of the acceptor from the convoluted spectrum of DTBT and fluorene absorption, we deconvolve the measured absorption spectrum with that of pure polyfluorene, to obtain a measure for the absorption spectrum of the acceptor, within an extended π-conjugated system, alone.

From the absorption and emission spectra (as shown in Fig.1 in the main text) we can calculate the Förster radius as[3, 4]:

$$r_F = \left[\frac{9 \ln 10}{128 \pi^5 N_A} \frac{\kappa^2 Q_D}{n^4} J \right]^{\frac{1}{6}} \tag{8.2}$$

where N_A is Avogadro's number, κ the dipole orientation factor, Q_D the photoluminescence quantum yield of the donor, n the refractive index of the medium and J the spectral overlap integral of donor emission and acceptor absorbance,

defined as:

$$J = \int \overline{f_D}(\lambda)\epsilon_A(\lambda)\lambda^4 d\lambda \tag{8.3}$$

where $\overline{f_D}$ is the normalised donor fluorescence emission spectrum and ϵ_A is the molar exctinction coefficient obtained from the absorption spectrum. We take[5, 3] $\kappa = \frac{2}{3}$, and for the donor quantum efficiency[6] $Q_D = 0.116$ and $n = 1.6$ as the refractive index for PS [7]. This gives the experimentally-determined Förster radius as $r_F = 4.9$ nm for our donor-acceptor pair.

Single-molecule spectroscopy

Experimental set-up

We perform single-molecule emission measurements on a home-built hyperspectral microscopy set-up. The optical path of the set-up is illustrated in Figure 3 of the main text. The set-up is constructed on a Nikon inverted microscope body, equipped with a high-NA, 100x oil immersion objective. The conjugated polymer samples are excited by a λ =405 nm laser diode (18mW, Thorlabs), which we first pass through a quarter wave plate to achieve circular polarisation, and subsequently expand and collimate, and clean-up with an iris, projected onto the back focal plane of the objective, providing wide-field illumination of the sample. The excitation beam and emission light are split with a Semrock dichroic mirror with a threshold wavelength of 409 nm.

For recording the emission spectrum of individual conjugated polymer chains embedded in PS films, the emission light is sent to a hyperspectral camera composed of a Kurios liquid-crystal tunable bandpass filter mounted onto an Andor Zyla 5.5 sCMOS camera. The tunable bandpass filter has a bandwidth (FWHM) of approximately 10 nm, and can be tuned at wavelengths between 420 and 730 nm at 1 nm intervals. We calibrate the optical response of the hyperspectral detection path, to account for the wavelength-dependence of the quantum efficiency of the camera chip and transmission coefficient of the bandpass filter, by comparing spectra for a mixture of three different conjugated polymers, benchmarked onto spectra recorded on a conventional Cary Eclipse fluorescence

spectrometer. The camera and tunable bandpass filter are internally-triggered through Micro-Manager software[8] to allow the sequential acquisition of a three-dimensional image hypercube by scanning the bandpass window from low to high wavelengths. The acquisition time per frame is choosen to ensure optimal use of the 16-bit dynamic range of the camera, and is typically between 200 and 400 ms/frame; this means that a hyperspectral image cube is acquired in 60-100 seconds.

Sample preparation

We first prepare stock solutions of FS1 and FS2 at 0.05 mg/ml in chloroform. Polymer films are made by casting a solution of polystyrene ($M_w = 350$ kg/mol, Sigma-Aldrich) in chloroform doped at 0.83 ppm with sensor polymer into a clean glass petridish. The film is air-dried for 48h to allow the chloroform to evaporate.

The films are removed from the petridish and cut into rectangular strips for stretching. Polymer film strips are stretched using a home-built manual stretching bench. The extensional strain ϵ is pre-determined and regulated by securing a stop block at the required distance on the rail. A rectangular piece of polymer film was clamped into the device and heated to just above the glass transition temperature of the polystyrene matrix for 1h. Heating of the film was done with the stretching bench in a horizontal position, to ensure the absence of extensional stress on the film during heating. To stretch the film, we tilt the bench, apply the stretch manually and immediately cool the film to fix the strained chain conformations. We estimate that the film cools to well below the T_g within seconds.

To prepare a sample for single-molecule experiments, we cut a 1x1 cm piece of the film and place it on a thin coverslip. We cover the film in optical-grade UV-curing expoxy (Norland 68) and press a second microscopy slide firmly onto the film to ensure a coplanar alignment of the film to avoid lensing. The glue is rapidly cured using a high-power UV curing lamp. The single-molecule measurements are performed under ambient conditions.

Data analysis

In each wide-field hyperspectral image we find several diffraction-limited single-molecule emission spots, whose spectral signature we extract by means of automated analysis routines coded in Matlab (these codes are available at request from the authors). We first identify the diffraction limited spots in the images, then apply the spectral calibration to obtain a quantitative hyperspectral image, run a background subtraction at each wavelength and then reconstruct the single-molecule emission spectra from the mean spot intensity as a function of wavelength.

For each molecule, our routine continues by automatically deconvolving the spectrum using a Monte Carlo least-squares fitting routine. We fit the emission profiles to a sum of log-normal distributions, each based on the emission spectrum of the donor and acceptor components. As a measure for the FRET efficiency, we take the integrated acceptor emission intensity over the total integrated intensity.

While the molecules we analyse are relatively photostable on the timescale of spectra acquisition, we occasionally observe bleaching during recording of an image hypercube, leading to a sudden truncation of the emission spectra. Data sets that exhibit this feature are not used for further analysis.

For each of the histograms of either energy transfer efficiency, we collect data for at least $n = 100$ single polymer chains, in many cases more, to ensure sufficient statistics. The number of molecules analyzed for each histogram is indicated in the figures below.

Additional single-molecule data

Energy transfer histograms

Here we show all additional energy transfer histograms not shown in the main text (Fig.4) constructed from the single molecule spectra we recorded for all recorded values of ϵ for both FS1 and FS2.

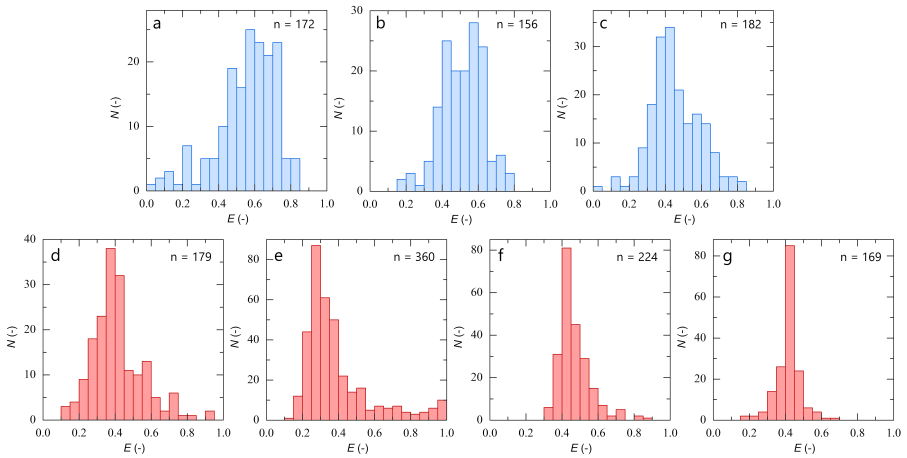

Figure 8.9: Experimental histograms of energy transfer efficiency from single-molecule experiments, with n the counted number of single-molecule spots indicated in the figure, for : a) FS1, $\epsilon = 0.42$, b) FS1, $\epsilon = 0.87$, c) FS1, $\epsilon = 1.44$, d) FS2, $\epsilon = 0$, e) FS2, $\epsilon = 0.42$, f) FS2, $\epsilon = 0.87$, g) FS2, $\epsilon = 1.71$.

Sample single-molecule spectra

In total we have recorded $\sim$ 1800 single molecule spectra to construct our experimental data. In addition to the three sample spectra in the main text, here we show 20 additional spectra for the sake of transparency, for each of the two samples FS1 and FS2.

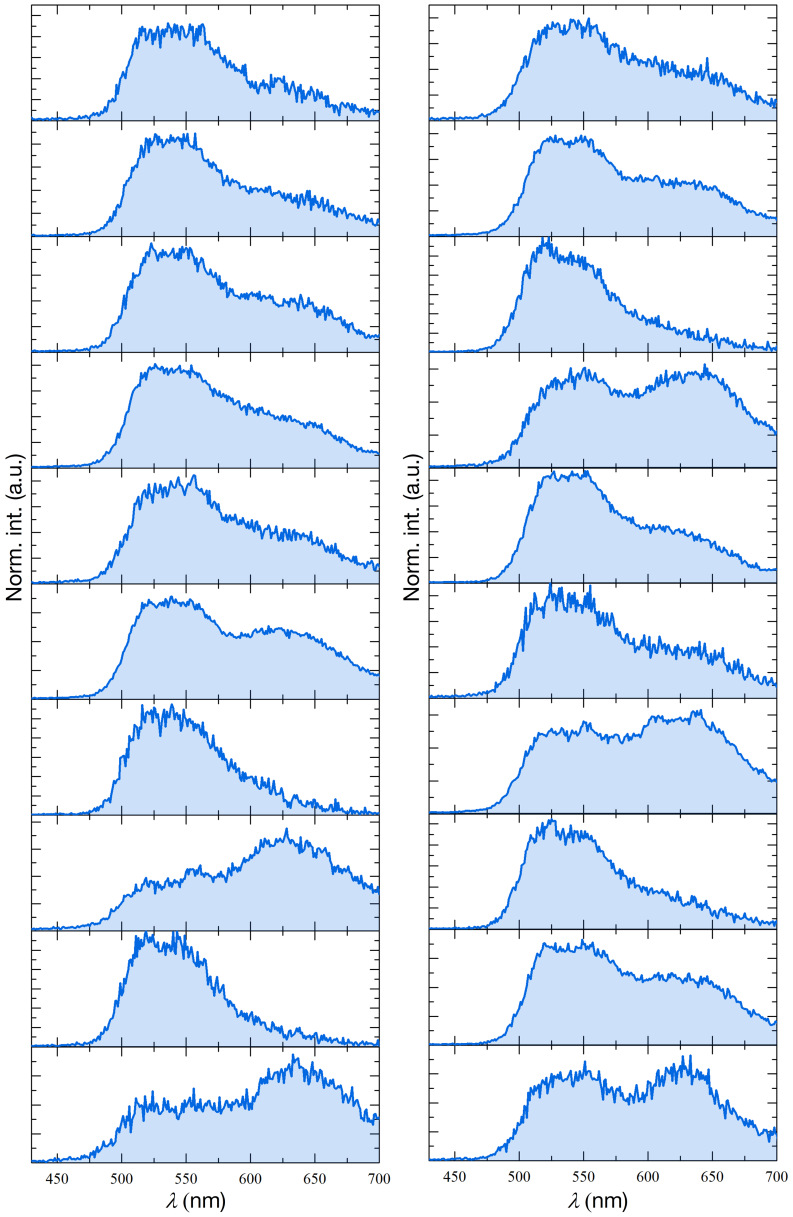

Figure 8.10: Additional sample single-molecule fluorescence spectra for **FS1**.

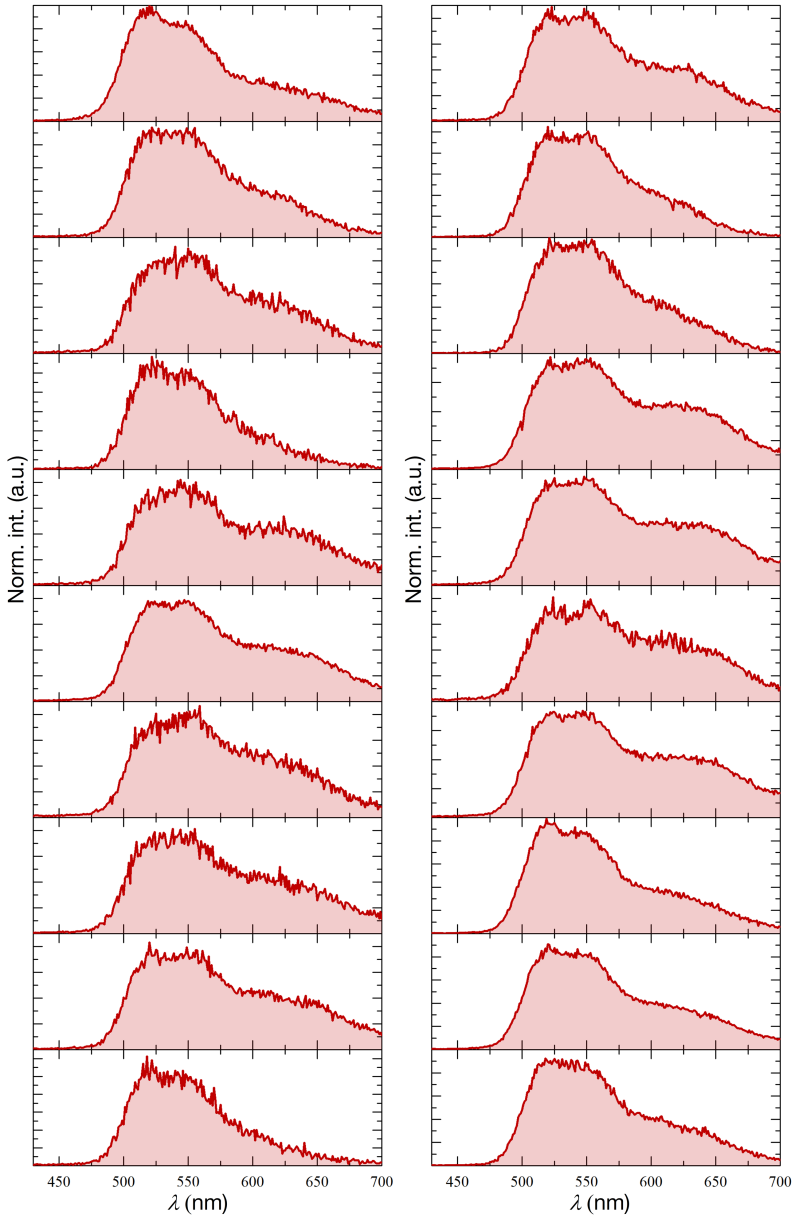

Figure 8.11: Additional sample single-molecule fluorescence spectra for **FS2**.

Monte Carlo simulations

We simulate polymer chains using Metropolis Monte Carlo simulations of the Kremer-Grest model[9]. Each chain consists of N statistical segments. In our conjugated polymers the entire polymer backbone consists of donor segments, randomly doped with acceptor moieties. For the sake of computational efficiency we coarse-grain these chains as bead-spring chains, where each bead represents a Kuhn segment, approximately equal to 7-8 monomer units. We prepare chains of N_D donor beads and N_A acceptors, with a total chain length $N = N_A + N_D$. For the sake of simplicity, we take identical bead sizes for the donor and acceptor units, which are $\sigma = l_K$ that is approximately equal to the Kuhn length of the polymer, determined to be 5.9 nm by Zhang et al. [10]. All quantities in the simulations are expressed in terms of the length σ and the energy scale ϵ; $\sigma = \epsilon = 1$. The beads are connected by $(N-1)$ finitely-extensible nonlinear elastic (FENE) springs, which gives rise to a bonding potential between adjacent segments:

$$U_{FENE} \begin{cases} \frac{-kr_{max}}{2} \ln\left[1 - \left(\frac{r}{r_{max}}\right)^2\right] & r \leq r_{max} \\ \infty & r > r_{max} \end{cases} \tag{8.4}$$

where r is the separation distance between beads and $r_{max} = 1.5\sigma$ the maximum extension of the FENE spring.

Interactions between all beads in the chain are treated by the truncated and purely repulsive Lennard-Jones potential, also known as the Weeks-Chandler-Anderson (WCA) potential:

$$U_{WCA} \begin{cases} 4\epsilon\left[\left(\frac{\sigma}{r}\right)^{12} - \left(\frac{\sigma}{r}\right)^{6}\right] + C(r_{cut}) & r \leq r_{cut} \\ 0 & r > r_{cut} \end{cases} \tag{8.5}$$

in which the potential is trunctated at a cut-off distance r_{cut} and shifted vertically with $C(r_{cut})$; for $r_{cut} = 2^{1/6}$ and $C(r_{cut}) = 1$, monomer-monomer interactions are purely repulsive.

To simulate individual polymer chains, we create an initial chain configuration that is relaxed during 10^8 MC steps. We subsequently fix the position of

the chain ends, i.e. monomer segments 1 and N, and during 10^9 MC steps move these to a predefined end-to-end distance L. The extensional strain ϵ on the chain is defined as $\epsilon = \frac{L-L_0}{L_0}$, in which L_0 is the root-mean-square end-to-end distance of the relaxed chain. After the stretching protocol, statistically-independent chain conformations are generated by allowing the chain to fluctuate during $10^5 N$ steps.

For each of these conformations, we generate both a random distribution of the acceptor molecules, to simulate the randomly-doped chains studied in our experiments, and a sequence-controlled chain, in which the acceptor molecules are positioned with equidistant spacing along the chain. This enables us to study the effect of random versus site-specific doping.

In the experiments we measure the ratio $E = I_A/(I_D + I_A)$ of acceptor to total emission intensity as a proxy for the energy transfer efficiency for a single polymer chain. For individual chains, in which there is no intermolecular energy transfer, two contributions to acceptor emission can be identified: i) transfer of the excited state along the semiconducting backbone by means of exciton diffusion and ii) non-radiative transfer through the dielectric medium by means of Förster resonant energy transfer (FRET). The excitonic transfer provides a baseline level of energy transfer [11]. As we are interested mainly in the second process, we present all of our results as the relative change in the emission ratio E/E_0.

The energy transfer efficiency of the second, non-excitonic process, can be computed from the simulated chain conformation by considering the rate of photon emission from the donor k_d and the rate of resonant energy transfer to the acceptor k_E. For a single donor and acceptor the Förster equation gives:

$$E_0 = \frac{k_E}{k_d + k_E} = \frac{1}{1 + \left(\frac{k_d}{k_E}\right)} \tag{8.6}$$

which exhibits a dependence on distance of the donor-acceptor pair r_{DA} as $k_D/k_E = (r_{DA}/r_F)^6$, with r_F the Förster radius at which $E = 0.5$.

For the scenario we study here, the chain is composed entirely of donor moieties, doped with several acceptors. Thus, each donor can transfer its energy to multiple acceptors. For the j-th donor, the rate of ET to the i-th acceptor is

characterised by k_E^{ij}. The energy transfer efficiency for the j-th donor can be expressed as:

$$E_j = \frac{\sum_i^{n_A} k_E^{ij}}{k_D + \sum_i^{n_A} k_E^{ij}} \tag{8.7}$$

Using the relation $k_D/k_E^{ij} = (r_{ij}/r_F)^6$, with r_{ij} the distance between j-th donor and the i-th acceptor, we can find:

$$E_j = \frac{\sum_i^{n_A} \left(\frac{r_F}{r_{ij}}\right)^6}{1 + \sum_i^{n_A} \left(\frac{r_F}{r_{ij}}\right)^6} \tag{8.8}$$

since we measure the emission spectrum averaged over a single polymer chain composed of n_D donors, the total single chain energy transfer efficiency due to FRET is given by:

$$E = \frac{1}{n_D} \sum_j^{n_D} E_j = \frac{1}{n_D} \sum_j^{n_D} \left(\frac{\sum_i^{n_A} \left(\frac{r_F}{r_{ij}}\right)^6}{1 + \sum_i^{n_A} \left(\frac{r_F}{r_{ij}}\right)^6} \right) \tag{8.9}$$

Note that this assumes that i) there is only non-radiative energy transfer implying that inner filter effects are negligible, ii) there is no donor-donor transfer and iii) the measurements involve only individual polymer chains, so that there is no intermolecular transfer.

To convert the results of our Monte Carlo simulations as a function of ϵ into a force-optical response curve, we need a force-extension law that describes the elasticity of a single chain under action of a stretching force f. We use a finite-extensibility freely-jointed chain model, describing the chain at the same level of coarse grained Kuhn segments as in the simulations, which gives a relationship between force f and extension ΔL as [12]:

$$\Delta L(f) = N l_k \left(\coth(x) - \frac{1}{x} \right) + \frac{Nf}{k_s} \tag{8.10}$$

with $x = F l_k / k_B T$, l_k the Kuhn length and k_s the segmental spring constant, which accounts for enthalpic spring forces between bonded monomers.

This segmental spring constant reflects the extensibility of the covalent C-C

Table 8.1: Literature values for the segmental spring constant k_s for C-C bonds in various polymer backbones.

Polymer	k_s	*Method*	*Reference*
Poly(hydroxyl ethyl methacrylate)-graft-ethylene glycol: In H2O	4.2 N/m	AFM	[13]
Poly(hydroxyl ethyl methacrylate)-graft-ethylene glycol: In PBS	10 N/m	AFM	[13]
Poly(methylene)	5-10 N/m	Ab-initio molecular mechanics calculations	[14]
poly(vinyl alcohol)	5-10 N/m	AFM	[15]

bond that forms the backbone of our polymer chain, and should thus be independent of the exact chemistry of the rest of the polymer. A review of existing literature values for k_s for C-C bonded polymer (see table below) shows that these values are all of the same order of magnitude, both from experimental studies and ab-initio molecular mechanics simulations. As a reasonable choice we thus use $k_s = 10\,\mathrm{J/m^2}$ to estimate the spring constant of a carbon-carbon bond in a polymer chain.

Dye-doped force sensors: simulations

We highlight the broader applicability of our approach by using our simulation method to predict the force-optical response of inert and optically-inactive polymer to which small-molecule fluorescent dyes are attached as a FRET pair. Also here, we randomly place the donor and acceptor moieites on the flexible chain, modelled with the Kramer-Grest approach detailed above. We choose $N = 50$ and simulate varying degrees of donor and acceptor labelling. We observe a very similar strain-optical response curves as compared to the results for ac-

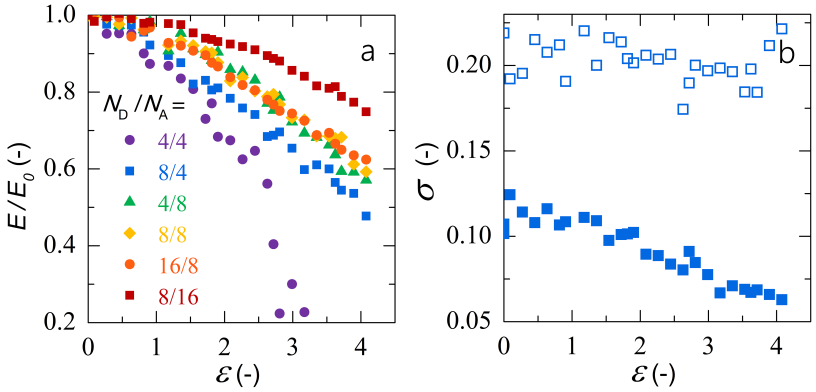

Figure 8.12: a) Strain-sensing curve for dye-doped polymers ($N = 50$) with doping degrees of the donor and acceptor as indicated. b) σ as a function of strain for a simulated conjugated polymer ($N = 50$, closed symbols) and a dye doped polymer, same as in a) with $N_D = 8$ and $N_A = 4$.

ceptor doped donor chains (ie. chromophore doped conjugated polymers) (see Fig.8.12a). Also here, the sensitiviy and range of the polymeric force sensors can be tailored by the doping degree and the ratio of donor to acceptor dyes. This highlights that the approach we have demonstrated in the main text, is not exclusive to conjugated polymers of the appropriate design, but can be extended to any polymeric object to which multiple donor and acceptor dyes can be tethered.

We also compare the width of the Gaussian distributions σ for a simulated conjugated polymer and these new dye-doped polymers (Fig.8.12b). Here, we observe a striking difference; while for the conjugated polymer (closed symbols), due to the high donor doping degree (the entire backbone is composed of donor units), the width of the distribution allows probing the chain entropy, and non-affinity as discussed in the main text. The dye doped polymer, due to the possibility of having a donor-acceptor pair on directly adjacent sites, not only shows a larger distribution width, but the large degree of chemical heterogeneity makes it impossible to resolve the stretching-induced changes in conformational entropy (open symbols).

References

[1] Miyaura, N., Yamada, K. & Suzuki, A. A new stereospecific cross-coupling by the palladium-catalyzed reaction of 1-alkenylboranes with 1-alkenyl or 1-alkynyl halides. *Tetrahedron Letters* **20**, 3437–3440 (1979).

[2] Grell, M. *et al.* Chain geometry, solution aggregation and enhanced dichroism in the liquidcrystalline conjugated polymer poly(9,9-dioctylfluorene). *Acta Polymerica* **49**, 439–444 (1998).

[3] Clegg, R. M. Chapter 1 Förster resonance energy transferâĂŤFRET what is it, why do it, and how it's done. *Laboratory Techniques in Biochemistry and Molecular Biology* **33**, 1–57 (2009).

[4] Forster, T. *Fluoreszenz organischer Verbindungen* (Vandenhoeck und Ruprecht, Göttingen, 1951).

[5] van der Meer, B. W. Kappa-squared: from nuisance to new sense. *Reviews in Molecular Biotechnology* **82**, 181–196 (2002).

[6] Hashim, Z., Howes, P. & Green, M. Luminescent quantum-dot-sized conjugated polymer nanoparticles-nanoparticle formation in a miniemulsion system. *J. Mater. Chem.* **21**, 1797–1803 (2011).

[7] Refractive index polystyrene. `https://refractiveindex.info/?shelf=organic&book=polystyren&page=Sultanova`. Accessed: 2017-6-12.

[8] Edelstein, A., Amodaj, N., Hoover, K., Vale, R. & Stuurman, N. Computer Control of Microscopes Using ÂţManager. In *Current Protocols in Molecular Biology* (John Wiley & Sons, Inc., 2001).

[9] Grest, G. S. & Kremer, K. Molecular dynamics simulation for polymers in the presence of a heat bath. *Phys. Rev. A* **33**, 3628–3631 (1986).

[10] Zhang, W., Gomez, E. D. & Milner, S. T. Predicting Chain Dimensions of Semiflexible Polymers from Dihedral Potentials. *Macromolecules* **47**, 6453–6461 (2014).

[11] Brédas, J.-L., Beljonne, D., Coropceanu, V. & Cornil, J. Charge-transfer and energy-transfer processes in π-conjugated oligomers and polymers: a molecular picture. *Chemical reviews* **104**, 4971–5004 (2004).

[12] Smith, S. B., Cui, Y. & Bustamante, C. Overstretching B-DNA: The Elastic Response of Individual Double-Stranded and Single-Stranded DNA Molecules. *Science* **271**, 795–799 (1996).

[13] Zhang, D. & Ortiz, C. Synthesis and single molecule force spectroscopy of graft copolymers of poly (2-hydroxyethyl methacrylate-g-ethylene glycol). *Macromolecules* **37**, 4271–4282 (2004).

[14] Zemanová, M. & Bleha, T. Isometric and isotensional force-length profiles in polymethylene chains. *Macromolecular theory and simulations* **14**, 596–604 (2005).

[15] Hugel, T. *et al.* Elasticity of single polyelectrolyte chains and their desorption from solid supports studied by afm based single molecule force spectroscopy. *Macromolecules* **34**, 1039–1047 (2001).

Part III

Pore Clogging

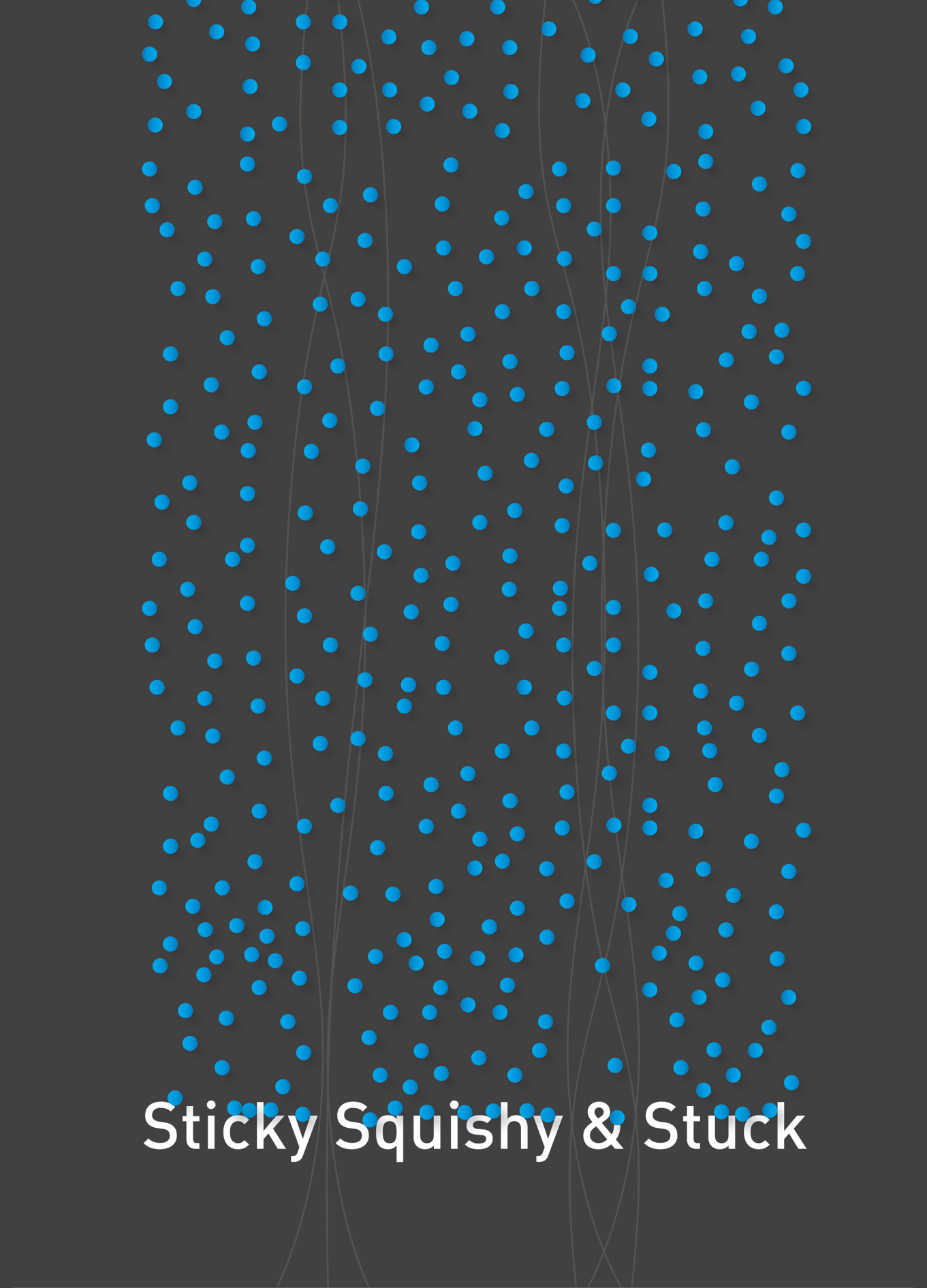
Sticky Squishy & Stuck

Chapter 9

Transition-state Theory Predicts Clogging at the Microscale

Clogging is one of the main failure mechanisms encountered in industrial processes such as membrane filtration. Our understanding of the factors that govern the build-up of fouling layers and the emergence of clogs is largely incomplete, so that prevention of clogging remains an immense and costly challenge. In this Chapter we use a microfluidic model combined with quantitative real-time imaging to explore the influence of pore geometry and particle interactions on suspension clogging in constrictions, two crucial factors which remain relatively unexplored. We find a distinct dependence of the clogging rate on the entrance angle to a membrane pore which we explain quantitatively by deriving a model, based on transition-state theory, which describes the effect of viscous forces on the rate with which particles accumulate at the channel walls. With the same model we can also predict the effect of the particle interaction potential on the clogging rate. In both cases we find excellent agreement between our experimental data and theory. A better understanding of these clogging mechanisms and the influence of design parameters could form a stepping stone to delay or prevent clogging by rational membrane design.

This chapter was published as:

T. van de Laar, S. ten Klooster, K. Schroën and J. Sprakel: *Transition-state Theory Predicts Clogging at the Microscale*, Sci. Rep. *6* (**2016**), 28450.

9.1 Introduction

Clogging is encountered at many length scales, ranging from the deposition of marginally-soluble asphaltenes at pipe walls in oil recovery [1], the formation of protein fouling layers in waste water treatment [2, 3], particle clogging during membrane filtration [4] or microfluidic operations [5, 6, 7]. Similar phenomena are encountered at much larger length scales such as in blockades of granular hopper flows [8], the emergence of traffic jams on merging lanes [9, 10] or in crowds swarming through narrow escape routes [11, 12]. It is speculated that the same physical principles govern the obstruction of flow through a narrow passage in many of these scenarios irrespective of their scale[13]. In all of these cases, preventing clogging is an immense challenge due to its often severe, costly and energy-consuming consequences. Yet this remains difficult as the generic mechanisms with which permeating flows become hindered or blocked remain largely unknown. This is especially the case for clogging at the microscopic scale as encountered during a plethora of membrane filtration processes [4].

At the microscale, clogging typically results from the accumulation of molecules or dispersed particles at a membrane surface, leading to the build-up of fouling layers; initially these reduce the permeability of channels or pores and ultimately lead to a complete blockage of the flow [4]. Fouling and clogging form one of the major sources of efficiency loss in membrane filtration processes. Remediating the formation of fouling layers and clogging as a whole currently requires complete cessation of the process, and the use of energy- and time-consuming cleaning strategies before the operation can be resumed [14]. Since the propensity of a certain flow geometry to clog depends on the ratio of its characteristic dimension to that of the particles or molecules which accumulate over time, clogging is particularly severe in microstructured devices; in addition to the obvious importance for membrane processes, the rise of microfluidics as an emerging technology makes it increasingly urgent to resolve [15].

To enable the development of effective strategies to delay fouling and the clogging that ensues, or to prevent it from occurring altogether, a deep understanding of the fundamental mechanisms that lead to this major source of efficiency-loss is essential, yet very incomplete to date. The size ratio of particles and constriction plays an important role, where two extremes can be identified.

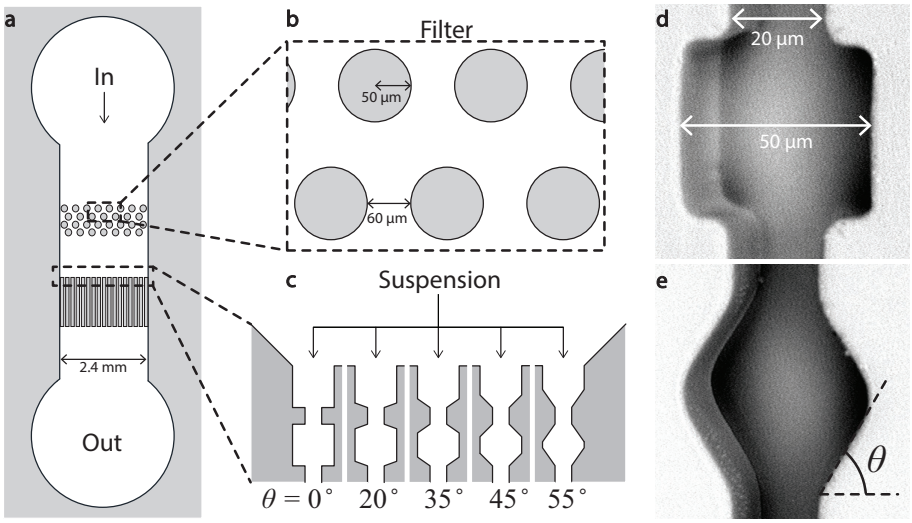

Figure 9.1: Overview of the multiplexed dead-end filtration micromodel: a) an overview of the device geometry, b) design of a pre-device filter which captures large contaminants such as dust or PDMS debris from the fluid, c) a schematic illustration of the five different entrance angles studied. Each channel features a series of 19 constrictions with identical geometry along the flow direction. For statistics each channel type is repeated 6 times on each device; this allows 6-repeat measurements and 5 different geometries to be explored in a single experiment. d) Scanning Electron Microscopy (SEM) picture of a $\theta = 0\,^\circ$ constriction with its dimensions indicated and e) a SEM picture of a $\theta = 55\,^\circ$ constriction with the entrance pore angle θ defined as indicated.

Either a single particle can block a constriction, for instance larger contaminants in a suspension of smaller particles [16] where these contaminants almost completely determine the rate of clogging. Or the case in which multiple particles are required to form an agglomerate large enough to cause bridging, so that the actual ratio between particle size and constriction width strongly determines the time it takes for clogging to occur. This results in a clogging process that appears to depend solely on the number of particles that pass through a constriction [6]. However, little is known about the influence of particle-particle and particle-wall interactions [17] and the geometry of the constrictions themselves [13].

In this Chapter we explore the influence of pore design and particle interactions on the clogging rate in dilute suspensions. We study clog formation ex-

perimentally using multiplexed microfluidic models for dead-end filtration and quantitative imaging. We observe a strong dependency of the clogging rate on both geometry and attraction strength. To account for these effects we derive an analytical model based on transition-state theory which provides a quantitative and predictive description of our experimental data.

9.2 Results and Discussion

We study clogging using a microfluidic device as a filtration micromodel, inspired by previous studies[5, 6, 7, 16]. These filtration micromodels mimic dead-end filtration. Our device consists of thirty channels in parallel; each channel consists of 19 constrictions in series with a width of 20 μm. These constrictions simulate the membrane pores and are the main site of clogging events. The thirty channels, situated next to each other, are divided in five sections of six channels. We vary the entrance pore angles, defined as θ, of the constrictions perpendicular to the flow direction between the different sections with $\theta = 55\,^{\circ}, 45\,^{\circ}, 35\,^{\circ}, 20\,^{\circ}$ and $0\,^{\circ}$. The distance between the constrictions in series (along the flow direction) is kept constant at 50 μm. We add a contaminant filter a few hundred micrometer upstream from the entrance of the device to remove large contaminants, such as dust, as these are reported to have a strong effect on the experimental observations [16]. An overview of the entire device is shown in Fig.9.1.

Upon flowing a purely repulsive suspension of particles, with a diameter of approximately 1/10 of the pore diameter, through our filtration micromodel, we observe a distinct sequence of events. Initially, all channels are permeated by the suspension. After some time, clogs begin to appear, after which the channel, upstream from the clog, becomes filled with a layer of densely packed particles, whereas only solvent permeates downstream from the blockade. This can be easily seen in our experimental images (Fig.9.2). As the flow continues, a filter cake forms due to the accumulation of particles towards the entrance of the filtration micromodel.

To characterise the statistics of clogging, we use automated image analysis to identify which channels clog when. To improve statistics, we repeat these measurements with at least 3 identical devices. We can now plot the fraction of

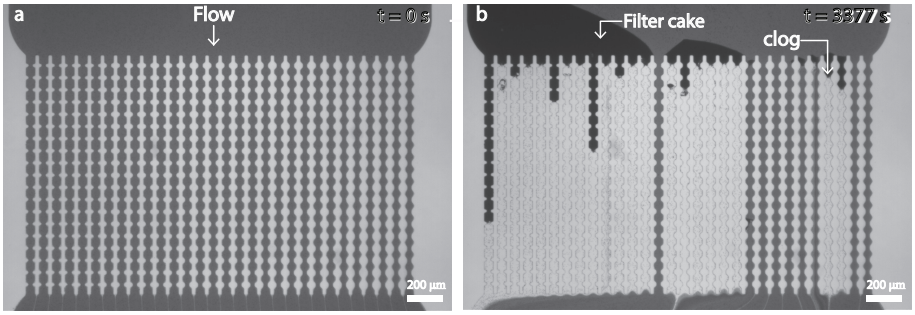

Figure 9.2: Brightfield microscopy images at t=0 (a) and t = 3377 s (b) for a repulsive suspension, in which flow direction, filter cake and a clog are indicated with arrows. Grey channels are perfused with the suspension; as a clog appears, the channel becomes white down-stream, as particle flow is blocked, while the channel turns dark upstream from the clog due to the accumulation of excess particles.

channels α which has clogged as a function of time. For the purely repulsive case, we see how α grows steadily over the course of several hours. These timescales are considerably larger than those reported previously for a similar geometry with $\theta = 0°$ [6], which we attribute to the addition of a surfactant in our experiments. This enhances the colloidal stability and prevents particle absorption to the PDMS walls [17].

As the formation of a clog requires the accumulation of multiple particles at the clogging site, a minimum clogging time must exist. In other words, at least the number of particles required to form a pore-spanning aggregate must have passed for clogging to occur. In our experiments, we flow the suspensions at high fluxes, such that this minimum time is very short compared to our experimental resolution; as such, we do not observe it with statistical significance here.

To quantify these data, we fit the experimental results to a Weibull model, often used to describe the kinetics of failure processes[18]:

$$\alpha = 1 - \exp\left[\frac{t}{\tau_c}\right]^{\beta} \tag{9.1}$$

in which, τ_c is the characteristic clogging time and β the stretch exponent, which reveals information about the underlying failure lifetime distribution. We find that β is close to unity for all values of θ; this indicates a well defined failure

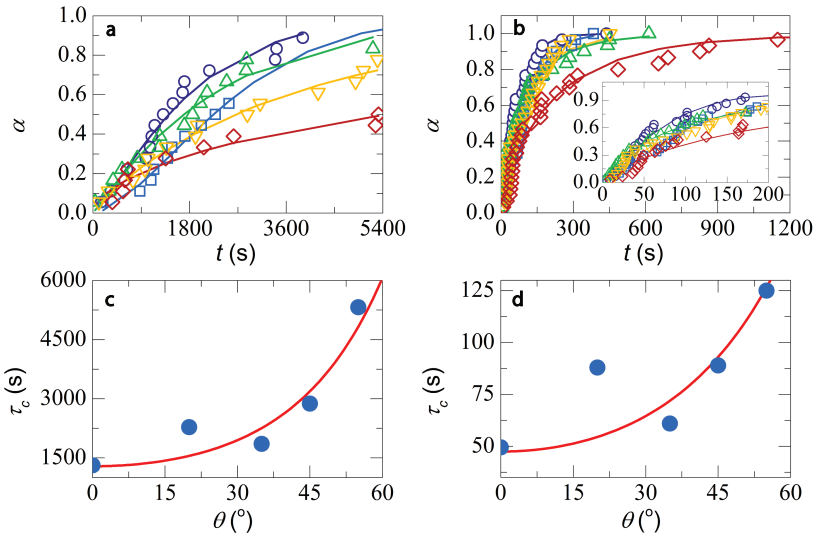

Figure 9.3: a-b: Fraction of clogged channels (α) as function of time t for a repulsive system (a) and one in which depletion attraction has been induced with $U_{dep} = 4.0$ k_BT (b) for different entrance angles θ= 0 ° (purple circle), 20 ° (blue square), 35 ° (green triangle), 45 ° (yellow triangle) and 55 ° (red diamond); lines are fits to a Weibull model. c-d: Characteristic clogging time τ_c (symbols) as function of θ for the repulsive (c) and attractive system (d). Drawn lines are a prediction using the transition-state model of Equation 9.7.

lifetime with a narrow distribution.

We find a clear impact of the pore geometry on the rate of failure of our micromodel. As the entrance angle becomes steeper, $\theta \rightarrow 0$, the characteristic clogging time decreases by almost a factor 4 as compared to the most shallow angle we study at $\theta = 55°$ (Fig.9.3c). A similar trend was observed previously for athermal grains passing through a hopper orifice [19].

The effect of channel shape on the local flow field may be responsible for the strong dependence of the failure rate on pore geometry. Our experiments are conducted at fluid Reynolds numbers around ~ 0.4; it is thus possible that corner vortices, or stagnant pockets develop for steeper entrance angles. To explore this hypothesis, we determine the flow field around a single pore entrance using particle imaging velocimetry (PIV). Interestingly, we see no deviations from

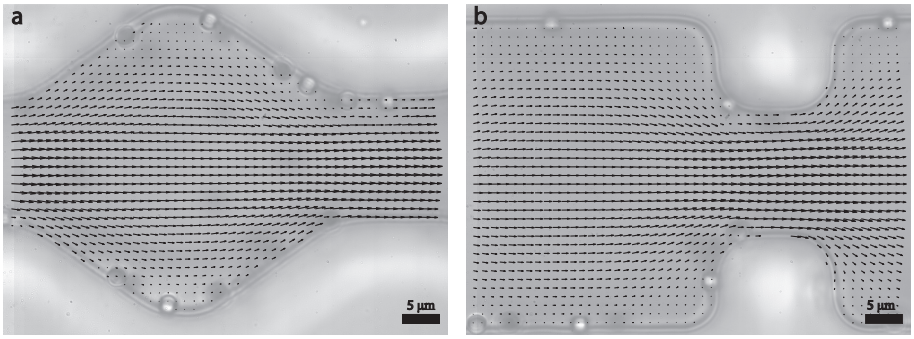

Figure 9.4: Flow profiles, as determined by PIV, of a shallow (a, θ= 55 °) and sharp entrance angle (b, θ= 0 °).

laminar flow, within our experimental resolution of $\sim$ 1μm, both for shallow and steep entrance angles (Fig.9.4). This illustrates, how local alterations of the flow field cannot explain the observed angular dependency.

Rather, we realise that clogging in the limit we investigate, i.e. where the particle size is smaller than the pore diameter, must be accompanied by the formation of particle bridges spanning the width of the channel. In turn, this must be the result of particle-wall and subsequent particle-particle aggregation. We note that at rest, these colloidal suspensions do not show any signs of particle aggregation; thus, the observed effects result purely from the combined action of confinement and flow. At the low volume fractions we study, the emergence of configurational arches, often found for granular flows[19], can be ruled out.

The potential energy of interaction between a colloidal particle and the solid wall, or between two particles, is composed of two opposing terms; at short distances, the particles will experience an attractive force due to van der Waals interactions. Typically, these van der Waals interactions for micronsized particles are sufficiently strong to induce irreversible aggregation. However, the surfactant adsorbed onto the particle surface, provides a steric repulsion that keeps the particle stabilized for some time. The combination of these two terms, results in a characteristic energy barrier of height E_{on}, that needs to be crossed before aggregation can occur (see Fig.9.5b). As a result, aggregation is thermally-activated and occurs at a rate that can be described by an Eyring-type equation as:

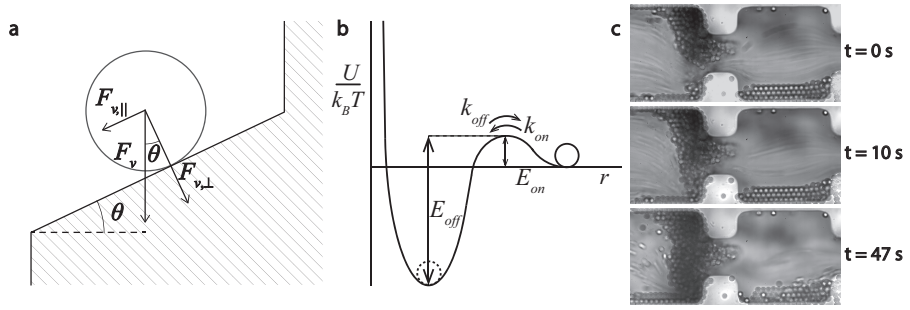

Figure 9.5: Schematic illustration of the angle-dependent viscous forces acting on a particle close to the wall (a) and the particle interaction potential with k_{on} and k_{off} the natural rate of agglomeration and detachment and E_{on} and E_{off} the corresponding energy barriers. c) a zoomed-in, time series of a clog forming at a single constriction, with flow from left to right.

$$k_{on,0} = \omega \exp\left[\frac{-E_{on}}{k_B T}\right] \tag{9.2}$$

in which ω is the attempt frequency, which can be related to the characteristic frequency of Brownian motion. In analogy, the spontaneous detachment of a particle from the wall or from a particle-particle pair can be described as

$$k_{off,0} = \omega \exp\left[\frac{-E_{off}}{k_B T}\right] \tag{9.3}$$

in which E_{off} is the energy barrier for particle dissociation.

Under flow, particles also experience a viscous force due to fluid flow around their impermeable surface. This can be approximated using the Stokes drag, neglecting lubrication effects, as $F_v = 6\pi\eta a v$, in which η is the fluid viscosity, a the particle radius and v the flow velocity of the fluid relative to the particle. For a particle which resides at a wall that is inclined at an angle θ with respect to the pore entrance, the viscous force can be decomposed in a contribution perpendicular to the surface, $F_{v,\perp} = F_v \cos\theta$, which pushes the particle against the wall, and a shearing-force which enhances detachment that acts parallel to the surface: $F_{v,\parallel} = F_v \sin\theta$, as illustrated in Fig.9.5a. For small particles, the

particle Reynolds number is low (in our experiments $Re_p \sim 6 \cdot 10^{-3}$), such that inertial lift can be ignored [20].

These hydrodynamic forces acting on particles at the channel walls will alter the agglomeration kinetics. To describe this, we adopt the transition-state approach of Kramers[21, 22]:

$$k_{on} = \omega \exp\left[\frac{-E_{on} + F_{v,\perp} \cdot \delta}{k_B T}\right] = k_{on,0} \exp\left[\frac{F_{v,\perp} \cdot \delta}{k_B T}\right] \tag{9.4}$$

where δ is the activation length, which is the range of the attractive Van Der Waals interactions, typically of order of one to a few nanometers. In an similar way, the hydrodynamic forces on the particles that act parallel to the wall, and thus perpendicular to the wall-particle bond, will aid in the natural rate of particle dissociation:

$$k_{off} = \omega \exp\left[\frac{-E_{off} + F_{v,\parallel} \cdot \delta}{k_B T}\right] = k_{off,0} \exp\left[\frac{F_{v,\parallel} \cdot \delta}{k_B T}\right] \tag{9.5}$$

in which E_{off} is the depth of the attractive Van Der Waals minimum. The balance between particle attachment and dissociation gives a total rate of particle accumulation as:

$$k = k_{on} - k_{off} \tag{9.6}$$

For the experiments we describe here, we use relatively large polystyrene particles, whose Van Der Waals interactions are very strong $E_{off} \gg k_B T$. As a result $k_{off} \approx 0$, so $k \approx k_{on}$ and therefore agglomeration will be irreversible. For a clog to appear, a sequence of several particle aggregation events must occur; this is also what we observe experimentally in a close-up of a forming clog at a single constriction (Fig.9.5c). Single aggregation events occur at a rate k; assuming that subsequent events are independent, the scaling of the overall clogging time is expected to follow $\tau_c \propto 1/k$. This leads to the following prediction for the characteristic clogging time:

$$\tau_c = \tau_0 \exp\left[\frac{-F_v \delta \cos\theta}{k_B T}\right] \tag{9.7}$$

in which $\tau_0 \propto 1/k_{on,0}$ is the characteristic time for particle agglomeration in absence of flow enhancement. We find an excellent agreement between our theoretical prediction and the experimental data (line Fig.9.3c). In this case, for surfactant stabilised polystyrene particles we find a $\tau_0 = 2.9 * 10^4$ s, reflecting the stability of the suspension towards spontaneous aggregation, and a total work performed by the drag forces to enhance agglomeration of $F_v\delta = 3.2\ k_BT$.

It has been shown previously[6, 13] that reduction of the repulsive barrier between particles strongly increases the propensity for clogging. Interestingly, our equation allows us to predict these effects by means of the effective energy barrier that particles need to cross before aggregating. Introducing an additional attractive force between the particles should reduce the energy barrier and thus enhance clogging. To explore this, we introduce a depletion interaction between the particles of U_{dep} ~4.0 k_BT; we predict that this affects the quiescent agglomeration time as $\tau_0(U_{dep}) = \frac{1}{\omega}e^{(E_{on}-U_{dep})/k_BT} = \tau_0(0)e^{-U_{dep}}$ = 470 s.

For the attractive system, we perform the same experiments and data analysis and indeed see a strong reduction in the failure time of the micromodel (Fig.9.3b). While the characteristic clogging time is two orders of magnitude lower, it shows the same dependency on pore entrance geometry. Interestingly, without additional fitting parameters our theory now quantitatively fits the experimental data (Fig.9.3d). Please note that we observe a distinct outlier in our data at a pore angle $\theta = 20°$; further investigation is required to evaluate if this effect is significant and what could be at its origin. Nonetheless, these data illustrate clearly how clogging can be strongly delayed by designing a membrane or filtration device with the appropriate geometry.

So far, we consider clogging as a process in which an independent sequence of events leads to the blockade of flow. While this allows us to make quantitative predictions of the clogging rates, we observe some cooperative effects in our experiments. First of all, we find cases where clogging of a particular channel exhibits intermittency. A clog which is formed sometimes detaches from the device walls in its entirety (Fig.9.6a-b). For the shallow angles, this occasionally leads to a full reestablishing of the permeating flow through that channel. For the steeper angles however, the clog only travels a few pores down where it anchors again.

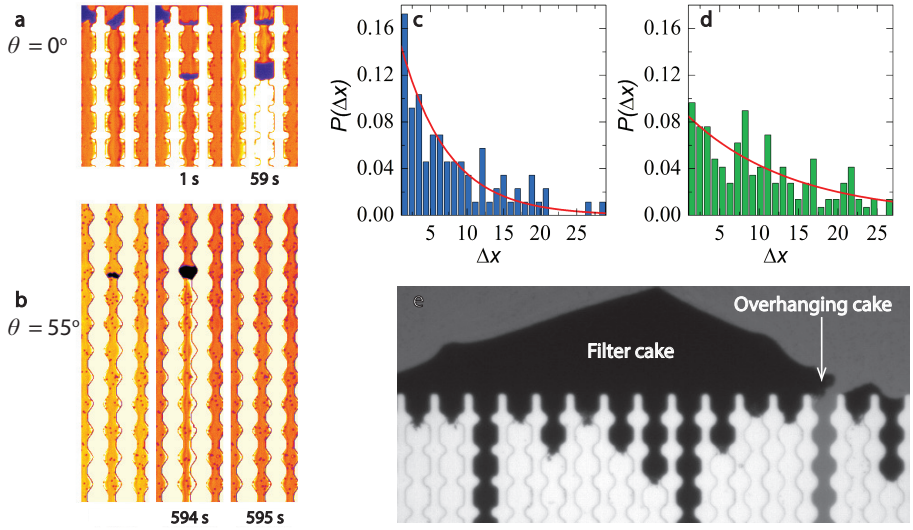

Figure 9.6: Experimental data showing detachment and displacement of an entire clog either to a new position downstream (a) or leading to complete declogging of the channel (b). Probability of the next clogging event occuring a distance Δx away, with x in units of channel number, for the repulsive (c) and attractive systems (d). Close-up brightfield microscopy image of a filtercake with overhang at the verge of blocking the neighboring channel (e)

Once a pore gets blocked, the permeation of fluid continues whereas particles cannot permeate further. As a result, a distinct filter cake develops upstream from a clog. If the filter cake grows until the top of the channel, it can form an overhanging structure, which in turn could affect the probability for the neighboring channels to clog (Fig.9.6e). To investigate this quantitatively, we determine the probability $P(\Delta x)$ that the next clogging event occurs at a distance Δx, where x is the channel number. If clogging of a single channel is fully independent, we should expect P to be independent of Δx. By contrast, we find a strong exponential dependence of the clog probability; this implies that it is more likely that neighboring channels clog in sequence, somewhat like a nucleation-and-growth scenario, rather than this happening as individual and uncorrelated events. It is important to note however, that this effect is subtle as compared to the large effect of pore geometry; thus, the pore geometry dependence can-

not be explained only by this cooperative effect but must result from the viscous force-induced particle agglomeration as discussed above.

Finally, we observe that the cooperative effect of the filter cake is more pronounced for the repulsive case, as the cake as ample time to form and will thus have a stronger effect on the spatial correlaction of clogging events (Fig.9.6c). This can be understood by considering the timescale of clogging relative to the time it takes to build up a filter cake. In dead-end filtration, the latter is governed only by the fluid flux and particle concentration, and is thus independent of attraction strength. If clogging occurs rapidly as compared to the build-up of the cake, its effect will be small (Fig.9.6d).

9.3 Conclusion

In this Chapter we describe how the mechanisms that underly particle clogging in dead-end filtration can be experimentally unravelled and quantitatively modelled. We show how, even though cooperative effects are observable, the characteristic failure rate of a filtration membrane can be understood based on the theoratical agglomeration kinetics of individual particles. Not only does this allow prediction of the strong geometry dependence of clog formation, but also of the effect of interparticle interactions.

While the micromodel presented here represents a highly idealised picture of a dead-end filtration membrane, several extensions could be imagined for future research to include complexity that is found in realistic membrane systems. For example, wall roughness, polydispersity in pore sizes or distance between pores, must be expected to have significant effects on the rate and spatial correlations of clogging. In principle, these effects could be explored with relative ease in the approach we described here. Moreover, with the microfluidic approach we use, introducing a crossflowing fluid across the membrane surface is feasible; since such a crossflow will in particular effect the filter cake build-up, it is expected to have strong effects on the cooperativity in clog events we discussed. Extending this approach, combining experimental observation on well-defined model systems and analytical theory, could lead to a deeper understanding of membrane failure and in the future provide new design rules for novel membrane systems

with improved operational lifetime.

9.4 Materials and Methods

Suspensions

We use a 4 wt% suspension of monodisperse polystyrene particles with a diameter of 3 μm in a density-matching mixture of 45 vol% water and 55 vol% deuterated water. We add 0.1 wt% pluronic F127 as a surfactant to sterically stabilise the particles. We synthesize the polystyrene particles by dispersion polymerisation [23]. In 150 ml butanol we dissolve 17 ml styrene monomer, 2.34 g poly(vinylpyrrolidinone)-k30, 0.64 g dioctyl sulfosuccinate sodium salt (AOT) and 0.170 g 2,2-azobis(2-methylpropionitrile) (AIBN). After mixing we purge the solution with nitrogen for 20 minutes and subsequently evacuate the round bottom flask. We allow the reaction to proceed overnight at 70°C. The particles are cleaned by repeated centrifugation and resuspension.

Polystyrene is well suited for this particular experiment due to the large mismatch in refractive index with the aqueous medium providing strong light scattering which we use for automated image analysis of clogging events. The particle size and concentration are chosen such that experimental clogging times are not excessively long, based on the data in [6].

In addition to the repulsive system, we also study clogging upon inducing an additional attractive force between our sterically-stabilised particles. We do so by means of the depletion interaction, that arises when small non-adsorbing colloidal particles, in this case silica nanoparticles (Ludox TM-40), are introduced to a suspension of larger microparticles [24]. The resulting attraction strength can be calculated as [25]:

$$\frac{U}{k_B T} = \frac{3}{2}\frac{a_l}{a_s}\phi_s \tag{9.8}$$

where $\frac{U}{k_B T}$ is the attraction strength in units of the thermal energy $k_B T$, a_l and a_s are the radii of the larger polystyrene particles and smaller Ludox particles respectively ($a_s \sim 7nm$) and ϕ_s is the volume fraction of the Ludox particles. For our experiments we choose an attraction strength $U \sim 4k_B T$.

Microfluidic experiments

We fabricate microfluidic devices following standard soft lithography methods [26], replica-templated from Sylgard 184 silicone rubber at a mixing ratio of 10:1. The PDMS is cured at 65 ° for at least 1.5 hours. We bond the PDMS devices onto glass microscopy slides following plasma treatment. After connecting the tubing, we flush the device with ethanol and water to remove any large contiminants which remain after device preparation. In all cases, the height of the devices is 40μm.We flow the suspension through our devices with a constant pressure of 100 mbar, controlled with an accuracy of 0.1 mbar, applied by an Elveflow OB1-MK3. By working at a constant pressure drop across the device the flow velocity per channel is constant prior to clogging and does not responds to possible clogging events in neighboring channels [27].

At this pressure difference the upper bound of the fluid Reynolds number becomes $Re_f \sim 0.4$, with a particle Reynolds number $Re_p \sim 6 \cdot 10^{-3}$ and a Peclet number $Pe \sim 5 \cdot 10^5$. These values are computed at the centre position of the bottleneck, where the flow velocity is maximum; they thus represent the upper bounds for these dimensionless numbers. This ensures complete laminar flow and domination of advective displacements of the particles[28].

The flow through the channels is imaged with brighfield microscopy (Zeiss Axiovert 200) aqcuiring images at one frame per second. Examples of the images we obtain during the experiments can be found in Fig9.2a and 9.2b. To extract quantitative data from the movies we process the images with custom analysis routines, which are available upon request. The first step in the analysis is the construction of a kymograph, in which one horizontal row of pixels is plotted as a function of time for consecutive frames. From these we can automatically recognise when and where a clogging event occurs as this leads to a distinct change in the light transmission both upstream and downstream from a clog.

We also determined the local flow fields using Particle Imaging Velocimetry (PIV) by recording a high-speed (2300 fps) movie around a single constriction with a high-speed camera (Phantom v9.1).

References

[1] de Boer, R. B., Leerlooyer, K., Eigner, M. R. P. & van Bergen, A. R. D. Screening of Crude Oils for Asphalt Precipitation: Theory, Practice, and the Selection of Inhibitors. *Society of Petroleum Engineers* **10**, 55–61 (1995).

[2] Chang, I.-S., Clech, P. L., Jefferson, B. & Judd, S. Membrane fouling in membrane bioreactors for wastewater treatment. *Journal of Environmental Engineering* **128**, 1018–1029 (2002).

[3] Ang, W. S. & Elimelech, M. Protein (BSA) fouling of reverse osmosis membranes: Implications for wastewater reclamation. *Journal of Membrane Science* **296**, 83–92 (2007).

[4] Griffiths, I. M., Kumar, A. & Stewart, P. S. A combined network model for membrane fouling. *Journal of colloid and interface science* **432**, 10–8 (2014).

[5] Genovese, D. & Sprakel, J. Crystallization and intermittent dynamics in constricted microfluidic flows of dense suspensions. *Soft Matter* **7**, 3889–3896 (2011).

[6] Wyss, H. M., Blair, D. L., Morris, J. F., Stone, H. A. & Weitz, D. A. Mechanism for clogging of microchannels. *Phys. Rev. E* **74**, 61402 (2006).

[7] Linkhorst, J., Beckmann, T., Go, D., Kuehne, A. J. C. & Wessling, M. Microfluidic colloid filtration. *Scientific Reports* **6**, 22376 (2016).

[8] Baxter, G. W. & Behringer, R. P. Cellular automata models of granular flow. *Physical Review A* **42**, 1017 (1990).

[9] Nagel, K. & Paczuski, M. Emergent traffic jams. *Phys. Rev. E* **51**, 2909–2918 (1995).

[10] Helbing, D. Traffic and related self-driven many-particle systems. *Rev. Mod. Phys.* **73**, 1067–1141 (2001).

[11] Schadschneider, A. *et al.* Evacuation dynamics: Empirical results, modeling and applications. In *Encyclopedia of complexity and systems science*, 3142–3176 (Springer, 2009).

[12] Pastor, J. M. *et al.* Experimental proof of faster-is-slower in systems of frictional particles flowing through constrictions. *Phys. Rev. E* **92**, 62817 (2015).

[13] Zuriguel, I. *et al.* Clogging transition of many-particle systems flowing through bottlenecks. *Scientific Reports* **4**, 7324 (2014).

[14] Lim, A. Membrane fouling and cleaning in microfiltration of activated sludge wastewater. *Journal of Membrane Science* **216**, 279–290 (2003).

[15] Mukhopadhyay, R. When microfluidic devices go bad. *Analytical chemistry* **77**, 429—-A (2005).

[16] Sauret, A. *et al.* Clogging by sieving in microchannels: Application to the detection of contaminants in colloidal suspensions. *Applied Physics Letters* **105** (2014).

[17] Bacchin, P., Marty, A., Duru, P., Meireles, M. & Aimar, P. Colloidal surface interactions and membrane fouling: Investigations at pore scale. *Advances in Colloid and Interface Science* **164**, 2–11 (2011).

[18] Rinne, H. *The Weibull distribution: a handbook* (CRC Press, 2008).

[19] To, K., Lai, P.-Y. & Pak, H. K. Jamming of Granular Flow in a Two-Dimensional Hopper. *Phys. Rev. Lett.* **86**, 71–74 (2001).

[20] Dinther, A. M. C., Schroën, C. G. P. H., Imhof, A., Vollebregt, H. M. & Boom, R. M. Flow-induced particle migration in microchannels for improved microfiltration processes. *Micro-*

fluidics and Nanofluidics **15**, 451–465 (2013).

[21] Hänggi, P., Talkner, P. & Borkovec, M. Reaction-rate theory: fifty years after Kramers. *Rev. Mod. Phys.* **62**, 251–341 (1990).

[22] Kramers, H. A. Brownian motion in a field of force and the diffusion model of chemical reactions. *Physica* **7**, 284–304 (1940).

[23] Paine, A. J., Luymes, W. & McNulty, J. Dispersion polymerization of styrene in polar solvents. 6. Influence of reaction parameters on particle size and molecular weight in poly(N-vinylpyrrolidone)-stabilized reactions. *Macromolecules* **23**, 3104–3109 (1990).

[24] Lekkerkerker, H. N. W. & Tuinier, R. *Colloids and the depletion interaction*, vol. 833 (Springer, 2011).

[25] Yodh, A. G. *et al.* Entropically driven self-assembly and interaction in suspension. *Philosophical Transactions of the Royal Society of London A: Mathematical, Physical and Engineering Sciences* **359**, 921–937 (2001).

[26] Xia, Y. & Whitesides, G. M. Soft Lithography. *Angewandte Chemie International Edition* **37**, 550–575 (1998).

[27] Acheson, D. J. *Elementary fluid dynamics* (Oxford University Press, 1990).

[28] Squires, T. M. & Quake, S. R. Microfluidics: Fluid physics at the nanoliter scale. *Rev. Mod. Phys.* **77**, 977–1026 (2005).

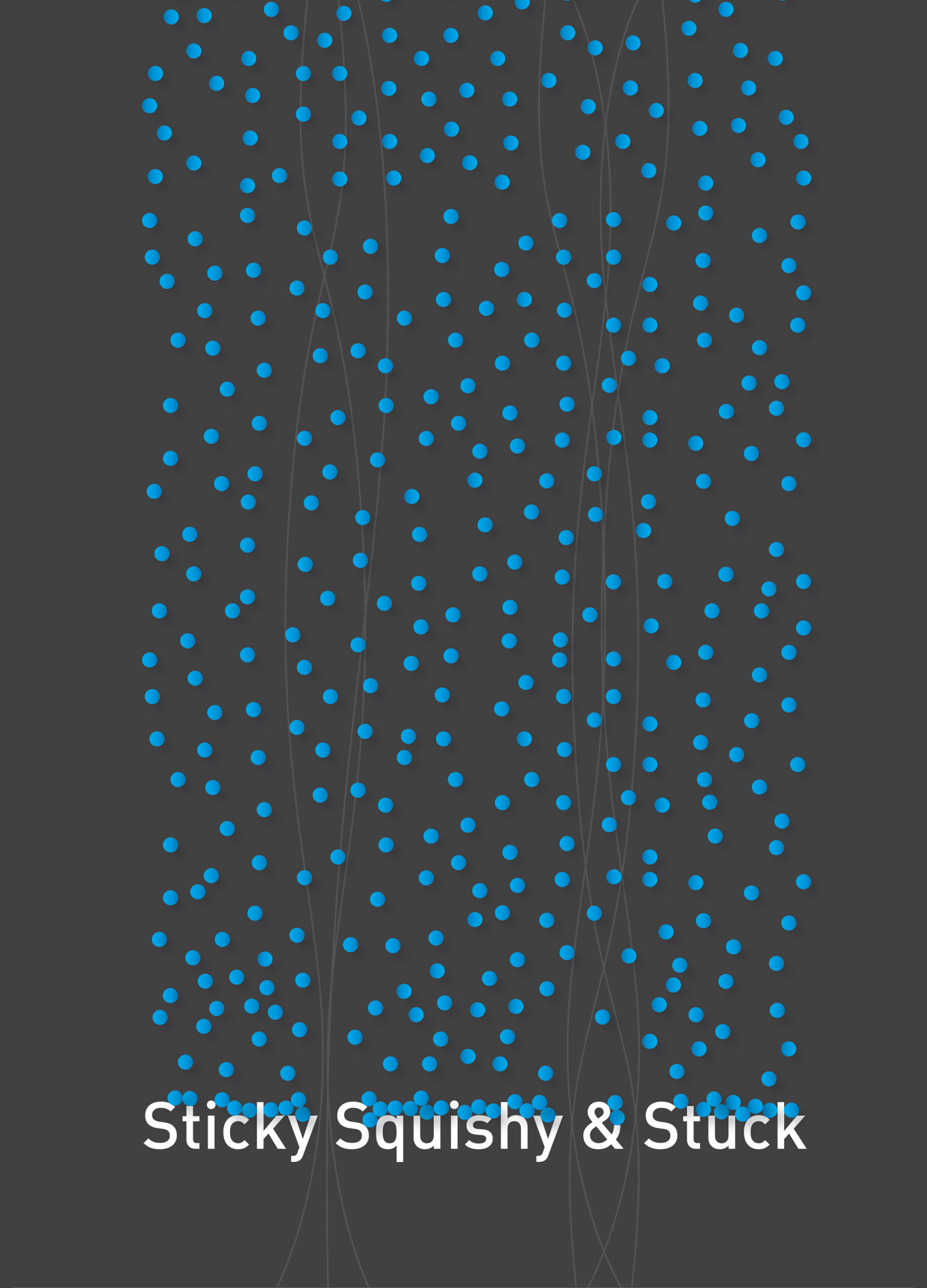
Sticky Squishy & Stuck

Chapter 10

From Cooperative to Uncorrelated Clogging in Cross-flow Microfluidic Membranes

The operational lifetime of filtration membranes is reduced by the clogging of pores and subsequent build-up of a fouling or cake layer. Designing membrane operations in which clogging is delayed or even mitigated completely, requires in-depth insight into its origins. Due to the complexity of the clogging process, simplified model membranes fabricated in microfluidic chips have emerged as a powerful tool to study how clogs emerge and deteriorate membrane efficiency. However, to date, these have focussed solely on dead-end filtration, while cross-flow filtration is of greater practical relevance at the industrial scale. As such, the microscopic mechanisms of clogging in crossflow geometries have remained relatively ill-explored. Here we use a microfluidic filtration model to probe the kinetics and mechanisms of clogging in crossflow. Our study exposes two findings: i) the primary clogging rate of individual pores depends only on the trans-membrane flux, whose strong effects are explained quantitatively by extending existing models with a term for flux-controlled flow-enhanced barrier crossing, ii) cross-membrane flow affects the pore-pore communication, leading to a transition from correlated to uncorrelated clogging of the membrane, which we explain qualitatively by deriving a dimensionless number which captures two essential regimes of clogging at the microscale.

This chapter was accepted as:

R. van Zwieten, T. van de Laar, J. Sprakel and K. Schroën: *From Cooperative to Uncorrelated Clogging in Cross-flow Microfluidic Membranes*, Sci. Rep. *8* (**2018**) , 5687.

10.1 Introduction

Membrane filtration is a crucial unit operation in a very wide variety of industrial processes, ranging from milk separation[1], pharmaceutical fractionation[2], waste-water treatment[3] and the removal of biological contaminants from donor blood[4]. Despite its ubiquitous use, the major causes of membrane performance deterioration, i.e. clogging and the subsequent build-up of filter cakes or fouling layers, remains a major challenge in the successful design of membrane operations. Clogging leads to large losses in productivity, due to reductions in flux and the cleaning required to keep the membrane functioning[5]. Different strategies exist to keep membranes operational, such as back pulsing, back flow reversal, various cleaning cycles and ultimately complete replacement[6, 7]. And while these procedures can enhance the operational efficiency to some extent, neither address the underlying mechanism of clogging[8].

Traditionally, three mechanisms for clogging are identified[9]; i) *sieving*, in which a single particle whose dimensions exceed the pore size is trapped at the pore entrance and immediately causes it to become blocked, ii) arching, in which multiple particles form a configurational arch over a pore, a scenario found in the passage of dense particulate flows through constrictions and iii) flow-induced aggregation, where multiple particles form an agglomerate by means of irreversible aggregation, either within the flow or at a pore wall, which builds gradually over time until it completely clogs a pore. In particular in the latter scenario, clogging is a complex phenomenon in which a large variety of factors play a role. Such as particle-particle and particle-wall interactions, colloidal stability, hydrodynamic interactions, the confinement ratio, particle concentration, membrane geometry, etc.[5, 10, 11, 12].

To disentangle this multidimensional phase space with the aim to arrive at a more predictive and generic description of aggregation-induced clogging[13, 14], microfluidic micromodels in which excellent and independent control can be obtained on these parameters, have proven valuable tools to study clogging at the microscale[15, 16, 17]. For example highlighting how particle interactions[16, 5, 18], polydispersity[19] and contaminants[9] play a role, the governing role of particle flux[15], the effects of complex collective dynamics[20, 21], how pore geometry influences clogging rates [17], and the effects of particle softness[22,

23, 24].

Interestingly, while most industrial processes use a cross-flow filtration strategy, in which a flux is established both across and over the membrane, these microfluidic model experiments have primarily focussed on dead-end filtration geometries. In industry, cross-flow geometries are used as they our found to remain operational longer, but the question remains what the exact mechanisms of this performance enhancement at the microscopic scale are.

In this Chapter we study clogging in a microfluidic clogging model that mimics cross-flow filtration. We study the effect of cross-flow velocity and trans-membrane flux on clogging by quantitative microscopic imaging of our cross-flow micromodel. We find that the rate of clogging only depends on the trans-membrane flux, which we explain quantitatively by extending existing models with a transition-state term that introduces the hydrodynamic enhancement of particle-wall and particle-particle sticking. Moreover, we show that the cross-flow across the membrane mainly influences the cake build-up that follows after the formation of a clog. A higher cross-flow flux reduces the rate of cake build-up and thus delays the communication and clogging between neighboring pores mediated by the filter cake. This results in a transition from correlated to uncorrelated membrane clogging; we qualitatively treat these effects by introducing a new dimensionless number describing this transition.

10.2 Results and Discussion

To study clogging in cross-flow filtration we design a cross-flow microfluidic filtration device, based on previous dead-end microfiltration designs [17, 16, 22, 9]. An overview of the device is given in Fig.10.1. A membrane is placed at the centre of a t-shaped cross-flow channel (with $W = 2.1$ mm) and consists of 30 parallel pores (width of pore, $L = 50\mu$m), each having 19 constrictions in series, with $L_c = 20\mu$m. All constrictions within the 30 parallel pores are equal and have the same 90 degree entrance angle (as shown in Fig.10.1c). The distance between the constrictions in a single pore along the trans-membrane flow direction is kept constant at 50 μm. As we aim to study clogging by aggregation, we need to eliminate large contaminants[9] from our fluid streams by means of a coarse

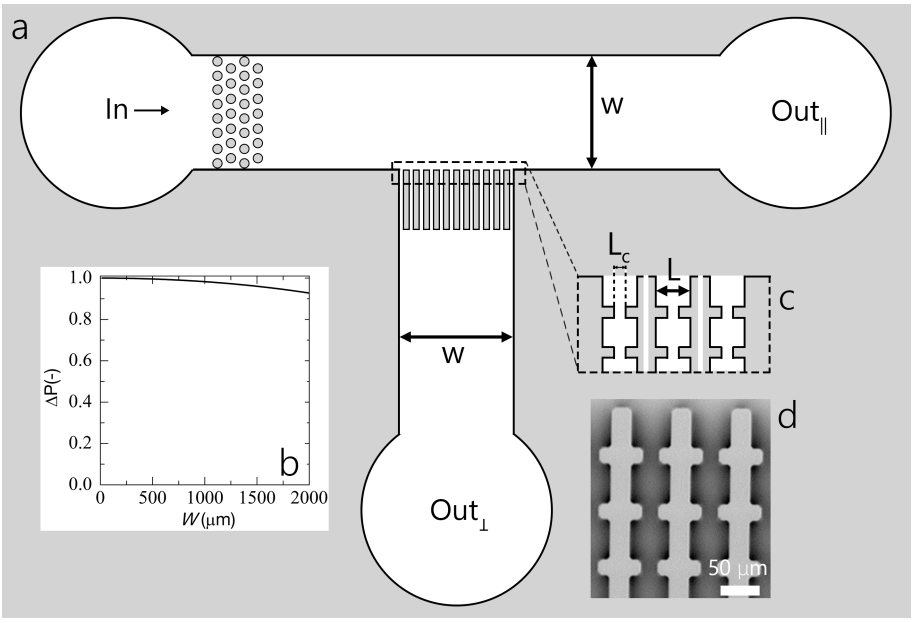

Figure 10.1: Overview of the multiplexed cross-flow filtration micromodel: (a) the device geometry, (b) the relative pressure drop over the total width of the multi-pore membrane , (c) detailed zoom-in to illustrate the membrane pores in more detail. Each pore features 19 constrictions in series, each of identical geometry, along the flow direction. The membrane consists of 30 pores within the same device; this allows 30-repeat measurements in a single experiment and the exploration of pore-pore communication. (d) Scanning Electron Microscopy (SEM) picture of the membrane micromodel.

pre-filtration element. This contaminant filter is composed of a hexagonal micropillar array a few hundred micrometers before the membrane (circles in Fig. 10.1a). As a reference measurement, we also study dead-end filtration in the same device, by leaving the cross-flow outlet ($out_{||}$ in Fig.10.1a) closed, so that all flow is directed through the membrane.

We flow a dilute suspension (3% wt) of polystyrene particles (radius $a \approx 1.2\mu$m, such that the confinement ratio is roughly a factor 8) through our micromodel using a pressure controlled set-up, where we can vary the pressure to change the cross-flow and trans-membrane fluxes (see Materials and Methods for details). Initially all pores transport dispersion, until a clog forms at one of the constrictions within the pore. Following the initial clog formation, the clog

acts as a sieve such that fluid passes but particles do not; as a result a filtration cake forms, first inside the pore and eventually spilling over the top of the membrane structure. As in our previous study on dead-end filtration, we accelerate the clogging process to within a realistic experimental time window by inducing a weak depletion attraction between our particles.

Inherently, the cross-flow design implies a pressure drop across the membrane from the first to the last pore. We have designed our devices in such a way to minimize this pressure drop such that each pore experiences almost the same initial conditions. We calculate the pressure drop across the 30-pore membrane using the Hagen-Poiseuille law[25]:

$$P = P_0 - \frac{32\eta\bar{u}}{d^2}(x - x_0) \tag{10.1}$$

where P_0 is the pressure at the first pore, η is the viscosity of the fluid, $\bar{u}$ is the average particle velocity, d the hydraulic diameter of the tube, x_0 the start of the membrane and x the position along the membrane surface ranging from x_0 to the end of the membrane. We approximate d^2 by the area of the entire membrane. As shown in Fig. 10.1b, the relative pressure drop is small for all conditions studied here, where W represents the width of the entire membrane surface.

Our experiments are run at fixed pressure as this ensures that clogging of one or more pores does not change the trans-pore flux for the remaining open pores. We directly measure the trans and cross-membrane fluxes at all applied pressures by collecting the outcoming fluid on a analytical balance when a particle-free fluid is flowed through the device. We average these data by collecting data for at least 90 minutes to ensure a high statistical certainty on these numbers. In this way, we determine directly both the cross-flow flux ($Q_{||}$) and the trans-membrane flux (Q_T).

Primary clogging rate

In order to obtain statistical information about the rate at which our cross-flow micromodel clogs we determine the time at which each separate pore clogs. To detect clogging events in individual pores we make use of the change in transmitted light intensity in a pore at the singular event of clogging. Initially, the

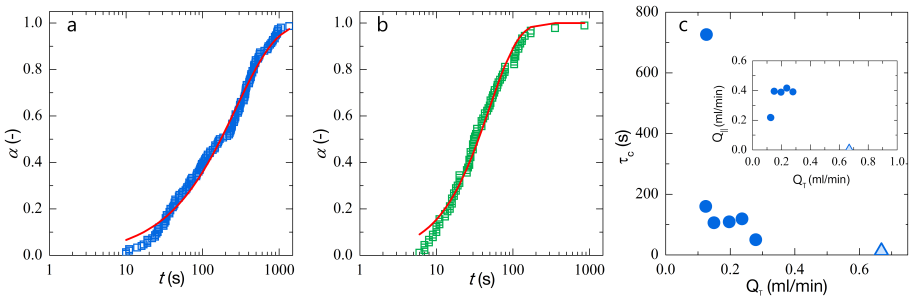

Figure 10.2: Fraction of clogged channels α as a function of time at a flow rate of 0.13 (a) and 0.24 ml/min. (b). (c) Characteristic clogging time τ_c as a function of trans-membrane flux. The light blue triangle in (c) represents the clogging time for dead-end filtration. The inset in (c) shows the relation between cross and trans membrane fluxes for all experiments described in this Chapter.

pore is permeated with the suspension, which creates a medium grey level in our brightfield tranmission imaging set-up due to weak scattering of the particle-laden fluid. As a pore clogs we observe a distinct change: downstream from the clog the intensity increases as only fluid permeates the clog and thus no scattering centres (particles) are found downstream, while the intensity decreases upstream as a filter cake builds. We threshold this raw data and subsequently use automated image analysis to detect when and where a clogging event occurs. We repeat each experiment in triplicate to ensure reasonable statistical certainty on the data discussed below.

We start by calculating the fraction of channels that have clogged, α, as a function of time after the suspension first enters the membrane. We observe that as time progresses more and more pores become clogged, with α showing a gradual increase over time (see Fig.10.2a). As we increase the trans-membrane flux, we see that α grows more rapidly as a function of time, i.e. clogging occurs faster (see Fig.10.2b, where Q_T is two times that of Q_T for Fig.10.2a).

To describe the dependence of α as a function of time we use the Weibull model[26], which describes clogging as a cascade of individual failure processes. The Weibull model is commonly used to describe a wide variety of failure kinetics which obey weakest-link scaling, such as many manufacturing processes and their produced goods[26], including those found in dead-end filtration[17]. The

Weibull distribution is formulated as:

$$\alpha = 1 - \exp\left[\frac{t}{\tau_c}\right]^{\beta} \tag{10.2}$$

where τ_c is a characteristic clogging time and β is the stretch exponent, which indicates the statistical distribution of failure times for individual pores. We fit the model to our data using least-squares regression, and find good quantitative agreement at all applied flow rates. We see that for all flow rates the value of β is close to unity, which indicates clogging occurs through a Poisson process with a well-defined characteristic failure time. Also here we note, that we have observed identical behavior in pure dead-end filtration in a similar geometry[17].

We measure τ_c for a given flux and plot these as a function of the trans-membrane flux, which was determined independently. We see that as the trans-membrane flux (Q_T) increases τ_c decreases dramatically (Fig.10.2c). We observe that τ_c strongly depends on Q_T, but how does it depend on the cross-flow flux? As these experiments are all performed at constant pressure to account for flow rate differences due to clogging it is impossible to independently vary the cross-flow and trans-membrane flow, as shown in the insert in Fig.10.2c. However, as the expectation is that cross-flow increases the clogging time, and we observe the opposite correlation, we postulate that in these cases the dominating factor governing the failure time is the trans-membrane flow. This is supported by the fact that for the two cases with the lowest values of $Q_{||}$, we find almost 3 orders of magnitude difference in τ_c, where the blue triangle in Fig. 10.2c represents a reference experiment in the same micromodel operated in dead-end mode, without any cross-flow over the membrane. We can also compare our results to those previously found in our dedicated dead-end microfiltration model[17]. At comparable flow rates and conditions we find that τ_c is in the same order of magnitude for both the cross-flow system and our dead-end system[17]. While a direct comparison is difficult due to different particle sizes and attraction strengths, the closest comparison shows that $\tau_c \approx 150$s for cross-flow and $\tau_c \approx 160$s for dead-end filtration[17]. Which again seems to indicate that τ_c here depends on Q_T, and not on the cross-flow flux $Q_{||}$.

To explain the steep decay in clogging time τ_c on the transmembrane flux Q_T we first consider the explanation for clogging postulated previously by others[16].

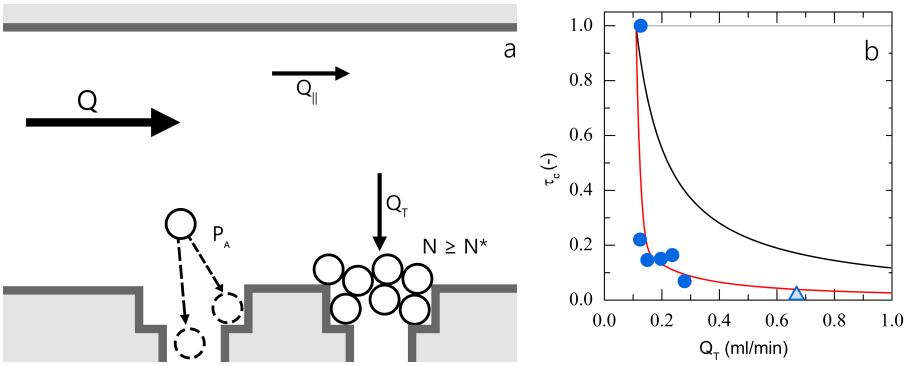

Figure 10.3: (a) Schematic representation of the clogging process, see main text for details. Normalised clogging time as a function of trans-membrane flux (b), where the symbols are experimental data, the red line is a fit to the model developed in this article, the black line indicates the prediction from previous theory in which hydrodynamic-enhancement of P_a is not accounted [16] and the grey horizontal line indicates the dependency found when taking the model of [16] and introducing the effects of residence time without hydrodynamic-enhancement of aggregation.

Here it is proposed that clogging occurs when a critical number of particles have passed the constriction, which would predict a dependency of $\tau_c \propto 1/Q_T$; as shown by the black line in Fig.10.3b, the experimentally observed decay is much steeper. Clearly, some additional effects must be taken into account. The previous explanation did not consider that the longer a particle resides in a pore, the higher its probability of sticking to a wall becomes. If these residence time effects are taken into account, with the residence time t_R scaling with $1/Q_T$, a flux-independent clogging rate would be expected (grey horizontal line in Fig.10.3b). It is clear that some additional effect must be considered to explain the experimentally observed steep decay of the clogging time with trans-membrane flux.

We reformulate the previously proposed model[16] in order to explain our observations, such that it takes the hydrodynamic enhancement of particle aggregation into account using a transition-state argument. We consider clogging as the consequence of sequential particle sticking events to the pore walls or particle agglomerates previously formed on those walls. When a critical number of particles N^* has accumulated on the walls, a clog will form. Note that we ignore the finite, but small, probability that a particle detaches from a grow-

ing agglomerate, i.e. we only consider particle association occurring at a rate k_a and the rate of dissociation $k_d \approx 0$ is assumed to be negligible. This assumption will be discussed in more detail below in the context of cake formation and erosion. We presume that particle sticking is a thermally-activated and mechanically-enhanced process, governed by thermal fluctuations and thus probabilistic in nature.

We identify two opposing effects. First, the probability of particle aggregation depends on its residence time in or near the constriction; the longer a particle resides near the constriction, the larger the probability it will stick and become immobilized. Thus, this predicts a decrease in the particle sticking probability P_a with trans-membrane flux Q_T (see Fig. 10.3a for a schematic illustration). Secondly, at higher fluxes the flow velocities and thus viscous drag forces exerted on the particles will be larger. These viscous forces can push particles against the wall, thereby enhancing the rate at which they cross the activation barrier for aggregation, and thus increasing their sticking probability with trans-membrane flux. The first effect predicts an increase in clogging time with Q_T, while the second decreases the clogging time.

For thermally-activated particle association onto a wall or existing pre-clog, the association process exhibits a Poisson distribution. The probability that a particle remains free P_f decays with the time it has been in proximity to the wall or pre-clog as:

$$P_f = e^{-k_a t} \tag{10.3}$$

where k_a is the association rate constant. The probability that a particle is stuck after a residence time t_R thus becomes:

$$P_a = 1 - e^{-k_a t_R} \tag{10.4}$$

Where the residence time t_R depends on the mean local flow velocity $\bar{v}$ and constriction length l as

$$t_R = \frac{l}{\bar{v}} \tag{10.5}$$

We can estimate the mean flow velocity from the flux as $\bar{v} = Q_T/An$, where A

is the cross-sectional area of one constriction and $n = 30$ the number of pores in parallel in our membrane micromodel design. Substituting the result above, yields for the sticking probability:

$$P_a = 1 - \exp\left[\frac{-k_a l A n}{Q_T}\right] \tag{10.6}$$

The rate of particle aggregation events k_a was established previously to be significantly enhanced by viscous forces acting on the particles in the shear flow [17]. These viscous forces can be approximated as the Stokes force on a spherical particle $F = \bar{v}\zeta = \frac{Q_T \zeta}{An}$, with $\zeta = 6\pi\eta a$ the Stokes drag coefficient in which η is the fluid viscosity and a the particle radius. Within the transition-state picture[27, 28] of thermally-activated and mechanically-enhanced processes the association rate constant can be defined as

$$k_a = k_{a,0} \exp\left[\frac{F\delta}{k_B T}\right] = k_{a,0} \exp\left[\frac{Q_T \zeta \delta}{k_B T A n}\right] \tag{10.7}$$

in which $k_B T$ is the thermal energy, δ the activation length, corresponding to the range of the attractive Van der Waals forces responsible for aggregation, typically in the order of one nm, and $k_{a,0}$ the aggregation rate constant in the absence of shear forces, which is set by the energy barrier that keeps the particles stable in suspension.

Finally, we suppose that clogging requires the sequential aggregation of a critical number of particles N^*, as shown in the right part of Fig. 10.3a. The number of stuck particles N increases with time as:

$$N = Q_T \rho P_a t \tag{10.8}$$

in which ρ is the number density of particles in the fluid stream that crosses the membrane at flux Q_T, which stick with a probability $P_a(t_R)$. At the clogging time $t = \tau_c$, the critical number of particles is reached $N = N^*$, such that the clogging time can be approximated as

$$\tau_c = \frac{N^*}{Q_T \rho P_a} \tag{10.9}$$

Using Equations 10.6, 10.7 and 10.9 we can now explore the dependence of the

characteristic clogging time on the trans-membrane flux, accounting for both the reducing effects of shorter residence times at higher fluxes and the enhancing effects of larger viscous forces at higher Q_T.

As can be seen from Fig.10.3b, our proposed theory provides a good qualitative explanation of the observed data. Thus indeed, an accurate predictive description of pore clogging must take the force-enhancement of barrier crossing into account. We note that to describe our data, we need a value of δ which is significantly smaller than that expected based on the geometry of our system ($\delta = 2^{-11}$ m), this difference could lie in the simplification made in the calculation of P_a using equation 10.6. Namely, this probability does not take into account that only a small fraction of all the particles that flow through the membrane gets in close enough contact with the membrane walls to be able to stick. Thus, while this approach is approximate and mean-field in nature, it appears to capture qualitatively the underlying physics. This also calls for the development of new and more precise models to describe these effects from a microscopic picture of the entire process; this is however out-of-scope for this Chapter. Based on these values we find a sharp increase in P_a as the transmembrane flux increases, going from almost zero at quiescent conditions ($P_a \approx 0.001$) to unity at higher fluxes ($P_a = 1$ for $Q_T > 0.2$ml/min); indeed, we find that at rest the dispersion is colloidally stable which must imply a very low value of P_a in the absence of hydrodynamic forces. We see that the behavior of P_a perfectly mirrors that of τ_c, where at low flow rates sticking is highly unlikely (resulting in a long clogging time), and as the flow rate increases $P_a \approx 1$ and τ_c decreases rapidly. Thus, the hydrodynamic enhancement of particle aggregation appears to be the dominant term in governing the rate of clogging.

Interestingly, our experimental data of clogging time versus flux cannot be described by considering only the passage of a critical number of particles, but requires taking hydrodynamically-enhanced barrier hopping into account, in contrast to the previously published data of Wyss et al.[16] that shows a simple reciprocal dependency on the flux. These two results are thus in apparent contradiction. Based on the work of Dressaire et al.[9], it has become clear that i) commercial dispersions often used in these experiments contain a very small (ppm) fraction of large contaminants which ii) lead to clogging by sieving which dom-

inates the clogging behavior if no precautions are taken to remove them prior to the dispersion arriving at the microfluidic model. Indeed, if large impurities clog a pore singularly and this determines the clogging rate, a simple reciprocal dependence on flux must be found. In both of these previous works, carboxylated polystyrene particles are used, prepared by emulsion polymerisation, in which it is known that small amounts (1 in 1 million[9]) of much larger particles are inevitably present. In this case, clogging occurs through a completely different mechanism. This could thus be the reason of the apparent contradiction remarked upon above. By contrast to these previous studies, we have introduced a micropillar filter at the entrance of our device, with the specific goal of removing such large impurities, thus enabling us to probe clogging by aggregation of the primary small particles under study. This hypothesis is further substantiated by the large difference in clogging times, despite working at similar volume fractions and pore-particle size ratios; e.g. in the work of Dressaire and Wyss, typical clogging times are in the range of 0.1-100 seconds[16, 9], while in our case for repulsive suspensions clogging takes one or two orders-of-magnitude longer, with clogging times ranging from half an hour to several hours[17].

Pore communication

Based on our experimental results, the transition-state model and comparison to previous results for dead-end filtration with the same particle dispersion[17], it becomes clear that application of a cross-flow flux does not impact the primary clogging process in these experiments. In our case, primary clogging, which is the singular event in which the flow of particles through the pores becomes blocked, occurs within the membrane, where the eroding effects of the cross-flow are negligible. However, while cross-flow does not alter the primary clogging rate of individual pores, it does effect the rate of failure of the membrane as a whole.

To date, the clogging of membrane micromodels has been described as the uncorrelated clogging of n individual pores. However, the growth of the filter cake on top of the membrane as the result of a single pore clogging, may affect the clogging rate of its neighbors. In such a scenario, clogging may become strongly

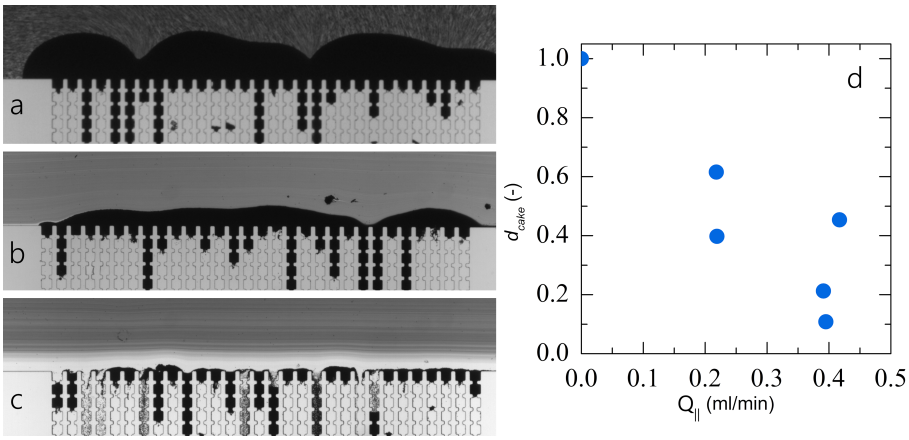

Figure 10.4: Representative images illustrating the formation of a filtercake during (a) dead-end filtration in our cross-flow micromodel, (b) cross-flow filtration at a cross-flow rate of 0.219 ml/min and (c) 0.395 ml/min. (d) Cake thickness d_{cake} as a function of cross-flow flux.

cooperative in which the clogging of a single pore enhances, through the filter cake, the clogging of neighboring pores and thus the failure of the membrane as a whole.

We first investigate how the cross-flow induced shear forces acting on a growing filter cake effect its thickness. We visually notice a significant reduction in the cake layer build-up when the cross-flow velocity is increased (see Fig.10.4a-c). From these microscopy images we can calculate the average cake thickness over the entire membrane structure; indeed, we find a strong decrease in the cake layer thickness as the cross-flow flux increases (Fig.10.4d).

The difference in cake build-up between dead-end (Fig.10.4a) and cross-flow filtration (see Fig.10.4b-c) are significant in two ways. First, the delay in cake growth reduced the growth in hydrodynamic resistance across the membrane and thus delays the time at which the pressure-flux relation deteriorates to such an extent that cleaning of the membrane is required. Secondly, if the filter cake mediates the communication between pores and thus the cooperativity of the failure of the membrane, cross-flow could change the mode of membrane failure.

To explore the extent of pore-pore communication we ask the question how

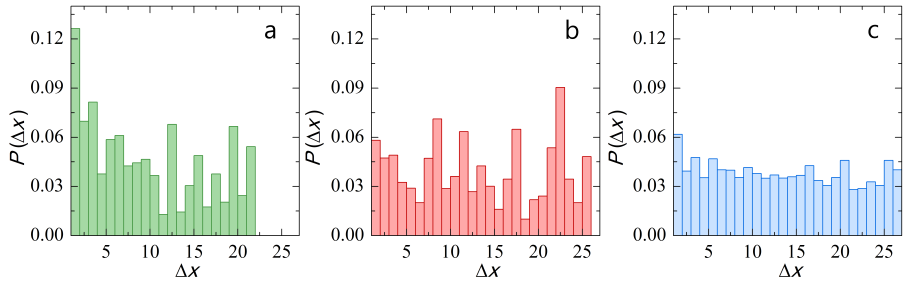

Figure 10.5: Weighted probability distributions of the distance to the next clogging event, where the distance Δx is expressed as the number of pores between two consecutive clogging events, for (a) dead-end filtration for purely repulsive particles, data as in[17] (b) dead-end filtration for a suspension with attractive forces ($U \approx 4k_BT$, data as in[17] and (c) cross-flow filtration for all combined data in this Chapter. The probability distributed are weighted for the conformational entropy as dictated by the device design, as described in the text.

the clogging of a given pore affects the clogging rate of its neighbors. To answer this question, we determine the distance, counted in number of pores, between to consecutive clogging events. If the clogging is uncorrelated, the distance between two clogging events should show a flat distribution, where the probability of finding the next clogging event some distance Δx away shows no preference for neighboring clogs. By contrast, if the clogging is correlated and cooperative, the probability of finding the next clogging event should be largest for the shortest distance Δx and decay rapidly after that.

For a fair evaluation of the distance-dependence of the next-clogging probability, we must account for the relative occurrence of possible pore distances by calculating a weighted probability function, where we assign weights to each value for Δx, based on how often this possibility can occur in our micromodel. This is essentially a weighting for the configurational entropy of the clogging process. For example, while almost every pore (except the most left and most right one) will have two pores at $\Delta x = 1$, only 2 out of the 30 pores will have a possible $\Delta x = 29$.

We find that for dead-end filtration of a purely repulsive system (Fig.10.5a, data reproduced from[17]) clogging is indeed strongly correlated, with the probability peaking at $\Delta x = 1$, mediated by overhanging filter cake[17]. Interesting,

we find that two changes in the set-up both reduce the correlations and lead to uncorrelated membrane failure: i) increasing the primary clogging rate by making the particles weakly attractive (Fig.10.5b) and introducing strong cross-flow (Fig.10.5c).

To explain this transition from cooperative to uncorrelated clogging of multipore membranes we must realize that two different rates play a role. On the one hand we have the primary clogging rate which dictates the rate at which particle-aggregation induced clog formation leads to pore blockage. On the other hand we have the rate of filter cake build-up; if the rate of cake build-up and spill-over into neighboring pores is much faster that the primary clogging rate, the clogging process becomes cooperative. By contrast, if primary clogging occurs more rapidly than cake-induced clogging, we must find an uncorrelated membrane failure processes.

The typical time it takes a single pore to clog is prescribed by Eq.10.9 as: $\tau_c = N^*/(Q_T \rho P_a)$. The characteristic time τ_{fc} it takes a growing filter cake to reach the neighboring pore, in a simplified picture, is a balance between growth rate $\dot{h}_+$ (in m/s) and the cross-flow induced erosion rate $\dot{h}_-$ (in m/s), as $\tau_{fc} = l/(\dot{h}_+ - \dot{h}_-)$. In this relation, l is the average depth within the pore at which a clog occurs, which itself is governed by a Poisson distribution for a device with many identical constrictions in series. The rate of cake growth depends on the flux through the pore Q_T/n, the volume fraction of particles in the incoming stream ϕ and the maximum close-packing volume fraction ϕ_c as:

$$\dot{h}_+ = \frac{Q_T \phi}{n A_p \phi_c} = \frac{Q_T \rho a^3}{n A_p \phi_c} \tag{10.10}$$

in which A_p is the cross-sectional area of the pore. The rate of cake erosion $\dot{h}_-$ will depend on the height of the cake on top of the membrane, the shear forces acting on the particles within the cake governed by $Q_\parallel$ and details of the particle-particle interactions in the cake, following a similar transition-state argument as derived above. For the purposes here of arriving at a qualitative understanding of the transition from cooperative to uncorrelated clogging, we simply assume that the erosion rate is a positive function of the cross-flow velocity $\dot{h}_-(Q_\parallel)$; a more quantitative analysis of the erosion rate is too involved for the current

purposes and may be topic for future study.

This allows us to define a dimensionless clogging number Cl as the ratio of the primary clogging time and the cake build-up time as:

$$Cl = \frac{\tau_c}{\tau_{fc}} \tag{10.11}$$

which defines the transition from correlated and cooperative membrane failure when $Cl \gg 1$ to uncorrelated failure of the membrane by a independent sequence of primary clogging events when $Cl \ll 1$.

With the above we can define the clogging number for crossflow filtration as:

$$Cl = \frac{N^*}{Q_T \rho P_a l} \left(\frac{Q_T \rho a^3}{\phi_c A_p} - \dot{h}_-(Q_\parallel) \right) \tag{10.12}$$

which can be simplified for dead-end filtration when $\dot{h}_-(Q_\parallel) = 0$ to:

$$Cl = \frac{N^* a^3}{P_a l \phi_c A_p} \tag{10.13}$$

which interestingly depends only on the pore geometry (N^*, l and A_p) and the particle stability (P_a).

Indeed, our experiments highlight how either increasing the sticking probability P_a, by introducing attractions (Fig.10.5b), or increasing the erosion rate $\dot{h}_-(Q_\parallel)$, by increasing $Q_\parallel$ (Fig.10.5c), can lower Cl to such an extent that the cooperativity of the membrane failure disappears, leading to an increasing in the membrane lifetime.

10.3 Conclusion

In this Chapter we explored the effects of trans- and cross-membrane fluxes on the clogging of pores and failure of multi-pore membranes. We find that the primary clogging occurs within the pores where it is unaffected by the cross-flow. Moreover, we show how the trans-membrane flux has a much steeper adverse effect on the clogging rate than predicted previously. We quantitatively explain these effects by introducing a term to account for the hydrodynamic enhance-

ment of particle aggregation into existing clogging theories. Finally, we show how the crossflow does not alter the primary clogging rate but alters the communication between pores in a multi-pore membrane. We find that the extent of pore-pore communication can be tuned by changing the ratio of the primary clogging rate versus the rate of cake build-up, leading to a transition from cooperative to uncorrelated clogging. We rationalize these finding by deriving a new dimensionless clogging number and support this concept using experimental observation of the pore-pore correlations. This exploratory study on the microscopic mechanisms of cross-flow filtration are performed in highly idealised conditions. Exploring the effects of non-uniform pore sizes, pore-pore fluid connections and the effects of particle properties and dispersity would be an interesting avenue for further research, as this would bridge the gap between the model approach taken here and the real world of membrane filtrations in industrial applications. Nonetheless, our findings give rise to deeper insight into the dominant mechanisms that govern clogging and membrane failure, and could form a stepping stone for the more efficient design of membrane operations with enhanced operational lifetime.

10.4 Materials and Methods

Experimental system

We use a 3 wt% suspension of monodisperse polystyrene particles, prepared by dispersion polymerization [29], with a diameter of 2.4 μm in a density matching mixture of 63 vol% water and 37 vol% deuterium oxide. We add 0.1 wt% pluronic F127 as a surfactant to sterically stabilize the particles and to prevent particle absorption to the PDMS walls [5]. The particle synthesis proceeds as follows: in 150 ml butanol we dissolve 17 ml styrene monomer, 2.34 g poly(vinylpyrrolidinone)-k30, 0.64 g dioctyl sulfosuccinate sodium salt (AOT) and 0.170 g 2,2-azobis(2-methylpropionitrile) (AIBN). We mix and purge the solution with nitrogen for 20 minutes to remove all oxygen and leave the flask under vacuum to perform the reaction. The reaction is left to proceed overnight at 70°C. The particles are cleaned by repeated centrifugation and resuspension cycles in which we slowly exchange from the alcoholic reaction solvent to the aqueous solvent mixture in

our experiments.

We induce weak attractive forces between the polystyrene particles, as this reduces the total time required for clogging and thus increases the efficiency of the experimental procedure, while maintaining the overall clogging behavior; these effects for the identical system have been explained in detail previously[17]. We introduce these attractive forces using depletion interaction, via the addition of silica nanoparticles (Ludox TM-40)[30], and estimate the resulting attraction strength as[31]:

$$\frac{U}{k_B T} = \frac{3}{2}\frac{a}{a_s}\phi_s \tag{10.14}$$

where U is the attraction strength in units of the thermal energy $k_B T$, a and a_s are the radii of the larger polystyrene particles and smaller Ludox particles respectively ($a_s \sim 7nm$) and ϕ_s is the volume fraction of the Ludox particles. For our experiments we choose an attraction strength $U = 2k_B T$, in between those used previously[17]. Prior to each experiment, the particle suspension is sonicated to make sure no particle aggregation occurs at rest.

Microfluidic experiments

We fabricate the microfluidic devices using standard soft litography methods[32]. The pattern is replica-templated in Sylgard 184 silicone rubber at a mixing ratio of base to catalyst of 10:1. We cure devices at 65° for at least 1.5 hours, and subsequently bond them onto glass slides using a oxygen-plasma treatment. In all of our experiments, the devices have a height of 40 μm. We use pressures of 28, 45, 63, 98, 133 and 168 mbar, controlled with an accuracy of 0.1 mbar, applied with an Elveflow OB1-MK3 pressure controller, resulting in transmembrane fluxes of 0.13, 0.23, 0.12, 0.15, 0.20 and 0.28 ml/min, respectively. The experiments are run at constant pressure such that the flux per pore remains constant, irrespective of the clogging of its neighbors [33]. One reference experiment was performed in dead-end geometry with the same device, at the highest inlet pressure of 168 mbar, while keeping the outlet orthogonal to the membrane closed. This results in a transmembrane flux of 0.67 ml/min.

We calculate the upper bound of the fluid Reynolds number to be $Re_f \leq 3$,

thus ensuring laminar flow conditions. The particle Reynolds number is computed to be $Re_p \leq 10^{-3}$ ensuring no inertial effects that may contribute to complexity in the clogging phenomena. The particle Peclet number is $Pe \sim 10^4$ indicating a flow dominated by advection. The microfluidic experiments are imaged using standard brightfield transmission microscopy (Zeiss Axiovert 200) equipped with a ThorLabs USB camera, at an acquisition rate of 1 Hz. The raw image time sequences are analyzed using a set of custom image processing routines as described previously[17].

References

[1] Brans, G., Schroën, C., Van der Sman, R. & Boom, R. Membrane fractionation of milk: state of the art and challenges. *Journal of Membrane Science* **243**, 263–272 (2004).

[2] Charcosset, C. Membrane processes in biotechnology: an overview. *Biotechnology advances* **24**, 482–492 (2006).

[3] Le-Clech, P., Chen, V. & Fane, T. A. Fouling in membrane bioreactors used in wastewater treatment. *Journal of membrane science* **284**, 17–53 (2006).

[4] Eknoyan, G. *et al.* Effect of dialysis dose and membrane flux in maintenance hemodialysis. *New England Journal of Medicine* **347**, 2010–2019 (2002).

[5] Bacchin, P., Marty, A., Duru, P., Meireles, M. & Aimar, P. Colloidal surface interactions and membrane fouling: Investigations at pore scale. *Advances in Colloid and Interface Science* **164**, 2–11 (2011).

[6] Lim, A. & Bai, R. Membrane fouling and cleaning in microfiltration of activated sludge wastewater. *Journal of membrane science* **216**, 279–290 (2003).

[7] Lee, H. *et al.* Cleaning strategies for flux recovery of an ultrafiltration membrane fouled by natural organic matter. *Water research* **35**, 3301–3308 (2001).

[8] Griffiths, I. M., Kumar, A. & Stewart, P. S. A combined network model for membrane fouling. *Journal of Colloid and Interface Science* **432**, 10–18 (2014).

[9] Sauret, A. *et al.* Clogging by sieving in microchannels: Application to the detection of contaminants in colloidal suspensions. *Applied Physics Letters* **105** (2014).

[10] Bacchin, P., Derekx, Q., Veyret, D., Glucina, K. & Moulin, P. Clogging of microporous channels networks: Role of connectivity and tortuosity. *Microfluidics and Nanofluidics* **17**, 85–96 (2014).

[11] Dersoir, B., de Saint Vincent, M. R., Abkarian, M. & Tabuteau, H. Clogging of a single pore by colloidal particles. *Microfluidics and Nanofluidics* **19**, 953–961 (2015).

[12] Chen, S., Liu, W. & Li, S. Effect of long-range electrostatic repulsion on pore clogging during microfiltration. *Physical Review E* **94**, 063108 (2016).

[13] Henry, C., Minier, J. P. & Lefèvre, G. Towards a description of particulate fouling: From single particle deposition to clogging. *Advances in Colloid and Interface Science* **185-186**, 34–

76 (2012).

[14] Schoenitz, M., Grundemann, L., Augustin, W. & Scholl, S. Fouling in microstructured devices: a review. *Chemical Communications* **51**, 8213–8228 (2015).

[15] Agbangla, G. C., Climent, É. & Bacchin, P. Experimental investigation of pore clogging by microparticles: Evidence for a critical flux density of particle yielding arches and deposits. *Separation and Purification Technology* **101**, 42–48 (2012).

[16] Wyss, H. M., Blair, D. L., Morris, J. F., Stone, H. A. & Weitz, D. A. Mechanism for clogging of microchannels. *Phys. Rev. E* **74**, 61402 (2006).

[17] van de Laar, T., ten Klooster, S., Schroën, K. & Sprakel, J. Transition-state theory predicts clogging at the microscale. *Scientific Reports* **6**, 28450 (2016).

[18] Georgieva, K., Dijkstra, D., Fricke, H. & Willenbacher, N. Clogging of microchannels by nano-particles due to hetero-coagulation in elongational flow. *Journal of colloid and interface science* **352**, 265–277 (2010).

[19] Mustin, B. & Stoeber, B. Deposition of particles from polydisperse suspensions in microfluidic systems. *Microfluidics and Nanofluidics* **9**, 905–913 (2010).

[20] Genovese, D. & Sprakel, J. Crystallization and intermittent dynamics in constricted microfluidic flows of dense suspensions. *Soft Matter* **7**, 3889–3896 (2011).

[21] Agbangla, G. C., Bacchin, P. & Climent, E. Collective dynamics of flowing colloids during pore clogging. *Soft Matter* **10**, 6303–6315 (2014).

[22] Linkhorst, J., Beckmann, T., Go, D., Kuehne, A. J. C. & Wessling, M. Microfluidic colloid filtration. *Scientific Reports* **6**, 22376 (2016).

[23] Zhu, G., Alexeev, A. & Balazs, A. C. Designing constricted microchannels to selectively entrap soft particles. *Macromolecules* **40**, 5176–5181 (2007).

[24] Hendrickson, G. R. & Lyon, L. A. Microgel translocation through pores under confinement. *Angewandte Chemie International Edition* **49**, 2193–2197 (2010).

[25] Sutera, S. P. & Skalak, R. The history of poiseuille's law. *Annual Review of Fluid Mechanics* **25**, 1–20 (1993).

[26] Rinne, H. *The Weibull distribution: a handbook* (CRC Press, 2008).

[27] Hänggi, P., Talkner, P. & Borkovec, M. Reaction-rate theory: fifty years after Kramers. *Rev. Mod. Phys.* **62**, 251–341 (1990).

[28] Kramers, H. A. Brownian motion in a field of force and the diffusion model of chemical reactions. *Physica* **7**, 284–304 (1940).

[29] Paine, A. J., Luymes, W. & McNulty, J. Dispersion polymerization of styrene in polar solvents. 6. Influence of reaction parameters on particle size and molecular weight in poly(N-vinylpyrrolidone)-stabilized reactions. *Macromolecules* **23**, 3104–3109 (1990).

[30] Lekkerkerker, H. N. W. & Tuinier, R. *Colloids and the depletion interaction*, vol. 833 (Springer, 2011).

[31] Yodh, A. G. *et al.* Entropically driven self-assembly and interaction in suspension. *Philosophical Transactions of the Royal Society of London A: Mathematical, Physical and Engineering Sciences* **359**, 921–937 (2001).

[32] Xia, Y. & Whitesides, G. M. Soft Lithography. *Angewandte Chemie International Edition* **37**,

550–575 (1998).

[33] Acheson, D. J. *Elementary fluid dynamics* (Oxford University Press, 1990).

Chapter 11

Sticky Squishy & Stuck

General Discussion

The main aim of this thesis was to understand the microscopic processes near, at, and within filtration membranes that ultimately may lead to membrane failure, or as we found out may also improve filtration behavior. In particular we addressed the question how we can design clever experiments to probe, quantify, visualize and disentangle i) the structure and dynamics of dense and non-ideal particle packings, ii) confined flows of complex fluids and iii) the mechanisms of pore clogging due to flow-induced aggregation. In this final chapter we look back at what we have accomplished in this thesis and place these findings in a wider context. We also illustrate the further development of these tools and findings to better understand processes occurring near and in membranes, with the aim to design better membrane separation technology based on these findings.

11.1 Colloidal and Atomic Glasses

In this section, our main research aim was to obtain a deeper insight into the effects of non-ideality, i.e deviations from hard sphere behavior by introducing attractions or softness, on the internal dynamics of colloidal glasses, as a proxy for the behavior of a membrane cake layer. In Chapter 3 we studied the effects of attractions, highlighting their highly non-trivial role in the glass transition and giving rise to two distinctly different types of colloidal glasses, a repulsive glass in which geometrical cages provide the mechanisms of kinetic arrest, and an attractive glass in which cohesive bonds cause the relaxations to slow down. Moreover, we evidenced that the transition from one to the other is discontinuous in nature and can be mapped onto the gel line in the colloidal phase dia-

gram. In Chapter 4 we developed a theoretical framework to explain the effect of particle softness on the fragility of the colloidal glass transition. Our microscopic theory provides a universal description of the colloidal glass transition that explains the mechanisms governing fragility in soft and compressible colloids. We verify this theory by quantitatively comparing our model with experimental data on a variety of soft colloidal systems. We have also explored the effects of particle softness in more depth in Chapter 5 by studying how such soft particles deform. By combining theory and experiments we show that these particles not only compress and shrink but also change their shape to accommodate the applied deformation. We show that both effects must be considered for a full, quantitative description of soft and compressible particles at high compression.

Our findings shed light on effects occuring in the cake layers that are formed during filtration processes. Typically, these layers consist of soft deformable components, such as proteins, which form a layer with varying attractive and repulsive forces; therefore very complex behavior is expected to take place. We have shown that the addition of slight attractive forces has large consequences, and thus should be considered when emulating real world problems like filtration cakes. Our work shows that variations in softness of particles will also lead to large differences in the behavior of dense packings. We have provided tools to analyse and understand this complex behavior, and our results can help elucidate the overall behavior of complex filtration cakes. For instance, the effects of protein filtration could be tested by fluorescently labeling proteins and observing their clogging behavior with confocal microscopy in a slightly modified version of our membrane microfluidic devices shown in Chapters 9 and 10.

These results not only help us understand the complex properties of a membrane cake, but also help our understanding of glasses in a broader sense. For example, colloidal glasses are considered a valuable model system for glass formation at the molecular scale[1, 2, 3, 4]. In particular, glasses of hard sphere colloidal particles have been studied extensively[3, 5], but this simple model system does not capture many of the complexities encountered at the molecular scale[5, 6]. As our results have highlighted the presence of cohesive bonds drastically change the glass transition, illustrating that the type of bonds formed between colloids

(or atoms) will have a large influence on the glass transition. Softness also has a large influence on the glass transition behavior, and allows the replication of the full spectrum of fragility as encountered at the molecular scale[5, 7]. Moreover, softness has recently been shown to also directly control the fragility of metallic glasses[8] (see Fig.11.1c, where the softness of the interatomic repulsion directly describes the fragility behavior), evoking strong similarities to our results for colloidal glasses. While our results have provided new insights into the effects of softness and cohesive bonding on the properties of glasses, and provide a universal description of the colloidal glass transition including fragility, much remains to be explored to understand glasses at much smaller length scales.

One of such unexplored topics is size disparity effects, which have recently been shown to have a tremendous influence on the behavior of a glassy system[10]. In the case of small particles (i.e. intruders) within a glassy matrix of much larger particles two distinctly different situations arise[10], depending on the size of these intruders. Sufficiently small intruders can diffuse freely on short times scales within the voids of the large matrix particles. As these voids become smaller (i.e. the volume fraction of the matrix particles increases) dynamics become arrested, but on long time scales the intruders still exhibit diffusive behavior (see Fig.11.1a). The intruder behavior changes drastically for slightly larger intruder particles, which starts to show strong anomalous dynamics. As the volume fraction of the matrix particles increases, an extended logarithmic decay becomes apparent, i.e. the intruders start to show glassy behavior[10] (see Fig.11.1b). Results such as these form a first step towards colloidal model systems that better describe behavior in real systems, such as binary metallic glasses[14] and nanocomposite materials[15]. Another interesting take on size disparity would be the investigation of glassy materials with small crystalline domains (i.e. size ratios closer to one, and comparable volume fractions), since such polycrystalline form is often found in bulk metallic glasses[16, 17].

Moreover, interactions in the molecular realm are rarely isotropic but often feature a distinct valency and directionality[18, 19]. With the surge of publications on new colloidal particle types in which these effects can be emulated[11, 12, 13, 20, 21, 22], this now makes it possible to also explore these effects on the glass transition and dynamics[23]. For example, to emulate directionality

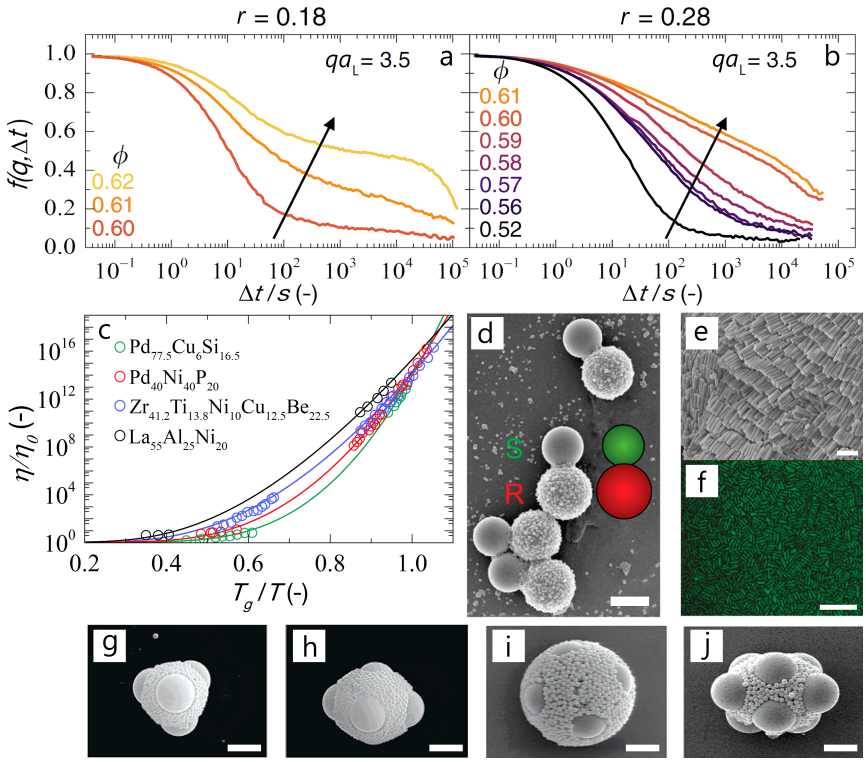

Figure 11.1: a-b) Collective intermediate scattering functions as a function of delay time Δt, for small intruders in a colloidal glass of larger particles. At large size differences (a) there are two distinct glass transitions, however, at smaller size differences (b) the intruders start to exhibit anomalous dynamics. Arrows indicate increasing ϕ. c) Normalized viscosity (η/η_0) as a function of glass-transition temperature (T_g/T) for different metallic glasses (circles, experimental data from[9]), lines show fitted curves based on the interionic repulsion. d) SEM image of colloidal patchy particles with smooth and rough parts, scale bar is 2 μm. e) SEM image of colloidal rods with an aspect ratio of ≈ 5, scale bar is 2 μm, f) Confocal image of similar rods (aspect ratio ≈ 3.6) in a disordered phase, scale bar is 10 μm. g-j) SEM images of bimodal colloidal clusters, with increasing number of large particles ($N = 4$, 5, 8 and 8 respectively), scale bar is 2 μm. Data in (a-b) adapted from[10], data in (c) adapted from[8], data in (d) adapted from[11], data in (e-f) reprinted from [12]. Copyright 2011 American Chemical Society. Data in (g-j) reprinted from [13]. Copyright 2005 American Chemical Society.

it is possible to create patchy particles where one end of the particle features a smooth surface and the opposite end features increased surface roughness[11]

(see Fig.11.1d), where due to the differences in surface roughness directionality in interactions arises[11]. Alternatively, the highly specific binding of DNA has been used to achieve valency[20]. Another departure from the simple hard sphere system can be achieved by the synthesis of anisometric colloids, such as rod-like particles[12]. Such colloidal rods feature a clear directional orientation that mirrors the behavior of molecular liquid crystals[12] (see Fig.11.1e-f). It is also possible to synthesize colloidal clusters that are nonisotropic, by combining small and large particles and fusing them (see Fig.11.1g-j), which yields flexible structures with control over different length scales[13].

While these novel particles are an interesting first step towards more complex materials, there are several limitations to their use, both in the produced quantity and their optical transparency[24]. To reach a complete microscopic understanding of the behavior of these non-isotropic, directional colloids further development of various synthesis routes is needed. High-yield, monodisperse particles are required for scattering techniques such as diffusive wave spectroscopy, that can be used to probe global dynamics[25]. A truly microscopic understanding, including their heterogeneous dynamics, will require optically transparent colloidal particles that enable in-depth studies in 3D utilizing confocal microscopy.

11.2 Flow Sensors in Confinement

Our main research aim in this section was to understand, measure and visualize complex flows in confinement. We have shown in Chapter 6 that even in highly concentrated suspensions of soft particles, segregation based on particle size takes place. We show that large clusters of particles exhibit cooperative, non-affine motion in order to accommodate fractionation at high densities. These results open up the way for a more sustainable process, by utilizing fractionation in flow at high concentrations, prior to using any filtration membranes. While processing at high concentrations is very complex, and mostly prevented in practice, this option intrinsically implies smaller process flows that are more economical e.g. by reducing evaporation, which is very energy intensive[26, 27].

In Chapter 7 we visualize and study the flow behavior of a displacing phase

in a complex, porous geometry and show that by understanding the flow behavior, the fluid properties of the displacing phase can be tuned to greatly increase displacement efficiency. Finally, in Chapter 8 we have made the first steps to develop a molecular flow sensor that would allow us to probe complex flows at the smallest scales.

Traditionally complex flows are visualized using PIV methods with tracer particles[28, 29]. This measurement approach places strict limits on the confinements that can be probed, as the tracer particles should not cause clogging, and should preferably not influence the flow behavior due to their presence. The molecular force sensors we have developed in Chapter 8 could be an alternative that does not have the previously mentioned limitations in its use. Depending on the hydrodynamic forces that the fluid exerts on these molecular flow sensors we measure a distinct optical signal, which could be used to spatially reconstruct an entire flow profile. This would allow us to measure in extreme confinements without disturbing the flow behavior. Such molecular sensors could be used to directly image forces in flows at the smallest scales, for instance in plant cells or animal tissue, or to visualize the flow through filtration membranes.

To explore this possibility we have developed a microfluidic tool to impose well-defined flow forces to our macro-molecular force sensors. By utilizing the converging flows in a flow-focusing junction, we can hydrodynamically stretch our polymers. A schematic illustration of this concept is shown in Fig.11.2a. Depending on their location in this flow-focusing stream we expect our polymers to exhibit different degrees of stretching (see Fig.11.2a for illustrations of an unstretched (1) and a stretched (2) polymer chain). Depending on their degree of stretching these flow sensors exhibit a distinct fluorescence emission spectrum (i.e. the FRET efficiency decreases as the polymers are stretched, as described in Chapter 8). This allows us to determine the degree of stretching at various locations within a microfluidic device by measuring the fluorescence emission, which allows us to correlate stretching to the hydrodynamic forces acting upon the polymer.

We record a full hyperspectral image series of our flow-focussing junction using our home-built hyperspectral microscope, as described in Chapter 8 (see Fig.11.2b, the two different streams are fluorescently labeled for clarity). We

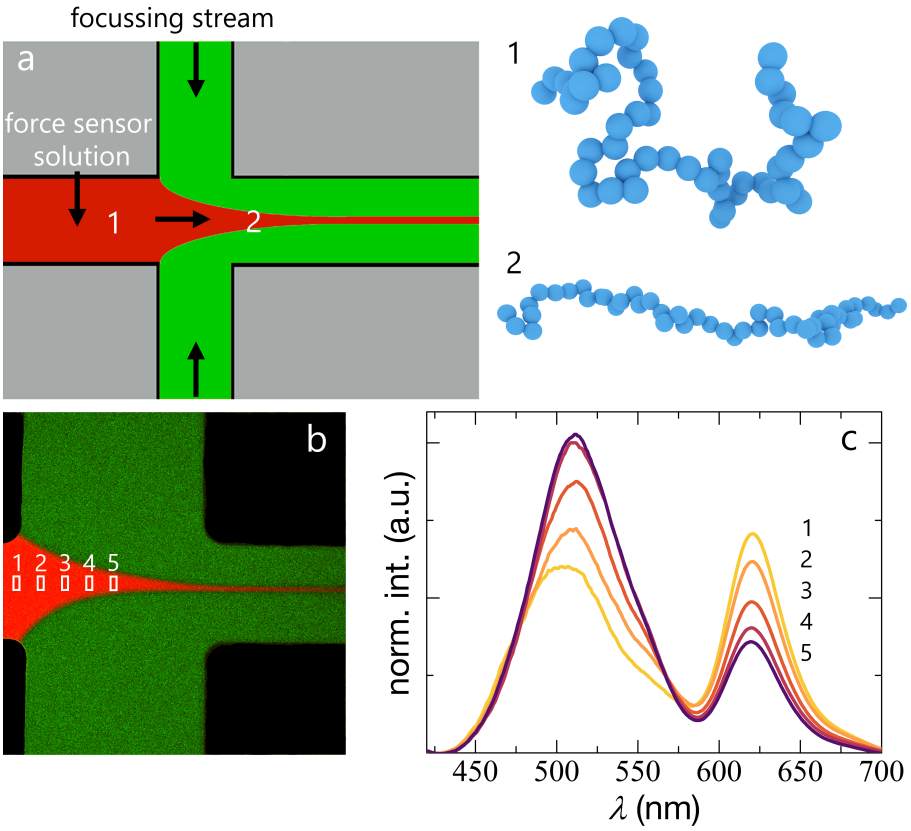

Figure 11.2: a) Schematic representation of the microfluidic device to stretch a force-sensing polymer in flow, with two images to illustrate the concept of a stretching polymer chain, b) shows an experimental confocal image of our microfluidic device where the different streams are colored with separate fluorescent dyes, boxes indicate parts of the image where fluorescent spectra are recorded as shown in c). c) Series of fluorescence emission spectra obtained for a force-sensing polymer flowing through our microfluidic device (numbers correspond to boxes in b), with the highest FRET efficiency found just before the start of the focusing junction, and the lowest FRET efficiency found during elongation.

compute the fluorescence emission spectrum at different locations from which we can see that as the flow converges the polymers are stretched more and more (see Fig.11.2c, the numbers correspond to the locations indicated in Fig.11.2b). We observe that the amount of acceptor excitation decreases (second peaks in

Fig.11.2c, $\lambda \approx 625$nm), while that of the donor (first peaks in Fig.11.2c, $\lambda \approx 510$nm) increases, indicating that the polymer is indeed undergoing stretching.

These preliminary results highlight that our molecular flow sensors would indeed allow us to measure flow profiles at the smallest scales with extremely high resolution. Both in the forces measured and spatially, as it is possible to measure an accurate emission spectrum for a single pixel, such that our resolution is only limited by the pixel size of our camera. Further research will focus on correlating the changes in FRET efficiency to the hydrodynamic forces, such that we can calibrate our flow sensors quantitatively; this is an ongoing effort within our group.

The details of flow in narrow pores in real membranes is not well understood as there are no experimental tools to visualize them. What we have shown in this thesis is that both complex structures as well as flow sensors are now within reach, and in the next section we will also highlight clogging. It is clear that the approach that we used here can contribute to gaining insights in various underlying mechanisms that are of essence to design novel membrane processes and operation procedures.

11.3 Universal Clogging Behavior

In the final section of this thesis we focus on a quantitative understanding of the microscopic mechanisms that lead to clogging. In Chapters 9 and 10 we have developed a model, based on transition-state theory, that quantitatively describes the effect of pore geometry (see Chapter 9), shear-enhanced aggregation (see Chapter 10) and particle interactions. We verified our model by extensive experiments using microfluidic devices mimicking membrane filtration with which we could independently test the effect of different variables. For example, we show how the local pore geometry greatly affects the rate at which clogging occurs, where we observe a factor 4 increase in the time till clogging of our microfluidic membrane device. Our model quantitatively describes these experimental observations and brings us closer to understanding clogging at the microscale.

These results shed light on many interesting concepts within membrane tech-

nology and design. We show the value of well-defined, micro-engineered pores where the entrance angle can be finely tuned, as this could drastically increase the operational lifetime of a filtration membrane. We provide experimental proof for the importance of attractive forces between particles, and the enormous negative effects such attraction has on the filtration process, where we observe that the presence of slight attractive forces can increase the clogging rate by at least an order of magnitude. The first steps in particle-agglomerated clogging are related to particles sticking to the wall, which could be drastically reduced by engineering the wall surface through surface chemistry, where anti-fouling brushes or monolayers could help delay clogging significantly[30, 31]. Our results also highlight the negative impact of larger particles (or larger impurities and agglomerates), whose sieving kinetics will completely dominate the clogging process[32]. In our experiments these negative effects are prevented by the addition of a dust filter. For actual membrane filtration processes, this implies that a pre-filter may be needed to prevent these negative effects. Finally we show the value of having a non-connected porous membrane structure, where every pore will clog separately. The negative effects of connected clogging behavior can be suppressed through the application of a cross-flow flux, or through micro-engineering the membrane structure such that every pore is sufficiently far away from their neighbors.

In a much broader context clogging is observed on many different length scales and in many different systems[33, 34]; blood flow through blood vessels[35], traffic jams[36, 37] and crowds of humans (or animals) passing through narrow passages[38, 39, 40]. Such observations raise the intriguing question whether or not there is a universality to clogging phenomena. Is there some underlying unifying description for clogging, irrespective of length scales? At first glance this certainly seems the case. For instance, a common feature encountered in virtually all clogging scenarios, ranging from mice moving through constrictions[41], clogging in silo's[42], colloidal particles moving through constrictions[43, 44], animals or people moving through narrow passages[38, 39] etc. is that of intermittency[33], i.e. the time between a clogged state and an unclogged state[33]. This time is usually referred to as the time in between bursts of movement, or the time lapse, τ. In all these different scenarios similar scaling relations are observed

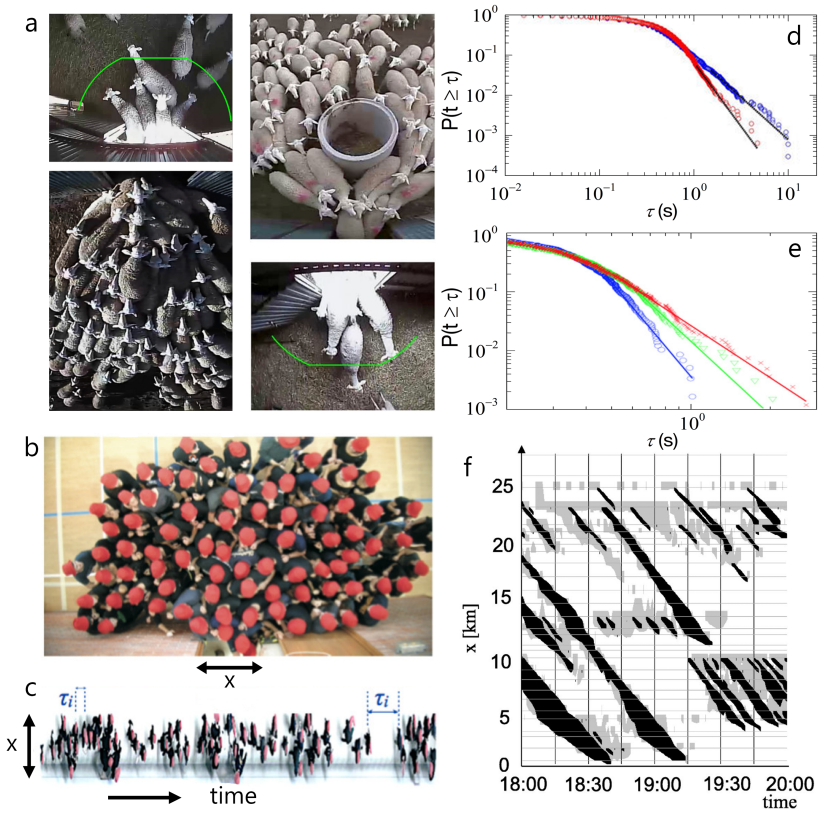

Figure 11.3: a) Sheep passing through a constricted entrance, with and without an obstacle, b) people passing through a narrow constricted doorway (with width x), c) spatiotemporal diagram of (b), where τ_i indicates the time lapse between passage of people through the doorway. d) cumulative distribution functions of the time lapse τ for sheep (from (a)), with (red line) and without (blue line) obstacle prior to the constriction, fitted lines show power law behavior. e) cumulative distribution functions of τ for humans (from (b-c)), for low (blue), medium (green) and high (red) competitiveness scenarios, lines show power law behavior. f) Histogram of traffic jams as a function of time and location, black shows traffic jams, which propagate throughout the traffic in time, gray shows slowed down, but moving traffic. Data in (a,d) reprinted with permission from [33] and [38], copyright 2015 by the American Physical Society. Data in (b-c,e) reprinted with permission from [39], copyright 2015 by the American Physical Society. Data in (f) reprinted with permission from [36], copyright 2002 by the American Physical Society.

for τ, here we highlight two specific cases; sheep moving through a constriction

and humans crowding through a narrow doorway[33, 39].

As a herd of sheep passes through a doorway at times these sheep will get stuck (or get clogged) at the narrow constriction, where τ can be directly measured (see Fig.11.3a for experimental data on sheep clogging, without (left) and with (right) additional obstruction). Similar observations can be made for humans moving through an obstruction, where τ is again the time in between bursts of movement (see Fig.11.3b and c for experimental data on humans moving through an obstructed doorway, where (c) shows a spatiotemporal diagram of such movement). If we compare the cumulative distribution functions for τ of these two very different clogging processes we see a striking resemblance. All these different clogging scenarios (e.g. colloidal flow, hopper flow, flow of humans and sheep) can be described by powerlaw behavior (see Fig.11.3d-e), independent of length scales or system specific differences[33]. Finally, we see similar intermittent behavior in the motion of traffic jams[36], where periods of complete stand-still alternate with slow periods of slow movement (Fig.11.3f, where black areas represent complete stand-still and gray areas show slow motion).

These results hint at a possible universal description of clogging, based on a transition between different intermittent regimes. Such a general approach would open up new avenues to control and tune flow through constrictions to minimize the negative effects of clogging[33]. For instance, by studying systems where clogging does not occur, and apply such lessons to other processes. However, we should also consider the possibility that such a general description is not possible due to the different complex natures of each separate clogging process, especially at the colloidal scale. Not only the differences in length scales, but differences in thermal and athermal systems, active and passive systems, interaction potentials, geometry effects, deformability etc. Perhaps the combination of these effects results in too specific problems for each length scale, that cannot be universally described.

In addition to studying universality in clogging, there are multiple interesting research avenues to pursue in colloidal clogging. For example, by changing the clogging geometry to a porous, interconnected system we can mimic membrane filtration much more closely. Clogging of odd particle shapes (such as those shown in Fig.11.1d-j) and clogging of soft particles (as shown in section 11.1 soft-

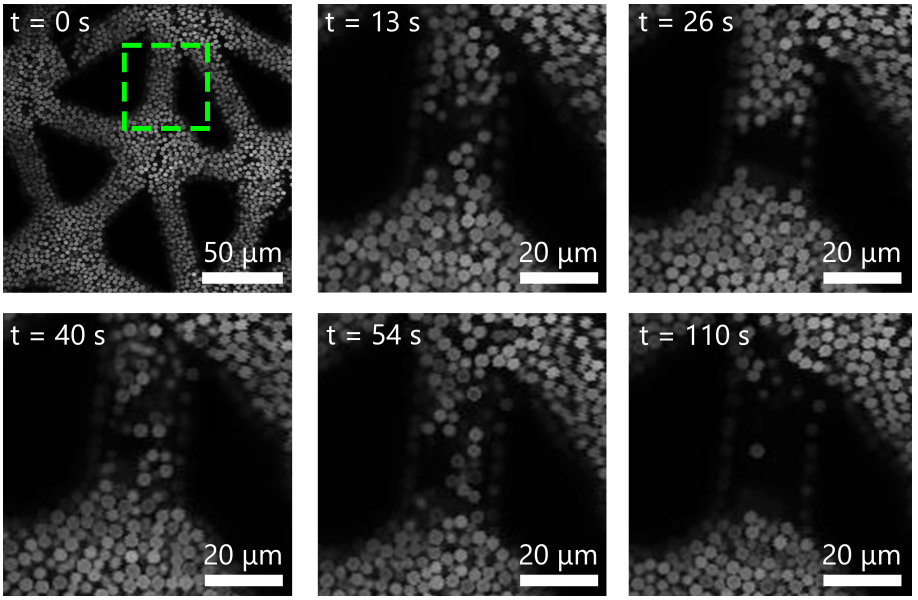

Figure 11.4: Confocal microscope time lapse images of a colloidal suspension flowing through a complex porous geometry (see Chapter 7 for details on the geometry), $t = 0$ shows a larger overview for the geometry, the subsequent images focus on a clog forming in a channel, where the channel blocks and unblocks over time, and ends in a completely blocked state.

ness has a large influence on the behavior of a glass, and is expected to also have a large influence on the clogging behavior) would both form a link that is closer to practical systems compared to the general hard sphere approach.

By utilizing our design for a porous network from chapter 7 we can study clogging in complex geometries as a proxy for membrane filtration. We see that clogging becomes a much more complex problem, since clogs can form and will divert the suspension around it towards other constrictions within the porous structure. While the structure is random we have full control over the parameters that determine the final structure, which would allow us to make a direct comparison between an interconnected membrane model and a micro-engineered model as we have used previously in Chapters 9 and 10. Such a comparison would allow us to disentangle the effects of an interconnected structure. In Fig.11.4 we show a time series of a single constriction clogging within a com-

plex pore network model, designed in a microchip. We observe that the flow is diverted around the constriction as clogging occurs. We also observe intermittent unclogging before the constriction finally becomes completely blocked. These preliminary results show that to understand clogging in complex geometries we will need to develop new analysis methods and new models to take into account effects such as interconnected constrictions.

11.4 Conclusion

While membrane failure is a very complex problem, by finding and creating a closer link to soft matter physics we can gain deeper insight and understanding into the separate problems that contribute to membrane failure, as the various sections in this thesis have shown. We have treated these problems as separate, while in reality there is a close link between all concepts. The major challenge will be to develop a systems approach and description of the full membrane process in a soft matter context, linking all theories describing the separate problems together and use a unified systems theory to guide the development and design of new processes and membranes.

However, based on the results presented in this thesis we can already speculate on the design of future filtration processes. An ideal filtration process would include well controlled, confined flows leading up to the membrane area, as to allow pre-fractionation due to shear-induced diffusion to occur. The membrane surface would contain micro-engineered pores so that the pore geometry can be tuned and optimized to reduce clogging. The total membrane area would also have to be kept relatively short, as to minimize the pressure differences that occur over the membrane area. A homogeneous pressure field, and thus well-controlled flow conditions are vital to ensure that we can predict and engineer our filtration set-up to minimize the negative effects of clogging, and that flow conditions remain favorable to promote pre-fractionation. Such speculation once more confirms the need for a systems approach to include all these effects into a single theory and description, so that we can truly develop, design and optimize membranes for the future.

References

[1] Lindsay, H. & Chaikin, P. Elastic properties of colloidal crystals and glasses. *The Journal of Chemical Physics* **76**, 3774–3781 (1982).

[2] Rosenberg, R., Thirumalai, D. & Mountain, R. Liquid, crystalline and glassy states of binary charged colloidal suspensions. *Journal of Physics: Condensed Matter* **1**, 2109 (1989).

[3] Pusey, P. N. & Van Megen, W. Phase behaviour of concentrated suspensions of nearly hard colloidal spheres. *Nature* **320**, 340–342 (1986).

[4] Pusey, P. N. & van Megen, W. Observation of a glass transition in suspensions of spherical colloidal particles. *Physical review letters* **59**, 2083 (1987).

[5] Hunter, G. L. & Weeks, E. R. The physics of the colloidal glass transition. *Reports on Progress in Physics* **75**, 066501 (2012).

[6] Sciortino, F. & Tartaglia, P. Glassy colloidal systems. *Advances in Physics* **54**, 471–524 (2005).

[7] Mattsson, J. *et al.* Soft colloids make strong glasses. *Nature* **462**, 83–86 (2009).

[8] Krausser, J., Samwer, K. H. & Zaccone, A. Interatomic repulsion softness directly controls the fragility of supercooled metallic melts. *Proceedings of the National Academy of Sciences* **112**, 13762–13767 (2015).

[9] Johnson, W. L., Demetriou, M. D., Harmon, J. S., Lind, M. L. & Samwer, K. Rheology and ultrasonic properties of metallic glass-forming liquids: A potential energy landscape perspective. *MRS bulletin* **32**, 644–650 (2007).

[10] Sentjabrskaja, T. *et al.* Anomalous dynamics of intruders in a crowded environment of mobile obstacles. *Nature communications* **7** (2016).

[11] Kraft, D. J. *et al.* Surface roughness directed self-assembly of patchy particles into colloidal micelles. *Proceedings of the National Academy of Sciences* **109**, 10787–10792 (2012).

[12] Kuijk, A., van Blaaderen, A. & Imhof, A. Synthesis of monodisperse, rodlike silica colloids with tunable aspect ratio. *Journal of the American Chemical Society* **133**, 2346–2349 (2011).

[13] Cho, Y.-S. *et al.* Self-organization of bidisperse colloids in water droplets. *Journal of the American Chemical Society* **127**, 15968–15975 (2005).

[14] Miracle, D. B. A structural model for metallic glasses. *Nature materials* **3**, 697–702 (2004).

[15] Novak, B. M. Hybrid nanocomposite materials - between inorganic glasses and organic polymers. *Advanced Materials* **5**, 422–433 (1993).

[16] Lewandowski, J., Wang, W. & Greer, A. Intrinsic plasticity or brittleness of metallic glasses. *Philosophical Magazine Letters* **85**, 77–87 (2005).

[17] Eckert, J., Das, J., Pauly, S. & Duhamel, C. Mechanical properties of bulk metallic glasses and composites. *Journal of materials research* **22**, 285–301 (2007).

[18] Bianchi, E., Blaak, R. & Likos, C. N. Patchy colloids: state of the art and perspectives. *Physical Chemistry Chemical Physics* **13**, 6397–6410 (2011).

[19] van Blaaderen, A. Materials science: colloids get complex. *Nature* **439**, 545–546 (2006).

[20] Wang, Y. *et al.* Colloids with valence and specific directional bonding. *Nature* **491**, 51–55 (2012).

[21] Wang, Y. *et al.* Three-dimensional lock and key colloids. *Journal of the American Chemical Society* **136**, 6866–6869 (2014).

[22] Zhang, G., Wang, D. & Möhwald, H. Decoration of microspheres with gold nanodots - giving colloidal spheres valences. *Angewandte Chemie International Edition* **44**, 7767–7770 (2005).

[23] Glotzer, S. C. & Solomon, M. J. Anisotropy of building blocks and their assembly into complex structures. *Nature materials* **6**, 557–562 (2007).

[24] Kodger, T. E., Guerra, R. E. & Sprakel, J. Precise colloids with tunable interactions for confocal microscopy. *Scientific reports* **5** (2015).

[25] Pine, D., Weitz, D., Chaikin, P. & Herbolzheimer, E. Diffusing wave spectroscopy. *Physical review letters* **60**, 1134 (1988).

[26] Schroën, K., van Dinther, A. & Stockmann, R. Particle migration in laminar shear fields: A new basis for large scale separation technology? *Separation and Purification Technology* **174**, 372–388 (2017).

[27] Drijer, I., van de Laar, T., Vollebregt, H. & Schroën, C. From highly specialised to generally available modelling of shear induced particle migration for flow segregation based separation technology. *Separation and Purification Technology* **192**, 99–109 (2018).

[28] Meinhart, C. D., Wereley, S. T. & Santiago, J. G. Piv measurements of a microchannel flow. *Experiments in fluids* **27**, 414–419 (1999).

[29] Adrian, R. J. & Westerweel, J. *Particle image velocimetry*. 30 (Cambridge University Press, 2011).

[30] Nady, N. *et al.* Modification methods for poly (arylsulfone) membranes: a mini-review focusing on surface modification. *Desalination* **275**, 1–9 (2011).

[31] Wang, Z., Pujari, S. P., van Lagen, B., Smulders, M. M. & Zuilhof, H. Highly polymer-repellent yet atomically flat surfaces based on organic monolayers with a single fluorine atom. *Advanced Materials Interfaces* **3** (2016).

[32] Sauret, A. *et al.* Clogging by sieving in microchannels: Application to the detection of contaminants in colloidal suspensions. *Applied Physics Letters* **105**, 074101 (2014).

[33] Zuriguel, I. *et al.* Clogging transition of many-particle systems flowing through bottlenecks. *Scientific reports* **4**, 7324 (2014).

[34] Sheldon, H. G. & Durian, D. J. Granular discharge and clogging for tilted hoppers. *Granular Matter* **12**, 579–585 (2010).

[35] Appelblad, M. & Engström, G. Fat contamination of pericardial suction blood and its influence on in vitro capillary-pore flow properties in patients undergoing routine coronary artery bypass grafting. *The Journal of Thoracic and Cardiovascular Surgery* **124**, 377–386 (2002).

[36] Kerner, B. S. Empirical macroscopic features of spatial-temporal traffic patterns at highway bottlenecks. *Physical Review E* **65**, 046138 (2002).

[37] Nagatani, T. The physics of traffic jams. *Reports on progress in physics* **65**, 1331 (2002).

[38] Garcimartín, A. *et al.* Flow and clogging of a sheep herd passing through a bottleneck. *Physical Review E* **91**, 022808 (2015).

[39] Pastor, J. M. *et al.* Experimental proof of faster-is-slower in systems of frictional particles flowing through constrictions. *Physical Review E* **92**, 062817 (2015).

[40] Seyfried, A. *et al.* New insights into pedestrian flow through bottlenecks. *Transportation*

Science **43**, 395–406 (2009).

[41] Saloma, C., Perez, G. J., Tapang, G., Lim, M. & Palmes-Saloma, C. Self-organized queuing and scale-free behavior in real escape panic. *Proceedings of the National Academy of Sciences* **100**, 11947–11952 (2003).

[42] Janda, A. *et al.* Unjamming a granular hopper by vibration. *EPL (Europhysics Letters)* **87**, 24002 (2009).

[43] Haw, M. Jamming, two-fluid behavior, and 'self-filtration' in concentrated particulate suspensions. *Physical review letters* **92**, 185506 (2004).

[44] Genovese, D. & Sprakel, J. Crystallization and intermittent dynamics in constricted microfluidic flows of dense suspensions. *Soft Matter* **7**, 3889–3896 (2011).

Summary

Separation of components is carried out at many different levels, ranging from sieving of particles, to gas separation. In all these fields membranes are known as greener, more sustainable options, and therefore it is not surprising that their use has seen a very steady increase over the years. Membrane filtration processes are widely used in large number of industrial applications, ranging from dairy processing, to pharmaceutical fractionation and waste-water treatment. For membrane processes such as micro- and ultrafiltration, in which pores act as gatekeepers, one of the major challenges is fouling and the associated clogging of membrane pores. Such clogging and fouling occurs due to the gradual accumulation of solid or semisolid matter in and on the membrane during its operational lifetime. This accumulated layer is commonly referred to as a filter cake and blocks flow through the membrane, which reduces the lifetime of a membrane and requires extensive cleaning. Delaying or preventing fouling would increase the lifetime of membranes and would contribute to a more sustainable process. However, solving the complex problem of fouling requires fundamental insight into what occurs within a membrane at the microscale, and that is generally not the sale that is considered when developing membrane systems.

In this thesis we combined experiments and theory to better understand the processes occurring near, at and within filtration membranes in order to further our understanding of fouling and clogging. We create links between problems encountered in membrane technology and those studied in soft matter science. We focus on three major themes; i) the structure and dynamics of dense and non-ideal particle packings, ii) confined flow of complex fluids and iii) the mechanisms of pore clogging. By studying these problems we have not only gained

insight in the microscopic processes and mechanisms that underlie membrane filtration but also further the fundamental understanding of these classical soft matter phenomena.

In **Chapter 2** we provide a technical overview of the various synthesis routes used in this thesis to design and make colloidal model systems that are tailored to the specific requirements of our various experiments. In **Chapter 3** we explore the effect of attractive forces on the colloidal glass transition. We show that attraction drastically changes the behavior of a colloidal glass, resulting in a solid-solid transition. We provide the first experimental proof of the predicted discontinuity for this solid-solid transition. The presence of small depletants which induce attractive interactions are common in real-world processing streams; studying the attractive glass transition brings us one step closer to linking colloidal glasses and the behavior of the fouling layer that forms on top of a membrane.

While hard spheres are extensively studied in soft matter science, these systems represent a very idealized situation. In the daily practice of large-scale processing, soft deformable particles are expected to determine the system behavior. In **Chapter 4** we derive a microscopic theory to explain how softness changes the behavior of colloidal glasses, in particular their fragility and strength. Our theory provides a universal description of the glass transition for soft colloidal systems. We use our theory to explain the mechanisms of fragility, which has a large influence on the ability to process glasses. As such, it will have a large influence on the properties of e.g. a filter cake. In **Chapter 5** we take this research one step further and investigate how soft particles deform in dense packings, and show that both shrinkage due to compression and deformation must be taken into account. This research opens up a way to understand the behavior of soft particles moving through constricted membrane pores, and builds the foundation to quantify differences encountered during filtration of rigid and soft particles.

In **Chapter 6** we show how flow through very narrow channels can be used to achieve a pre-fractionation. Our results explore the limits of this fractionation technique (called shear-induced diffusion) to understand if, and how such fractionation occurs at very high concentrations up to volume fractions of 0.6

or higher for deformable particles. Ultimately, this could lead to energy efficient fractionation processes that can be carried out at higher concentrations. Such a process would be radically different from current process technologies which focus on diluted feed streams. In **Chapter 7** we develop a microfluidic device to study and visualize two-phase flow in a random porous network. We show that by understanding the complex displacement cascade we can tailor the displacing fluid properties in such a way that we can greatly enhance the displacement efficiency. These results illustrate the power of direct visualization at the microscopic scale to gain quantitative understanding of the important parameters. In **Chapter 8** we make the first steps toward a novel flow sensor that would enable the direct, quantitative visualization of flows in extreme confinements (i.e. nm scale). These sensors would offer unprecedented visualization capabilities of flows even at the nanometer scales. We calibrate these sensors at the single-molecule scale, which is the first demonstration of optical force sensing in single molecules.

Finally we investigate pore clogging, which leads to the build-up of a filter cake and is the start of decreased membrane performance. A large variety of factors play a role in how, when and where a clog forms. To disentangle these effects we developed microfluidic tools to study clogging at the single pore level. In **Chapter 9** we show how small changes in the pore geometry have a massive impact on the clogging behavior. The angle under which a constriction is placed with respect to the flow direction can delay clogging by at least a factor 4. Again, we show the large effects that slight attractive forces can have, leading to a decrease in clogging time of more than an order of magnitude. We account for both these effects by developing a new model based on transition-state theory. The generated insights can be used in the design of smarter, micro-engineered membranes in which the effects of clogging are delayed, and ideally prevented. In **Chapter 10** we take our microfluidic approach one step further and modify our design to emulate a cross-flow membrane system; the most prevalent membrane filtration configuration in industry. We show that the flow through the membrane completely dictates the clogging behavior in the pore and we extend our model to explain these effects. Moreover, we show that, while the cross-flow flux does not influence the rate of primary clogging directly, it does influence the

build-up of a cake layer and its effect on neighboring pores. These results help us understand which factors play a pivotal role in membrane clogging, and form a basis from which we could design new, and improved membrane systems.

The work in this thesis highlights how a soft matter approach, utilising the tools from soft matter science can help shed light on the complex processes that occur during membrane filtration. Through direct visualization at the microscopic scale, combined with quantitative theory we gain a deep, microscopic understanding of a wide variety of processes. In the **General Discussion** we put our work in a broader context, provide routes to develop the work further and reflect on how our results can be used in the future design of innovative membrane filtration systems.

List of Publications

THIS DISSERTATION:

- T. van de Laar, H. Schuurman, P. van der Scheer, J.M. van Doorn, J. van der Gucht and J. Sprakel: **Light from Within; Sensing Weak Strains and femtoNewton Forces in Single Molecules** *Chem*, 4(2), 269-284 (2018) (Chapter 8)
- R. Zwieten, T. van de Laar, J. Sprakel and K. Schroën: **From Cooperative to Uncorrelated Clogging in Cross-flow Microfluidic Membranes** *Scientific Reports 8, 5687* (2018) (chapter 10)
- T. van de Laar, K. Remmers, K. Schroën and J. Sprakel: **Oil Displacement by Visco-Elastic Fluids in a Disordered Micromodel** submitted
- T. van de Laar, K. Schroën and J. Sprakel: **Synthesis of Colloidal Systems** manuscript in preparation
- I. Bouhid De Aguiar, T. van de Laar, M. Meireles, A. Bouchoux, J. Sprakel and K. Schroën: **Deswelling and Deformation of Microgels in Concentrated Packings** *Scientific Reports* 7, 10233 (2017) (Chapter 5)
- P. van der Scheer, T. van de Laar, J. van der Gucht, D. Vlassopoulos and J. Sprakel: **Fragility and Strength in Nanoparticle Glasses** *ACS Nano* 11(7), 6755-6763 (2017) (Chapter 4)
- T. van de Laar, R. Higler, K. Schroën and J. Sprakel: **Discontinuous Nature of the Repulsive-to-Attractive Colloidal Glass Transition** *Scientific Reports* 6, 22725 (2016) (Chapter 3)□

- T. van de Laar, S. ten Klooster, K. Schroën and J. Sprakel: **Transition-state Theory Predicts Clogging at the Microscale** *Scientific Reports* 6, 28450 (2016) (Chapter 9)
- T. van de Laar, K. Schroën and J. Sprakel: **Cooperativity and Segregation in Confined Flows of Soft Binary Glasses** *Physical Review E* 92, 022308 (2015) (Chapter 6)

OTHER WORK:

- I. Drijer, T. van de Laar, H.M. Vollebregt and C.G.P.H. Schroën: **From Highly Specialised to Generally Available Modelling of Shear Induced Particle Migration for Flow Segregation Based Separation Technology.** *Separation and Purification Technology* 192, 99-109 (2018)
- J.M. van Doorn, J. Bronkhorts, R. Higler, T. van de Laar and J. Sprakel: **Linking Particle Dynamics to Local Connectivity in Colloidal Gels** *Physical Review Letters* 118, 188001 (2017)
- J. Appel, N. de Lange, H.M. van der Kooij, T. van de Laar, J.B. ten Hove, T.E. Kodger and J. Sprakel: **Temperature Controlled Sequential Gelation in Composite Microgel Suspensions** *Particle and Particle Systems Characterization* 32, 764-770 (2015)

Acknowledgments

A not so long time ago, in a lab not so very far away... Hier is het dan, na 4 jaar werk is m'n thesis af. Ik ben erg blij dat ik nu kan zeggen dat dit boekje de verzameling is van m'n werk de afgelopen 4 jaar!

Natuurlijk is alles in dit boekje niet alleen mijn werk, maar het resultaat van vele fantastische samenwerkingen en uitstekende begeleiding. Als eerste wil ik graag Joris en Karin bedanken voor de geweldige begeleiding en alles daaromheen tijdens deze 4 jaar. Of eigenlijk al tijdens m'n MSc thesis, wat er uiteindelijk voor heeft gezorgd dat ik nu hier sta. En dat ondanks het raarste solicatie gesprek ooit! Er was altijd ruimte en tijd om het over het werk te hebben, maar ook altijd ruimte voor niet werkgerelateerde dingen. Zonder jullie steun en begeleiding was dit eindresultaat nooit iets geworden waar ik zo trots op ben.

Daarnaast wil ik graag al m'n collega's bedanken bij FPE en PCC. Thank you all for the great atmosphere and countless hours of fun discussing research, but also the less serious sides of work and life! In het bijzonder wil ik iedereen in de quarantaine zone bedanken, ook al ben ik in de laaste paar maanden soms thuis gaan schrijven, het was altijd weer een feest om het kantoor binnen te lopen. Je zou kunnen zeggen dat ik daar nooit boos om kon worden.

Ook wil ik graag al m'n studenten bedanken voor de tijd en energie die we samen in dit project hebben gestoken; Karlijn, Pieter, Andrea, Sten, Kieke, Hent, Ralph en Henk. Ik vond het een eer en een groot plezier jullie allemaal te hebben mogen begeleiden. Jullie waren een belangrijk onderdeel van waarom ik altijd met plezier naar m'n werk ben gegaan. Ik ben dan ook erg blij dat zoveel van jullie werk rechtreeks in dit boekje is opgenomen!

Naast collega's en studenten wil ik ook graag al m'n vrienden bedanken, vooral iedereen in Wageningen. Dankzij jullie was niet alleen het werk leuk, maar was er naast werk ook altijd iets leuks om naar uit te kijken. Of het nu Dungeons & Dragons was, froyo, films, series of eten, altijd was er iets te doen!
Als laatste wil ik graag m'n familie bedanken voor de steun en goede adviezen. Pap en mam, dankzij jullie opvoeding sta ik hier, en ik denk niet dat ik jullie daar ooit genoeg voor kan bedanken. Lisette, ik vind het super dat jij bij mij op het podium staat, een beter zusje zou ik niet kunnen wensen.
Finally, Signe, I'm incredibly happy I get to celebrate this moment with you, and I hope we'll get plenty more great moments to share together.

Houdoe en bedankt!

Ties

About the Author

Ties Xander van de Laar was born on the 14th of October, 1988, in Veghel, the Netherlands. He went to high school at the Zwijsen College, where he obtained his VWO diploma in 2007 with a major in Nature and Technology.

Later that year he started his study in Food Technology at Wageningen University with a minor in Operations Research and Logistics. After finishing his BSc he continued his education at Wageningen University with a master in Food Technology with a specialization in Sustainable Food Process Engineering. As part of his masters he went To Copenhagen University for a minor in dairy processing. Finally he went to the United States for an internship at Mars Chocolate, working on novel process improvements related to the M&M production process.

After finishing his MSc in 2013, Ties went on to work as a PhD candidate at Wageningen University in the laboratory of Food Process Engineering and the Physical Chemistry and Soft Matter group. This thesis, entitled 'Sticky, Squishy and Stuck: a soft matter approach to membrane failure', is the result of that PhD project.

Overview of completed training activities

Discipline specific activities

OSPT course: Numerical methods for engineers, The Netherlands (ISPT, 2014)

Flow and clogging in bottlenecks workshop, Spain (CECAM, 2014)

Dutch Soft Matter Meeting, The Netherlands (2014-2016)*

Jülich Soft Matter Meeting, Germany (Jülich, 2015)*

APS March meeting, United States (APS, 2015)*

Physics@FOM, Netherlands (FOM, 2015)*

Topical Workshop Dense Suspension Flow, United Kingdom (Softcomp, 2015)

Int. Membrane Science and Technology Conference, Australia (IMSTEC, 2016)*

Condensed Matter CMD26, The Netherlands (EPS, 2016)*

MechanoChemBio conference, Germany (MPI, 2017)*

CHAINS, The Netherlands (NWO, 2017)*

*poster or oral presentation

General courses

VLAG PhD week, The Netherlands (VLAG, 2014)

Global Young Scientist Summit: GYSS@One-North, Singapore (NRF Singapore, 2016)

Career Orientation, The Netherlands (WGS, 2017)

Journal Club, The Netherlands (2014-2017)

Optionals

Group meetings & colloquia (2014-2017)

Digital lab journal pilot (2014-2015)

PhD trip Brazil & Chile (2015)

The research described in this thesis was supported financially
by the Institute for Sustainable Process Technology (ISPT)

Printed by Digiforce - Proefschriftmaken.nl in 125 copies